

Modeling and Applications of Acoustic and Electromagnetic Wave Interaction

by
Amelia Marie Buerkle

A dissertation submitted in partial fulfillment
of the requirements for the degree of
Doctor of Philosophy
(Electrical Engineering)
in The University of Michigan
2007

Doctoral Committee:

Professor Kamal Sarabandi, Chair
Professor David R. Dowling
Professor Brian E. Gilchrist
Professor Amir Mortazawi

TABLE OF CONTENTS

LIST OF FIGURES	iv
LIST OF TABLES	xii
CHAPTER	
I. Introduction	1
1.1 Motivation for Multi-sensor Systems	1
1.2 Definition of Acousto-Electromagnetic Wave Interaction	2
1.3 Advantages Over Single-Sensor Systems	3
1.4 Overview of Previous Work	5
1.5 Summary of Contribution	10
1.6 Document Overview	10
II. Applications	12
2.1 Buried Object Detection	12
2.2 Tumor Detection	18
2.3 Non-destructive Evaluation	27
III. Acousto-EM Model Development	29
3.1 Overview	29
3.2 Boundary Perturbation	32
3.3 Density Modulation	37
IV. Implementation in the Finite-difference Time-domain Method	39
4.1 Brief Introduction to Basic FDTD	39
4.2 Implementation	43
V. Physical Model	57
VI. Case Studies of the Bistatic Doppler Component	61
6.1 Polyethylene Cylinder	62
6.2 Layered Cylinder	76
6.3 Observations	84
VII. Wideband, Bistatic Doppler Component for Applications in NDE	90
7.1 Introduction	90

7.2 Bistatic Doppler Component Results	93
VIII. Time-Reversal Focusing for Applications in NDE	117
8.1 Source Focusing Using Time Reversal	118
8.2 Processing the Scattered Field	119
8.3 Results Using Focusing of the Unshifted Received Fields	121
8.4 Processing the Doppler Component Scattered Field	129
IX. Systems for Detection	135
9.1 System Overview	135
X. Antennas for Detection	143
10.1 Double-resonant DRA design	144
10.2 Magneto-dielectric resonator antenna design	164
10.3 DRA Array Design	165
XI. Conclusions	176
11.1 Future Work	177
APPENDICES	180
BIBLIOGRAPHY	198

LIST OF FIGURES

Figure

1.1	Diagram of acousto-EM wave interaction. Acoustic or seismic excitation causes the object to vibrate. The incident electromagnetic wave is modulated by the object vibration giving rise to the Doppler component in the scattered signal.	3
1.2	Sample spectrum of electromagnetic field scattered from an object mechanically vibrating at acoustic frequency f_a . The unshifted electromagnetic frequency is denoted by f_{EM}	4
2.1	Proposed approach using acousto-EM wave interaction for the detection and identification of buried objects.	17
2.2	A typical vibro-acoustographic imaging system. Two confocal US beams produce a single AM US beam at the desired focal point. Cyclic vibration of the tissue at the focal point gives rise to the acoustic emission. The amplitude and/or phase of the acoustic emission is detected with a hydrophone and a raster image is formed. Experiments are carried out in a water tank to avoid acoustic impedance mismatches between the US source, hydrophone, and background medium.	22
2.3	A possible configuration using acousto-EM wave interaction for obtaining the Doppler response of tumors. A single AM US source provides an acoustic plane wave and the depth resolution. The microwave imaging system provides the remaining two dimensions of resolution and detects the Doppler component. The US source is stationary and the non-contact microwave array can be scanning or stationary depending on the array size.	24
2.4	Two-dimensional cut of a possible approach using acousto-EM wave interaction for medical imaging of dielectric and elasticity properties of tissue. The two US beams produce an AM signal with modulation frequency $\Delta\omega$ along a \hat{z} directed line. The microwave imaging system detects the Doppler component and provides resolution along the z axis. The US sources and microwave system are stationary and use beam steering to focus on different regions. The microwave imaging system is non-contact.	25
3.1	Two effective time scales of the problem. The electromagnetic solution reaches steady state before the object state has changed substantially. The QS approximation considers snapshots of the object at various instances over the acoustic time scale, labeled τ_i	31
3.2	Applying sheet boundary conditions to the vibrating object's surface replaces it with a stationary scatterer having time varying surface impedance and admittance.	34
4.1	Two-dimensional FDTD mesh for TM and TE polarizations.	42

4.2	Current locations on <i>PEC</i> and dielectric objects for TM polarization.	45
4.3	Current locations on <i>PEC</i> and dielectric objects for TE polarization.	46
4.4	The boundary perturbation Doppler component of the bistatic RCS obtained from two-dimensional TE FDTD analysis. The result is shown for the $n = 2$ mode of a circular dielectric cylinder with radius $a = 0.75\lambda_o$, $\epsilon_r = 2.2$, and $\Gamma_2 = 0.02\lambda_o$	47
4.5	The boundary perturbation Doppler component of the bistatic RCS obtained from two-dimensional TM FDTD analysis. The result is shown for a circular dielectric cylinder with radius $a = 1.0\lambda_o$, $\epsilon_r = 2.0$, and $\delta = 0.01\lambda_o \cos(2\phi)$	48
4.6	The boundary perturbation Doppler component of the bistatic RCS obtained from two-dimensional TE FDTD analysis. The result is shown for the $n = 2$ mode of a circular <i>PEC</i> cylinder with radius $a = 1.0\lambda_o$ and $\delta = 0.005\lambda_o \cos(2\phi)$	48
4.7	The boundary perturbation Doppler component of the bistatic RCS obtained from two-dimensional TM FDTD analysis. The result is shown for the $n = 2$ mode of a circular <i>PEC</i> cylinder with radius $a = 1.0\lambda_o$ and $\delta = 0.01\lambda_o \cos(2\phi)$	49
4.8	Doppler component of the bistatic RCS for a square cylinder for TE polarization; $a = 0.75\lambda_o$, $\epsilon_r = 2.2$, and boundary perturbation $\delta = 0.02\lambda_o \cos(2\phi)$	50
4.9	Doppler component of the bistatic RCS for a square cylinder for TM polarization; $a = 1.00\lambda_o$, $\epsilon_r = 2.0$, and boundary perturbation $\delta = 0.01\lambda_o \cos(2\phi)$	50
4.10	The density modulation Doppler component of the bistatic RCS obtained from two-dimensional TE FDTD analysis. The result is shown for the $n = 2$ mode of a circular polyethylene cylinder with radius $\rho_o = 1.0\lambda_o$ and $\epsilon_r = 2.25$	53
4.11	The density modulation Doppler component of the bistatic RCS obtained from two-dimensional TM FDTD analysis. The result is shown for the $n = 2$ mode of a circular polyethylene cylinder with radius $\rho_o = 1.0\lambda_o$ and $\epsilon_r = 2.25$	53
4.12	The magnitude and divergence of the displacement within a square, homogeneous polyethylene cylinder. The dimensions of the cylinder are 10 cm \times 10 cm and the permittivity is 2.25.	54
4.13	Bistatic TM and TE Doppler components for a 10 cm square polyethylene cylinder; the mode frequency is $f_a = 3485$ Hz; the electromagnetic frequency is 3 GHz.	55
4.14	Illustration of time stepping; t indicates the unperturbed time scale and t' indicates the perturbation field time scale.	55
5.1	Basic flowchart of the simulation approach to the evaluation of acousto-EM wave interaction.	58
5.2	A typical ANSYS model used to simulate fluid plane-wave scattering from an elastic target. The nodes on the fluid and solid elements at the fluid-structure boundary are shown inset.	59
6.1	Geometry of the acoustic scattering problem.	63

6.2	ANSYS model used to simulate an acoustic plane-wave scattering from a polyethylene cylinder.	67
6.3	Boundary perturbation obtained from ANSYS simulations of a homogeneous polyethylene cylinder at three distinct modes of vibration.	68
6.4	The magnitude and divergence of the displacement within a homogeneous polyethylene cylinder for the lowest order (2, 1) mode.	69
6.5	Bistatic TM Doppler component (normalized to the unperturbed backscatter RCS value) for the (2, 1) mode of a 10 cm radius polyethylene cylinder; $f_a = 1.8$ kHz, $f_e = 3$ GHz. The boundary perturbation relative to the cylinder radius is $\delta/a = 2 \times 10^{-6}$	69
6.6	Bistatic TE Doppler component for (2, 1) mode of a 10 cm radius polyethylene cylinder; $f_a = 1.8$ kHz, $f_e = 3$ GHz.	70
6.7	The magnitude of the displacement within a homogeneous polyethylene cylinder for the (2, 2) mode.	70
6.8	Bistatic TM Doppler component (normalized to the unperturbed backscatter RCS value) for the (2, 2) mode of a 10 cm radius polyethylene cylinder; $f_a = 3.63$ kHz, $f_e = 3$ GHz. The boundary perturbation relative to the cylinder radius for this mode is $\delta/a = 7.5 \times 10^{-7}$	71
6.9	Bistatic TM Doppler component (normalized to the unperturbed backscatter RCS value) for the (0, 1) mode of a 10 cm radius polyethylene cylinder; $f_a = 4.82$ kHz, $f_e = 3$ GHz. The boundary perturbation relative to the cylinder radius for this mode is $\delta/a = 2 \times 10^{-7}$	72
6.10	The magnitude and divergence of the displacement within a homogeneous polyethylene cylinder for a shear mode at $f_a = 5232.95$ Hz.	73
6.11	Boundary perturbation obtained from ANSYS simulations of a homogeneous polyethylene cylinder at the (1, 2) mode of vibration, corresponding to a shear mode.	74
6.12	The magnitude of the forward-scattered pressure for two modes of a homogeneous polyethylene cylinder versus acoustic frequency. The solid line corresponds to the (1, 2) mode, which is a shear mode. The forward-scattered pressure for the non-shear (6, 1) mode is also shown for reference.	75
6.13	The total bistatic Doppler component (normalized to the unperturbed backscatter RCS value) for both TM and TE polarizations. These results are for the (1, 2) mode of a 10 cm radius polyethylene cylinder; $f_a = 5.2$ kHz, $f_e = 3$ GHz.	75
6.14	Geometry of the acoustic scattering problem for a layered cylinder.	77
6.15	Illustration of the geometry for the layered cylinder simulation in ANSYS.	79
6.16	The boundary perturbation, u_r , corresponding to the third order $n = 0$ mode at $f_a = 74.13$ kHz.	80
6.17	The magnitude and divergence of the displacement within the layered cylinder for the (0, 3) mode at $f_a = 74.13$ kHz.	80

6.18	Boundary and volumetric current locations for the layered cylinder.	81
6.19	Normalized TM Doppler component scattered from the layered cylinder for the (0, 3) mode.	82
6.20	Normalized TE Doppler component scattered from the layered cylinder for the (0, 3) mode.	82
6.21	The boundary perturbation, u_r , corresponding to the seventh order $n = 2$ mode at $f_a = 73.4$ kHz.	83
6.22	The magnitude and divergence of the displacement within the layered cylinder for the (2, 7) mode at $f_a = 73.4$ kHz.	83
6.23	Normalized TM and TE Doppler component scattered from the layered cylinder at $f_a = 73.4$ kHz, the (2, 7) mode. The electromagnetic frequency is 2.5 GHz.	84
6.24	The boundary perturbation, u_r , corresponding to the third order $n = 8$ mode at $f_a = 73.8$ kHz.	85
6.25	The magnitude and divergence of the displacement within the layered cylinder for the (8, 3) mode at $f_a = 73.8$ kHz.	85
6.26	Normalized TM and TE Doppler component scattered from the layered cylinder at $f_a = 73855.9$ kHz, the (8, 3) mode. The electromagnetic frequency is 2.5 GHz.	86
6.27	A qualitative explanation for the nulls in the bistatic Doppler components of the (2, l) family of modes. Δ represents the phase relative to the electromagnetic signal that interacts with the unperturbed, circular cylinder.	87
6.28	A qualitative explanation for the nulls in the bistatic Doppler components of the (1, l) family of modes. Δ represents the phase relative to the electromagnetic signal that interacts with the unperturbed, circular cylinder.	88
7.1	The ANSYS model used to simulate a void within the target.	91
7.2	The ANSYS nodes on the boundary of the crack overlaid on the \hat{z} FDTD grid points. The FDTD points that are missing correspond to the void that models the crack.	92
7.3	Illustration of the three cracks within the polyethylene cylinder. Each crack is analyzed individually.	94
7.4	Radial displacement, u_ρ , on the boundary of the polyethylene cylinder for the (2, 1) mode of the four crack cases.	95
7.5	Radial displacement, u_ρ , on the boundary of the polyethylene cylinder for the (2, 2) mode of the four crack cases.	96
7.6	The magnitude and divergence of the displacement inside the cracked cylinder for the (2, 1) mode. The same quantities for the uncracked cylinder are shown in Figures 6.4(a) and 6.4(b), respectively.	96

7.7	Scattered acoustic pressure at the (2, 1) resonance for the original, uncracked polyethylene cylinder and the three cracked polyethylene cylinder models. The observation distance is $R_o = 0.16m \approx 0.86\lambda_a$	98
7.8	Scattered acoustic pressure at the (2, 2) resonance for the original, uncracked polyethylene cylinder and the three cracked polyethylene cylinder models. The observation distance is $R_o = 0.16m \approx 1.7\lambda_a$	98
7.9	The unshifted TM polarized RCS of the polyethylene cylinder for the four cracked cases at $f_e = 5$ GHz.	100
7.10	The unshifted TE polarized RCS of the polyethylene cylinder for the four cracked cases at $f_e = 5$ GHz.	100
7.11	The Doppler component for the (2, 1) mode of the solid, uncracked polyethylene cylinder. The Doppler component is normalized to the unshifted RCS at $\phi = 0^\circ$	101
7.12	The Doppler component for the (2, 1) mode of the solid polyethylene cylinder with crack #1. The Doppler component is normalized to the unshifted RCS at $\phi = 0^\circ$	102
7.13	The Doppler component for the (2, 1) mode of the solid polyethylene cylinder with crack #2. The Doppler component is normalized to the unshifted RCS at $\phi = 0^\circ$	103
7.14	The Doppler component for the (2, 1) mode of the solid polyethylene cylinder with crack #3. The Doppler component is normalized to the unshifted RCS at $\phi = 0^\circ$	103
7.15	The Doppler component for the (2, 2) mode of the solid, uncracked polyethylene cylinder. The Doppler component is normalized to the unshifted RCS at $\phi = 0^\circ$	104
7.16	The Doppler component for the (2, 2) mode of the solid polyethylene cylinder with crack #1. The Doppler component is normalized to the unshifted RCS at $\phi = 0^\circ$	104
7.17	The Doppler component for the (2, 2) mode of the solid polyethylene cylinder with crack #2. The Doppler component is normalized to the unshifted RCS at $\phi = 0^\circ$	105
7.18	The Doppler component for the (2, 2) mode of the solid polyethylene cylinder with crack #3. The Doppler component is normalized to the unshifted RCS at $\phi = 0^\circ$	106
7.19	The ANSYS model of the cracked layered cylinder. The inset is zoomed in around the crack.	106
7.20	Radial displacement, u_ρ , on the concrete and steel cylinder boundaries of the layered cylinder for the (0, 3) mode. Both cracked and uncracked results are shown.	108
7.21	Radial displacement, u_ρ , on the concrete and steel cylinder boundaries of the layered cylinder for the (2, 7) mode. Both cracked and uncracked results are shown.	108
7.22	The magnitude and divergence of the displacement inside the cracked layered cylinder for the (0, 3) mode. The same quantities for the uncracked cylinder are shown in Figures 6.17(a) and 6.17(b), respectively.	109
7.23	The magnitude and divergence of the displacement inside the cracked layered cylinder for the (2, 7) mode. The same quantities for the uncracked cylinder are shown in Figures 6.22(a) and 6.22(b), respectively.	109

7.24	The stationary layered cylinder RCS for both TM and TE polarizations at $f_e = 5$ GHz.	110
7.25	The Doppler component for the (0, 3) mode of the uncracked layered cylinder for TM and TE polarizations. The Doppler component is normalized to the unshifted RCS at $\phi = 0^\circ$	111
7.26	The Doppler component for the (0, 3) mode of the cracked layered cylinder for TM and TE polarizations. The Doppler component is normalized to the unshifted RCS at $\phi = 0^\circ$	111
7.27	The Doppler component for the (2, 7) mode of the uncracked layered cylinder for TM and TE polarizations. The Doppler component is normalized to the unshifted RCS at $\phi = 0^\circ$	112
7.28	The Doppler component for the (2, 7) mode of the cracked layered cylinder for TM and TE polarizations. The Doppler component is normalized to the unshifted RCS at $\phi = 0^\circ$	112
7.29	The relative sensitivity of the TM Doppler component for various bistatic angles at an electromagnetic frequency of 3 GHz. Four crack cases are shown.	114
7.30	The relative sensitivity of the TM Doppler component for various bistatic angles at an electromagnetic frequency of 4 GHz. Four crack cases are shown.	115
8.1	The source focusing problem geometry used in the FDTD simulation.	123
8.2	The 15×15 grid of focal points used in the FDTD simulation. Spacing between points is 8 mm, or $0.08\lambda_0$, at the FDTD mesh frequency of 3 GHz.	123
8.3	Sequence of snapshots of the electric field in the TM FDTD mesh as the incident wave propagates into the cylinder. The signal is reconstructed at time step $n = 1820$ at the desired focal point, which the origin in this case.	124
8.4	The scattering intensity coefficient within a homogeneous polyethylene cylinder and a polyethylene cylinder with one FDTD cell having $\epsilon_r = 15$	126
8.5	The focal point and inclusion locations within the cylinder. The plot area in Figures 8.4(a) and 8.4(b).	127
8.6	The scattering intensity coefficient, d_i , of equation (8.2) processing only scattered field contributions, s_j^a , the difference between the received signals with and without the inclusion.	127
8.7	The scattering intensity coefficient within a homogeneous polyethylene cylinder and a polyethylene cylinder with one FDTD cell having $\epsilon_r = 1$	128
8.8	The scattering intensity coefficient, d_i , of equation (8.2) processing only scattered field contributions, s_j^a , the difference between the received signals with and without the void.	129

8.9	The Doppler component scattering intensity coefficient within a homogeneous polyethylene cylinder for two modes. The focal point is located at the origin, or center of the cylinder.	131
8.10	Doppler fields scattered from the cylinder in the (2, 1) resonant mode without the crack, with crack #1, and with crack #3. The focal point is chosen to be at (0 cm, 0 cm).	133
8.11	Doppler fields scattered from the cylinder in the (2, 1) resonant mode without the crack, with crack #1, and with crack #3. The focal point is chosen to be at (-4.0 cm, 0 cm).	134
9.1	A block diagram of the acoustic and electromagnetic system.	136
9.2	Block diagram of a basic lock-in amplifier.	141
10.1	Diagram of antenna design. The dielectric resonator is coupled to a microstrip-fed slot in the ground plane.	145
10.2	The length of the microstrip is varied. $L_s = 2.33$ cm, $w_s = 0.5$ cm, and $d = 0.33$ cm (a) $L_m = 0.67$ cm (b) $L_m = 0.83$ cm (c) $L_m = 1$ cm	151
10.3	The length of the slot is varied. $w_s = 0.5$ cm, $d = 1$ cm, $L_m = 0.167$ cm (a) $L_s = 3.33$ cm, 0.33 cm longer on both ends of the DRA (b) $L_s = 2.67$ cm, the same size as the DRA (c) $L_s = 2.33$ cm, 0.167 cm shorter than the DRA at both ends (d) $L_s = 2$ cm, 0.33 cm shorter than the DRA at both ends.	155
10.4	The x and y dimensions of the DRA are varied. The height, h , remains at 1.67 cm, $L_s = 2$ cm, and $w_s = 0.5$ cm. (a) $a = b = 2.67$ cm (b) $a = 3.34$ cm, $b = 2.67$ cm (c) $a = 2.67$ cm, $b = 3.34$ cm (d) $a = b = 3.34$ cm. The ground plane is 6 cm square.	156
10.5	The slot, $L_s = 2$ cm, $w_s = 0.5$ cm, is moved back along the microstrip in the $-y$ direction. (a) $d = 0.5$ cm, $L_m = 0.67$ cm (b) $d = 0.42$ cm, $L_m = 0.75$ cm (c) $d = 0.33$ cm, $L_m = 0.83$ cm (d) $d = 0.25$ cm, $L_m = 0.92$ cm (e) $d = 0.167$ cm, $L_m = 1$ cm	157
10.6	Return loss for the 5.5 cm ground plane design (a) measured (b) simulated	158
10.7	E-plane and H-plane antenna patterns for the 5.5 cm ground plane design at the DRA resonance of $f = 2.5$ GHz. Measurements are shown in bold and simulations in regular line weight.	160
10.8	Return loss for the 8 cm ground plane design (a) simulated (b) measured	161
10.9	E-plane antenna patterns for the 8 cm ground plane design (a) $f = 2.17$ GHz (b) $f = 2.57$ GHz. Measurements are shown in bold and simulations are shown in regular line weight.	162
10.10	H-plane antenna patterns for the 8 cm ground plane design (a) $f = 2.17$ GHz (b) $f = 2.57$ GHz. Measurements are shown in bold.	163
10.11	Monolithic four-by-four array of RDRA's fabricated using CSLA. One cell of the array is shown in detail with the dimensions of the RDRA, supports, and coupling aperture.	168

10.12	Four-by-four microstrip feed network with dogbone-shaped coupling apertures. The design is replicated to feed the eight-by-eight array.	169
10.13	The eight by eight array in the measurement fixture. Copper tape (not shown) is used around the border of the frame to ensure electrical contact with the ground plane.	170
10.14	Measurement results for the RDRA array.	173
10.15	E- and H-plane radiation patterns at 20 GHz for the eight-by-eight array in the measurement fixture. Absorber is placed around the frame periphery in reduce its effects on the pattern.	174
A.1	Percent bandwidth versus the log of the MDRA intrinsic impedance. The slot-fed MDRA of dimensions $a \times b \times h$ is also shown.	184
A.2	Magnetic Q_m and relative permeability, μ'_r , of the hexaferrite magneto-dielectric versus frequency.	186
A.3	Probe fed DRA with parasitic probe.	187
A.4	Circularly polarized probe fed DRA.	188
A.5	The simulated return loss for the design shown in Figure A.4. Two fed, wire probes are used in this simulation; no parasitic probes are present.	190
A.6	The return loss simulated for the final design. Wider probes are used as in the antenna in the measurement section.	191
A.7	Fabricated antenna in measurement setup with feed and parasitic elements.	192
A.8	Diagram of feed network using microstrip and a hybrid coupler.	193
A.9	The return loss and isolation of the dual linearly polarized design.	194
A.10	Return loss and isolation measured with the CP feed network.	195
A.11	E and H plane patterns at $f = 265$ MHz.	196
A.12	E and H plane patterns at $f = 285$ MHz.	196

LIST OF TABLES

Table

2.1	Comparative summary of four imaging systems including the proposed acousto-EM method.	27
6.1	Parameters used in ANSYS simulation of acoustic scattering from a solid, polyethylene cylinder.	66
6.2	Parameters used in ANSYS simulation of acoustic scattering from a layered concrete and steel cylinder.	78
7.1	Crack dimensions and locations for the solid polyethylene cylinder.	93
7.2	Mode resonant frequencies for the (2, 1) and (2, 2) modes of a solid, polyethylene cylinder. Three different cracks are considered.	95
7.3	Mode resonant frequencies for the three modes of the layered cylinder. One crack, shown in Figure 7.19, is considered.	107
A.1	Probe dimensions and locations for the dual linearly polarized and CP designs. . .	192
A.2	Gain measurement results for the dual linearly polarized design on 50 cm ground plane (* 30 cm sq).	197

CHAPTER I

Introduction

1.1 Motivation for Multi-sensor Systems

In many applications requiring the detection and identification of buried or obscured objects single-sensor systems, which provide sensitivity to a single target property, are not capable of providing sufficiently accurate results. It is oftentimes necessary in such cases to develop systems with sensitivity to multiple target properties to obtain the desired accuracy. Such multi-sensor systems, which combine relevant single-sensor technologies and their advantages, provide additional information about the target and are a logical next step in obtaining a more reliable system.

This research is based on using the interaction of acoustic and electromagnetic waves to detect and distinguish objects. Since both acoustic and electromagnetic target properties determine how the waves interact, sensitivity to both types of target properties is inherent in the approach. Acousto-electromagnetic (acousto-EM) wave interaction phenomena produces information which is unavailable using separate acoustic and/or electromagnetic sensors. As a result, an additional data space, which augments those from individual acoustic and electromagnetic sensors, is obtained, allowing for more accurate detection and identification.

1.2 Definition of Acousto-Electromagnetic Wave Interaction

Acousto-EM wave interaction refers to the interaction of acoustic and electromagnetic waves that occurs when an electromagnetic wave scatters from an object under seismic or acoustic illumination, as shown in Figure 1.1. The incident acoustic excitation causes boundary displacement and density modulation on and within the object, which both contribute to the Doppler component. The vibration of the object under acoustic excitation gives rise to a frequency modulated electromagnetic scattered field, the spectrum of which contains a small Doppler component shifted in frequency by the acoustic frequency of vibration, as shown in Figure 1.2. The Doppler component depends on both the object physical parameters (density, dielectric contrast from background, geometry, shear modulus, etc.) and electromagnetic and acoustic source parameters (acoustic: frequency and power, electromagnetic: frequency and polarization). At certain acoustic frequencies, determined by the density contrast between the object and the background and the object's mechanical properties [1], the boundary and density modulations are enhanced and the largest Doppler component is obtained. Therefore, the prediction and extraction of the resonant frequencies and Doppler component, or object signature, would be extremely useful for detection and imaging purposes.

It is noted that the interaction is considered as a one-way process; in other words, the acoustic wave, or pressure variation affects the local index of refraction which in turn results in scattering and reflection of the interrogating electromagnetic signal. The converse scenario of electrostriction, where the propagating electromagnetic field intensity creates a local mechanical deformation which, in turn, is capable of generating acoustic waves and affecting the propagation of existing acoustic waves,

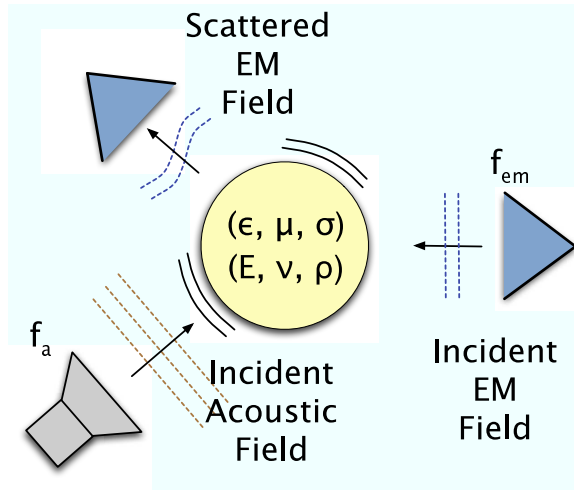


Figure 1.1: Diagram of acousto-EM wave interaction. Acoustic or seismic excitation causes the object to vibrate. The incident electromagnetic wave is modulated by the object vibration giving rise to the Doppler component in the scattered signal.

is not considered.

1.3 Advantages Over Single-Sensor Systems

As noted above, the Doppler component arising from acoustic and electromagnetic wave interaction is sensitive to multiple target properties. The advantages of the acousto-EM system over single-sensor, all-acoustic or all-electromagnetic, systems are summarized in the following paragraphs.

- Advantages over an all-acoustic system
 - One advantage of using the acousto-EM approach is increased sensitivity to the target interior. The large acoustic impedance mismatch between most solids and the surrounding fluid, air, in this case, implies that coupling acoustic energy into the target is difficult. As a result, much of the incident acoustic energy is reflected from the target boundary and only a small amount penetrates into the interior. This is especially true away from target resonances; at resonance the coupling of acoustic energy into the

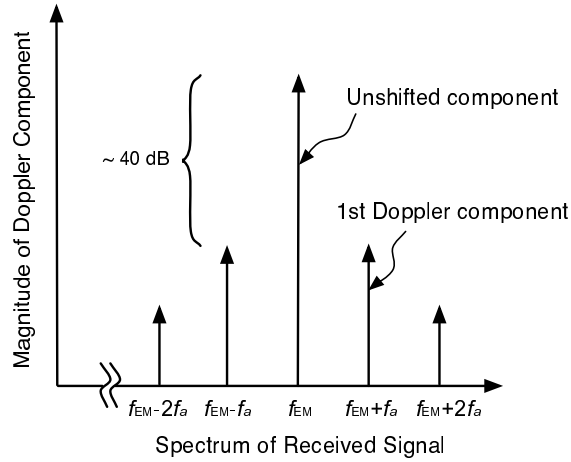


Figure 1.2: Sample spectrum of electromagnetic field scattered from an object mechanically vibrating at acoustic frequency f_a . The unshifted electromagnetic frequency is denoted by f_{EM} .

target is improved. Chapter VII compares the sensitivity of both acoustic and electromagnetic waves to flaws within the target.

- In high acoustic clutter environments, measuring the bistatic scattered pressure is difficult because multi-path signals can arrive at the receiver simultaneously, saturating the return and obscuring the desired signal. The acousto-EM approach, however, can separate direct-path and reflected acoustic signals scattering off of nearby objects. Since only the resonant target has displacements large enough to produce the Doppler component in the scattered electromagnetic field, the proposed approach effectively isolates the resonant target.
- Acoustic systems have difficulty detecting shear modes because the shear waves cannot propagate into the surrounding fluid. In an acousto-EM system, detection does not rely on acoustic wave propagation back to the receiver. Therefore, the proposed approach does not suffer from this limitation and can remotely detect the target motion caused by the acoustic excitation.

- In an acoustic imaging system, higher frequencies are sometimes required to achieve sufficient resolution to detect certain features of interest. In the acousto-EM approach, lower frequencies, which experience much lower loss in air, are adequate since the acoustic energy is used to excite resonant modes of the target rather than to image the target.
- Advantages over an all-electromagnetic system
 - An electromagnetic system cannot look inside metallic, metal-coated, or very electromagnetically lossy targets because the electromagnetic wave does not penetrate significantly into the target interior. An acousto-EM system, however, can detect acoustic resonance frequencies and is also sensitive to the boundary perturbation which occurs at the acoustic resonances. This information, which is unavailable using a conventional electromagnetic system, provides additional information about the target which aids in detection and identification.
 - The electromagnetic signal level and bistatic patterns do not change significantly at electromagnetic resonances of the target. As a result, information embedded in these resonances cannot be used for identification. In an acousto-EM system, mechanical resonances, which also contain information about the target properties, are used as an additional target descriptor.

1.4 Overview of Previous Work

This section outlines previous research on the interaction of electromagnetic and acoustic waves and seeks to provide historical background for this research. Brillouin first studied the effects of sound fluctuations of thermal origin on the propagation of electromagnetic waves in fluids and solids in the early 1920's [2, 3]. He predicted

that electromagnetic waves would undergo a Doppler shift as a result of interaction with acoustic phonons [3]. Experiments performed nearly ten years later verified this prediction by observing the Doppler shift on light scattering from propagating acoustic wavefronts within liquid media [4]. The maximum scattering angles are determined by the relative acoustic and electromagnetic wavelengths and correspond to the Bragg condition; the Doppler shift on the electromagnetic signal indicates the velocity of the acoustic wavefronts [4, 5]. With the invention of highly chromatic light sources, such as lasers, subsequent experiments were able to more easily discern the Doppler shift and measure the velocity of the hypersonic acoustic waves [5]. The invention of lasers also created the need for means of controlling the laser light beams. Numerous devices based on the acousto-optic effect were subsequently developed out of this practical necessity. An interesting account of the history of acousto-optics and a discussion of acousto-optical devices is presented in reference [2].

Another application of acoustic and electromagnetic wave interaction is atmospheric temperature profiling and air quality estimation. The idea of using the interaction for temperature profiling originated in the early 1960's while practical system development began in the early 1970's [6, 7, 8]. The first Radio Acoustic Sounding System (RASS) was developed at Stanford University to measure atmospheric temperature profiles in the lower troposphere [6]. More recent deployment of RASS has been for studying air quality via temperature profile information [9].

A basic RASS tracks the velocity of sound waves propagating in the atmosphere using an electromagnetic radar system [6]. An acoustic source launches a spherical pulse into the atmosphere; as the pulse propagates, its speed is affected by the local temperature. The pressure variations, due to compression and rarification of the atmosphere from the acoustic wave, slightly affect the local permittivity. A radar

system simultaneously emits an electromagnetic signal which reflects off the slight pressure variation. The radar system then measures the reflected electromagnetic signal as a function of range, determines the acoustic wave propagation speed, and infers the local temperature. To be sure, the reflected signal is quite small; however, two features of the system yield a measurable signal. First, since the acoustic and electromagnetic sources are in close proximity on the ground, the acoustic wavefronts acts as a spherical reflector focusing the reflected electromagnetic wave at the radar receiver. Second, a Bragg condition is set up by using an acoustic wavelength that is approximately one half of the electromagnetic wavelength. This ensures that successive reflected electromagnetic wavefronts add coherently at the receiver. Advantages of RASS include its relatively low cost in comparison with radiosonde measurement and its real-time capabilities [6, 9]. In addition, it is entirely ground-based and does not expend equipment launching it into the atmosphere.

In order to minimize the acoustic scattering and loss and to maximize the possible measurement range, a very low acoustic frequency is generally used. The original system developed at Stanford used 85 Hz and 36 MHz as the acoustic and electromagnetic frequencies, respectively [6]. This system was capable of measuring temperatures up to altitudes of 3 km in low wind conditions and 1 km in average wind conditions. More recent systems using more complex radar systems and signal processing are capable of measurement up to the tens of kilometers [10]. The system described in [11] uses a higher acoustic frequency of 1 kHz in order to reduce system size; this system works up to altitudes of about 1 km. RASS for air quality measurement use even higher acoustic frequencies, on the order of 2 – 3 kHz, and can provide data up to altitudes on the order of only hundreds of meters [9]; the electromagnetic portions of these systems operate at UHF.

The work outlined above relies on maintaining an appropriate relationship between the electromagnetic and acoustic wavelengths to maximize the reflected electromagnetic signal. Another body of research uses the wave interaction to formulate an inverse problem where the desired unknowns are the local, pressure dependent material parameters within a given region [12]. The model has initially been tested using data obtained by simulating the electromagnetic signal propagation through Debye media with the finite-difference time-domain (FDTD) method [13]. The change to the local index of refraction as a result of the propagating pressure wave is modeled as a linear perturbation with coefficients derived from physical considerations and the Debye material model. A subsequent experimental system sought to measure the wave interaction using a TEM half-plane antenna and a slab of agar gel enclosed in plexiglass [14]. In the experiments, the electromagnetic signal is a short, approximately 8 ns, pulse and the acoustic excitation is provided by an ultrasound transducer operating at 215 kHz. The pressure wave amplitude in the agar was estimated to be on the order of 0.1 Pa. The experiment was ultimately unsuccessful since no sizeable return of the reflected electromagnetic signal was measured [14]. A required pressure wave amplitude of 8×10^8 Pa in the agar is predicted to be necessary in order to yield a measurable reflected signal; measurable is assumed to be a signal that is 0.1% of the incident wave. The authors do not mention using any target resonance or the Bragg condition to enhance electromagnetic scattering.

It is expected that under the conditions in the experiment carried out in [14] it would be nearly impossible to detect the Doppler component of the scattered electromagnetic field. For discrete targets, away from resonance, an incident acoustic wave largely scatters from the target surface, leaving the target largely unperturbed, and creating little displacement to induce the Doppler effect. Likewise, in the above

experiment, there is very little density modulation in the agar gel from which an electromagnetic wave would scatter. In the model presented herein, the normal resonant modes of discrete objects are used to enhance the Doppler shifted portion of the scattered electromagnetic signal.

Systems using both the acoustic approach and the electromagnetic approach have also been under investigation for applications in buried object detection. This approach was first suggested in the context of landmine detection in [15, 16]. In one system, surface acoustic waves interact with a buried target, causing displacements on the soil surface and the target [17, 18]; a ground penetrating radar (GPR) system is then used to detect these displacements. Reference [19] also alludes to using the resonances of the target to enhance the Doppler component. A numerical finite-difference model of elastic wave propagation in two and three-dimensions has been developed and qualitative agreement with experiments in a laboratory environment has been established [20, 19]. Displacements as small as 1 nm have been detected.

Analytical work has also predicted the Doppler component scattered from resonant dielectric and metallic cylinders. The analytical solution is derived using perturbation analysis in conjunction with the quasi-stationary approximation, which will be described, and known acoustic scattering solutions. In the case of dielectric cylinders, the analysis is separated into the boundary and density modulation contributions to the Doppler field. Sheet boundary conditions have also been developed to accurately and efficiently model small perturbations to scatterer boundaries [21]. These will be used extensively in the derivation of the boundary perturbation Doppler component. In the following chapters, additional previous work specific to certain aspects of the acousto-EM model will be mentioned where appropriate.

1.5 Summary of Contribution

This research generalizes the theoretical acousto-EM model of the scattered Doppler component to arbitrary two-dimensional targets. Previously, the Doppler component was only known for infinite cylindrical geometries. The extended model described herein can be used to test and verify the utility of the acousto-EM approach in more general cases. A qualitative summary of Doppler component characteristics is initiated to generalize the results from the simple cases considered herein. In addition, the potential for the approach in a particular application, non-destructive evaluation, is considered. It is demonstrated that the Doppler component could be a useful means of locating and detecting flaws within a target.

1.6 Document Overview

The document can be outlined as follows. Chapter I defines the acousto-EM approach, presents its advantages, and provides historical background and previous work that investigates acoustic and electromagnetic wave interaction. Chapter II describes three specific applications of acousto-EM wave interaction. The time-domain model and important simplifying assumptions are discussed in Chapter III. Implementation of the model is covered in Chapter IV; verification of the implementation is presented where analytical solutions are available. The two-step physical model, which is the core of the general two-dimensional model, is discussed in Chapter V. The first step is the simulation of acoustic scattering which produces the required target displacements; the second step is the electromagnetic simulation which uses the acoustic displacements to produce the Doppler component. Case studies are presented in Chapter VI; the bistatic Doppler component at a single electromagnetic frequency is presented for various modes of homogeneous and layered cylindrical

geometries. Relevant observations that seek to generalize the Doppler component from the relatively simple cases considered herein are also stated at the conclusion of this chapter. The application of acousto-EM interaction to non-destructive evaluation is presented in Chapter VII. This chapter compares the sensitivity of acoustic waves, the unshifted electromagnetic fields, and the Doppler component to small flaws within the target. Unique target signatures are obtained for the wideband, bistatic Doppler component; the signatures demonstrate the Doppler component sensitivity to the target interior. Chapter VIII describes a time-reversal focusing approach that is used to locate flaws interior to the target. Focusing localizes the incident electromagnetic field at a desired focal point. Appropriate processing of the scattered fields produces an image related to the amount of scattering from each point within the target; increased scattering of the Doppler component fields is observed where the interior displacements and strain is maximized, i.e. near flaws. It is also demonstrated that focusing yields more information regarding location of the flaw as well as increased sensitivity to the flaw than the bistatic Doppler component scattered from the target. Finally, systems for detection are discussed in Chapter IX; various considerations and issues which may arise in a practical system are addressed in this chapter. Relevant research on antenna designs amenable to incorporation in a receiver for an acousto-EM system is also presented. Conclusions and future work are outlined in Chapter XI.

CHAPTER II

Applications

There are various areas where acousto-EM wave interaction could be used in a multi-sensor system for remote detection and identification. This chapter focuses on the following three, primary applications: buried object detection, tumor detection, and non-destructive evaluation. Enormous research efforts have been devoted to each topic; this chapter only attempts to provide relevant references. Within each section, current work is reviewed and then a description of how the acousto-EM approach could be used in that application is provided.

2.1 Buried Object Detection

An important area of ongoing research is the detection and identification of buried man-made targets for civilian and military applications. Among civilian applications, the detection of pipes and tunnels under the earth's surface is important for maintenance and environmental protection purposes. Military applications include the detection of landmines and unexploded ordnance devices.

A 2003 survey reports that there are approximately 45-50 million landmines worldwide that remain to be cleared [22]. In spite of global efforts to remove landmines, it is estimated that there are between 15,000-20,000 victims each year. These devices are easy and inexpensive to deploy during conflicts; however, they remain active in-

definitely until they are cleared or detonated by either the intended military target or by civilians. There are hundreds of various types of mines which fall into two main categories, anti-tank (AT) mines and anti-personnel (AP) mines. Anti-tank mines are much larger and are designed to inflict damage on military tanks and vehicles. Anti-personnel mines, however, pose a greater threat to civilian safety. Anti-personnel mines are further classified as “blast” or “fragmentation” mines [22]. Blast mines are generally triggered by pressure and are buried at shallow depths. They usually have little metallic content and a plastic casing. This type of mine inflicts damage by causing the activating object, i.e. a foot, to fragment and blast upwards. Fragmentation mines, on the other hand, contain material fragments which are sent radially outward upon detonation. Bounding mines, which are buried, upon detonation are propelled upward and subsequently explode, sending fragments about one meter off the ground in a large radius, fall into this category. Other types of fragmentation mines are mounted on stakes or tree trunks. Fragmentation mines are usually larger than blast mines and have higher metal content, making them easy to detect with a metal detector. On the other hand, they are often detonated with a trip wire, prohibiting location with a hand-held detector.

Numerous single sensor technologies have been developed for buried object detection. Ideally, a system would provide a high probability of detection with low false alarm rates using remote interrogation. Most of these approaches for landmine detection suffer from high false alarm rates. Each false alarm must be carefully handled and treated as if it were a mine, limiting the speed and cost of demining with these approaches. The oldest and most developed detection methodology is a metal detector. These devices operate based on electromagnetic induction (EMI) [23]. Current flowing in a transmitting coil produces a time-varying magnetic field

in the ground. If metallic targets are present, eddy currents will be induced on their surface, producing an additional, lower intensity magnetic field which is detected by a receiver coil. Metal detectors were first used in World War I and were further refined during World War II. The technology has changed little since its development in the early 20th century, however, device operation has been improved and the size and weight have been reduced. EMI detectors are capable of extreme sensitivity to metal content in the soil. However, with increased sensitivity comes increased false alarm rate due to metallic clutter. This is the primary limitation of detection modalities based on EMI. This approach is also unable to provide object depth information.

Non-metallic objects, which are more difficult to detect because of the low dielectric contrast from the background soil medium, require a different approach for successful detection. Non-metallic mine detection originated with the balanced bridge approach during World War II [24]. Basically, sub-surface anomalies, such as mines, change the radiation resistance of a transmitting antenna, producing a measurable change in the signal at the receiver antenna. As the technology matured, more complex systems were developed using multiple antennas and arrays. The approach has many limitations, including its inherent sensitivity to variations in antenna height and tilt and soil moisture; it also has limited sensitivity to small AP mines and limited capability to distinguish between mines and clutter.

GPR has been extensively investigated for use in buried object detection [25]. In this approach radio or microwaves are used to interrogate an area under test. Contrast in the dielectric properties of the ground and buried targets produce reflected waves which are subsequently detected and processed. The choice of operational frequency is critical to system performance; lower frequencies provide improved signal depth penetration while wideband systems provide improved range resolution.

An important advantage of GPR systems is the ability to conduct investigations remotely, minimizing operator risk. Detection accuracy is limited in cases where dielectric contrast between the mine and the background soil medium is low enough to be comparable to variations within the heterogeneous soil itself. In addition, the backscattered signal from the mine is small compared with the primary backscattered signal due to rough surface scattering at the soil-air interface. This method is also subject to environmental conditions, such as soil moisture, implying that, while a particular setup may be optimized for certain conditions, it can yield poor results in others.

Another system which is being developed uses acoustic waves to detect landmines [26, 22]. In this approach acoustic energy is coupled into seismic waves which propagate in the ground. Rather than placing the acoustic source in contact with the surface and coupling to Rayleigh waves, which propagate near the ground surface, an airborne acoustic source remotely couples to Biot Type II waves which propagate in the air holes within the soil. This provides more efficient coupling of the acoustic energy, reaching depths of approximately 0.5 m below the ground surface. The interaction of the mine container with the soil on top of it produces linear and nonlinear disturbances which are used for detection. The container and the soil on top of it form a mass (soil) spring (container) system; at the system resonance maximum surface displacement is obtained. Advantages include insensitivity to the mine material and the ability to reject clutter such as rocks, roots, or pieces of metal which do not interact as much with the soil. Detection is currently done with a laser Doppler vibrometer (LDV) which measures displacements on the soil surface. LDV detection presents the primary limitations to this technology. Performance is poor in heavily vegetated areas and at low look angles. In addition, the LDV is sensitive

to environmental conditions, such as temperature and humidity. Alternate means of detection, such as GPR and ultrasound (US) systems, have also been suggested.

Many different hybrid systems employing multiple sensors which collect independent data sets are also being investigated [27]. The objective is to use sensors with sensitivity to different mine characteristics so the data complement each other. Data fusion may be performed at different levels, such as the pixel level for sensors with similar resolution or in post-processing. The U.S. Army has developed the Handheld Standoff Minefield Detection Systems (HSTAMIDS or AN/PSS-12) which combines a GPR system with metal detection capabilities to provide high probability of detection with low false alarm rates for both metallic and non-metallic AT and AP mines [28]. Another system uses GPR, an infrared camera, and an EMI sensor operating on separate platforms and then integrates the data using a specially developed algorithm [29]. Issues from irregular sampling, differing data formats produced by each sensor, as well as positioning errors from independent sensor platforms present difficulties in data fusion.

Systems based on both the acoustic and electromagnetic phenomena have also been under investigation for applications involving buried object detection. A system suggested in [26, 30] simultaneously uses both an acoustic system (with LDV detector) and a GPR system. The interaction between the container and soil on top of it creates the displacement on the soil surface. Since the GPR system is most sensitive to mines buried at moderate depths while acoustic systems are most sensitive to shallow mines these approaches complement each other. In addition, the combined system takes advantage of the fast detection and resolution capabilities of GPR as well as its sensitivity to dielectric contrast. Yet another approach, which is briefly discussed in Section 1.4, combines acoustic excitation with electromagnetic

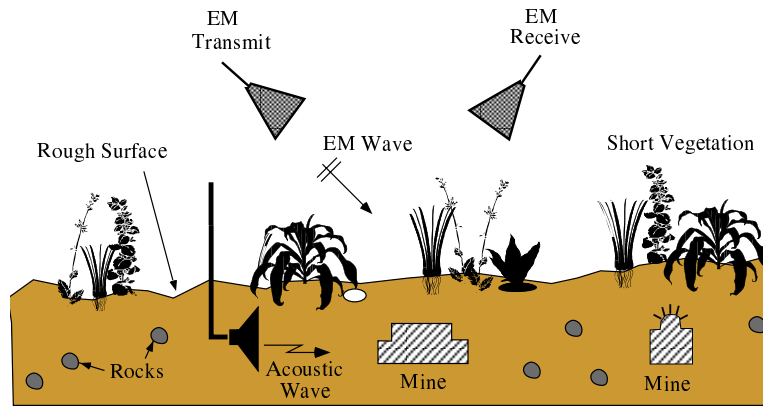


Figure 2.1: Proposed approach using acousto-EM wave interaction for the detection and identification of buried objects.

detection, overcoming the limitations of LDV detection used in acoustic systems. In this system, soil surface displacements above acoustically excited mines are detected using GPR.

The present research models the electromagnetic response of such targets in a similar system, which is shown in Figure 2.1. However, in this case the acoustic source frequency is chosen to induce the mine or buried target to enter a resonant mode of vibration. Under this condition, the displacement of the mine and soil surface is greatly enhanced. While it is more straightforward to detect soil displacement away from resonance as in [20, 19], additional information contained in the scattered field due to object vibration and the target resonances would be useful for detection and recognition. As mentioned in Section 1.4, analytical work has been carried out to predict the scattered Doppler component for infinite dielectric and metallic cylinders [31, 1]. Analysis of the scattered field for more general cases, however, is necessary for practical application of this technique in buried object detection.

2.2 Tumor Detection

Although, the largest research efforts in acoustic and electromagnetic wave interaction have been for buried object detection, the approach could also be used in a non-invasive scheme for the early detection of tumors. A very large amount of research has been dedicated to tumor detection. In this section microwave imaging and two methods of elastography are described. The proposed acousto-EM approach is also presented and its advantages are outlined.

Recently, microwave imaging has been under investigation for cancer screening because of its ability to take advantage of the dielectric contrast between normal and possibly cancerous tissue at microwave frequencies (1-10 GHz) [32, 33]. It is also lower in cost than traditional means of detection. In the area of breast cancer research ultra-wideband (UWB) radar systems have been under development since about 1998. These systems employ antenna arrays in conjunction with specialized beam forming techniques to identify locations of heightened scattering that indicate possible tumors. One approach is microwave-imaging via space-time (MIST) beam-forming which “spatially focuses the backscattered signals to discriminate against clutter and noise while compensating for frequency-dependent propagation effects [33].” The beam is scanned over various locations by using appropriate time shifts between signals and adjusting processing parameters. This method has shown positive results in experimental settings, detecting breast tumors less than 5 mm in size in a three-dimensional multilayer breast phantom that accurately reflected human tissue dielectric properties [34]. While the dielectric contrast between normal and malignant breast tissue is large (greater than 2:1), in other tissues, such as the kidney, the contrast is quite low (about 5%) [35]. This suggests a limitation of microwave

imaging in detecting other types of cancer.

Palpation has been used for centuries to detect cancerous tissue which is often much stiffer than noncancerous tissue. Elastography is a relatively new imaging approach which effectively is remote palpation [36, 37]. Elastographic imaging seeks to map mechanical properties of tissue, particularly the elastic (or Young's) modulus or the shear modulus, both of which vary over orders of magnitude within tissue, to provide high quality images. This is in contrast to conventional US which distinguishes tissue type based on acoustic impedance. The acoustic impedance, in turn, is determined by the bulk modulus of the tissue, which does not vary significantly in soft tissue [38]. Since the mechanical attributes of tumors are not necessarily correlated with distinguishing properties used in other detection techniques, such as water content in magnetic resonance (MR) imaging or dielectric properties in microwave imaging, elastographic imaging is capable of discerning tumors which otherwise could have gone undetected [39, 40]. In addition, the contrast between the elastic modulus of normal and malignant tissue is often greater than the contrast of other properties such as dielectric permittivity. For example, the elastic modulus of breast tumors and surrounding tissue can differ by a factor as high as 90 [36]; as mentioned above, dielectric contrast in breast tissue is much lower. Regions with low dielectric contrast, such as kidneys, which are not good candidates for microwave imaging, have also successfully been imaged with this technique [41].

The general approach in elastographic imaging is to use some type of mechanical excitation to cause tissue displacement and then use a means of detection to measure relevant quantities from which the elastic properties of the tissue can be extracted. The mechanical vibration is usually induced using static or dynamic acoustic excitation. Static excitation methods slowly compress the tissue and then detect dis-

placements by some means (e.g. MR or US). An estimate of strain (change in length) is formulated, then related to the distribution of applied stress (force per unit area), and elastic parameters are extracted. Dynamic methods apply a transient or harmonic excitation causing tissue vibration. The displacement is then detected and related to elastic properties of the tissue. The radiation force of ultrasound, which can be applied to a desired location within the tissue, is an excellent means of creating internal static or dynamic excitation noninvasively because existing US hardware can be used to generate the signal in any desired temporal shape or appropriate frequency range. Dynamic methods are advantageous because they have potential to yield additional tissue information over a spectrum of frequencies; as mentioned in [42], dynamic stress also “allows one to analyse the object based on its structural vibration properties as opposed to its ultrasonic parameters.” Two schemes of particular interest are sonoelastography and vibro-acoustography. Their application is described in more detail in what follows; further information on additional means of elastographic imaging may be found in the references.

Sonoelastography, also known as shear wave elasticity imaging, uses shear waves to discern tissue properties such as shear viscosity and shear modulus [42, 38]. The radiation force of a focused, low frequency (less than $1kHz$) amplitude modulated (AM) US beam induces localized acoustic waves. Shear waves at these frequencies have wavelengths on the order of millimeters and propagate according to the shear modulus, which varies over orders of magnitude in soft tissue. In addition, shear waves are attenuated about three orders of magnitude more so than compressional waves [38]. As a result, they remain localized about the US focal point, reducing the effects of neighboring tissue. Compressional waves are not used in this approach because they have a wavelength much longer than the scale of interest and propagate

according to the bulk modulus which varies little in soft tissue. The shear waveform and amplitude is detected by optical means, phase sensitive MR imaging, or Doppler US. Resolution is limited by how well the shear wave remains localized, which depends on the US focal region and the tissue properties. This makes it difficult to estimate resolution in general; an optimistic estimate for MR detection would be about 0.7 mm in diameter, the focused US beamwidth at 3 MHz, by 0.5-2 mm in depth, typical MR resolution. Disadvantages of sonoelastography include inapplicability to regions of hard tissue where the shear waves do not remain well localized. Detection is problematic as well. Optical detection cannot be used in practical medical applications and MR imaging is expensive. It has also been suggested that in order to achieve displacements large enough to be observed with Doppler US ($\sim \mu\text{m}$) the US signal intensity would likely be above maximum recommended levels [42]. Finally, scanning time is relatively long since the image is acquired one point at a time.

Vibro-acoustography uses ultrasound radiation force to excite tissue at acoustic frequencies and then detect the resulting acoustic emission, or acoustic field in response to cyclic vibration, with a hydrophone or microphone [42, 43, 44]. Figure 2.2 depicts a typical vibro-acoustography system. Rather than using a single amplitude modulated (AM) US source, which causes acoustic emission along the path between the source point and the desired focal point, two confocal US beams at frequencies $\omega \pm \Delta\omega/2$ interfere with each other, producing an AM US beam with modulation frequency $\Delta\omega$. Cyclic displacement of the tissue caused by the radiation force of the AM US beam gives rise to the acoustic emission. The signal depends on the local elastic and mechanical properties as well as the dynamic response of the tissue at the particular acoustic frequency. A hydrophone is used to detect the acoustic signal emitted from the focal point and the amplitude and/or phase versus position is

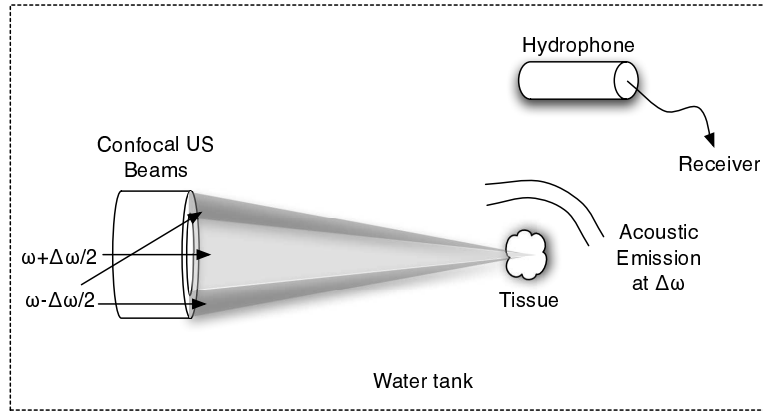


Figure 2.2: A typical vibro-acoustographic imaging system. Two confocal US beams produce a single AM US beam at the desired focal point. Cyclic vibration of the tissue at the focal point gives rise to the acoustic emission. The amplitude and/or phase of the acoustic emission is detected with a hydrophone and a raster image is formed. Experiments are carried out in a water tank to avoid acoustic impedance mismatches between the US source, hydrophone, and background medium.

mapped to form the image. Vibro-acoustographic experiments are generally carried out in a water tank, as shown in Figure 2.2, with both the US source and hydrophone submerged in the water for improved acoustic coupling. In vivo imaging requires that the US source and detector be held to the skin surface because of the large acoustic impedance mismatch at the skin-air interface.

Since the two US signals propagate along different paths dynamic radiation force, which induces mechanical vibration and motion, is produced only at the focal point, reducing the influence of tissue between the source and the focal point. In addition, using two interfering beams rather than a single, amplitude modulated beam reduces the depth of the focus volume. The spatial resolution is ultimately limited by attenuation within the tissue which limits the US frequency and resulting beamwidth. Using typical parameters, one study cites a resolution diameter of about 0.7 mm and a depth or image layer thickness of about 9 mm [44]. Hydrophones are extremely sensitive and are capable of detecting acoustic intensities as small as 10^{-15} W/cm^2 or a few nanometers in displacement. It is noted that a recent vibro-acoustography study

on brachytherapy metal seed imaging found it advantageous to image at acoustic resonances of the seeds for improved contrast and signal to noise ratio.

Disadvantages of vibro-acoustography include background interference from acoustic signals in the measurement environment. Since the hydrophone is not at all directive, multipath signals and sensitivity to acoustic boundaries become an issue. Also, as shown in [44], the detected signal is proportional to a medium transfer function, which describes the frequency response of the receiving hydrophone and the propagation effects of the background media. This is an inevitable consequence of detecting the acoustic signal after it has propagated through the intervening tissue between the focal point and the hydrophone. However, since the acoustic compressional wavelength is usually large relative to the focal region, the radiation is often assumed to originate from a point source and the transfer function is assumed constant for every point in the region of interest. Another result of detecting the signal after it has propagated through the neighboring tissue is the loss of information contained in the shear waves, which are rapidly attenuated at these frequencies [45]. Since only the compressional waves are able to propagate to the hydrophone vibro-acoustography cannot detect shear modes of resonance. Another disadvantage is long acquisition time since the US source must focus on one point at a time. Also, as mentioned above, in vivo imaging requires that both the US source and hydrophone be held in contact with the skin because of the large acoustic impedance mismatch at the skin-air interface.

There are various configurations in which an acousto-EM approach could be used. Figure 2.3 shows one configuration where a single AM US source produces an acoustic plane wave for mechanical excitation. The microwave imaging system would provide the remaining two-dimensions of resolution. For reference, the microwave imaging

system described in [33] has resolution on the order of 5 mm. Possible types of the microwave imaging system include a large adaptive array capable of focusing on different spots and/or a scanning array. Acoustic resonances of discrete scatterers within the field of view could be detected by sweeping the amplitude modulation frequency. This system is appropriate for detecting individual lesions or microcalcifications and inferring their properties from the Doppler component and resonant frequencies, not necessarily obtaining a very high resolution image.

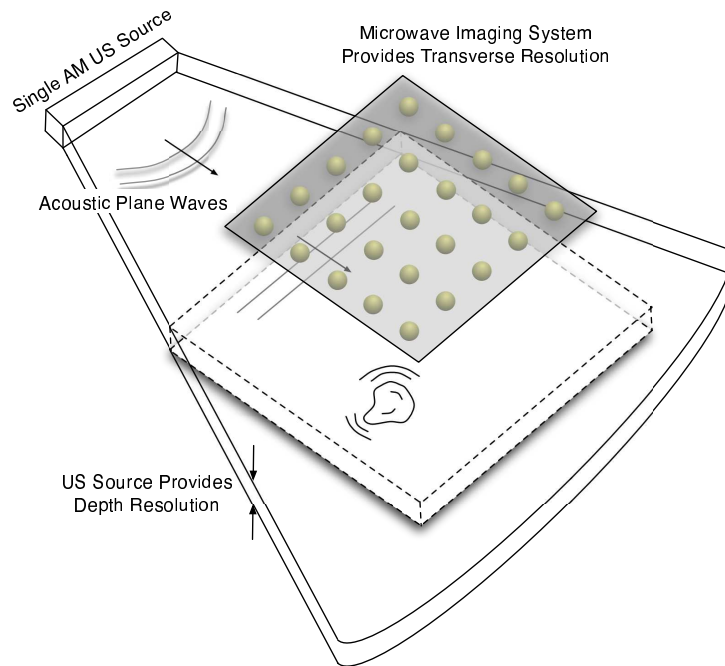


Figure 2.3: A possible configuration using acousto-EM wave interaction for obtaining the Doppler response of tumors. A single AM US source provides an acoustic plane wave and the depth resolution. The microwave imaging system provides the remaining two dimensions of resolution and detects the Doppler component. The US source is stationary and the non-contact microwave array can be scanning or stationary depending on the array size.

Figure 2.4 illustrates a two-dimensional view of an alternate configuration where two planar US beams intersect along a line to produce the AM US signal as in vibroacoustography. The depth resolution along the focal line and Doppler component detection would be provided by a microwave imaging system. The line of intersection

between the US beams would be varied over the x - y plane using US beam steering techniques, forming a three dimensional image of the region. In this case, a different interpretation of the acoustic response would be necessary since it is determined by the local tissue parameters rather than the resonant response of a discrete lesion or tumor. The advantage of this approach over vibro-acoustography is reduced acquisition time as a result of using the microwave system for detection and to provide resolution along one dimension.

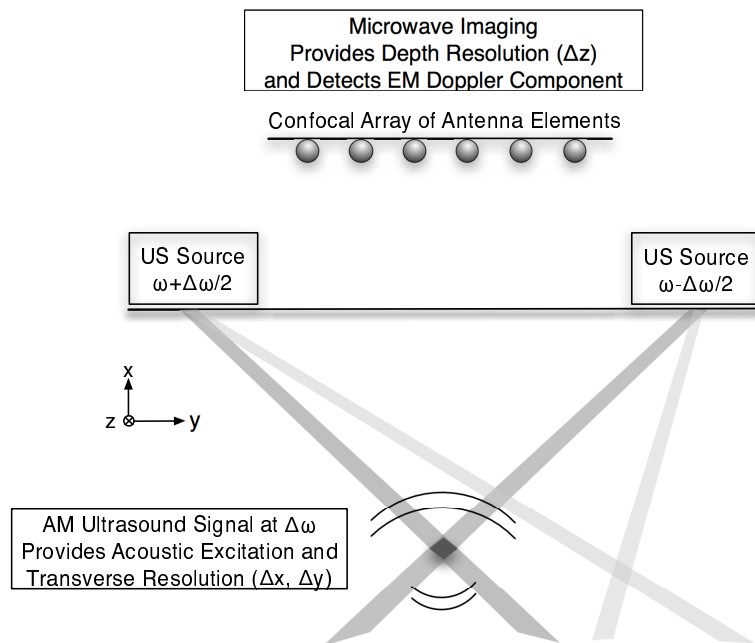


Figure 2.4: Two-dimensional cut of a possible approach using acousto-EM wave interaction for medical imaging of dielectric and elasticity properties of tissue. The two US beams produce an AM signal with modulation frequency $\Delta\omega$ along a \hat{z} directed line. The microwave imaging system detects the Doppler component and provides resolution along the z axis. The US sources and microwave system are stationary and use beam steering to focus on different regions. The microwave imaging system is non-contact.

The proposed acousto-EM system combines the advantages of vibro-acoustography and microwave imaging, while making use of the unique properties of the electromagnetic Doppler signature. Using both US and microwave systems to achieve resolution allows for faster image acquisition in two or three dimensions. The imaging system does not need to move since spatial beamforming of the backscattered electromag-

netic signals can be carried out following measurement. In addition, the microwave sensor is capable of picking up the entire acoustic signature of interest from within the object, before the signal has been affected by undesirable acoustic propagation effects. This allows both compressional and shear waves to be detected. In contrast, the two previous imaging techniques are sensitive to only one type of acoustic wave. The proposed approach is also capable of acoustic spectroscopy for tumor feature extraction. By continuously varying the frequency of the acoustic source and monitoring the Doppler component of microwave backscatter unique acoustic resonances of the object, which are functions of its geometry, size, and material properties, can be determined remotely. In the proposed system, both dielectric and elastic properties can be extracted; these combined attributes would provide a comprehensive description of the tumor and allow detection in regions of low dielectric contrast. The microwave imaging system is also less susceptible to background noise and more directive than the hydrophone used for detection in vibro-acoustography; it is also lower in cost than MR imaging used in shear wave imaging. Finally, while some reflection of the electromagnetic signal does occur at the skin surface, the microwave system is capable of remote detection, allowing easier bistatic measurement of the Doppler signal.

Table 2.1 is a comparative summary of the relevant properties of microwave imaging, sonoelastography, vibro-acoustography, and the first proposed acousto-EM imaging approach; parameters indicated in [33] and [34] are used for the microwave (and acousto-EM) systems. Individually, the US acoustic source and microwave imaging systems have already successfully been applied in various experimental studies [34, 43, 44]. In order to employ acousto-EM wave interaction in this application, a connection between the observed Doppler component and resonant frequencies and

	<i>Microwave</i>	<i>Sonoelastography</i>	<i>Vibro-acoustography</i>	<i>Acousto-EM</i>
Acoustic Source	NA	AM US beam	Confocal US beams	AM US plane wave
Detection Method	NA	MRI	Hydrophone	Microwave
Compressional Waves	No	No	Yes	Yes
Shear Waves	No	Yes	No	Yes
Dielectric Contrast	Yes	No	No	Yes
Acoustic Spectroscopy	No	Yes	Yes	Yes
Est. Image Resolution	$\lesssim 5$ mm cube	$700 \mu\text{m sq} \times 2$ mm	$700 \mu\text{m sq} \times 9$ mm	$700 \mu\text{m} \times \lesssim 5$ mm sq
Detector Placement	Remote	Remote	Near surface	Remote
Acquisition Time	Short	Long	Long	Short
Background Noise	Low	Low	High	Low
Cost	Low	Expensive	Low	Low

Table 2.1: Comparative summary of four imaging systems including the proposed acousto-EM method.

the tumor geometry and elasticity needs to be developed.

2.3 Non-destructive Evaluation

Testing structural integrity is an important part of maintaining the nation’s infrastructure. Aging bridges and roadways need to be inspected to ensure their continued safe use. The development of means of non-destructive evaluation (NDE) is crucial to keeping the cost of maintenance to a minimum. Concrete, in particular, is difficult to image because of the high degree of heterogeneity and its coarse, aggregate nature. Radiographic means of inspection, such as X-ray or gamma-ray tomography, have been employed since the late 1960’s [46]. These systems are capable of providing resolution as high as 1 mm, however, they are expensive and their use requires training and safety precautions. Infrared thermography is another, less expensive means of inspection [47]. The images produced by this method, however, are difficult to interpret and are sensitive to conditions in the testing environment, such as weather. GPR has been used for NDE of concrete structures. Advantages of this type of imaging include low reflection of microwave energy at the concrete-air interface and high contrast between background concrete and steel reinforcements. One drawback is sensitivity to moisture content which greatly affects the dielectric properties of the

concrete under test. Acoustic imaging, another low cost imaging method, is based on acoustic wave propagation in the medium. Adequate resolution, however, requires a small beam size which necessitates using a large transducer or operating at high acoustic frequency. Coupling high frequency acoustic waves into concrete is difficult because of rapid attenuation. On the other hand, large transducers are impractical. As mentioned in [48], the principles of vibro-acoustography are also applicable to this area.

The acousto-EM approach could lead to a system which uses an acoustic source for excitation and a radar system for electromagnetic detection of the Doppler component. Since the acoustic portion of the system does not need to provide the resolution, the problems with acoustic imaging mentioned above would be mitigated. In addition, as in the case of medical imaging, the acousto-EM approach is not hindered by acoustic wave coupling out of the concrete. The information gained from the proposed approach could augment that from GPR analysis, yielding a more descriptive image. The relationship between the Doppler component and subsurface cracks, delaminations, or metallic reinforcements, however, needs to be developed in order to use an acousto-EM approach in NDE applications. The results of an investigation into the sensitivity of the Doppler EM signature to small internal flaws are presented in Chapter VII. It is demonstrated that the Doppler component is quite sensitive to the presence of flaws and, as such, is a viable alternative for further investigation in NDE applications.

CHAPTER III

Acousto-EM Model Development

3.1 Overview

In this chapter the model for acoustic and electromagnetic wave interaction is presented. The assumptions inherent in the model are first discussed along with relevant references. Then the analytical formulation is outlined. Details regarding implementation are given in the next chapter.

A great deal of effort has been devoted to the prediction of acoustic or electromagnetic scattering from moving or vibrating objects. These models take on various degrees of complexity. In references [49] and [50] one-dimensional electromagnetic scattering from a planar, perfectly conducting plate is analyzed for various plate displacements, including bulk motion and sinusoidal vibration. The FDTD is used in [51] to analyze one and two-dimensional scattering from vibrating perfectly conducting planar objects; this formulation requires knowledge of the incident fields, however, and is not as general as the formulation presented in Chapters III and IV.

The problem of acoustic scattering from a vibrating object is more complicated than the electromagnetic case. Depending on the target motion and frequency, there are two mechanisms that can give rise to a frequency modulated scattered field [52]. The first is the target vibration and the second is nonlinear interaction of the

incident pressure wave with the scattered pressure wave due to the target motion. This second mechanism can dominate the scattered acoustic field in certain regimes of vibration frequency; it is, however, due only to the nonlinear nature of acoustic wave propagation in the surrounding medium. As such, it is not relevant in the acousto-EM model.

The referenced publications distinguish between bulk target motion, which gives rise to the standard Doppler shifted scattered field, and target rotation or vibration, which modulates the scattered fields, similar to frequency modulation. The second case is termed the micro-Doppler effect to distinguish it from the bulk or static Doppler shift. The micro-Doppler component is analyzed for point scatterers and cubes in [53]. As in the present case, the micro-Doppler effect embeds additional information about the target into the scattered electromagnetic field.

This analysis relies on the Doppler shift on the electromagnetic wave due to the target vibration. Three important assumptions are made about the wave interaction and how the Doppler shift is imparted to the electromagnetic wave. First, interaction between the two types of waves away from the target is neglected. This is permissible since scattering from the resonant target itself is many orders of magnitude larger than scattering from density fluctuations in the acoustic medium when no special conditions are imposed, such as the Bragg condition. As mentioned in Section 1.4, an unsuccessful attempt was made to measure the wave interaction away from a resonant target.

The second assumption is that relativistic effects can be ignored. In the previously referenced studies on electromagnetic scattering from moving targets, these effects are accounted for using relativistic boundary conditions. In this model, however, the low acoustic frequency of motion or vibration can be used to simplify the analysis.

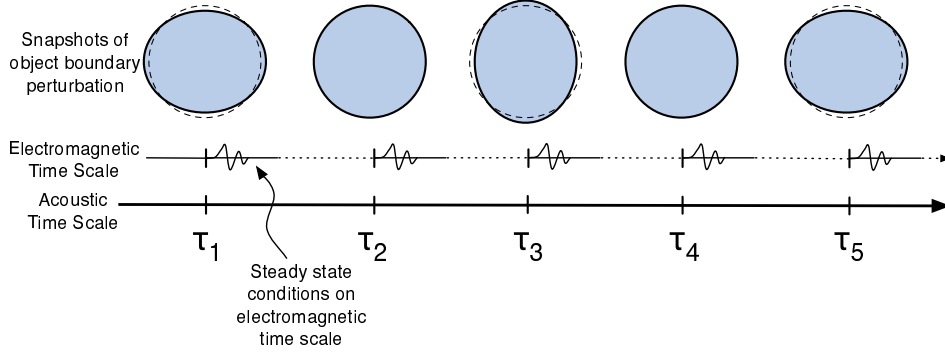


Figure 3.1: Two effective time scales of the problem. The electromagnetic solution reaches steady state before the object state has changed substantially. The QS approximation considers snapshots of the object at various instances over the acoustic time scale, labeled τ_i .

Since the acoustic frequency (on the order of kHz), is much less than the electromagnetic frequency (on the order of GHz), the problem effectively has two time scales. One is quickly varying corresponding to the electromagnetic frequency and the other is slowly varying with the acoustic frequency. Basically, the electromagnetic solution reaches a steady state condition before the object state has changed substantially, as illustrated in Figure 3.1. This allows the use of the quasi-stationary (QS) approximation. With the QS approximation a sequence of stationary positions corresponding to a particular mode of vibration are considered, i.e. snapshots of the object at various instances over the acoustic time scale, labeled τ_i in Figure 3.1, are considered individually. Therefore, the analysis for scattering from a slightly unperturbed object is the same as that to be used in the case of a vibrating object. The latter case, however, requires an additional step of reconstructing the sequence of solutions to reflect the time varying boundary of the scatterer. The number of required samples depends on the acoustic waveform and is ultimately determined by the Nyquist sampling theorem. For example, sinusoidal motion requires two samples; or, a single sample is required if only the amplitude information is desired.

While the analysis for the perturbed and vibrating cases is equivalent from the

modeling perspective, the interpretation of the resulting scattered fields is not. For a perturbed object, the scattered perturbation fields are not Doppler shifted and are at the same EM frequency as the incident wave. For the vibrating object, modulation of the incident wave occurs and the scattered, perturbation fields are the Doppler component, shifted away from the incident EM wave frequency by an amount equal to the acoustic frequency of motion.

The third assumption in the acousto-EM model is that the source of the Doppler component can be separated into contributions from the boundary perturbations and the interior density modulation. This was initially proposed in the context of acousto-EM in [1]. It is a reasonable simplification of the wave interaction process, given the nature of electromagnetic scattering.

Finally, the solution for the total scattered field, \mathbf{E} , is assumed to be of the form $\mathbf{E} = \mathbf{E}_o + \tilde{\mathbf{E}}$. That is, the total scattered field is composed of two parts, the unperturbed field, \mathbf{E}_o , scattered from the stationary, unperturbed object and a small perturbation component, $\tilde{\mathbf{E}}$, scattered as a result of the object perturbation. This form of solution is used throughout the analysis. As previously discussed, the frequency of the perturbation component, $\tilde{\mathbf{E}}$, depends on whether or not the perturbation is static with respect to time or varies, as in the case of a vibrating target. In the remainder of this document it is assumed that the target is vibrating and the perturbation fields of interest are the Doppler component.

3.2 Boundary Perturbation

One difficulty in brute force computational analysis of scattering from an acoustically vibrating object or a perturbed stationary object is the fine discretization required to resolve the object's motion. Even at a mechanical resonance of the tar-

get, the surface displacement of the object is quite small. While the actual value depends on the background and target materials and the incident acoustic power, for practical acoustic excitation, the displacement is on the order of tenths of microns. Therefore, capturing the effects of surface vibrations using direct discretization would require resolution smaller than the expected surface displacement. Another issue is accurately calculating the small Doppler component of the scattered field which, as seen in Figure 1.2, is orders of magnitude smaller than the unshifted field scattered from the stationary object. This makes extracting the Doppler component from straightforward numerical computation nearly impossible.

A recently derived general class of boundary conditions called sheet boundary conditions (SBC) has provided the necessary tools to significantly simplify the analysis [21, 54]. These boundary conditions are applied on the unperturbed object boundary and account for any object motion or boundary deformation. By replacing the moving object with a stationary object having special sheet impedance and admittance, these boundary conditions allow a single discretization of the unperturbed object. In addition, they allow separate computation of the first-order Doppler component, independent of the unshifted scattered fields. The method of moments has previously been used to verify the SBC and their application to simulate scattering from vibrating circular dielectric and metallic cylinders [21, 54]. It is noted that these boundary conditions are applicable for arbitrary perturbations to scatterers of any geometry. They also apply to lossy dielectrics and perfect electric conductors.

Figure 3.2 depicts the application of the SBC; the subscript 1 refers to the region external to the cylinder and 2 refers to the interior. The time varying sheet impedance and admittance, $Z_{1,2}^s(\tau)$ and $Y_{1,2}^s(\tau)$, respectively, account for the boundary motion. τ represents acoustic time.

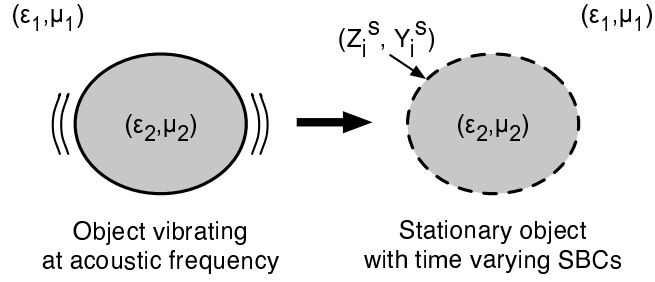


Figure 3.2: Applying sheet boundary conditions to the vibrating object's surface replaces it with a stationary scatterer having time varying surface impedance and admittance.

As mentioned, the SBC separate the dominant, unperturbed component due to scattering from the stationary object, \mathbf{E}_o , from the Doppler component due to the boundary perturbation and object motion, $\tilde{\mathbf{E}}$. This advantage of the SBC implies that the solution to the unperturbed problem may be found once and then used to find the scattered fields for any boundary perturbation or acoustic vibration.

The SBC are derived in [21] by considering solutions to scattering from cylinders with slightly perturbed boundaries. As noted, relativistic effects are neglected. The expressions are given by

$$(3.1) \quad \hat{n} \times (\mathbf{E}_1 - \mathbf{E}_2) = \hat{n} \times \hat{n} \times (Z_1^s \mathbf{H}_1 + Z_2^s \mathbf{H}_2)$$

$$(3.2) \quad -\hat{n} \times (\mathbf{H}_1 - \mathbf{H}_2) = \hat{n} \times \hat{n} \times (Y_1^s \mathbf{E}_1 + Y_2^s \mathbf{E}_2)$$

where $(\mathbf{E}_1, \mathbf{H}_1)$ are the fields external to the boundary and $(\mathbf{E}_2, \mathbf{H}_2)$ are the fields internal to the boundary. Also, \hat{n} is the unit normal to the object boundary. The sheet impedances and admittances, (Z_1^s, Y_1^s) and (Z_2^s, Y_2^s) , reside on the exterior and interior, respectively, of the interface between the scatterer and the background medium as shown in Figure 3.2. The scatterer is retained after the boundary conditions are applied. Second order boundary conditions are required for one of the two expressions; for TM (TE) it is necessary to use higher order conditions for the

magnetic (electric) field. For TM, the second order boundary condition is given by

(3.3)

$$-\hat{n} \times (\mathbf{H}_1 - \mathbf{H}_2) = \hat{n} \times \hat{n} \times \left[\gamma_1 \mathbf{E}_1 + \frac{\partial}{\partial s} \left(A_1 \frac{\partial}{\partial s} \mathbf{E}_1 \right) + \gamma_2 \mathbf{E}_2 + \frac{\partial}{\partial s} \left(A_2 \frac{\partial}{\partial s} \mathbf{E}_2 \right) \right]$$

where the partial derivative is with respect to the arc length along the tangent of the object boundary. The coefficients in equations (3.1) and (3.3) for TM polarization are given by

$$\begin{aligned} Z_1^s &= -jk_1\delta Z_1 & Z_2^s &= +jk_2\delta Z_2 \\ \gamma_1 &= \frac{-jk_1\delta}{Z_1} & \gamma_2 &= \frac{+jk_2\delta}{Z_2} \\ A_1 &= \frac{-j\delta}{k_1 Z_1} & A_2 &= \frac{+j\delta}{k_2 Z_2} \end{aligned}$$

where $k_{1,2}$ and $Z_{1,2}$ are the propagation constants and intrinsic impedances in regions 1 and 2, respectively, and δ is the perturbation to the object boundary.

The second order boundary condition for TE is given by

$$(3.4) \quad \hat{n} \times (\mathbf{E}_1 - \mathbf{E}_2) = \hat{n} \times \hat{n} \times \left[\eta_1 \mathbf{H}_1 + \frac{\partial}{\partial s} \left(B_1 \frac{\partial}{\partial s} \mathbf{H}_1 \right) + \eta_2 \mathbf{H}_2 + \frac{\partial}{\partial s} \left(B_2 \frac{\partial}{\partial s} \mathbf{H}_2 \right) \right]$$

The coefficients in equations (3.2) and (3.4) for TE polarization may be found using duality. The following is obtained:

$$\begin{aligned} Y_1^s &= \frac{-jk_1\delta}{Z_1} & Y_2^s &= \frac{+jk_2\delta}{Z_2} \\ \eta_1 &= -jk_1\delta Z_1 & \eta_2 &= +jk_2\delta Z_2 \\ C_1 &= \frac{-j\delta Z_1}{k_1} & C_2 &= \frac{+j\delta Z_2}{k_2} \end{aligned}$$

Note that all parameters on the right-hand sides of (3.1) - (3.4) are proportional to δ . Hence for an unperturbed problem,

$$(3.5) \quad \hat{n} \times (\mathbf{E}_{\mathbf{o}1} - \mathbf{E}_{\mathbf{o}2}) = 0$$

$$(3.6) \quad -\hat{n} \times (\mathbf{H}_{\mathbf{o}1} - \mathbf{H}_{\mathbf{o}2}) = 0$$

where, as before, subscripts 1 and 2 refer to the regions exterior and interior to the boundary, respectively. Relating total fields, e.g. $\mathbf{E}_{1,2} = \mathbf{E}_{\mathbf{o}1,\mathbf{o}2} + \tilde{\mathbf{E}}_{1,2}$, in equations (3.1) and (3.3) with the sheet boundary conditions and retaining only terms which are first order in δ yields the following for TM polarization:

$$(3.7) \quad \hat{n} \times (\tilde{\mathbf{E}}_1 - \tilde{\mathbf{E}}_2) = \hat{n} \times \hat{n} \times (Z_1^s + Z_2^s) \mathbf{H}_\mathbf{o}$$

$$(3.8) \quad -\hat{n} \times (\tilde{\mathbf{H}}_1 - \tilde{\mathbf{H}}_2) = \hat{n} \times \hat{n} \times \left[(\gamma_1 + \gamma_2) \mathbf{E}_\mathbf{o} + \frac{\partial}{\partial s} \left((A_1 + A_2) \frac{\partial}{\partial s} \mathbf{E}_\mathbf{o} \right) \right]$$

where continuity of the unperturbed tangential fields, e.g. $\mathbf{E}_\mathbf{o} = \mathbf{E}_{\mathbf{o}1} = \mathbf{E}_{\mathbf{o}2}$, along the object boundary is used to simplify the result. Similar expressions for TE may be obtained using equations (3.2) and (3.4):

$$(3.9) \quad \hat{n} \times (\tilde{\mathbf{E}}_1 - \tilde{\mathbf{E}}_2) = \hat{n} \times \hat{n} \times \left[(\eta_1 + \eta_2) \mathbf{H}_\mathbf{o} + \frac{\partial}{\partial s} \left((B_1 + B_2) \frac{\partial}{\partial s} \mathbf{H}_\mathbf{o} \right) \right]$$

$$(3.10) \quad -\hat{n} \times (\tilde{\mathbf{H}}_1 - \tilde{\mathbf{H}}_2) = \hat{n} \times \hat{n} \times \left((Y_1^s + Y_2^s) \mathbf{E}_\mathbf{o} \right)$$

On the left side of equations (3.7), (3.8), (3.9), and (3.10) is the unknown, Doppler component of the scattered fields and on the right side are the known fields for the unperturbed problem. To the first order, these fields act as electric and magnetic surface currents on the unperturbed object, generating the Doppler component. The unperturbed problem need only be solved once and then the unknown fields may be found for arbitrary boundary perturbations using the appropriate $\delta(\mathbf{r}, \tau)$.

It is emphasized that the boundary perturbation, δ , is the component of the displacement normal to the target boundary. This is a reasonable approximation considering that the boundary perturbation Doppler component accounts for electromagnetic scattering that occurs at material interfaces. The density modulation Doppler component, which will be discussed in the next section, accounts for shear displacements which produce variations in material density.

The first order approximations made in the SBC derivation imply that the boundary conditions produce accurate results only for small boundary perturbations. The limit on the magnitude of δ depends on the polarization as well as the target geometry and permittivity, among other factors. A value on the order of several hundredths of a wavelength would be typical. Implementing the SBC in FDTD will be discussed in Section 4.2.1.

3.3 Density Modulation

The second contribution to the Doppler component is from density fluctuations within the vibrating object. The derivation of this section closely follows that of reference [1]. This Doppler component is derived for dielectric cylinders by modeling the permittivity as the sum of the background value and a small fluctuation due to the displacements, or density variation, within the cylinder. The total permittivity is then written as $\epsilon_t(\mathbf{r}, \tau) = \epsilon + \delta_\epsilon \tilde{\epsilon}(\mathbf{r}, \tau)$, where ϵ is the background permittivity, δ_ϵ is a perturbation parameter, and $\delta_\epsilon \tilde{\epsilon}(\mathbf{r}, \tau)$ represents the fluctuation. The dependence of permittivity on both position and acoustic time scale is emphasized. As derived in the appendix of [1], the fluctuation can be related to the displacements, $\mathbf{u}(\mathbf{r}, \tau)$, within the object by

$$(3.11) \quad \delta_\epsilon \tilde{\epsilon}(\mathbf{r}, \tau) = -(\epsilon - \epsilon_o) \nabla \cdot \mathbf{u}(\mathbf{r}, \tau).$$

The derivation in [1] expands the fields within the object in a perturbation series in terms of the parameter δ_ϵ . The series and the above expression for the permittivity are then used in the two-dimensional wave equation. Equating powers of δ_ϵ and

keeping only the first order solution results in the following expression for TM:

$$\begin{aligned}
(3.12) \quad \nabla^2 \tilde{E}_z + k_d^2 \tilde{E}_z &= -\omega^2 \mu \tilde{\epsilon}(\mathbf{r}, \tau) E_{zo} \\
&= j\omega \mu J_{z\epsilon}
\end{aligned}$$

where $k_d = \omega \sqrt{\mu \epsilon}$ is the propagation constant in the background, unperturbed object. The typical source term on the right hand side of the wave equation is also shown; $J_{z,\epsilon}$ is the equivalent volumetric current which generates the perturbation fields $(\tilde{\mathbf{E}}, \tilde{\mathbf{H}})$. The derivation for TE follows the same procedure, producing the following, similar relationship:

$$\begin{aligned}
(3.13) \quad \nabla^2 \tilde{H}_z + k_d^2 \tilde{H}_z &= \left[-j\omega \nabla \tilde{\epsilon}(\mathbf{r}, \tau) \times \mathbf{E}_{zo} \right]_z - \omega^2 \mu \tilde{\epsilon}(\mathbf{r}, \tau) H_{zo} \\
&= j\omega \epsilon M_{z\epsilon}
\end{aligned}$$

The currents on the right sides of equations (3.12) and (3.13) are functions of only the known, unperturbed fields and the displacement within the object. Solving these expressions for the currents yields

$$\begin{aligned}
(3.14) \quad J_{z\epsilon} &= j\omega \tilde{\epsilon} E_{oz} \\
M_{z\epsilon} &= \left[-\frac{\nabla \tilde{\epsilon}}{\epsilon_o} \times \mathbf{E}_o \right]_z + j\omega \mu \frac{\tilde{\epsilon}}{\epsilon_o} H_{oz}
\end{aligned}$$

As with the boundary perturbation component, the unknown, first order Doppler component fields, $(\tilde{\mathbf{E}}_z, \tilde{\mathbf{H}}_z)$, are generated by the known, unperturbed fields $(\mathbf{E}_o, \mathbf{H}_o)$. Any continuous inhomogeneity within the scatterer may be accounted for using the currents in equation 3.14; abrupt material transitions, however, should be handled with the sheet boundary conditions of Section 3.2. Implementation of the density modulation Doppler component in FDTD will be discussed in Section 4.2.2.

CHAPTER IV

Implementation in the Finite-difference Time-domain Method

The analysis in Chapter III demonstrates that the Doppler component fields are generated by currents, which are functions of the unperturbed fields, placed on the surface and within the scatterer. This chapter describes how the currents are implemented in the electromagnetic simulation. The FDTD method is chosen to realize the electromagnetic simulation for various reasons. First, incorporating material inhomogeneity is straightforward. Access to field values throughout the computational domain is provided without additional overhead; this also allows placement of current sources at the desired locations in the simulation domain. In addition, since FDTD is a time-domain simulation, a single analysis is capable of providing information about a range of frequencies.

The remainder of this chapter provides a brief overview of FDTD then reviews implementation of the Doppler component sources in the FDTD simulation. Finally, a summary of the electromagnetic simulation is given.

4.1 Brief Introduction to Basic FDTD

The FDTD method is based on replacing the continuous temporal and spatial derivatives in Maxwell's equations with finite difference equations which are amenable

to numerical computation. A leapfrog approach is used to sequentially update spatially offset electric and magnetic field values. The basic algorithm was introduced in 1966 by Yee to study scattering from a rectangular PEC cylinder [55]. In 1975 Taflove and Brodwin reintroduced Yee's formulation to consider scattering from a dielectric target [56]. Since Yee's initial work a great deal of research has been devoted to generalizing the FDTD method. In this section only developments and details relevant to the FDTD code used in the acousto-EM implementation of the model in Chapter III are discussed. The reader is referred to references [57] and [58] for additional information.

The spatial sampling in the FDTD mesh is chosen to achieve the desired accuracy; as few as ten points per wavelength is adequate in some analyses. Maintaining stability requires that a limit is placed on the time step size, Δt , for a given spatial sampling increment, Δ . The stability limit, referred to as the Courant limit, ultimately restricts the relative temporal and spatial sampling such that the electromagnetic wave cannot propagate more than one spatial increment in one time step. For a two-dimensional simulation on a cartesian mesh with equal spatial sampling increments, Δ , in each direction, the Courant limit is given by $\Delta t \leq \Delta/(\sqrt{2}c)$, where c is the propagation speed in free space. The time step must be smaller than this limit in order to maintain field stability and finite energy. Numerous investigations into the stability of various forms of the FDTD method have been carried out; reference [57] reviews both stability criteria and other sources of computational error, such as dispersion and discretization errors, inherent in the FDTD method.

The development of absorbing boundary conditions, especially Berenger's perfectly matched layers (PML) [59, 60], led to increased use of FDTD in solving a variety of electromagnetic problems involving unbound domains. Gedney reformu-

lated Berenger's PML using a more physical and simpler development to obtain uniaxial PML (UPML) [61]; this form of absorbing boundary condition is used in the FDTD simulations presented herein.

The FDTD method has also been used to simulate complex media. Lossy or dispersive media can be handled in FDTD using an auxiliary differential equation (ADE) approach, which relates the electric flux density, \mathbf{D} , and the electric field, \mathbf{E} , with an ordinary differential equation based on the form of the permittivity [62]. This requires storing and updating the flux density as well as the electric field at each time step. When using the ADE approach for dispersive media with the UPML formulation, it becomes necessary to store and update two auxiliary variables for electric fields; two auxiliary variables are required for the magnetic field if magnetic loss is also being considered.

A near-field to far-field (NF-FF) transformation is introduced in [63, 64] to obtain field quantities in the far-field without extending the size computational domain to include the far-field region. Equivalent currents, formulated using field quantities in the near-field, are placed on a rectangular enclosure of the domain. The free space Green's function is then used to calculate the fields radiated by the equivalent currents in the far-field. Initially, the NF-FF transformation applied only to a single electromagnetic frequency. However, in [65, 66] the transformation is presented in the time-domain, which takes full advantage of the time-domain simulation and results in scattering information over a range of electromagnetic frequencies. An improvement to the accuracy of both the frequency and time-domain NF-FF transformations is introduced in [67]; this approach is used in the FDTD results presented herein.

In all of the results presented in the remainder of this document, the FDTD method is implemented on a standard, two-dimensional cartesian grid. As usual for

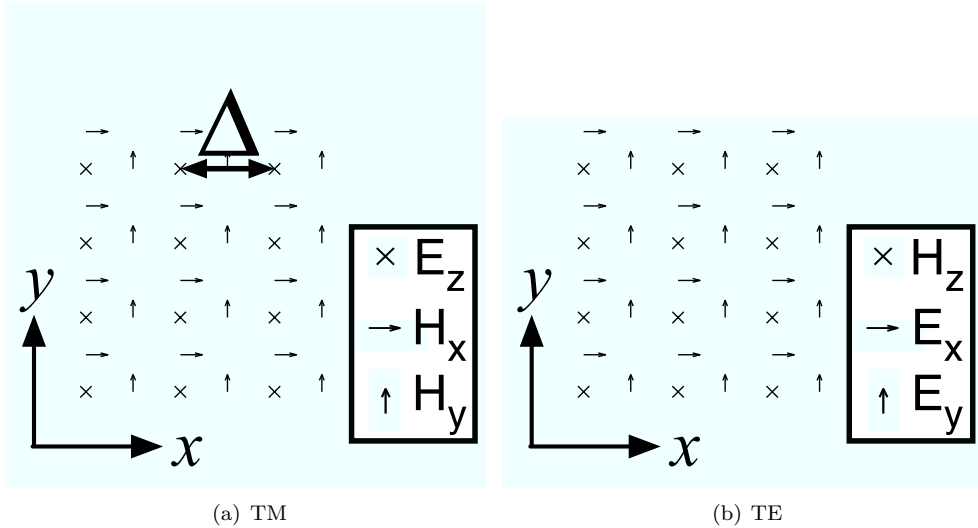


Figure 4.1: Two-dimensional FDTD mesh for TM and TE polarizations.

two-dimensional electromagnetic problems, the field components of interest may be separated into two polarizations: transverse magnetic (TM) and transverse electric (TE), where the reference direction is along \hat{z} and the simulation takes place in the $x - y$ plane. Figure 4.1 depicts the mesh for each polarization and indicates the relevant field components.

Various types of sources, including plane wave sources, sheet currents, and volumetric currents are included in the acousto-EM implementation according to the methods outlined in [57]. Implementation of a plane wave source is carried out using the total-field scattered-field (TF/SF) formulation; this allows the scattered field to be extracted from total field values in a portion of the computational domain, making it easier to calculate scattered fields in the far-field. Sheet and volumetric currents are introduced by adding the appropriate source terms in the update equations. Further details regarding the sources used in the FDTD implementation of the acousto-EM model will be given in the remaining sections of this chapter.

4.2 Implementation

In the following expressions $t = n\Delta t$ is used to denote the time scale of the unperturbed fields and $t' = q\Delta t$ represents the perturbation field time scale; Δt is the FDTD time step.

4.2.1 Boundary Perturbation in FDTD

Currents, which are functions of the unperturbed solution according to equations (3.7), (3.8), (3.9), and (3.10), placed on the surface of the object will generate the boundary perturbation Doppler component. Here, the boundaries are generally defined in terms of the contour of discontinuity of the constitutive parameters throughout the computational domain. The currents are simply the negative of the expressions obtained in equations (3.7) and (3.8) for TM or the corresponding expressions for TE, i.e. $-\mathbf{M} = \hat{n} \times (\tilde{\mathbf{E}}_1 - \tilde{\mathbf{E}}_2)$ and $-\mathbf{J} = -\hat{n} \times (\tilde{\mathbf{H}}_1 - \tilde{\mathbf{H}}_2)$. Using $\epsilon_i = \epsilon'_i + \sigma_i/j\omega$ and $\mu_i = \mu'_i$ in the coefficient expressions and transforming the currents to the time domain yields the following expressions for TM:

$$(4.1) \quad J_{z\delta}^q = \hat{n} \times \hat{n} \times \left[\delta(\epsilon'_2 - \epsilon'_1) \frac{\partial E_{oz}}{\partial t} \Big|_{n-\frac{1}{2}} + \delta(\sigma_2 - \sigma_1) E_{oz} \Big|_{n-\frac{1}{2}} + \frac{\partial}{\partial s} \left(\delta \left(\frac{1}{\mu_1} - \frac{1}{\mu_2} \right) \sum_{i=0}^{i=n-1} \left(\frac{\partial E_{oz}}{\partial s} \right)_i \Delta t \right) \right]$$

$$(4.2) \quad M_{s\delta}^{q+\frac{1}{2}} = -\hat{n} \times \hat{n} \times \left[\delta(\mu_2 - \mu_1) \frac{\partial H_{os}}{\partial t} \Big|_n \right]$$

and for TE:

$$(4.3) \quad J_{s\delta}^{q+\frac{1}{2}} = \hat{n} \times \hat{n} \times \left[\delta(\epsilon'_1 - \epsilon'_2) \frac{\partial E_{os}}{\partial t} \Big|_n + \delta(\sigma_1 - \sigma_2) E_{os} \Big|_n \right]$$

$$(4.4) \quad M_{z\delta}^q = \hat{n} \times \hat{n} \times \left[\delta(\mu_2 - \mu_1) \frac{\partial H_{oz}}{\partial t} \Big|_{n-\frac{1}{2}} + \left(\frac{1}{\epsilon'_1} e^{-(\sigma_1/\epsilon'_1)(n-1)\Delta t} - \frac{1}{\epsilon'_2} e^{-(\sigma_2/\epsilon'_2)(n-1)\Delta t} \right) * \frac{\partial}{\partial s} \left(\delta \frac{\partial H_{oz}^{n-1}}{\partial s} \right) \right]$$

where the subscripts s and z refer to current components tangent to the object boundary, lying in (along \hat{s}) and perpendicular to (along \hat{z}) the two-dimensional plane of simulation, respectively. It is noted that the boundary perturbation is a function of both position and acoustic time, i.e. $\delta = \delta(\mathbf{r}, \tau_i)$. Integration resulting from division by the factor $j\omega$ is replaced with a discrete sum as is appropriate to FDTD. The integrand field values are assumed to be constant over each time step. The integrated field values are taken at the unperturbed time step preceding the perturbation field time step. The convolution in equation (4.4) is efficiently implemented following the method of [68]. For PEC surfaces the derivation is modified by setting the fields in region two to zero or, equivalently, by neglecting the terms from region 2 in equations (4.1)-(4.4).

The location of source points on the boundary depends on the which polarization, TE or TM, is being considered and it depends on whether the material is a PEC or a dielectric. Figures 4.2 and 4.3 illustrate the two-dimensional FDTD grid, scatterer boundary, and SBC current locations for dielectric and PEC objects. The locations were chosen based on the agreement of the scattered fields with the analytical solutions for circular cylinders; changing the locations, for example, moving the TE currents to the exterior object boundary, does not greatly affect the results. Implementing the \hat{z} directed current is straightforward once the tangent, \hat{s} , has been determined and the required derivatives have been found. The currents lying in the tangent direction are more complicated. The staggered nature of the FDTD grid means that these current components are made up of \hat{x} - and \hat{y} -directed current elements that are not collocated. In addition, on curved surfaces, using the unit vector normal to the scatterer boundary in equations (4.2) and (4.3) produces \hat{x} - and \hat{y} -directed currents which are each composed of both \hat{x} - and \hat{y} -directed fields.

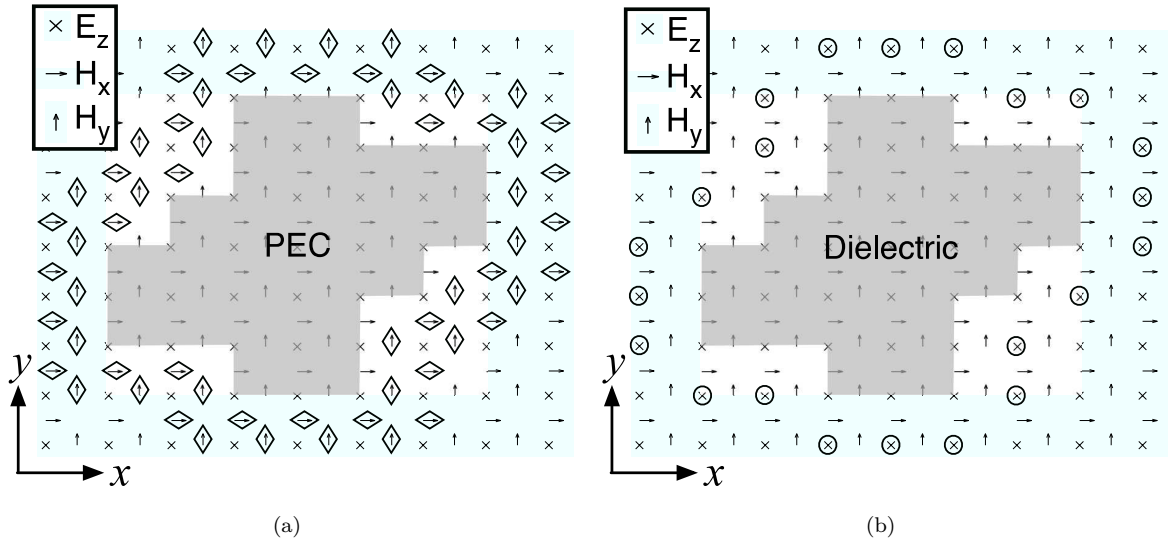


Figure 4.2: Current locations on *PEC* and dielectric objects for TM polarization.

This is implemented by averaging the field values at neighboring components on the same side of the scatterer boundary. The insets in Figure 4.3(b) highlight the current locations used for averaging. The center \hat{x} - (\hat{y} -) directed current uses all of the neighboring \hat{y} - (\hat{x} -) directed components that are present on the same side of the boundary. For example, at each J_x current point on a dielectric boundary, the four neighboring E_y locations are checked. Those field locations also lying inside the boundary are averaged to provide an approximate E_y value at the J_x current location. Straight boundaries, of course, are simpler, requiring the use of only the tangent field components in the current expressions.

It is noted that the derivative with respect to the surface tangent direction is implemented differently on dielectric and PEC boundaries for TE polarization; TM polarization does not require surface derivatives for nonmagnetic scatterers. On dielectric boundaries, the surface derivative is taken using finite differences in the \hat{x} and \hat{y} directions using the field values at neighboring current locations and then dot multiplying by the surface tangent vector, \hat{s} , at the current location. On PEC

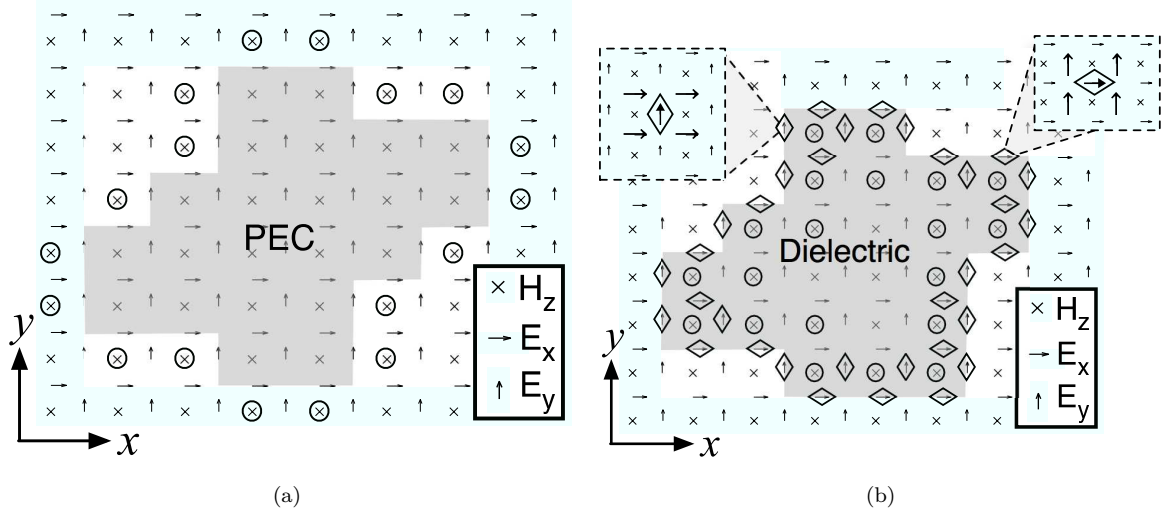


Figure 4.3: Current locations on *PEC* and dielectric objects for TE polarization.

boundaries, the derivative is taken using the difference between neighboring point field values and then dividing by the length between the two points, i.e. $\partial/\partial s \approx \Delta v/\Delta s$, where Δv represents the change in field value and Δs is the distance between the neighboring points. The two different derivatives produced more accurate results for their respective materials on the circular and straight edge boundaries considered in this analysis.

The surface currents have units of amperes per unit length (A/m). The FDTD update expressions, however, assume the current is an average value per unit cell area having dimensions of amperes per square meter (A/m^2). All currents are divided by the cell size, Δ , to obtain the correct line source current dimension.

Verification of SBC in FDTD

This section presents the results of implementing the sheet boundary conditions as described in Section 4.2.1. Results for a circular dielectric and PEC cylinders are shown. In all cases the boundary perturbation is typical of the $n = 2$ resonant mode of a circular cylinder, that is $\delta \propto \cos(2\phi)$. The amplitude is prescribed in terms of

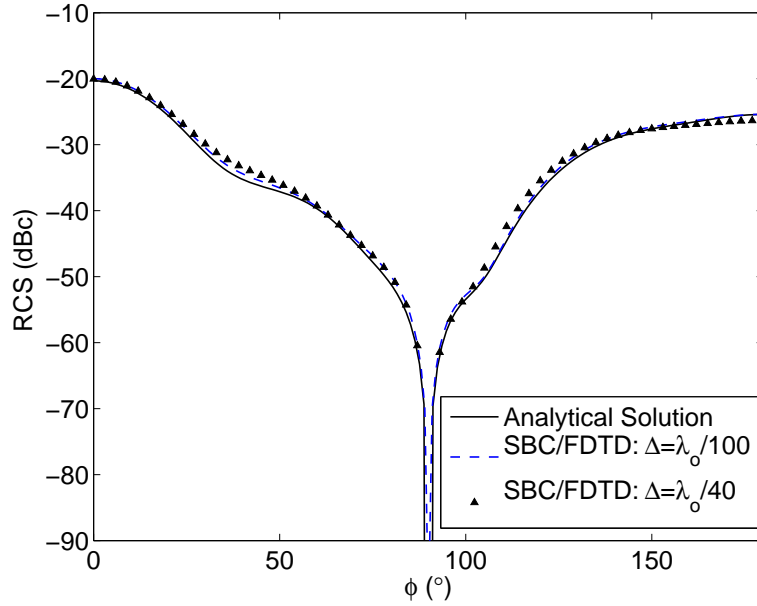


Figure 4.4: The boundary perturbation Doppler component of the bistatic RCS obtained from two-dimensional TE FDTD analysis. The result is shown for the $n = 2$ mode of a circular dielectric cylinder with radius $a = 0.75\lambda_o$, $\epsilon_r = 2.2$, and $\Gamma_2 = 0.02\lambda_o$.

the unshifted electromagnetic wavelength. Results for physical amplitudes obtained from acoustic simulation will be shown in Chapter VI.

A circular cylinder with $\epsilon_r = 2.2$ and radius $a = 0.75\lambda_o$ is analyzed using the two-dimensional TE FDTD formulation. The boundary perturbation is $\delta(\phi) = 0.02\lambda_o \cos(2\phi)$. The FDTD results are compared with the analytical solution in Figure 4.4. The TM result for a dielectric cylinder with $\epsilon_r = 2.0$, radius $a = 1.0\lambda_o$, and $\delta = 0.01\lambda_o \cos(2\phi)$ is shown in Figure 4.5.

The PEC cylinder radius is $a = 1.0\lambda_o$ and the boundary perturbation is $\delta = 0.005\lambda_o \cos(2\phi)$ and $\delta = 0.01\lambda_o \cos(2\phi)$, for TE and TM polarizations, respectively. The results are compared with the analytical results from [69] in Figures 4.6 and 4.7.

There is no analytical solution for the boundary perturbation to a square cylinder undergoing mechanical vibration. However, one advantage of the SBC and the FDTD implementation of the SBC is applicability to arbitrary geometries. The following

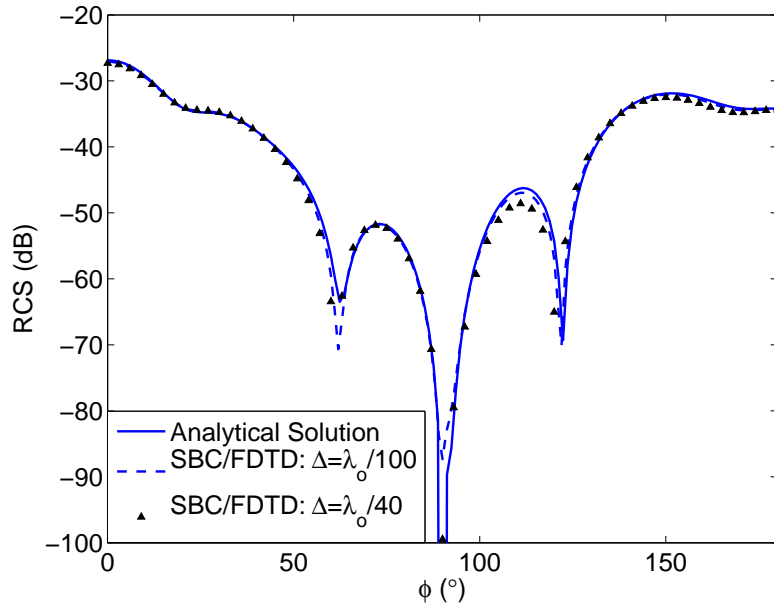


Figure 4.5: The boundary perturbation Doppler component of the bistatic RCS obtained from two-dimensional TM FDTD analysis. The result is shown for a circular dielectric cylinder with radius $a = 1.0\lambda_o$, $\epsilon_r = 2.0$, and $\delta = 0.01\lambda_o \cos(2\phi)$.

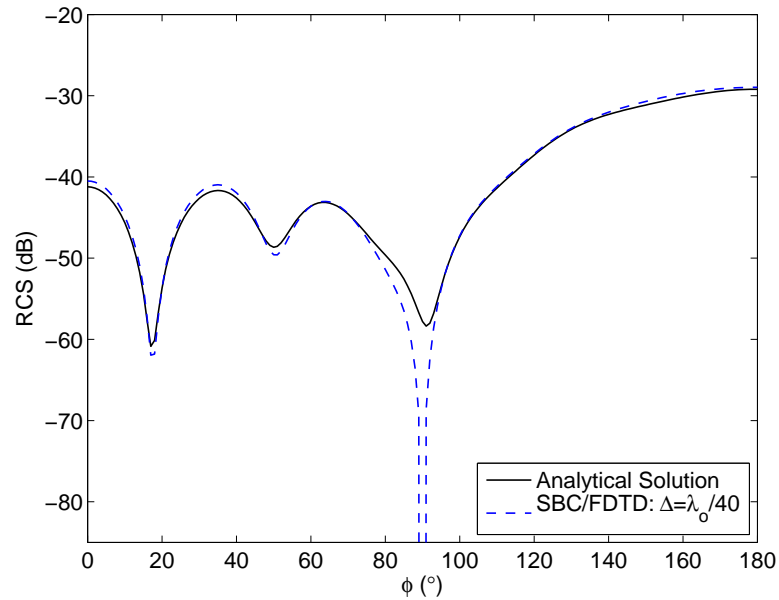


Figure 4.6: The boundary perturbation Doppler component of the bistatic RCS obtained from two-dimensional TE FDTD analysis. The result is shown for the $n = 2$ mode of a circular PEC cylinder with radius $a = 1.0\lambda_o$ and $\delta = 0.005\lambda_o \cos(2\phi)$.

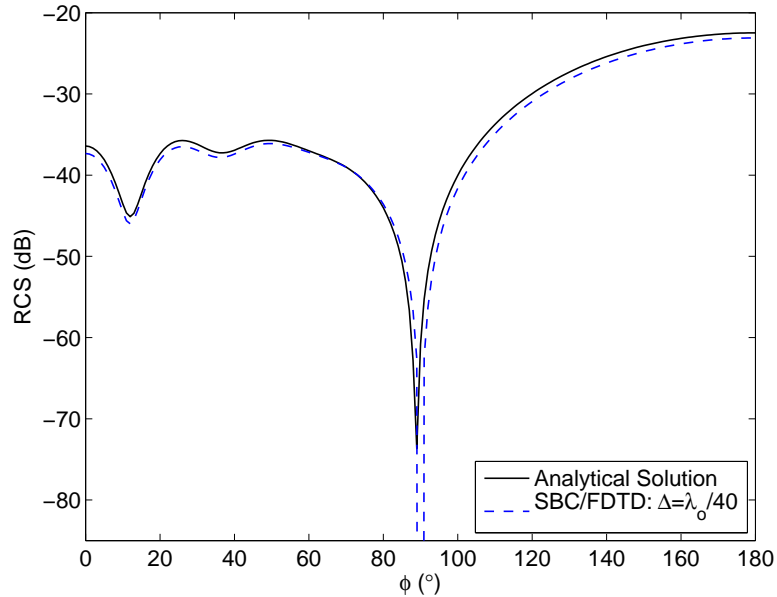


Figure 4.7: The boundary perturbation Doppler component of the bistatic RCS obtained from two-dimensional TM FDTD analysis. The result is shown for the $n = 2$ mode of a circular PEC cylinder with radius $a = 1.0\lambda_o$ and $\delta = 0.01\lambda_o \cos(2\phi)$.

results demonstrate agreement between a method of moments implementation of the SBC and the FDTD formulation for a prescribed boundary perturbation. The method of moments formulation incorporates the SBC and uses the standard pulse-basis and point-matching techniques [21]. The TE polarized Doppler component of the bistatic RCS for a square cylinder with radius $a = 0.75\lambda_o$, $\epsilon_r = 2.2$, and $\delta = 0.02\lambda_o \cos(2\phi)$ is shown in Figure 4.8. The TM polarized Doppler component of the bistatic RCS of a square cylinder with $a = 1.00\lambda_o$, $\epsilon_r = 2.0$, and $\delta = 0.01\lambda_o \cos(2\phi)$ is shown in Figure 4.9.

The first-order assumptions in the derivation of the SBC and the currents in Section 4.2.1 place the upper bound on the magnitude of acceptable boundary perturbation. The maximum permissible magnitude depends on many parameters but is on the order of multiple hundredths of a wavelength. The SBC and the associated currents are accurate down to zero boundary perturbation; in fact, as the boundary

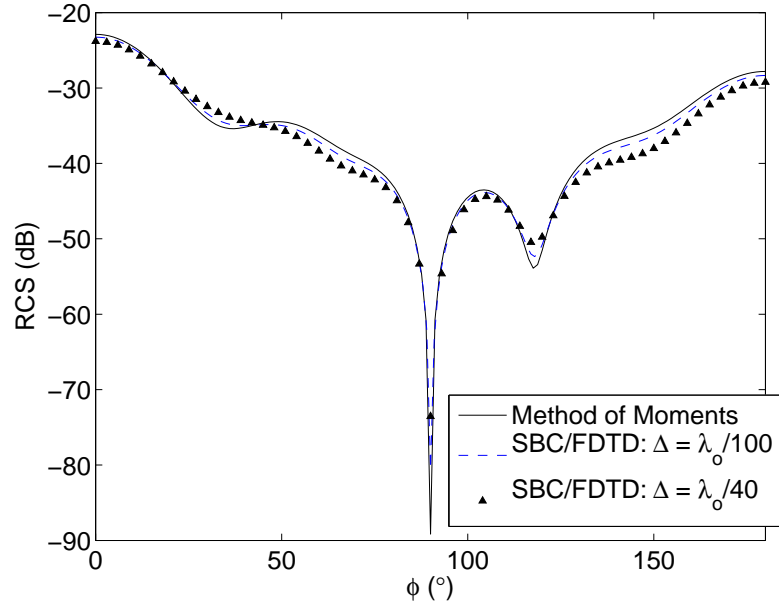


Figure 4.8: Doppler component of the bistatic RCS for a square cylinder for TE polarization; $a = 0.75\lambda_o$, $\epsilon_r = 2.2$, and boundary perturbation $\delta = 0.02\lambda_o \cos(2\phi)$.

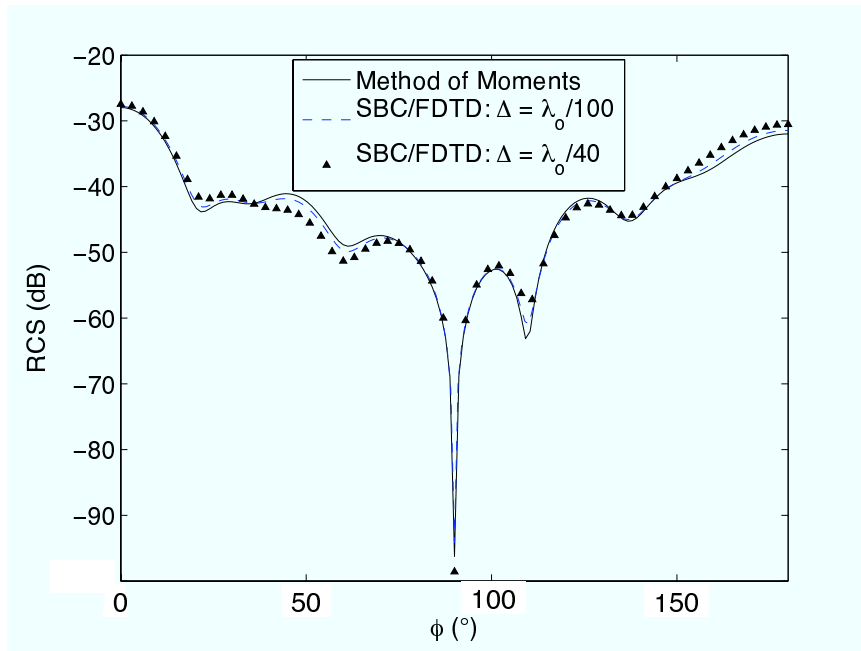


Figure 4.9: Doppler component of the bistatic RCS for a square cylinder for TM polarization; $a = 1.00\lambda_o$, $\epsilon_r = 2.0$, and boundary perturbation $\delta = 0.01\lambda_o \cos(2\phi)$.

perturbation is reduced, the results become more accurate because of the first order approximations used in the derivation. There is, of course, a noise floor in the simulation established by rounding error and finite precision; this noise floor ultimately places the lower limit on the permissible boundary perturbation magnitude. Once the perturbation fields fall below the noise floor then the results would be incorrect. However, this occurs at very small values of boundary perturbation, which are not of practical interest. Boundary perturbation magnitudes as small as $10^{-6} - 10^{-7}\lambda_o$, which are of the same order as magnitudes that can be expected in practice, have been tested and yield Doppler components that agree with the analytical solution.

Another type of error in the results is introduced by the stair-case approximation inherent in the FDTD method; this error is present for any boundary perturbation magnitude and function. Discretization error contaminates the unperturbed fields and also dictates the SBC current locations, making averaging necessary, which introduces additional error. The results for a circular cylinder, which is a worst-case scenario in terms of discretization, are shown above and indicate good agreement with the analytical solution. The Doppler component for two FDTD cell sizes is also shown in Figures 4.4 and 4.5 to provide an indication of the effects of cell size.

4.2.2 Density Modulation in FDTD

The density modulation currents from equation (3.14) are rewritten using equation (3.11) and with $\epsilon = \epsilon'_2 + \sigma_2/j\omega$. It is assumed that region 1, exterior to the target, is free-space ($\epsilon_1 = \epsilon_o$, $\sigma_1 = 0$). Transforming to the time domain yields the following expressions for TM:

$$(4.5) \quad J_{z\epsilon}^q = -\epsilon_o(\epsilon'_2 - 1)\nabla \cdot \mathbf{u} \frac{\partial E_{oz}}{\partial t} \Big|_{n-\frac{1}{2}} - \sigma_2 \nabla \cdot \mathbf{u} E_{oz} \Big|_{n-\frac{1}{2}}$$

and for TE:

$$(4.6) \quad M_{z\epsilon}^q = (\epsilon'_2 - 1) \left[-\mu \nabla \cdot \mathbf{u} \frac{\partial H_{oz}}{\partial t} \Big|_{n-\frac{1}{2}} + \left(\nabla \nabla \cdot \mathbf{u} \times \mathbf{E}_o \Big|_{n-\frac{1}{2}} \right)_z \right] + \frac{\sigma_2}{\epsilon_o} \left[-\mu \nabla \cdot \mathbf{u} H_{oz} \Big|_{n-\frac{1}{2}} + \left(\nabla \nabla \cdot \mathbf{u} \times \sum_{i=0}^{i=n-1} \mathbf{E}_o \Big|_i \Delta t \right)_z \right]$$

Implementing the volumetric currents is straightforward once the divergence of the displacement, $\nabla \cdot \mathbf{u}$, is known within the scatterer. At each \hat{z} field location a current value from equation (4.5) or (4.6) is added into the field update equation. Since the update equations assume an average value per unit cell area no correction factor related to the cell size needs to be applied, as it did in the SBC implementation.

Verification of Density Modulation Doppler Component in FDTD

The results for the $n = 2$ mode of a solid polyethylene cylinder are shown here to verify the above FDTD formulation against the analytical solution in [1]. The analytical form for the divergence of the displacement within a solid circular elastic cylinder is discussed in Chapter VI. The incident acoustic plane wave used in the analytical solution has an amplitude of 1 Pa; the material properties for polyethylene are given in Section 6.1 of Chapter VI. The results for TE and TM polarizations are shown in Figures 4.10 and 4.11, respectively.

The agreement between the density modulation Doppler component and the analytical solution is quite good. In general, it is better than that for the boundary perturbation Doppler component since it is less susceptible to the inherent discretization errors in the FDTD method.

The density modulation Doppler component for a mode of a square cylinder is also presented. The square cylinder dimensions are 10 cm \times 10 cm, the permittivity is 2.25, and the cylinder material is polyethylene. The mode frequency is $f_a = 3485$ Hz. There is no analytical solution for acoustic scattering from a square cylinder to

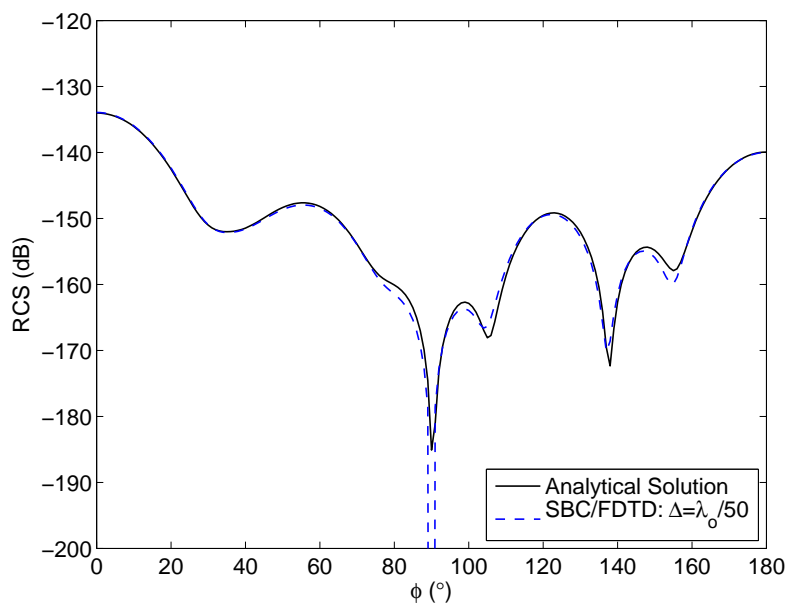


Figure 4.10: The density modulation Doppler component of the bistatic RCS obtained from two-dimensional TE FDTD analysis. The result is shown for the $n = 2$ mode of a circular polyethylene cylinder with radius $\rho_o = 1.0\lambda_o$ and $\epsilon_r = 2.25$.

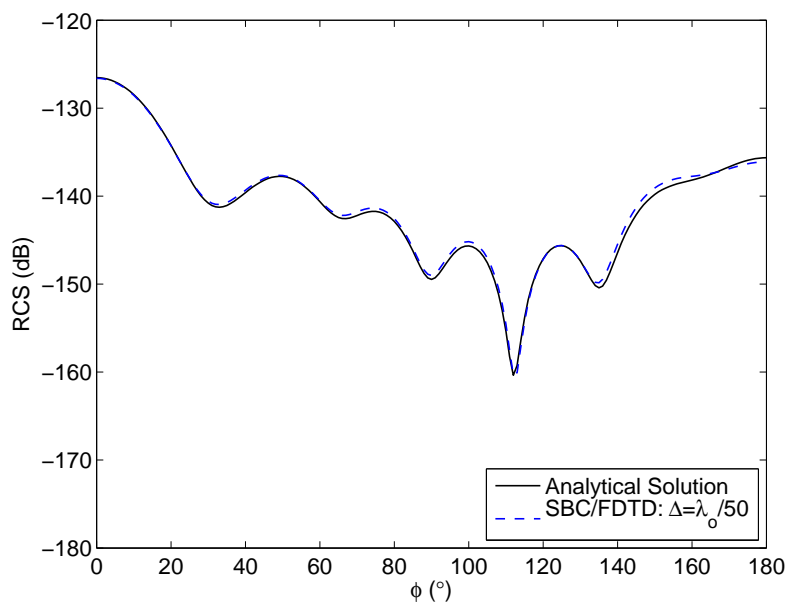


Figure 4.11: The density modulation Doppler component of the bistatic RCS obtained from two-dimensional TM FDTD analysis. The result is shown for the $n = 2$ mode of a circular polyethylene cylinder with radius $\rho_o = 1.0\lambda_o$ and $\epsilon_r = 2.25$.

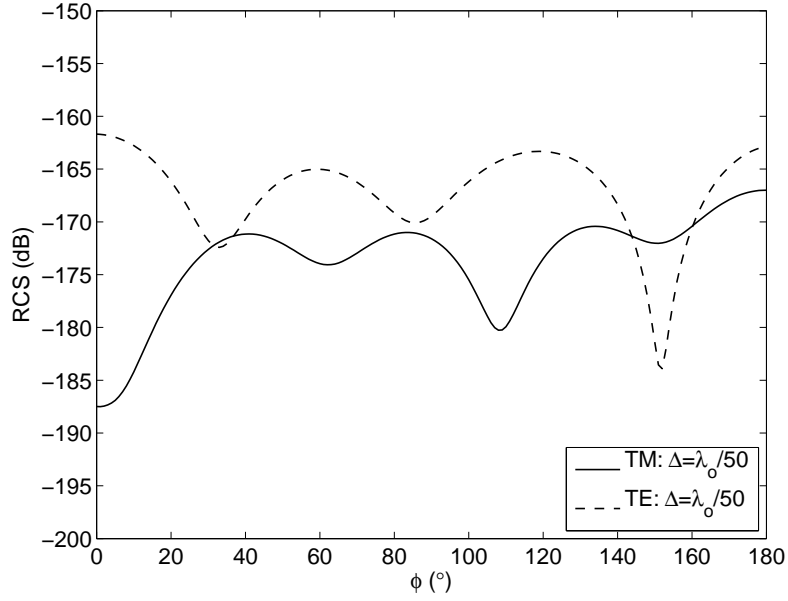


Figure 4.13: Bistatic TM and TE Doppler components for a 10 cm square polyethylene cylinder; the mode frequency is $f_a = 3485$ Hz; the electromagnetic frequency is 3 GHz.

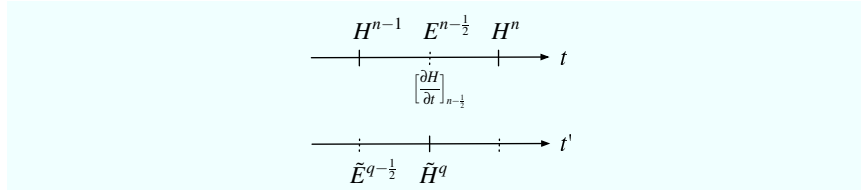


Figure 4.14: Illustration of time stepping; t indicates the unperturbed time scale and t' indicates the perturbation field time scale.

time step then the time derivative of H_{z0} coincides with the magnetic field update on the perturbation field time scale, t' . This is illustrated for the TE_z fields in Figure 4.14.

The unperturbed problem of scattering from the stationary object is run once and the fields $(\mathbf{E}_o, \mathbf{H}_o)$ on the boundary and within the scatterer are stored. Additional FDTD simulations are run where the only sources are the surface and volume currents generating the perturbation fields $(\tilde{\mathbf{E}}, \tilde{\mathbf{H}})$; the number of additional simulations, or how many τ_i are considered, depends on the acoustic time variation of the mode. For example, a single mode with sinusoidal displacements requires two simulations

for complete amplitude and phase information.

CHAPTER V

Physical Model

As seen in the previous chapters, in order to calculate the Doppler component, the displacement on the surface (δ) and the divergence of the displacement ($\nabla \cdot \mathbf{u}$) within the target are required. The gradient of the divergence of the displacement is also required for TE polarization. Analytical solutions for these quantities and the associated mode shapes do not exist for arbitrary targets. In such cases, computer simulations of the acoustic scattering problem are used. A flowchart depicting the full two-step simulation is shown in Figure 5.1. First, the acoustic simulation is used to obtain the appropriate modal displacements. In the second step, electromagnetic simulation uses the displacement information to produce the Doppler component.

ANSYS¹ software is chosen for the acoustic simulation in the present research; its most important attribute, in this case, is the ability to model fluid-structure interactions (FSI). The software constructs a system of equations based on a user-defined finite element model composed of elements and nodes. An appropriate means of solving the system of equations is chosen depending on the structure and complexity of the system matrix. In this research ANSYS is used to consider fluid (air) plane wave scattering from an elastic target. A typical model used to obtain results such as those of Chapter VI is shown in Figure 5.2. The fluid is modeled using four node

¹ANSYS, Inc., <http://www.ansys.com>

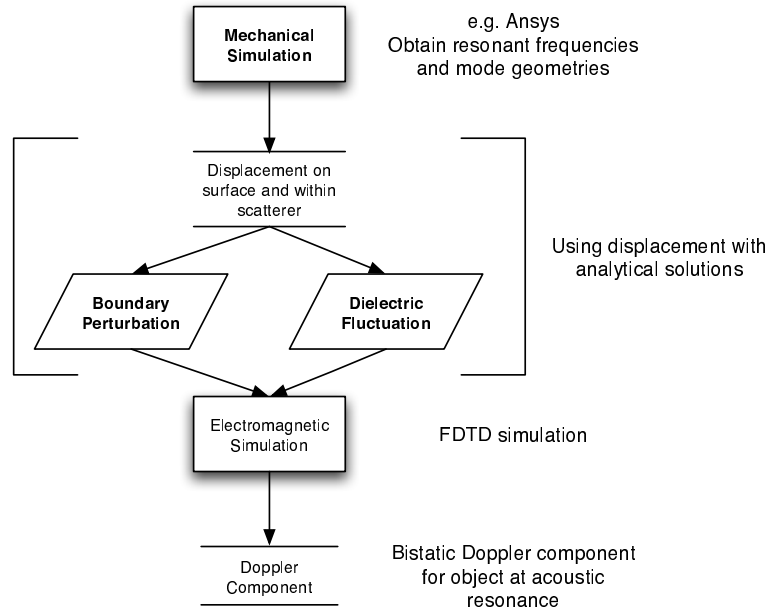


Figure 5.1: Basic flowchart of the simulation approach to the evaluation of acousto-EM wave interaction.

elements that account for two-dimensional pressure variations but, generally, have zero displacement. The fluid elements lying next to the scatterer, however, are permitted to be displaced as required by the boundary conditions on the scatterer. The FSI flag is set on these elements, allowing them to couple the fluid and the elastic structure and accurately model the physical interaction between the acoustic waves and the elastic waves. The inset in Figure 5.2 shows the nodes at the fluid-structure boundary. The elastic structure is composed of eight node structural elements. The elements are confined to the $x - y$ plane, that is, no displacement is allowed in the \hat{z} direction. The mid-point nodes on the sides of the solid elements on the fluid-solid boundary are removed so the two nodes on the fluid elements coincide with the two remaining nodes on the solid element. This is depicted in Figure 5.2. In order to absorb the outgoing fluid waves absorbing elements are placed on the periphery of the simulation domain. The ANSYS manual recommends placing the boundary at least 0.2λ away from the scatterer, where λ is the wavelength in the fluid of the

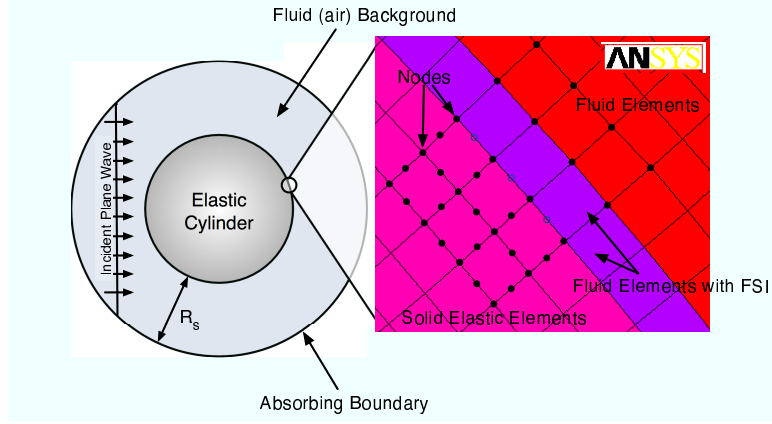


Figure 5.2: A typical ANSYS model used to simulate fluid plane-wave scattering from an elastic target. The nodes on the fluid and solid elements at the fluid-structure boundary are shown inset.

dominant frequency component. The element size is determined by the minimum wavelength of interest, which depends on the frequency and the shear and longitudinal wave velocities within the model. Specific model parameters will be discussed in more detail in Chapters VI and VII.

Once the model is built and meshed, acoustic scattering is simulated using harmonic analysis. The frequency of the excitation is swept over an appropriate range to excite a resonant mode of the target. The nodal displacements on the object boundaries are stored at the resonant frequency to use within the FDTD model of the boundary perturbation Doppler component. The divergence of the displacement is also saved in the target interior at the resonant frequency to use in the density modulation Doppler component. Conveniently, this quantity is readily available as the sum of the trace of the strain tensor:

$$(5.1) \quad \nabla \cdot \mathbf{u} = \sum_{i=1}^3 \varepsilon_{ii} = \sum_{i=1}^3 \frac{\partial u_i}{\partial x_i}$$

where x_i represents the orthogonal coordinate directions and ε is the strain.

Once the displacement information is obtained from ANSYS it is interpolated to the FDTD grid points. One and two-dimensional interpolation is used for the

boundary and interior displacements, respectively. A cubic spline approximation package (CSAgrid²) is used to perform the interpolation. For TE polarization the gradient of the divergence of displacement within the object is also required. In order to calculate this quantity, delaunay triangulation is used to find each node's nearest neighbors. This is implemented with a qhull³ library function. A quadratic surface is then fit to the function $(\nabla \cdot \mathbf{u})$ values at the node and neighboring node locations. An exact fit is available with five neighboring points; otherwise, a least squares solution is found. A linear system of equations is solved for the gradient, which varies linearly over the area defined by the nodes. The algorithm is explained further in reference [70]. Finally, the gradient of $\nabla \cdot \mathbf{u}$ is interpolated to the FDTD grid points.

²CSAgrid, <http://ngwww.ucar.edu/ngdoc/ng/ngmath/csagrid/csahome.html>

³Qhull, <http://www.qhull.org/html/qdelaun.htm>

CHAPTER VI

Case Studies of the Bistatic Doppler Component

The purpose of this Chapter is to inform the reader about the forward problem, that is, predicting the Doppler component from a known target. At the conclusion of this Chapter, various observations are made on the form of the Doppler component for given mode and target parameters.

The Doppler components for various modes of cylindrical geometries are considered. The first case is a homogeneous polyethylene cylinder; the results for three different resonant modes are given. The second case is a layered steel and concrete cylinder. Further details regarding both the ANSYS and FDTD simulations will also be given in the following sections.

In all of these results, the Doppler component is presented as a radar cross section (RCS) defined by

$$(6.1) \quad RCS = \lim_{r \rightarrow \infty} 2\pi r \frac{|\tilde{\mathbf{E}}|^2}{|\mathbf{E}_i|^2}$$

where r is the radial distance from the origin, $\tilde{\mathbf{E}}$ is the Doppler component, and \mathbf{E}_i is the Fourier transform of the incident pulse. The magnitudes are normalized to the maximum stationary target RCS; the units are, therefore, dB below carrier, or dBc.

6.1 Polyethylene Cylinder

The first part of this section gives a brief overview of acoustic scattering from homogeneous elastic cylinders. The ANSYS model used to simulate acoustic scattering from a 10 cm polyethylene cylinder is described. Finally, the results of the ANSYS and FDTD simulations for the Doppler component of various resonant modes are presented. Results in this section are shown at a single electromagnetic frequency, $f_e = 3$ GHz; wideband Doppler component results will be shown in Chapter VII.

6.1.1 Acoustic Scattering from a Homogeneous Elastic Cylinder

Plane acoustic wave scattering from homogeneous elastic cylinders has been considered numerous times. In this case, the approach of Faran [71] and Doolittle [72], which represents the solution as an infinite series of normal modes, is most appropriate. The following analysis outlines only the results relevant to the acousto-EM model; the reader is directed to the references for the complete solution of the problem.

The geometry of the problem is shown in Figure 6.1; the cylinder radius is denoted as a . The density and acoustic wave speed in the fluid are given by (ρ_f, c_f) ; the density, Young's modulus, and Poisson ratio for the elastic cylinder material are given by (ρ_s, E, ν) , respectively. Using the following relationships, the shear and longitudinal wave speeds, c_s and c_l , respectively, in the elastic solid may be found:

$$(6.2) \quad c_s = \sqrt{\frac{E}{2\rho_s(1+\nu)}}$$

$$(6.3) \quad c_l = \sqrt{\frac{E(1-\nu)}{\rho_s(1+\nu)(1-2\nu)}}.$$

The unknowns in the scattering problem are the displacements within the cylinder, \mathbf{u} , and the scattered pressure, p_s , in the fluid region. Acoustic time dependence of

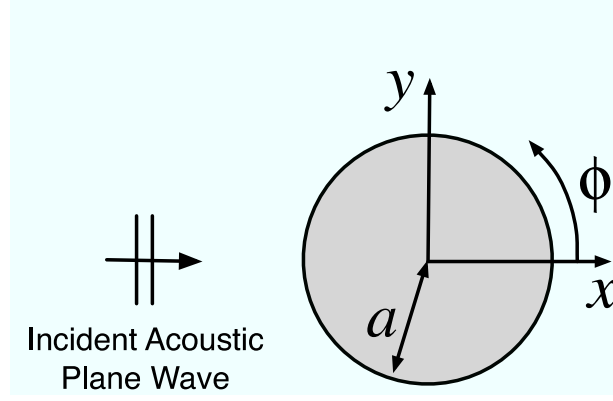


Figure 6.1: Geometry of the acoustic scattering problem.

the form $e^{j\omega_a t}$ is understood throughout the analysis.

The incident pressure plane wave, which propagates in the \hat{x} -direction in the fluid, may be rewritten as an infinite series of bessel functions as follows:

$$(6.4) \quad p_i = P_o e^{-jk_f x}$$

$$(6.5) \quad = P_o \sum_{n=0}^{\infty} \varepsilon_n (-j)^n J_n(k_f r) \cos(n\phi)$$

where P_o is the wave amplitude, $k_f = \omega_a/c_f$ is the propagation constant in the fluid, and J_n is the order n bessel function of the first kind. The radial component of the displacement is related to the incident pressure wave using

$$(6.6) \quad u_{i,r} = \frac{1}{\rho_f \omega_a^2} \frac{\partial p_i}{\partial r}.$$

The equation of motion inside the solid, elastic medium may be simplified into separate wave equations. One equation represents longitudinal waves, which are characterized by particle motion along the direction of wave propagation; the other equation represents shear waves, which are characterized by particle motion perpendicular to the direction of propagation. Using scalar and vector potentials, the solution for the displacements appearing in the separate wave equations may be found. The symmetry of the scattering geometry is used to obtain displacements of

the following form:

$$(6.7) \quad u_r = \sum_{n=0}^{\infty} \left[\frac{nb_n}{r} J_n(k_s r) - a_n \frac{d}{dr} J_n(k_l r) \right] \cos(n\phi)$$

$$(6.8) \quad u_\phi = \sum_{n=0}^{\infty} \left[\frac{na_n}{r} J_n(k_l r) - b_n \frac{d}{dr} J_n(k_s r) \right] \sin(n\phi)$$

$$(6.9) \quad u_z = 0$$

where $k_s = \omega_a/c_s$ and $k_l = \omega_a/c_l$ are the shear and longitudinal wave numbers in the solid. The divergence of the displacement, which also can be found analytically, is given by

$$(6.10) \quad \nabla \cdot \mathbf{u} = k_l^2 \sum_{n=0}^{\infty} a_n J_n(k_l r) \cos(n\phi).$$

Finally, the scattered pressure is of the following form:

$$(6.11) \quad p_s = \sum_{n=0}^{\infty} c_n \left[J_n(k_f r) - jY_n(k_f r) \right] \cos(n\phi)$$

where Y_n is the order n bessel function of the second kind. The normal displacement in the fluid associated with the scattered pressure wave, $u_{s,r}$, is found using equation (6.6) with p_s replacing p_i .

The unknown coefficients a_n , b_n , and c_n are found by imposing the appropriate boundary conditions at the fluid-solid interface at $r = a$. The boundary conditions are as follows:

1. the total pressure in the fluid ($p_i + p_s$) must be equal to the normal component of the stress in the solid
2. the total normal displacements in the fluid ($u_{i,r} + u_{s,r}$) must be equal to the normal displacement in the solid (u_r)
3. the tangential stress on the boundary of the cylinder must be equal to zero

Formulas relating displacement and stress within the cylinder are given in the references. The three boundary conditions provide three equations with which to solve for the three, unknown coefficients. The coefficient matrix determinant, defined as $D(n, \omega_a)$, is a function of the mode number, n and the acoustic frequency, ω_a . The resonant modes are a result of the determinant of the coefficient matrix going to zero, creating an unforced or free mode of vibration at certain acoustic frequencies. These frequencies are solutions of the equation $D(n, \omega_a) = 0$ [73]. There are infinitely many solutions of this equation for each mode, $n = 0, 1, 2, \dots$; the solution order is denoted by $l = 1, 2, 3, \dots$. For example, the (n, l) mode corresponds to the l^{th} solution of the equation $D(n, \omega_a) = 0$. Physically, the mode number n determines the axial dependence of the mode; higher numbers implies that there is greater variation as a function of axial angle, ϕ , within the cylinder. The mode number l denotes the amount of radial variation; where, again, larger values indicate increased variation. The two mode numbers uniquely characterize the resonant modes of the cylinder.

Near the (n, l) resonance of the cylinder the displacement is primarily produced by the order n term in the infinite series, which dominates the other terms. This implies that near the resonance corresponding the $(2, l)$ mode, for example, the radial displacement has axial dependence that is proportional to $\cos(2\phi)$. The constant of proportionality depends on the coefficients, the cylinder radius, and the elastic material. The radial variation associated with the $(2, l)$ mode depends on the solution order l .

For application in the acousto-EM model the frequencies of the resonant modes of the cylinder and the functional form of the displacement, \mathbf{u} , within the cylinder are of interest. As will be seen in the following sections, the axial dependence of the radial displacement is an important factor in determining the boundary perturbation

	<i>Young's modulus</i> (E , GPa)	<i>Density</i> (ρ_s , kg/m ³)	<i>Poisson Ratio</i> (ν)	c_s (m/s)	c_l (m/s)
Polyethylene	0.621	900	0.42	492.9	1327.2
Air	–	1.2	–	–	340

Table 6.1: Parameters used in ANSYS simulation of acoustic scattering from a solid, polyethylene cylinder.

Doppler component. The divergence of the displacement given in equation (6.10) is also important in determining the density modulation Doppler component.

6.1.2 ANSYS Model

The polyethylene cylinder is simulated in ANSYS using the parameters found in Table 6.1. The finite element mesh is generated at 10 kHz so that the same mesh may be used for a range of various modes, three of which are considered herein. The element size is determined by the shortest wavelength in the model in order to guarantee adequate resolution throughout. In this case, the shortest wavelength occurs in air and the nominal element size is chosen to be $\lambda_{a, mesh}/24$, where $\lambda_{a, mesh}$ is the acoustic wavelength in air at 10 kHz. The simulation dimensions are shown in Figure 6.2. The acoustic excitation is a 1Pa amplitude plane wave incident from the left, as indicated in the figure. The large distance between the cylinder and the absorbing fluid elements is required to obtain an approximately plane incident wavefront and close agreement with the analytical scattering solution.

6.1.3 (2, 1) Mode

The lowest order resonant mode of a 10 cm polyethylene cylinder is the $n = 2$ mode. The analytic acoustic resonant frequency obtained from solving equation () is found to be $f_a = 1844.8$ Hz [74]. The resonant frequency found in ANSYS is within 1 Hz of the analytical value and the maximum deviation of the displacement from the analytical solution is smaller than 5%.

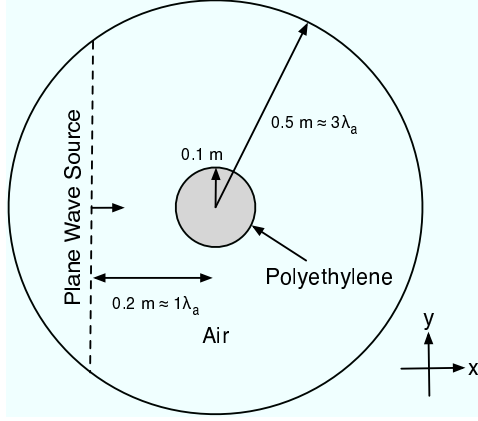


Figure 6.2: ANSYS model used to simulate an acoustic plane-wave scattering from a polyethylene cylinder.

The boundary perturbation for the $(2, 1)$ mode is shown in Figure 6.3, where the expected $\cos(2\phi)$ dependence in equation (eqn:acousticdisp) is observed. The maximum boundary perturbation relative to the cylinder radius for an incident pressure wave having $1Pa$ amplitude, is $\delta/a = 2 \times 10^{-6}$. The magnitude and divergence of the displacement within the cylinder are also obtained from ANSYS and interpolated to the FDTD grid points. These quantities are shown in Figures 6.4(a) and 6.4(b), respectively. The divergence of the displacement, which is related to the strain according to equation 5.1, determines the density modulation Doppler component for TM polarization; for TE polarization, the gradient of this quantity is also a factor.

The results are presented at an electromagnetic frequency of $f_e = 3$ GHz. At this frequency, the cylinder radius is $1\lambda_e$. The cylinder permittivity is $\epsilon_r = 2.25$, the cell size, Δ , is $\lambda_e/100$, and the time step, Δt , is $0.98\Delta/(\sqrt{2}c)$, or 0.98 of the two-dimensional Courant limit. The UPML is 14 cells thick and there are 5 cells between the boundary of the cylinder and the total-field/scattered-field boundary. An \hat{x} -directed plane wave is launched from the TF/SF boundary. The total FDTD grid size is 249 cells square and the simulation is run for 5000 time steps.

Sheet currents are placed on the surface of the cylinder to produce the boundary

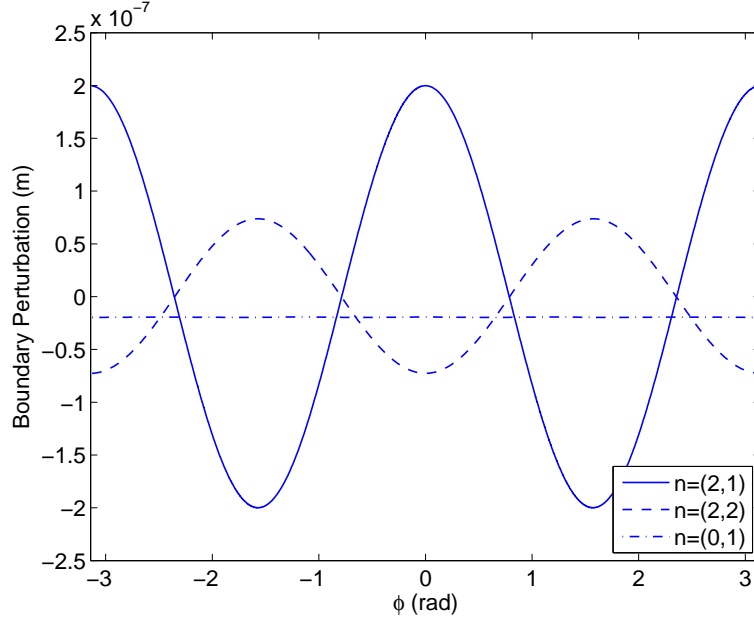


Figure 6.3: Boundary perturbation obtained from ANSYS simulations of a homogeneous polyethylene cylinder at three distinct modes of vibration.

perturbation Doppler component; for TM only $J_{z,\delta}$ is present and for TE only $J_{s,\delta}$ is present because the cylinder is nonmagnetic and its conductivity is zero. Currents are also present throughout the cylinder cross-section to generate the density modulation Doppler component. The results of the individual contributions to the Doppler component for both TM and TE polarization are shown in Figures 6.5 and 6.6, respectively; the analytical solutions are also shown. For this mode, the boundary perturbation contribution dominates the total Doppler component for both polarizations. The characteristic null at $\phi = 90^\circ$ is a result of the $\cos(2\phi)$ dependence of the radial displacement at the cylinder boundary.

6.1.4 (2,2) Mode

The analytical resonant frequency of the (2,2) mode is 3634 Hz, which is equal to that obtained in the ANSYS simulation. The displacement associated with the (2,2) mode has the same axial dependence as the (2,1) mode while having addi-

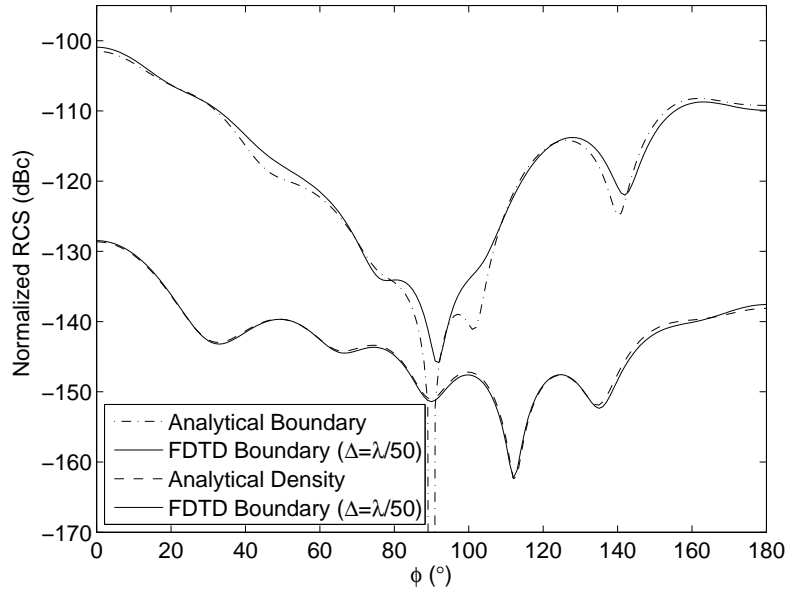


Figure 6.6: Bistatic TE Doppler component for (2, 1) mode of a 10 cm radius polyethylene cylinder; $f_a = 1.8$ kHz, $f_e = 3$ GHz.

tional variation along the radial direction. The boundary perturbation relative to the cylinder radius for this mode is $\delta/a = 7.5 \times 10^{-7}$. The magnitude of the displacement within the cylinder is shown in Figure 6.7. The boundary perturbation, as seen in Figure 6.3, is similar to that of the (2, 1) mode but smaller in magnitude. The divergence of the displacement, which is not shown, is also similar to that of the (2, 1) mode except it is about 22 times larger.

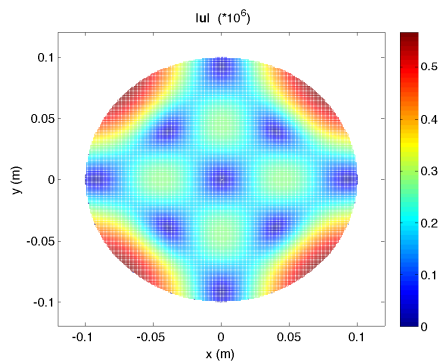


Figure 6.7: The magnitude of the displacement within a homogeneous polyethylene cylinder for the (2, 2) mode.

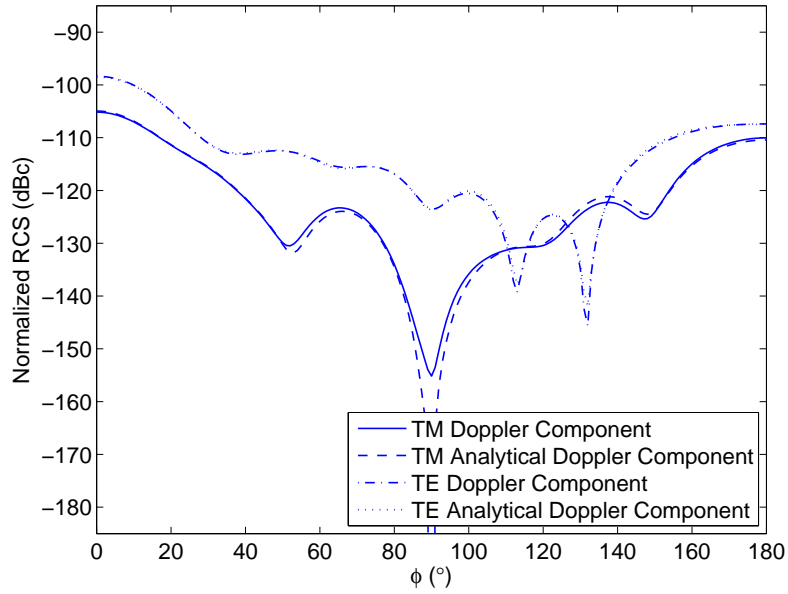


Figure 6.8: Bistatic TM Doppler component (normalized to the unperturbed backscatter RCS value) for the (2, 2) mode of a 10 cm radius polyethylene cylinder; $f_a = 3.63$ kHz, $f_e = 3$ GHz. The boundary perturbation relative to the cylinder radius for this mode is $\delta/a = 7.5 \times 10^{-7}$.

The FDTD simulation parameters are identical to those listed for the (2, 1) mode. The Doppler component for both TM and TE polarizations at 3 GHz are shown in Figure 6.8. The analytical solutions are also shown for comparison. The density modulation contribution for the (2, 2) mode, which is not shown separately in Figure 6.8, is higher than for the (2, 1) mode. This is expected since the variation of the displacement within the cylinder is much greater for the higher order mode. This is especially true for TE polarization, which has an even larger contribution from density modulation because of the gradient operation in equation (3.14). As expected, the boundary perturbation contribution to the Doppler component is similar to that of the (2, 1) mode. The boundary perturbation for TM polarization dominates the total Doppler component of this mode, leaving the characteristic null at $\phi = 90^\circ$.

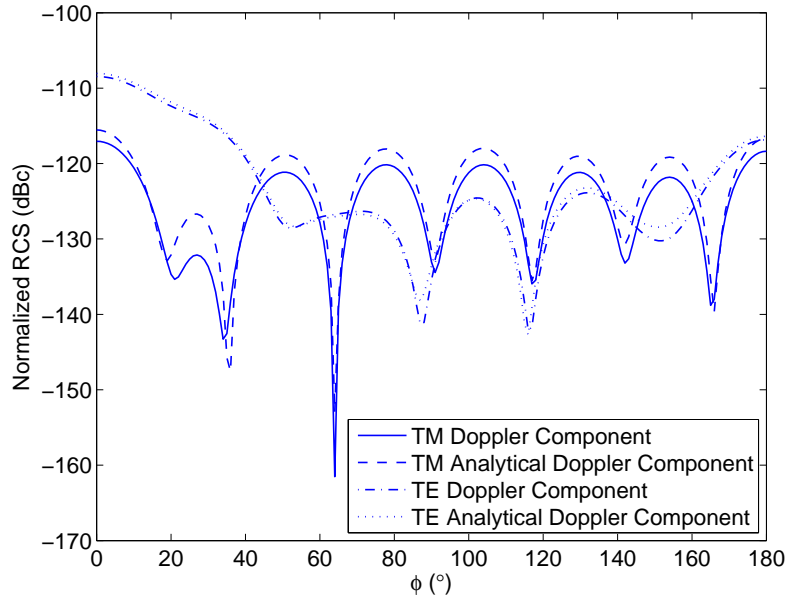


Figure 6.9: Bistatic TM Doppler component (normalized to the unperturbed backscatter RCS value) for the (0,1) mode of a 10 cm radius polyethylene cylinder; $f_a = 4.82$ kHz, $f_e = 3$ GHz. The boundary perturbation relative to the cylinder radius for this mode is $\delta/a = 2 \times 10^{-7}$.

6.1.5 (0,1) Mode

The analytical resonant frequency of the (0,1) mode is 4818.7 Hz, which is 0.1 Hz lower than the ANSYS simulation value. This mode is characterized by axially uniform contraction and expansion. The boundary displacement, therefore, is approximately constant along the perimeter of the cylinder, as seen in Figure 6.3. The boundary perturbation relative to the cylinder radius for this mode is $\delta/a = 2 \times 10^{-7}$. The divergence of the displacement within the cylinder is also axially symmetric and is not shown. The Doppler component for both TM and TE polarizations at 3 GHz is compared with the analytical solution in Figure 6.9. The axially symmetric displacement and strain yield a series of peaks and nulls in the bistatic return for the Doppler component.

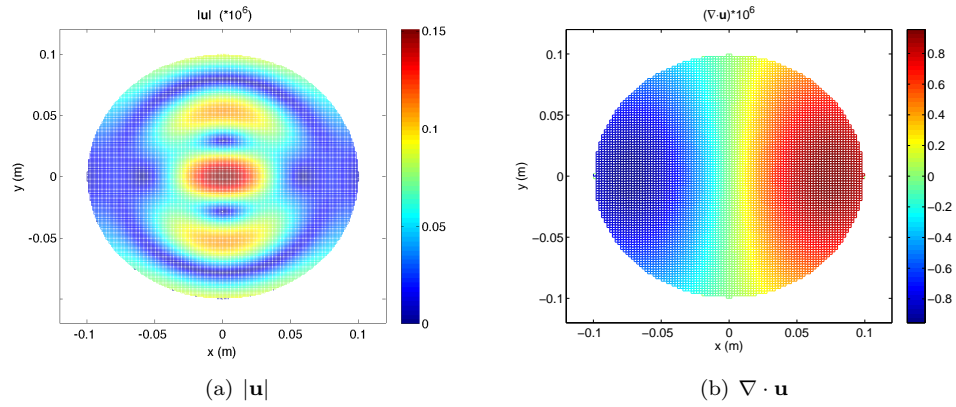


Figure 6.10: The magnitude and divergence of the displacement within a homogeneous polyethylene cylinder for a shear mode at $f_a = 5232.95$ Hz.

6.1.6 (1,2) Shear Mode

One advantage of the acousto-EM approach is its ability to detect shear modes of resonance. An all-acoustic system would have difficulty detecting shear modes because the scattered shear waves cannot propagate in the surrounding fluid (air). The acousto-EM system can remotely detect the modes, independent of the intervening fluid. The Doppler component for the (1,2) mode at $f_a = 5232.95$ Hz is presented to demonstrate this advantage.

The magnitude and the divergence of the displacement associated with this mode are shown in Figures 6.10(a) and 6.10(b), respectively. Both the radial and axial displacements on the boundary of the cylinder are shown in Figure 6.11. The radial boundary displacement for this mode is approximately ten times smaller than that of the (2,1) mode considered previously; this is expected for a shear mode which, as seen in Figure 6.11, has larger displacement in the axial direction, along the cylinder boundary.

The forward-scattered ($\phi = 0^\circ$) pressure versus acoustic frequency at an observation point 16 cm from the cylinder boundary is also plotted in Figure 6.12. This

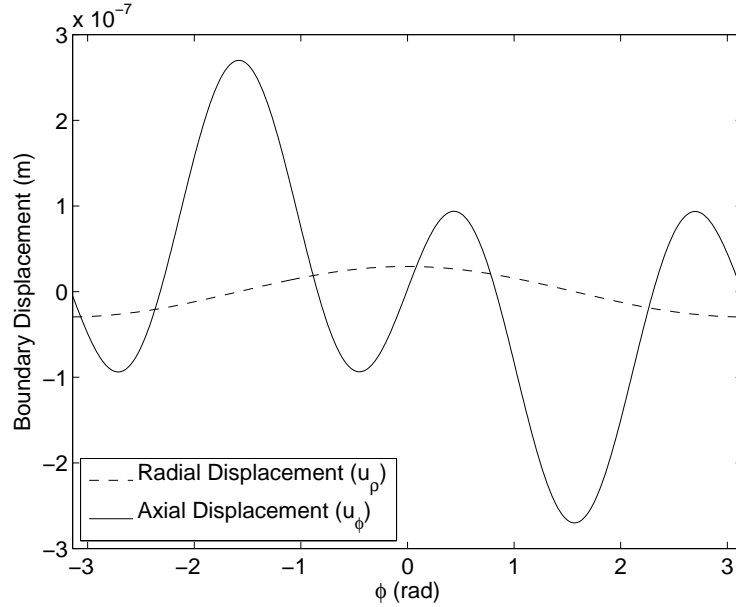


Figure 6.11: Boundary perturbation obtained from ANSYS simulations of a homogeneous polyethylene cylinder at the (1, 2) mode of vibration, corresponding to a shear mode.

plot shows the limited sensitivity of acoustic scattering to shear modes of resonance. For comparison, the plot also shows the scattered pressure at the neighboring (6, 1) mode at $f_a = 5374.1$ Hz; this mode is not a shear mode and, as observed in the figure, produces much larger scattered pressure.

The total Doppler component at 3 GHz is shown for TM and TE polarizations in Figure 6.13. The individual contributions are not shown, however, it is noted that the density modulation contribution is comparable to and, at some angles, greater than the boundary perturbation contribution. This is expected given the small radial displacement associated with this mode. The discrepancy between the FDTD result and the analytical solution is due to error in the displacements obtained with the ANSYS model.

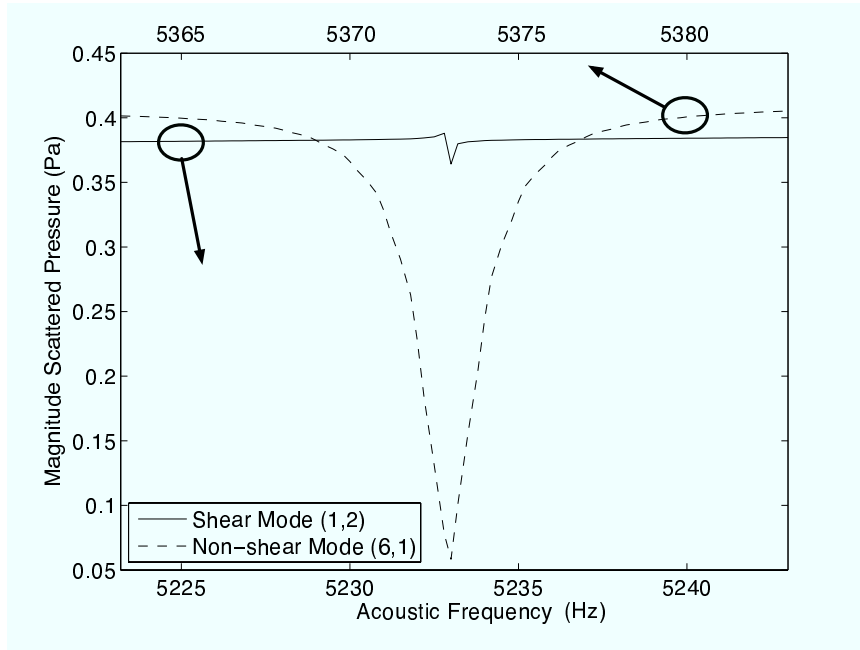


Figure 6.12: The magnitude of the forward-scattered pressure for two modes of a homogeneous polyethylene cylinder versus acoustic frequency. The solid line corresponds to the (1,2) mode, which is a shear mode. The forward-scattered pressure for the non-shear (6,1) mode is also shown for reference.

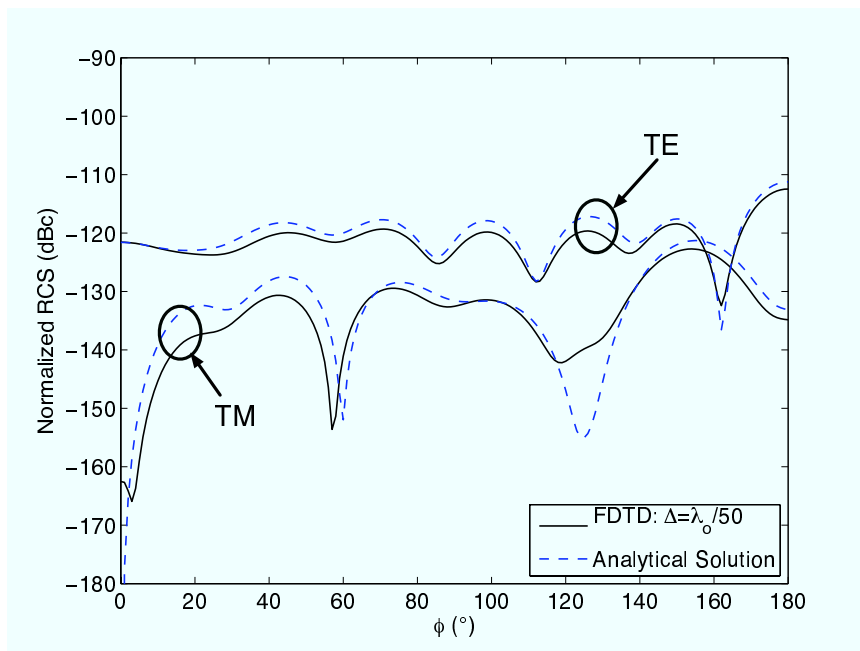


Figure 6.13: The total bistatic Doppler component (normalized to the unperturbed backscatter RCS value) for both TM and TE polarizations. These results are for the (1,2) mode of a 10 cm radius polyethylene cylinder; $f_a = 5.2$ kHz, $f_e = 3$ GHz.

6.2 Layered Cylinder

The analytical solution for the Doppler component in the previous case of a homogeneous cylinder exists and serves to validate the FDTD implementation described in Chapter IV. The layered cylinder, which is considered in this section, illustrates how to extend the model to an inhomogeneous object. Instead of an acoustic plane wave source, the model employs a line source in contact with the outer boundary of the cylinder. This is intended to simulate a contact transducer placed on the object surface.

Acoustic scattering from a layered elastic cylinder is first reviewed. The ANSYS model used to simulate acoustic scattering from a layered cylinder having material properties similar to reinforced concrete is then described. Finally, the results of the ANSYS and FDTD simulations for the Doppler component of various resonant modes are presented. Results in this section are shown at a single electromagnetic frequency of $f_e = 2.5$ GHz; wideband Doppler component results will be shown in Chapter VII.

6.2.1 Acoustic Scattering from a Layered Elastic Cylinder

The analytical solution for acoustic scattering from a layered elastic cylinder follows the same procedure as that for the homogeneous cylinder in Section 6.1.1. The scattering geometry is shown in Figure 6.14. There are two distinctions, however. The first difference between this and the previous, homogeneous case is the type of source which is used to excite the acoustic mode of resonance. In this case, a line source is placed at the outer cylinder boundary at $r = a$. This changes the functional form of the incident pressure and displacement; however, it does not affect the procedure used to solve for the unknown coefficients and the resonant modes.

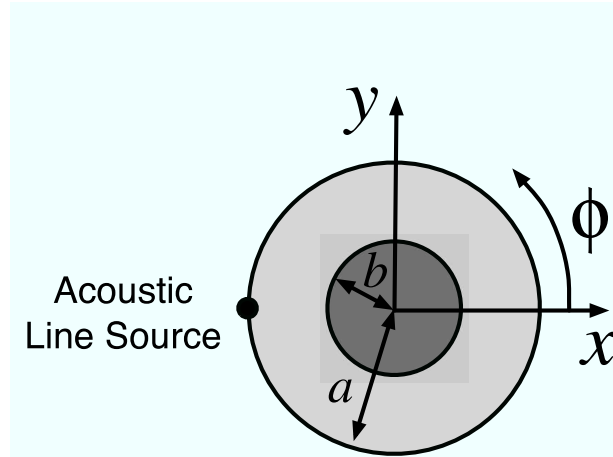


Figure 6.14: Geometry of the acoustic scattering problem for a layered cylinder.

The second difference, as seen in Figure 6.14, is that boundary conditions must be applied at two boundaries. One boundary is at $r = a$, the outer cylinder radius, and the second is at $r = b$, the inner cylinder radius. The boundary conditions listed in Section 6.1.1 apply without modification at the fluid-elastic interface at $r = a$. At the elastic-elastic interface at $r = b$, the boundary conditions are as follows:

1. tangential (u_ϕ) and radial (u_r) displacement must be continuous across the boundary,
2. tangential and radial stress must be continuous across the boundary.

Along with the three boundary conditions at $r = a$, there are five total equations to solve for the unknown coefficients. The addition of the third, inner cylinder region, however, also increases the number of unknown coefficients to five. The system of equations and unknowns is solved for the unknown coefficients as in the homogeneous case; the determinant of the coefficient matrix, $D(n, \omega_a)$, again, may be used to find the resonant mode frequencies for the layered structure. The pair of mode numbers, (n, l) , is still used to characterize the acoustic modes.

Further details regarding scattering from layered elastic cylinders may be found in

	<i>Young's modulus</i> (E , GPa)	<i>Density</i> (ρ_s , kg/m ³)	<i>Poisson Ratio</i> (ν)	c_s (m/s)	c_l (m/s)
Concrete	30	2200	0.2	2383.7	3892.5
Steel	195	7860	0.29	3101	5701.8
Air	—	1.2	—	—	340

Table 6.2: Parameters used in ANSYS simulation of acoustic scattering from a layered concrete and steel cylinder.

reference [75], which deals with line sources, and reference [76], which deals with the slightly more complicated problem of elastic wave scattering from layered cylinders.

6.2.2 ANSYS Model

The layered cylinder is shown in Figure 6.15. The outer cylinder of 8 cm radius is concrete and the inner cylinder of 1.5 cm radius is steel; the material parameters used in the ANSYS simulation are given in Table 6.2. Material inhomogeneity within the cylinder is neglected.

The element size is $\lambda_a/24$, where λ_a is the approximate shear wavelength within the cylinder at 75 kHz. The acoustic wavelength in the surrounding air is about $0.15\lambda_a$; accordingly, the nominal element size is reduced by about 20 in the fluid. The sampling in this region is still relatively coarse, though, at about 5 points per wavelength in some areas. The source point is indicated in Figure 6.15; a 1N force is applied over the face of the boundary element, normal to the cylinder surface, in the \hat{x} direction. In the analytical solution, the line source is placed at the outer boundary of the concrete region, but is still considered to be inside the concrete. This makes it difficult to relate the source amplitude in the analytical solution, which is a scalar potential function, to that in the ANSYS simulation, which is a force. For this reason, the analytical displacement is normalized to the ANSYS result and agreement between the mode shapes is considered.

Three modes are investigated in this section. Two of these modes correspond the

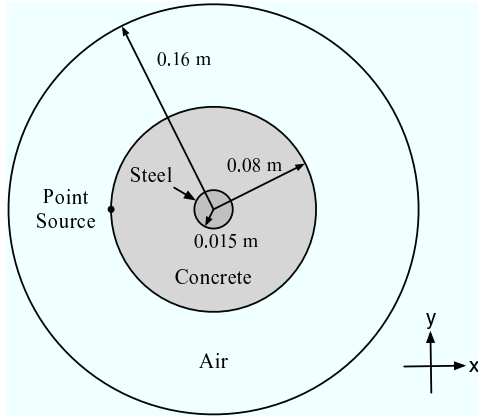


Figure 6.15: Illustration of the geometry for the layered cylinder simulation in ANSYS.

modes of an isolated, 1.5 cm radius steel cylinder in an infinite, concrete background. The displacement and strain associated with the third mode is primarily localized in the outer concrete layer.

6.2.3 (0, 3) Mode

The first mode considered here is the third order $n = 0$ mode of the layered cylinder; the analytical resonant frequency is $f_a = 74126.8$ Hz. The simulated resonant frequency is $f_a = 74127.5$ Hz. The radial boundary displacement, u_r , at both cylinder boundaries is shown in Figure 6.16; the slight variation at the steel boundary is due to the choice of ANSYS points used in the interpolation. The magnitude of the displacement, \mathbf{u} , for this mode is shown in Figure 6.17(a). Similar to the (0, 1) mode of the solid cylinder, this mode has no axial variation; the radial variation is greater, however, because this is a higher order mode. The average error between the displacement found with ANSYS and the normalized analytical solution is less than 1%. The divergence of the displacement, shown in Figure 6.17(b) exhibits the same axial symmetry.

The FDTD simulation frequency is $f_e = 2.5$ GHz; the radius of the concrete cylinder is $1.5\lambda_e$. The concrete is modeled using $\epsilon_r = 7.0$ with conductivity $\sigma = 0.06$.

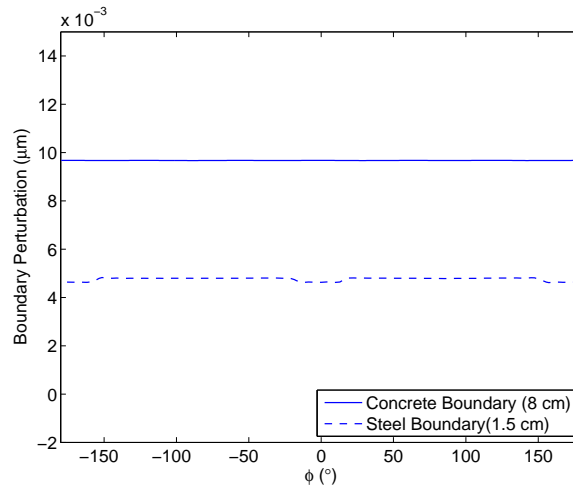


Figure 6.16: The boundary perturbation, u_r , corresponding to the third order $n = 0$ mode at $f_a = 74.13$ kHz.

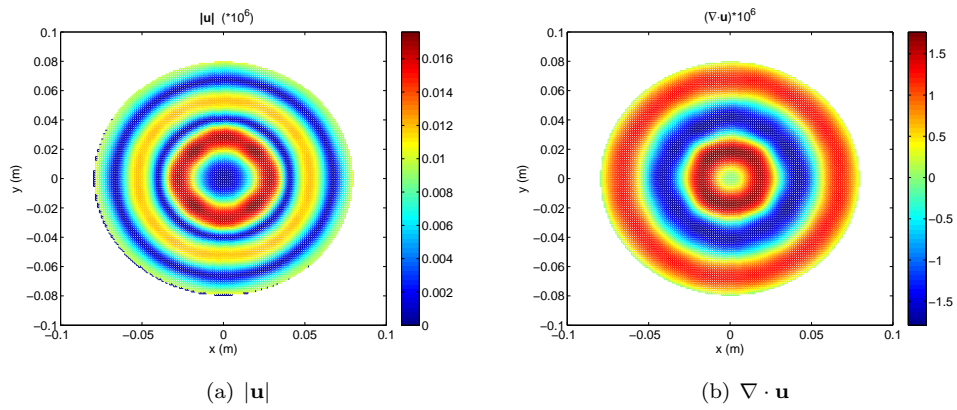


Figure 6.17: The magnitude and divergence of the displacement within the layered cylinder for the $(0, 3)$ mode at $f_a = 74.13$ kHz.

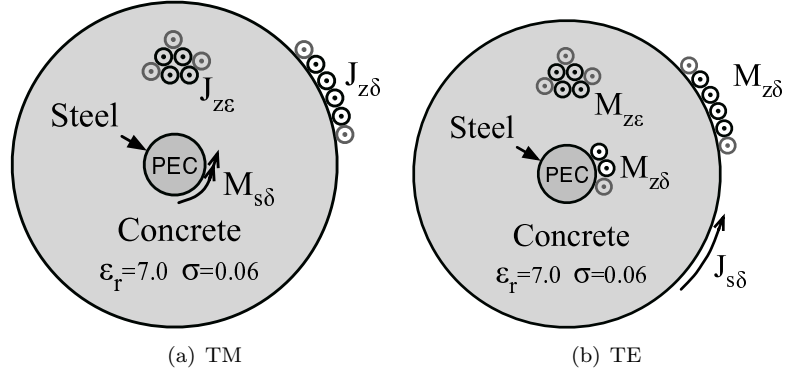


Figure 6.18: Boundary and volumetric current locations for the layered cylinder.

The steel is modeled as a PEC. The cell size, Δ , is $\lambda_e/100$, and the time step, Δt , is $0.98\Delta/(\sqrt{2}c)$. The UPML is 10 cells thick and there are 5 cells between the boundary of the cylinder and the total-field/scattered-field boundary. An \hat{x} -directed plane wave is launched from the left TF/SF boundary. The total grid size is 174 cells square and the simulation is run for 5000 time steps.

The locations of the currents used to generate the Doppler component for TM and TE polarizations are shown in Figure 6.18. On the PEC cylinder magnetic currents are present for both polarizations. The resulting Doppler components for TM and TE polarizations are shown in Figures 6.19 and 6.20, respectively. The TM Doppler component has comparable contributions from both sources. The TE Doppler component is much higher than TM because it has a much higher contribution from density modulation.

6.2.4 (2, 7) Mode

The second mode considered is the (2, 7) mode. This mode exhibits similar displacement characteristics as the (2, 1) mode of an isolated 1.5cm steel cylinder in a homogeneous concrete background. The analytical resonant frequency is at 73456 kHz; the ANSYS simulation produced the resonance at 73459 kHz. The radial boundary

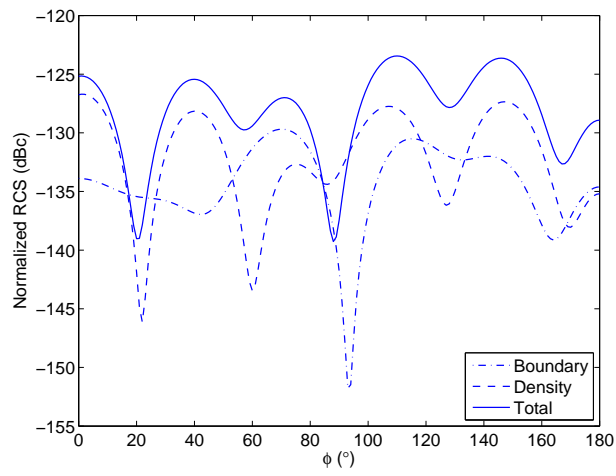


Figure 6.19: Normalized TM Doppler component scattered from the layered cylinder for the $(0, 3)$ mode.

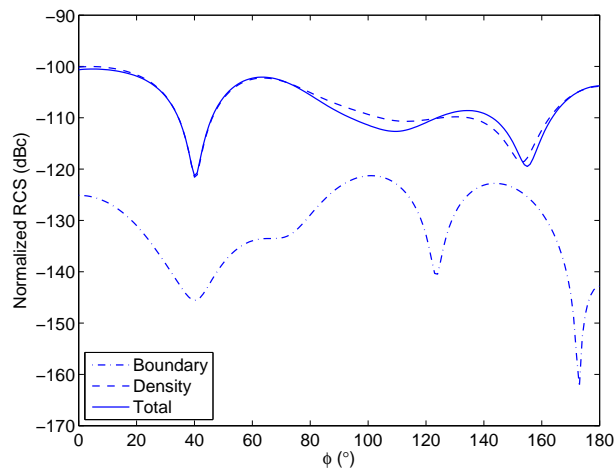


Figure 6.20: Normalized TE Doppler component scattered from the layered cylinder for the $(0, 3)$ mode.

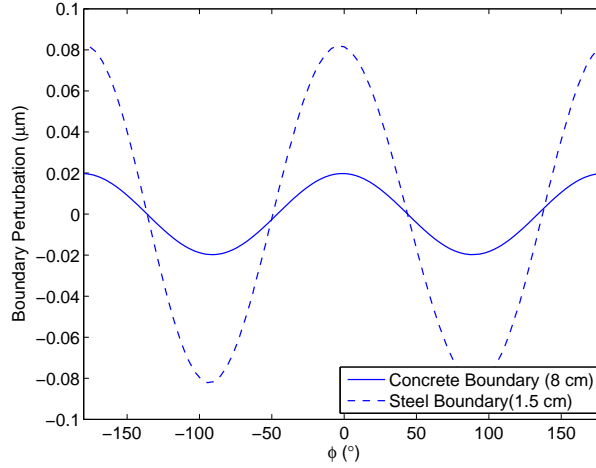


Figure 6.21: The boundary perturbation, u_r , corresponding to the seventh order $n = 2$ mode at $f_a = 73.4$ kHz.

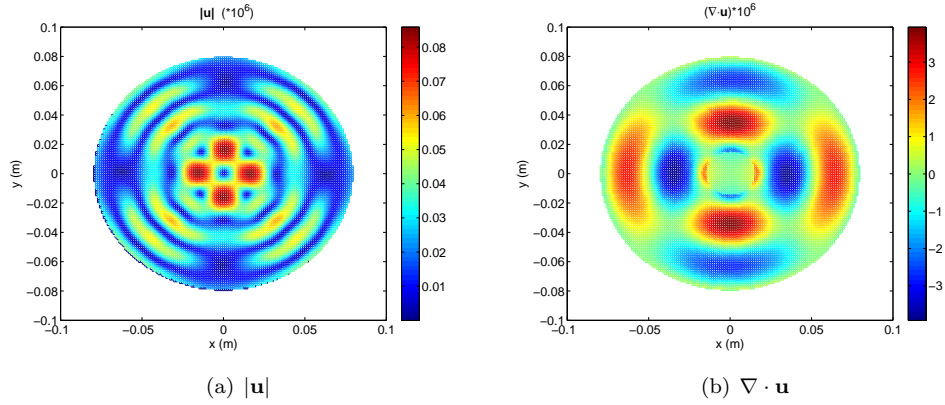


Figure 6.22: The magnitude and divergence of the displacement within the layered cylinder for the $(2, 7)$ mode at $f_a = 73.4$ kHz.

displacement at both cylinder boundaries is shown in Figure 6.21. The magnitude of the displacement within the cylinder is shown in Figure 6.22(a). The excitation of the inner cylinder is evident in both figures which show larger displacements near the steel cylinder boundary. The divergence of the interior displacement is also shown in Figure 6.22(b).

The FDTD simulation parameters are identical to those used with the $(0, 3)$ mode. The total Doppler component for both TM and TE polarizations is shown in Figure 6.23. Again, the TE Doppler component is much higher than the TM component.

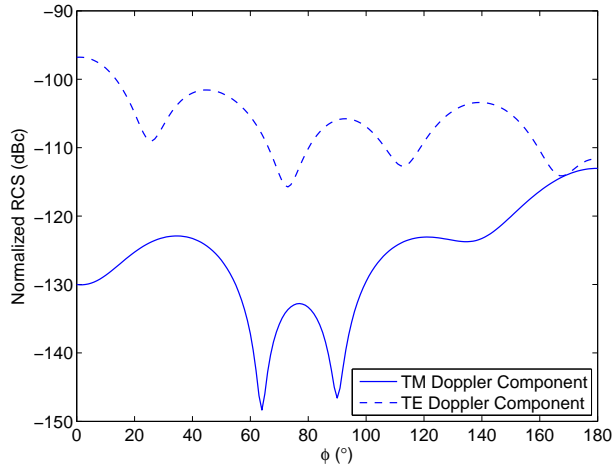


Figure 6.23: Normalized TM and TE Doppler component scattered from the layered cylinder at $f_a = 73.4$ kHz, the $(2, 7)$ mode. The electromagnetic frequency is 2.5 GHz.

6.2.5 $(8, 3)$ Mode

The final mode considered for the layered cylinder is the $(8, 3)$ mode. The analytical resonance frequency is at 73852.9 Hz; in the ANSYS simulation the resonance is at 73855.9. The displacement associated with this mode is primarily localized near the outer concrete cylinder boundary. Very little displacement occurs in the inner steel cylinder. The radial boundary perturbation at the concrete-air boundary is shown in Figure 6.24, where the $\cos(8\phi)$ variation is evident.

Again, the same FDTD simulation parameters are used as for the other modes. The total Doppler component for both TM and TE polarizations is shown in Figure 6.26.

6.3 Observations

In this section various observations and conclusions based on the Doppler component results in Sections 6.1 and 6.2 are stated. The purpose is to identify critical or sensitive target and mode parameters in the previous two cases. This is done in an effort to generalize those results and begin to elucidate relationships between the

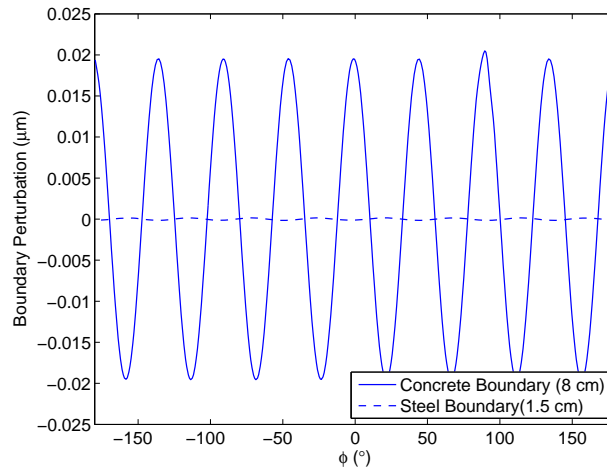


Figure 6.24: The boundary perturbation, u_r , corresponding to the third order $n = 8$ mode at $f_a = 73.8$ kHz.

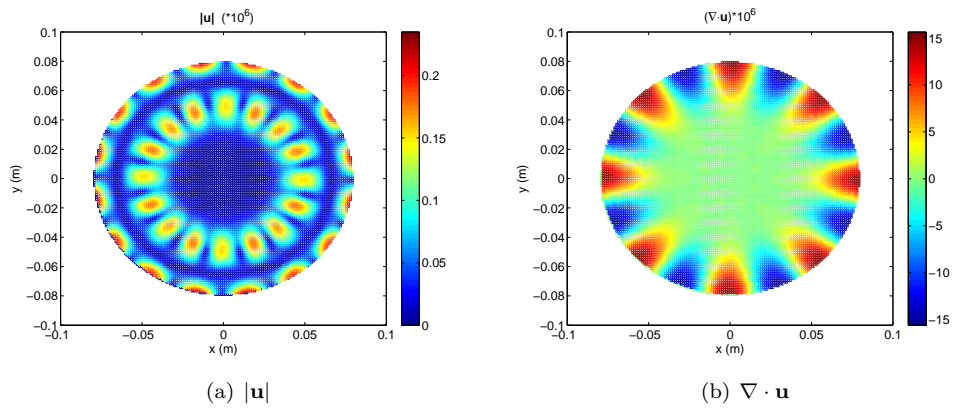


Figure 6.25: The magnitude and divergence of the displacement within the layered cylinder for the $(8, 3)$ mode at $f_a = 73.8$ kHz.

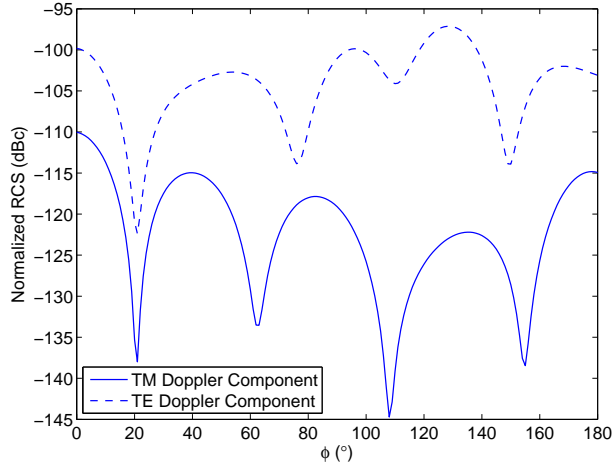


Figure 6.26: Normalized TM and TE Doppler component scattered from the layered cylinder at $f_a = 73855.9$ kHz, the (8, 3) mode. The electromagnetic frequency is 2.5 GHz.

target, the mode, and the resulting Doppler component. System level details, such as those describing the acoustic and electromagnetic sources, are discussed in Chapter IX.

It is noted that, at this point, it is more instructive to begin by considering the simplest case of a homogeneous cylinder. The physical interaction of the acoustic and electromagnetic waves within the layered target is more complex. As a result, it is more difficult to extract conclusions from the Doppler component for this geometry. Many of the following observations, however, still hold regardless of the target geometry.

The boundary perturbation Doppler component for cylindrical geometries often exhibits predictable bistatic variation as a result of the regular radial displacement, which, as seen in equation (6.7), exhibits cosinusoidal variation with axial angle, ϕ . The $(2, l)$ modes display the null at $\phi = 90^\circ$, for example, while the $(1, l)$ modes have a null at 0° , the $(3, l)$ modes have nulls at 60° and 120° , and the $(4, l)$ modes have nulls at 45° and 135° . Qualitatively, the nulls may be explained by considering the additional phase the electromagnetic signal acquires as it propagates through the

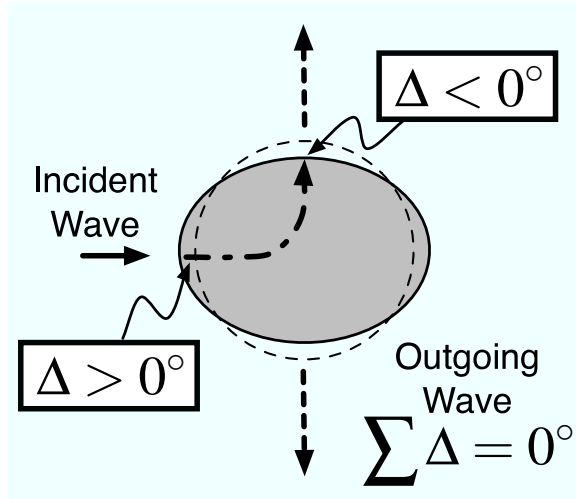


Figure 6.27: A qualitative explanation for the nulls in the bistatic Doppler components of the $(2, l)$ family of modes. Δ represents the phase relative to the electromagnetic signal that interacts with the unperturbed, circular cylinder.

cylinder. For example, for the $(2, 1)$ mode the electromagnetic signal accumulates additional phase as it enters the cylinder because the boundary is moved outward, forcing the wave to propagate slightly further within the cylinder. The portion of the field scattered towards $\phi = 90^\circ$, however, upon exiting encounters a boundary that is closer than the unperturbed, circular boundary would have been; this results in a net loss of phase equal to that which was gained upon entering. Since the Doppler component is a measure of the phase modulation on the incident electromagnetic signal it produces a null in that direction, reflecting the zero net phase change on the incident wave as a result of the perturbed boundary. This is depicted for the $(2, l)$ and $(1, l)$ families of modes in Figures 6.27 and 6.28, respectively. In these figures, Δ represents the phase relative to the electromagnetic signal that interacts with the unperturbed, circular cylinder.

The relative magnitude of the two Doppler component contributions depends on many factors. In the homogeneous polyethylene cylinder case, it is observed that the boundary perturbation is the primary source of the total Doppler component for the

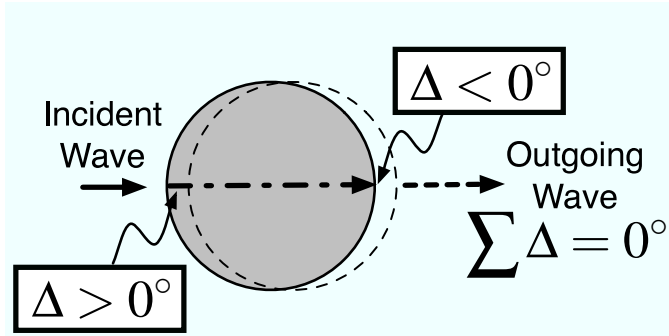


Figure 6.28: A qualitative explanation for the nulls in the bistatic Doppler components of the $(1, l)$ family of modes. Δ represents the phase relative to the electromagnetic signal that interacts with the unperturbed, circular cylinder.

$(2, 1)$ mode. In cases where this contribution dominates the total Doppler component, the bistatic variation can be used to infer which mode is under observation.

For higher order modes including those of the layered cylinder it is observed that the density modulation contribution dominates the response. In general, increasing the order of a given mode will increase the contribution from the density modulation Doppler component. This is expected since the radial variation interior to the target increases with mode order and produces larger strains within the target. This is observed in Section 6.1.4, where the divergence of the displacements for the $(2, 1)$ and $(2, 2)$ modes are compared and that of the higher order $(2, 2)$ mode is noted to be 22 times larger. In addition, the boundary contribution generally decreases with mode order; this can be seen in Figure 6.3, where u_ρ for the $(2, 1)$ mode is approximately two times larger than u_ρ for the $(2, 2)$ mode. This suggests using higher order modes in cases where additional sensitivity to the target interior is desired. Polarization could also be used to enhance sensitivity to the target interior. TE polarization is generally more sensitive to strain within the cylinder because of the gradient operation in the density modulation Doppler component seen in equation 3.14.

The target material is important as well. For the same acoustic and electro-

magnetic source parameters and the same mode of resonance, certain materials will experience larger displacements and strain than other materials, producing a correspondingly larger Doppler component. As an example, the maximum boundary perturbation for the $(2, 1)$ of two different material circular cylinders is compared. The first cylinder is polyethylene, which for an incident 1 Pa amplitude acoustic plane wave, has $u_{\rho, max} = 0.168\mu m$; the scattered Doppler component is about -100 dBc, or 100 dB below the unshifted cylinder RCS. A concrete cylinder, however, will have radial displacement that is almost a factor of ten smaller and, as a result, the Doppler is only -120 dBc.

The surrounding fluid medium can be important. All of the results shown are from acoustic scattering in air. If the target were in another fluid the results would be different. If the fluid remains a gas, though, the interaction between the elastic solid and the fluid will be weak, comparable to that obtained with air [77]. Liquid fluids would have more complex interaction with the target but this case is of limited concern since electromagnetic scattering from the target is considered.

CHAPTER VII

Wideband, Bistatic Doppler Component for Applications in NDE

7.1 Introduction

In Chapter VI the Doppler components for various modes of two cylindrical targets are presented. This chapter shows how the Doppler component could be useful in non-destructive evaluation (NDE). The effects of introducing a flaw or crack in the target on both the scattered acoustic pressure and the scattered electromagnetic fields are considered. It is intended to demonstrate the sensitivity of the Doppler component to small cracks or voids in the target.

Modeling cracks in the ANSYS and FDTD models is first discussed. In the following section wideband, bistatic Doppler components are presented for the two geometries in Chapter VI. The effects of both crack orientation and location on the Doppler component for different modes is investigated. In the remainder of the Chapter, focusing to achieve higher sensitivity within the target is discussed; results for this analysis are also presented.

7.1.1 Modeling Cracks in ANSYS and FDTD

Cracks in the ANSYS model are introduced by removing solid elastic elements and replacing them with fluid (air) elements. The fluid elements within the crack

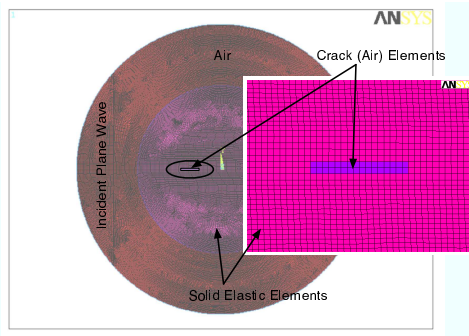


Figure 7.1: The ANSYS model used to simulate a void within the target.

are permitted to move in the transverse plane like fluid elements immediately surrounding the cylinder. These elements account for fluid-structure interactions that take place. A picture of the ANSYS model of the solid polyethylene cylinder with the crack is shown in Figure 7.1.

The modeling approach described above produces a void or hole rather than a hairline crack. The nodes of neighboring elements could be altered to yield such a crack. However, in that case the question of what material fills the crack in the acoustic scattering simulation is left unanswered. The element removal approach described above is used to obtain the results in this Chapter; it is deemed more accurate in terms of producing physical results.

The FDTD model is also modified to include the crack. The crack dimensions from ANSYS are translated into FDTD field locations, as shown in Figure 7.2. The missing FDTD points correspond to the void or crack. In the unperturbed FDTD simulation, the crack is modeled by reducing the relative permittivity to that of free space within the crack. Volumetric currents, which produce the dielectric modulation Doppler component, are also removed at the points interior to the crack. The boundary perturbation Doppler component is modified to include additional currents surrounding the crack. Only displacements perpendicular to the crack boundary, in

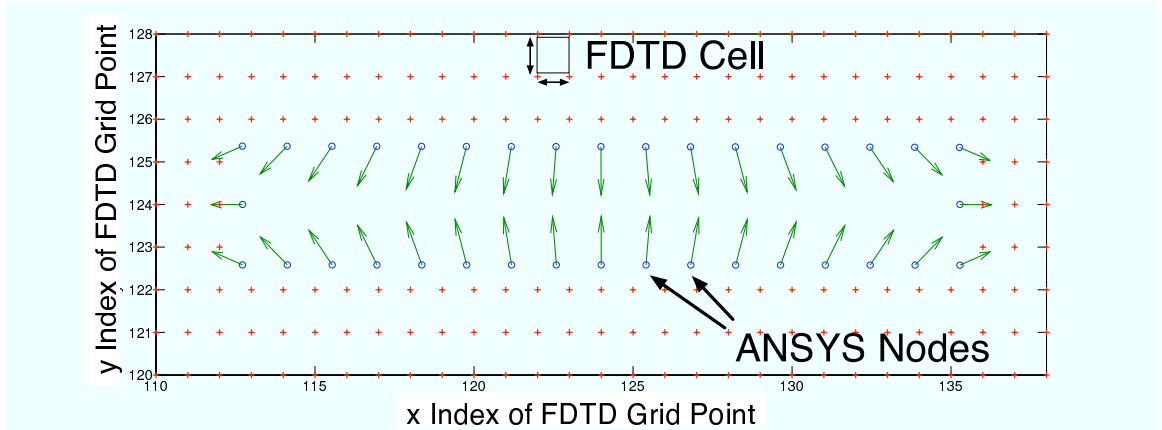


Figure 7.2: The ANSYS nodes on the boundary of the crack overlaid on the \hat{z} FDTD grid points. The FDTD points that are missing correspond to the void that models the crack.

the direction of the surface normal, are included. For example, if the crack is oriented along the \hat{x} direction, as it is in Figure 7.2, only u_y is used in the sheet currents. It is noted that the presence of the crack affects the displacement throughout the cylinder cross-section; as will be shown, the degree of the effects of the crack depend on both the mode and the crack orientation and size. The modifications to the Doppler component currents, i.e. removing the volumetric current sources within the crack and adding sheet currents around the crack, do not affect the resulting Doppler components appreciably. These modifications are secondary contributions to the overall effect the crack has on the total Doppler component; those changes caused by the altered boundary perturbation and displacement are much larger.

The algorithm used to interpolate the ANSYS data to the FDTD grid points is also different when a crack is present. Using the original algorithm, the large strain values concentrated around the crack edges create ripples in the interpolated function away from the vicinity of the crack. This is an expected consequence of the spline-based approach in the CSA grid algorithm. A slower, nearest neighbor interpolation is used if a crack is present, resulting in much more accurate interpolation.

	Δx	Δy	x_o	y_o
Crack 1	2.4cm	2.8mm	0cm	0cm
Crack 2	2.8mm	2.0cm	0cm	0cm
Crack 3	2.3cm	2.8mm	-3.7cm	0cm

Table 7.1: Crack dimensions and locations for the solid polyethylene cylinder.

7.2 Bistatic Doppler Component Results

In this section the sensitivity of the bistatic Doppler component to flaws or cracks within the target is investigated. The effect of various cracks on the Doppler component for the cylindrical targets in Chapter VI are considered. Crack orientation and location are varied between cases.

In Chapter VI the bistatic Doppler component was presented at a single electromagnetic frequency. One of the advantages of using the finite-difference time-domain method, however, is the ability to recover wideband scattering information. The results in this Chapter are plotted against both bistatic angle on the abscissa and electromagnetic frequency on the ordinate. The results from Chapter VI correspond to a single horizontal line in the expanded plots.

7.2.1 Cracked Polyethylene Cylinder

The polyethylene cylinder from Chapter VI is modified to include a small crack. Three different crack orientations are considered. Table 7.1 lists the crack dimensions $(\Delta x, \Delta y)$ and center locations (x_o, y_o) . Figure 7.3 illustrates the crack locations within the cylinder. Cracks 1 and 3 are oriented along the \hat{x} axis while crack 2 is along the \hat{y} direction.

In the remainder of this section the effect of the crack on the ANSYS results is briefly discussed and then both acoustic and electromagnetic scattering from the cracked cylinder are considered. The sensitivity of both wave types is compared.

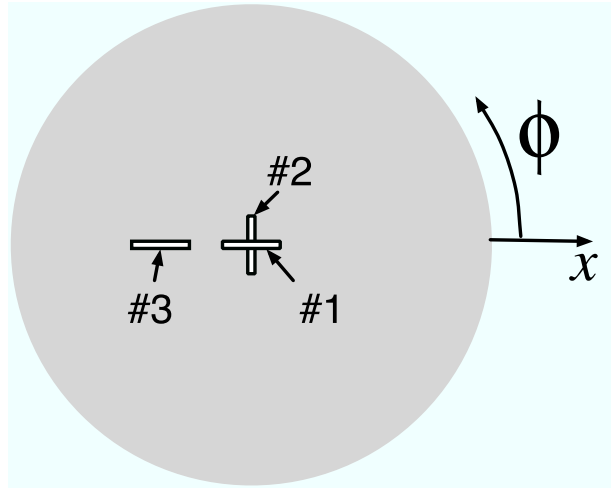


Figure 7.3: Illustration of the three cracks within the polyethylene cylinder. Each crack is analyzed individually.

ANSYS Results for Cracked Cylinder

The resonant frequencies found for the cracked and uncracked models at the first and second order $n = 2$ modes considered in Section 6.1 are shown in Table 7.2. In all cases, the acoustic resonant frequency shifts. The frequency should decrease as a result of the presence of a void or crack. The resonance frequency for the (2,2) in the case of crack #3 is seen to slightly increase, however. This discrepancy is most likely a result of imperfections in the ANSYS model. It is also noted that, in the case of crack #2, the (2,2) mode splits into two modes separated by less than $1Hz$; this is probably due to the slight asymmetry in the crack geometry caused by nonsquare ANSYS elements. The displacement associated with the resonance chosen for analysis is slightly larger and rotated with respect to the cylinder axis from the unselected resonance.

As expected, the presence of the crack perturbs the displacement and strain distributions within and on the boundary of the cylinder. The radial displacement, u_ρ , on the boundary of the cylinder is shown for the (2,1) mode in Figure 7.4. The same information is plotted in Figure 7.5 for the (2,2) mode. It is observed that the offset

	$f_a, (2,1)$	$f_a, (2,2)$
Without crack	1844.2	3634.1
Crack 1	1806	3572.5
Crack 2	1813.7	3587.3
Crack 3	1820.1	3634.8

Table 7.2: Mode resonant frequencies for the (2, 1) and (2, 2) modes of a solid, polyethylene cylinder. Three different cracks are considered.

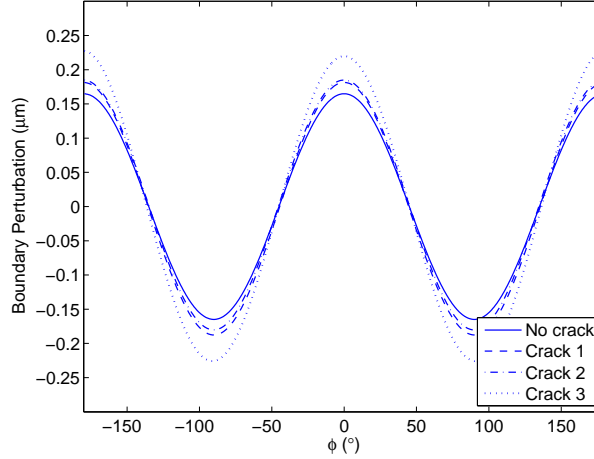


Figure 7.4: Radial displacement, u_ρ , on the boundary of the polyethylene cylinder for the (2, 1) mode of the four crack cases.

crack has a larger effect on the radial displacement for the (2, 1) mode while the centered cracks have a larger effect on the (2, 2) mode. This is counterintuitive since both the strain and the displacement are minimum at the cylinder center. However, the crack, as will be seen, induces very large strains and displacement in its immediate vicinity. Relative to the uncracked cylinder, this introduces a larger change in regions of minimum initial displacement and strain.

The displacement and divergence of the displacement for the Case #1 cracked cylinder at the (2, 1) mode are shown in Figures 7.6(a) and 7.6(b), respectively. It is seen that these quantities immediately surrounding the crack are many orders of magnitude larger than in the remaining cross-sectional area. The ANSYS results for the other modes are not shown, however, they exhibit the same trend.

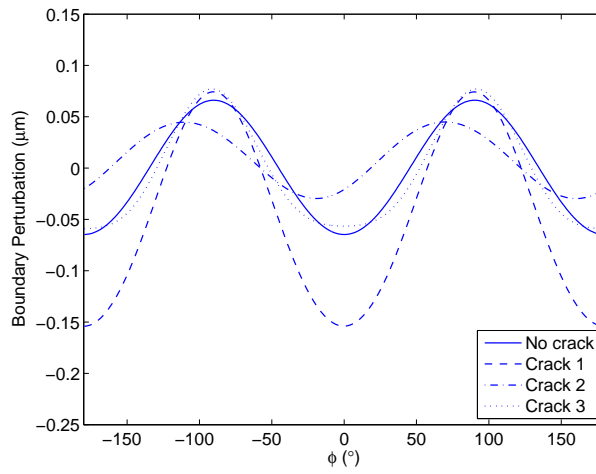


Figure 7.5: Radial displacement, u_ρ , on the boundary of the polyethylene cylinder for the (2, 2) mode of the four crack cases.

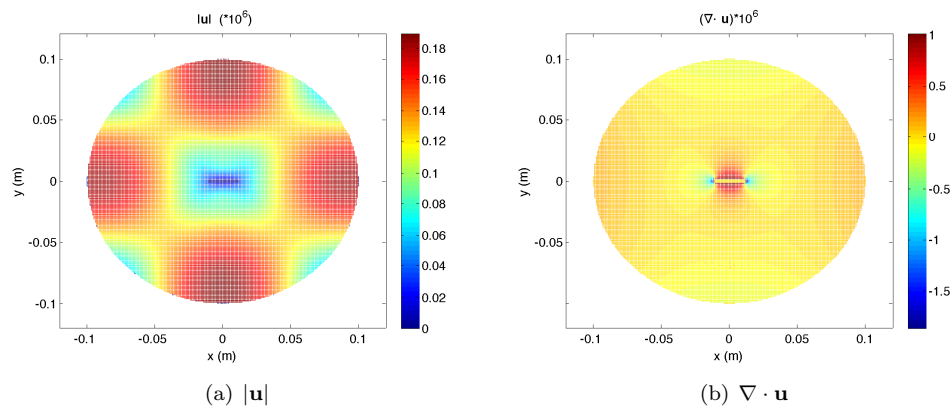


Figure 7.6: The magnitude and divergence of the displacement inside the cracked cylinder for the (2, 1) mode. The same quantities for the uncracked cylinder are shown in Figures 6.4(a) and 6.4(b), respectively.

Acoustic Scattering

Away from acoustic resonance, the target is nearly impenetrable to incident acoustic energy. At resonances of the target, however, the acoustic wave is able to penetrate into the interior. One of the advantages of an acousto-EM system over an all-acoustic system listed in Chapter I is that electromagnetic waves can penetrate more easily into the target interior and, as a result, are more sensitive to target composition. This is true in general away from resonance. At resonance, however, where the acousto-EM approach is based, this advantage is minimized. To what extent the advantage holds will be explored in this section where the sensitivity of the scattered acoustic pressure to changes in the cylinder interior will be contrasted with the sensitivity of the Doppler component.

The total pressure scattered at resonance in each case is obtained from ANSYS simulation; the incident pressure is then simulated in the absence of the cylinder. Their difference, the scattered pressure, is plotted versus bistatic angle at a distance of $R_o = 0.16m$ away from the cylinder boundary for the four cylinder models (the original, uncracked cylinder and the three cracked cylinders) at the two resonances previously considered. The $(2, 1)$ mode is shown in Figure 7.7; the observation distance in terms of the wavelength in air at resonance is approximately $R_o = 0.85\lambda_a - 0.87\lambda_a$. The scattered pressure for the $(2, 2)$ modes is shown in Figure 7.8; the corresponding observation distances in terms of acoustic wavelength are $R_o = 1.69\lambda_a - 1.72\lambda_a$.

The scattered pressure at the $(2, 1)$ mode is much less affected by the presence of the cracks than the $(2, 2)$ mode. This is because the crack is approximately two times larger in terms of the shear and longitudinal wavelengths at the second order mode, which increases its effect on the propagating elastic waves. As seen in Figure 7.5,

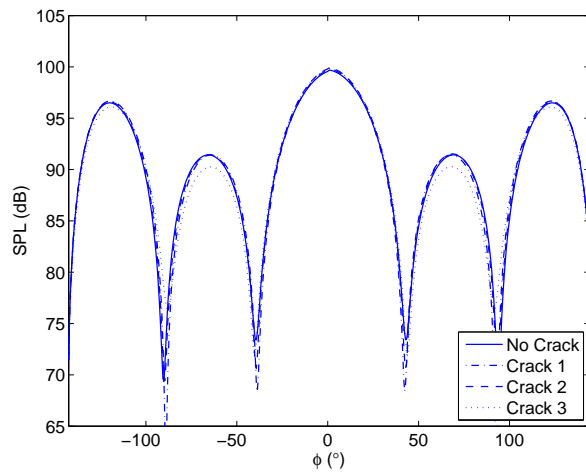


Figure 7.7: Scattered acoustic pressure at the $(2, 1)$ resonance for the original, uncracked polyethylene cylinder and the three cracked polyethylene cylinder models. The observation distance is $R_o = 0.16m \approx 0.86\lambda_a$

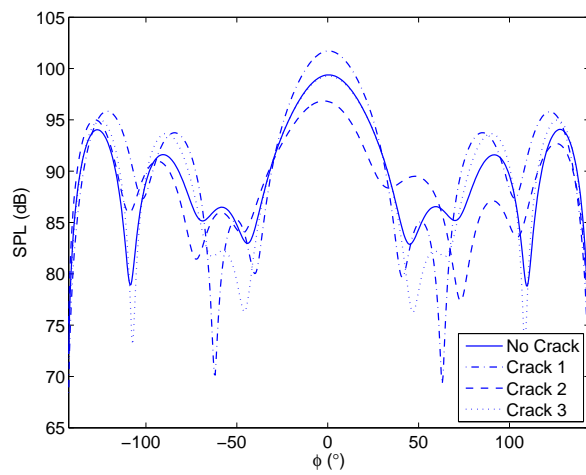


Figure 7.8: Scattered acoustic pressure at the $(2, 2)$ resonance for the original, uncracked polyethylene cylinder and the three cracked polyethylene cylinder models. The observation distance is $R_o = 0.16m \approx 1.7\lambda_a$

this results in a larger change to the radial displacement on the cylinder boundary mode and a larger change in the scattered pressure at the (2,2). Also, as noted above, the (2,2) mode split in the case of crack #2; the scattered pressure for the other mode exhibited the same assymetry in the scattered pressure except flipped over the y -axis.

Electromagnetic Scattering and the Doppler Component

In order to demonstrate the level of sensitivity that can be expected using conventional RCS measurement to detect flaws, the RCS of the stationary cylinder with and without the crack is first considered. The unshifted RCS of the cylinder does exhibit slight sensitivity to the presence of the crack. However, this occurs only at frequencies above about 2 GHz, where the crack dimensions are larger with respect to the electromagnetic wavelength. As a best-case scenario, in terms of sensitivity over the electromagnetic frequency range considered herein, the TM and TE polarized RCS are shown at $f_e = 5$ GHz in Figures 7.9 and 7.10. At this frequency the wavelength inside the polyethylene cylinder is about $\lambda_e = 0.04m$; the crack is between $0.7\lambda_e$ and λ_e . Both polarizations demonstrate more sensitivity at angles near $\phi = 180^\circ$, corresponding to backscatter, and virtually no sensitivity in the forward scattering direction. From these plots it is difficult to determine which polarization is more sensitive to each crack orientation.

The total Doppler component for the four cases are plotted over the electromagnetic frequency range 0.5 – 5 GHz and as a function of bistatic angle. All Doppler component plots for the cracked cylinder are shown on the same colormap scale as the uncracked cylinder of the corresponding polarization. Figures 7.11(a) and 7.11(b) are the TM and TE Doppler components, respectively, scattered from a solid, uncracked polyethylene cylinder at the (2,1) mode of resonance. The previous result

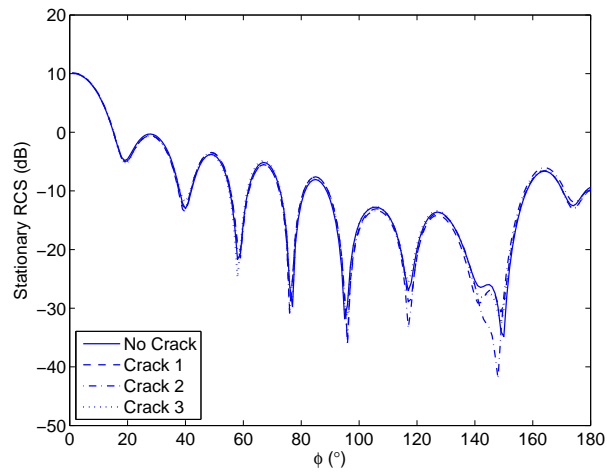


Figure 7.9: The unshifted TM polarized RCS of the polyethylene cylinder for the four cracked cases at $f_e = 5$ GHz.

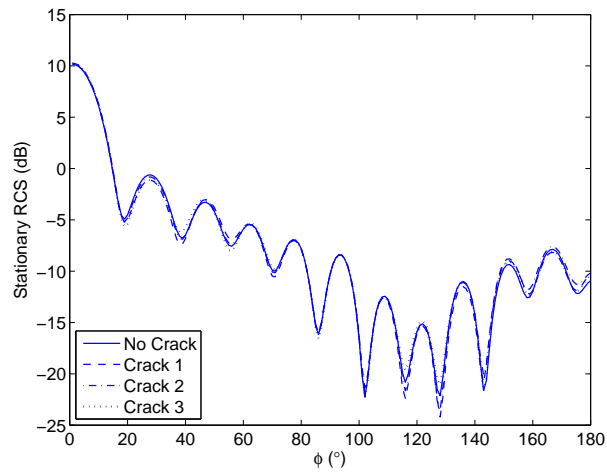


Figure 7.10: The unshifted TE polarized RCS of the polyethylene cylinder for the four cracked cases at $f_e = 5$ GHz.

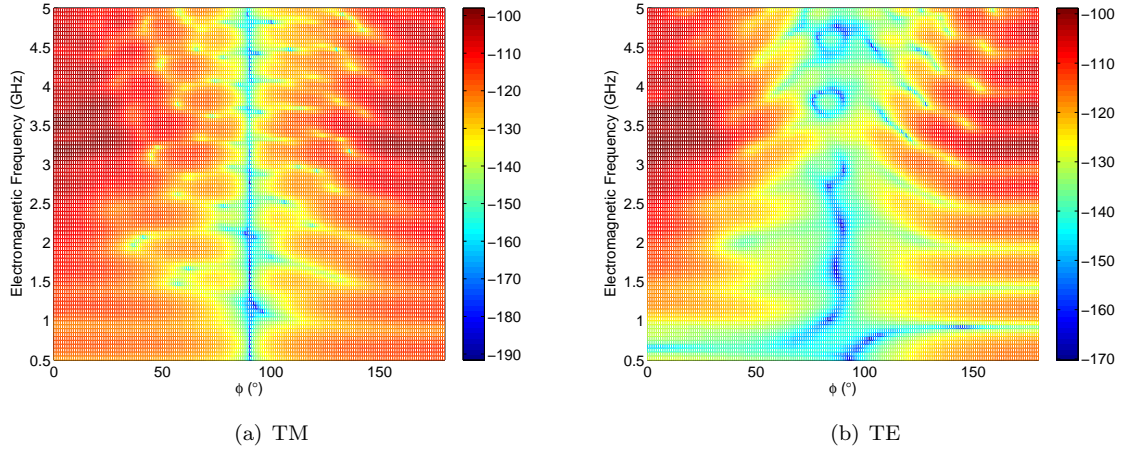


Figure 7.11: The Doppler component for the $(2, 1)$ mode of the solid, uncracked polyethylene cylinder. The Doppler component is normalized to the unshifted RCS at $\phi = 0^\circ$.

shown in Section 6.1.3 corresponds to the line at 3 GHz. The characteristic null at $\phi = 90^\circ$ is evident in the case of TM polarization over the entire frequency range; for TE it is less evident at some frequencies because of the larger contribution from the dielectric modulation Doppler component.

The Doppler component scattered from the solid cylinder with crack #1, which is centered at the origin and lies along the \hat{x} direction, is shown in Figure 7.12. In this case, the null at $\phi = 90^\circ$ is filled in because the larger strain surrounding the crack increases the contribution from the dielectric modulation Doppler component. For TE the effect of the crack is less evident in the Doppler component, especially at lower frequencies. The Doppler component scattered from the solid cylinder with crack #2, which is centered at the origin and lies along the \hat{y} direction, is shown in Figure 7.13. The effect of the \hat{y} -oriented crack on the Doppler component is approximately the same as the the previous \hat{x} -oriented crack. The null is filled in for both cases. The Doppler component scattered from the solid cylinder with crack #3, which is offset in \hat{x} from the origin and lies along the \hat{x} direction, is shown in Figure

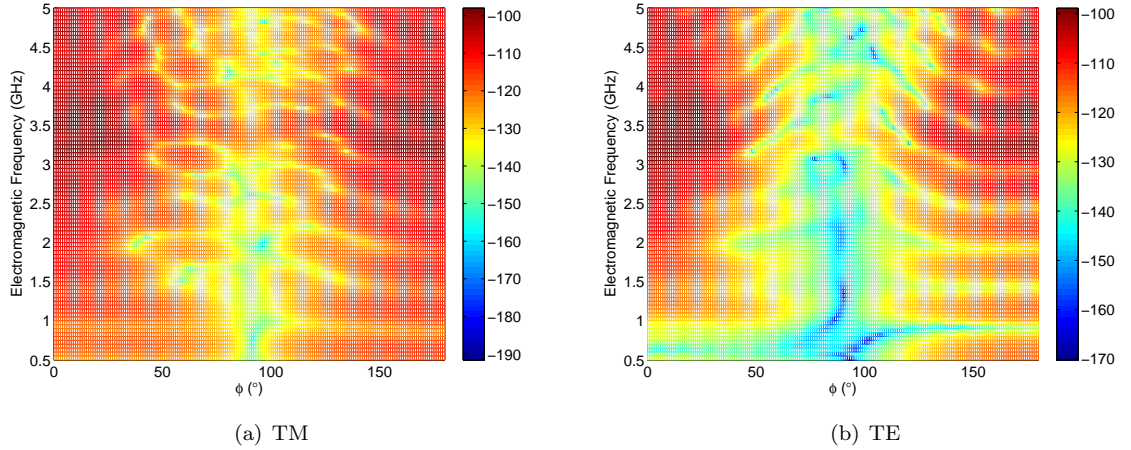


Figure 7.12: The Doppler component for the (2,1) mode of the solid polyethylene cylinder with crack #1. The Doppler component is normalized to the unshifted RCS at $\phi = 0^\circ$.

7.14. Again, the effects of the offset crack on the Doppler component are similar to the \hat{x} and \hat{y} cracks.

Figures 7.15(a) and 7.15(b) are the TM and TE Doppler components, respectively, scattered from a solid, uncracked polyethylene cylinder at the (2,2) mode of resonance. As with the (2,1) mode, the null at $\phi = 90^\circ$ is evident for TM polarization and less so for TE polarization.

The Doppler component scattered from the solid cylinder with crack #1 is shown in Figure 7.16. Crack #1 has a larger effect on both the TM and TE Doppler components for the (2,2) mode than the (2,1) mode. For TM polarization the null is entirely filled in; rather than one contribution dominating the total Doppler component, both contributions are responsible for the effect of the crack in modifying the Doppler component. For TE polarization the crack induces less scattering of the Doppler-shifted fields between $\phi = 30^\circ$ and $\phi = 50^\circ$.

The Doppler component scattered from the solid cylinder with crack #2 is shown in Figure 7.17. For TM polarization the effect of the \hat{y} -oriented crack #2 are similar

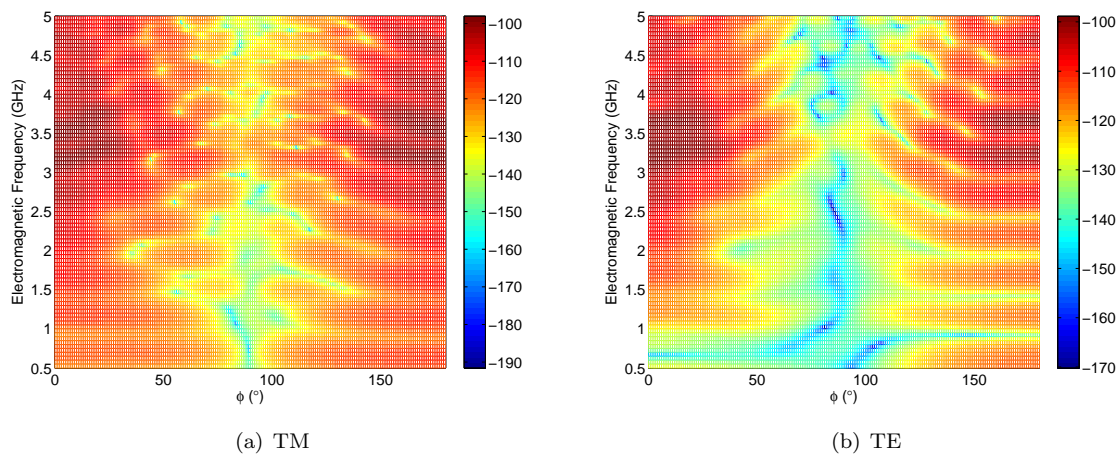


Figure 7.13: The Doppler component for the $(2,1)$ mode of the solid polyethylene cylinder with crack #2. The Doppler component is normalized to the unshifted RCS at $\phi = 0^\circ$.

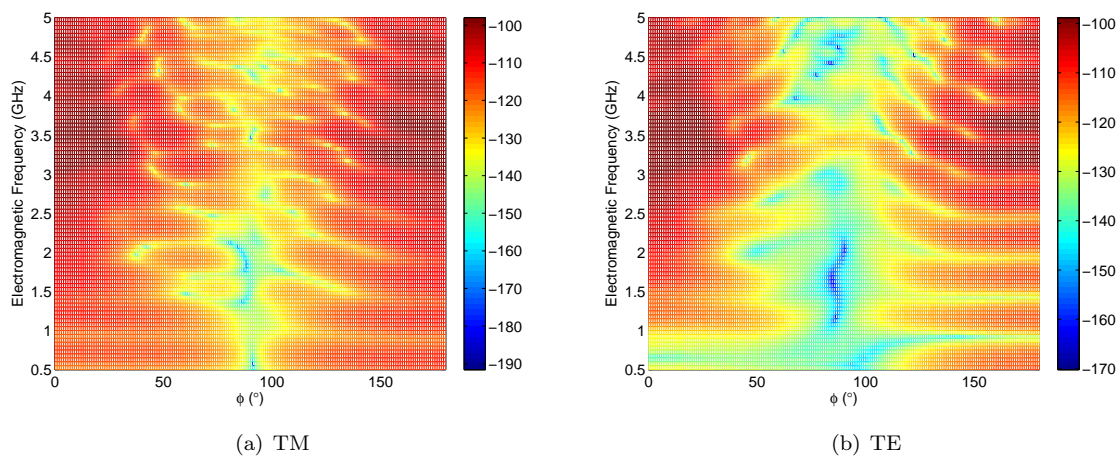


Figure 7.14: The Doppler component for the $(2,1)$ mode of the solid polyethylene cylinder with crack #3. The Doppler component is normalized to the unshifted RCS at $\phi = 0^\circ$.

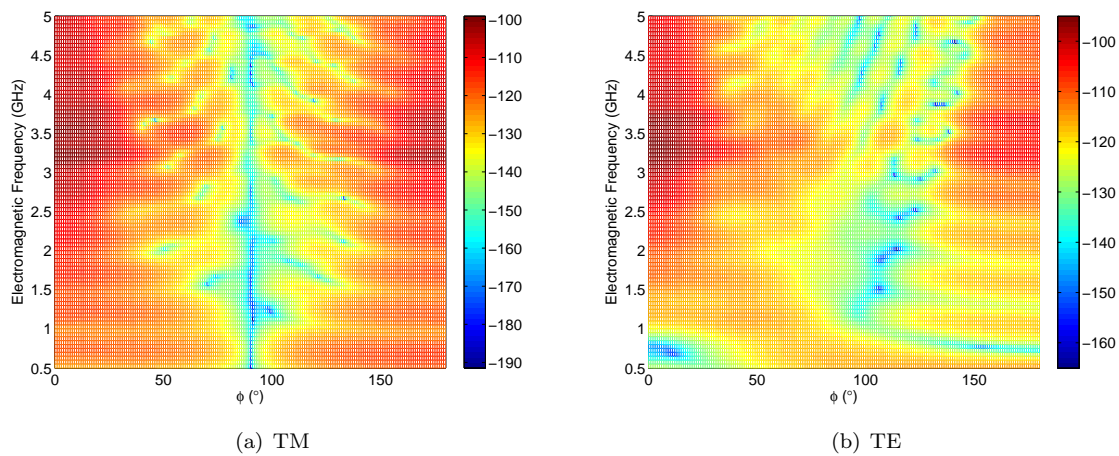


Figure 7.15: The Doppler component for the (2,2) mode of the solid, uncracked polyethylene cylinder. The Doppler component is normalized to the unshifted RCS at $\phi = 0^\circ$.

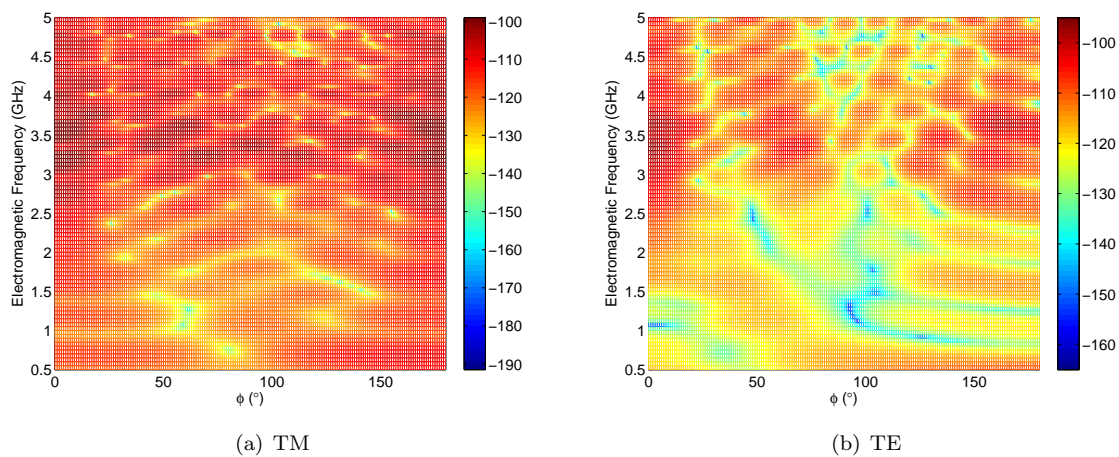


Figure 7.16: The Doppler component for the (2,2) mode of the solid polyethylene cylinder with crack #1. The Doppler component is normalized to the unshifted RCS at $\phi = 0^\circ$.

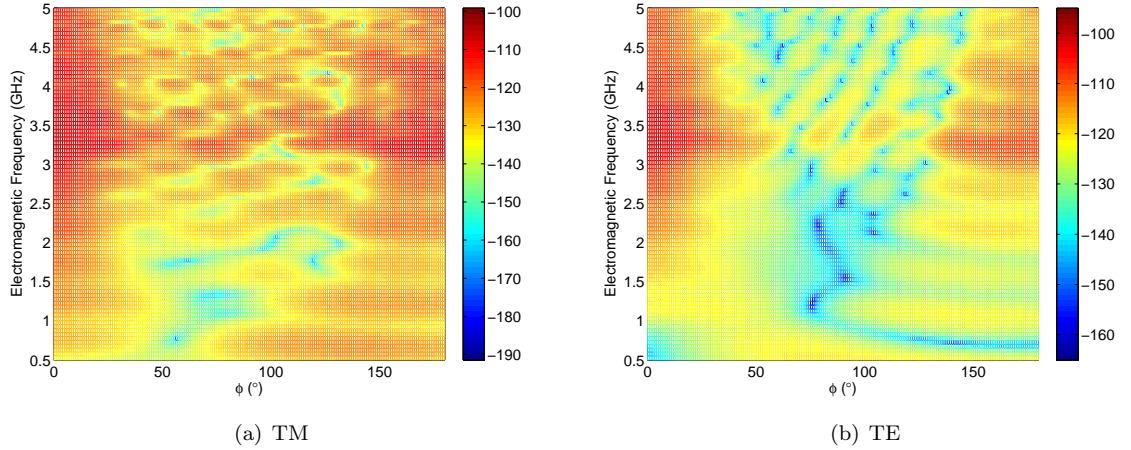


Figure 7.17: The Doppler component for the (2, 2) mode of the solid polyethylene cylinder with crack #2. The Doppler component is normalized to the unshifted RCS at $\phi = 0^\circ$.

in nature but less pronounced than those of crack #1. For TE polarization, crack #2 has a similar effect in that the Doppler component is reduced at lower bistatic angles; it is also significantly lower at $\phi = 90^\circ$ at low electromagnetic frequency.

The Doppler component scattered from the solid cylinder with crack #3 is shown in Figure 7.18. The offset crack #3 affects the TM Doppler component in a similar manner as the other cracks considered above. For TE polarization crack #3 has a smaller effect on the Doppler component compared to the other crack cases. This is unexpected since the crack is located in a region of both larger displacement and strain. However, it is consistent with the scattered acoustic pressure at the (2, 2) mode which was also more affected by the crack than the other two modes.

7.2.2 Cracked Layered Cylinder

This section details the effect of a crack in the layered cylinder from Section 6.2. The crack is in the \hat{y} direction just above the inner steel cylinder, as shown in Figure 7.19. Its dimensions are $\Delta x \approx 0.8mm$ and $\Delta y \approx 6.5mm$.

The acoustic pressure scattered from the layered cylinder is not shown. The high

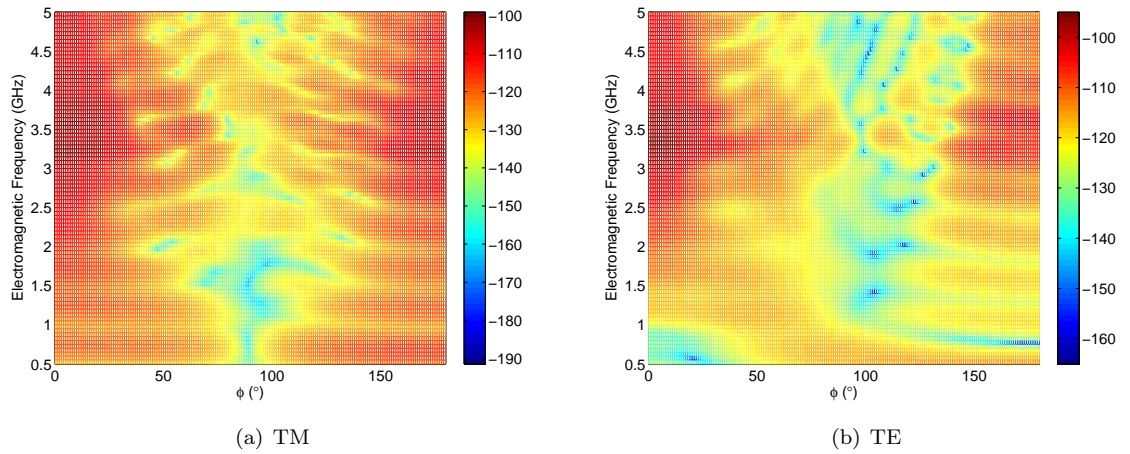


Figure 7.18: The Doppler component for the (2, 2) mode of the solid polyethylene cylinder with crack #3. The Doppler component is normalized to the unshifted RCS at $\phi = 0^\circ$.

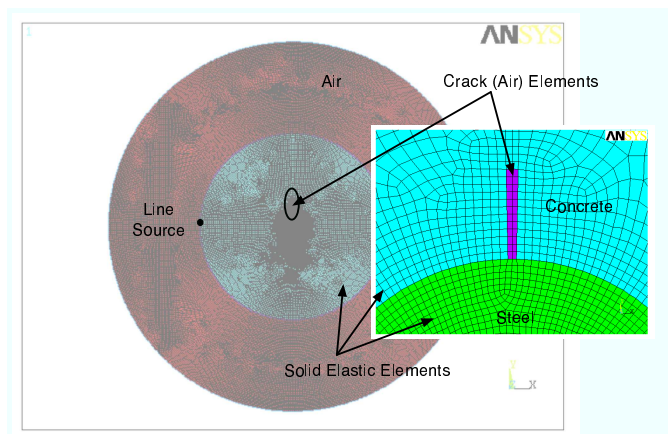


Figure 7.19: The ANSYS model of the cracked layered cylinder. The inset is zoomed in around the crack.

frequency of the modes considered makes sufficient sampling in the air difficult, as in the uncracked case, the sampling in air can be as coarse as about five points per wavelength. The remainder of this section will describe the effects of the crack on the ANSYS results and the electromagnetic scattering.

7.2.3 ANSYS Results for the Cracked Layered Cylinder

The resonant frequencies for the cracked and uncracked cylinder models at the three modes considered in Section 6.2 are shown in Table 7.3. In the first two cases,

	$f_a, (0,3)$	$f_a, (2,7)$	$f_a, (8,3)$
Without crack	74128.1	73459.1	73855.9
With Crack	74042.0	73441.3	73855.8

Table 7.3: Mode resonant frequencies for the three modes of the layered cylinder. One crack, shown in Figure 7.19, is considered.

the acoustic resonant frequency shifts because the crack is located near regions of large displacement and strain. For the (8, 3) mode, however, the shift is very small. The displacement for this mode is confined to the edge of the outer concrete cylinder, away from the inner steel cylinder where the crack is located. Since the crack leaves the (8, 3) mode largely unperturbed, the remaining ANSYS and electromagnetic scattering results for this mode are not given.

The boundary perturbation on the cylinder surfaces with and without the crack for the (0, 3) mode is shown in Figure 7.20. The same result for the (2, 7) mode is shown in Figure 7.21. The magnitude of the displacement for the (0, 3) mode with the crack is shown in Figure 7.22(a); the divergence of the displacement for the same mode is shown in Figure 7.22(b). These quantities are shown for the (2, 7) of the cracked cylinder in Figures 7.23(a) and 7.23(b), respectively. As observed in Figures 7.20-7.23(b), the presence of the crack has a large effect on the mode shape. In the next section the results of using the perturbed displacements in the acousto-EM model will be shown.

7.2.4 Electromagnetic Scattering and the Doppler Component

As in the previous case, the RCS of the stationary cylinder with and without the crack will first be examined to demonstrate the level of sensitivity to flaws using conventional means. The bistatic radar cross of the layered cylinder with and without the crack, calculated using the unshifted field values, is shown in Figure 7.24 for an electromagnetic frequency of $f_e = 5$ GHz. Again, this frequency, which is a best

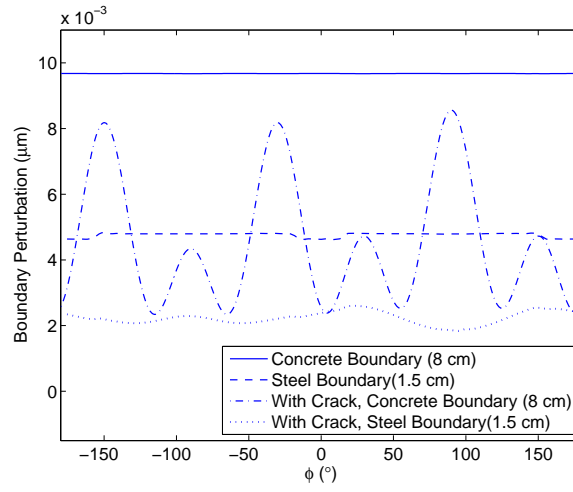


Figure 7.20: Radial displacement, u_ρ , on the concrete and steel cylinder boundaries of the layered cylinder for the (0,3) mode. Both cracked and uncracked results are shown.

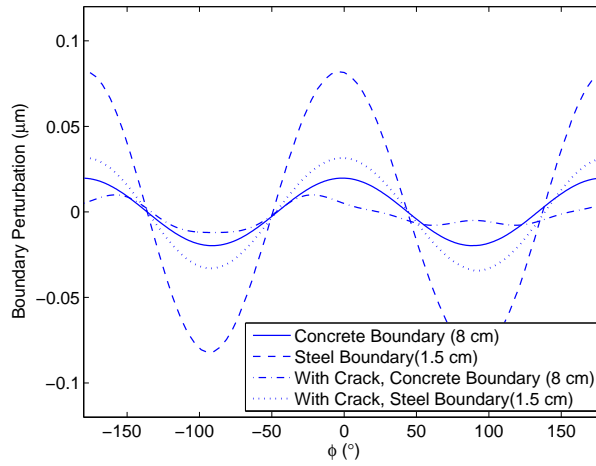


Figure 7.21: Radial displacement, u_ρ , on the concrete and steel cylinder boundaries of the layered cylinder for the (2,7) mode. Both cracked and uncracked results are shown.

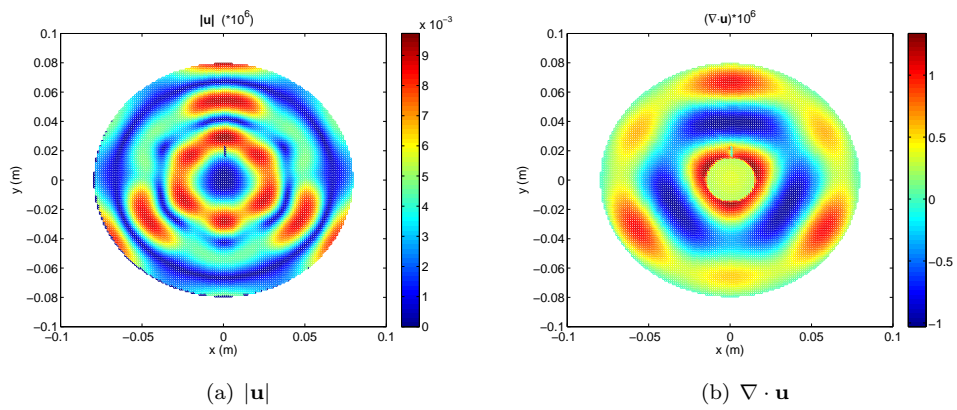


Figure 7.22: The magnitude and divergence of the displacement inside the cracked layered cylinder for the $(0,3)$ mode. The same quantities for the uncracked cylinder are shown in Figures 6.17(a) and 6.17(b), respectively.

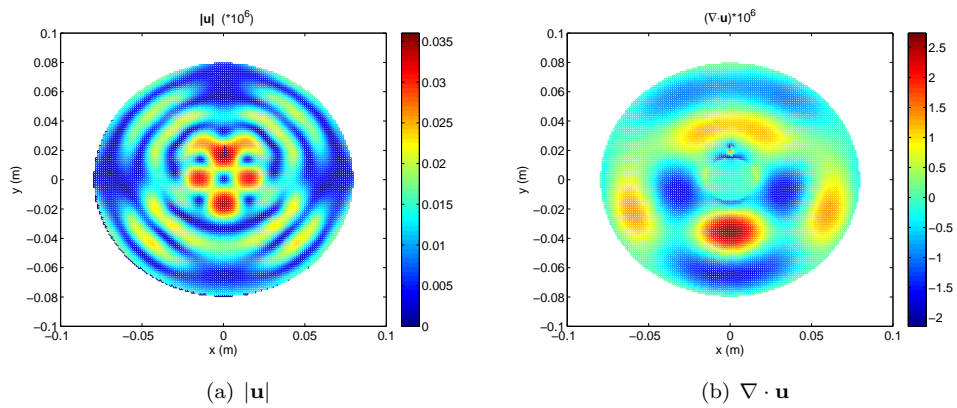


Figure 7.23: The magnitude and divergence of the displacement inside the cracked layered cylinder for the $(2,7)$ mode. The same quantities for the uncracked cylinder are shown in Figures 6.22(a) and 6.22(b), respectively.

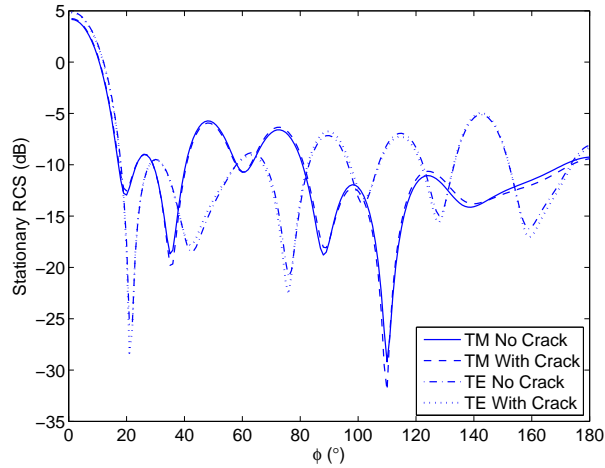


Figure 7.24: The stationary layered cylinder RCS for both TM and TE polarizations at $f_e = 5$ GHz.

case scenario in terms of sensitivity, is relatively high, considering loss and scattering inside of concrete. The maximum difference between the two cases is less than $1dB$.

The total Doppler component for the $(0, 3)$ mode without the crack is shown for TM and TE polarizations in Figure 7.25. The results for the total Doppler component with the crack are shown in Figure 7.26.

The total Doppler component for the $(2, 7)$ mode without the crack is shown for TM and TE polarizations in Figure 7.27. The results for the total Doppler component with the crack are shown in Figure 7.28.

7.2.5 Relative Sensitivity of the Doppler Component

It is seen in Sections 7.2.1 and 7.2.2 that the bistatic Doppler component is sensitive to the presence of small flaws in the target interior. A means of quantifying the improved sensitivity of the Doppler component relative to the sensitivity of the unshifted fields scattered from the stationary target is desired. A parameter referred to as the relative sensitivity of the Doppler component is defined and described for various cracked cases of the homogeneous polyethylene cylinder in the $(2, 1)$ mode of

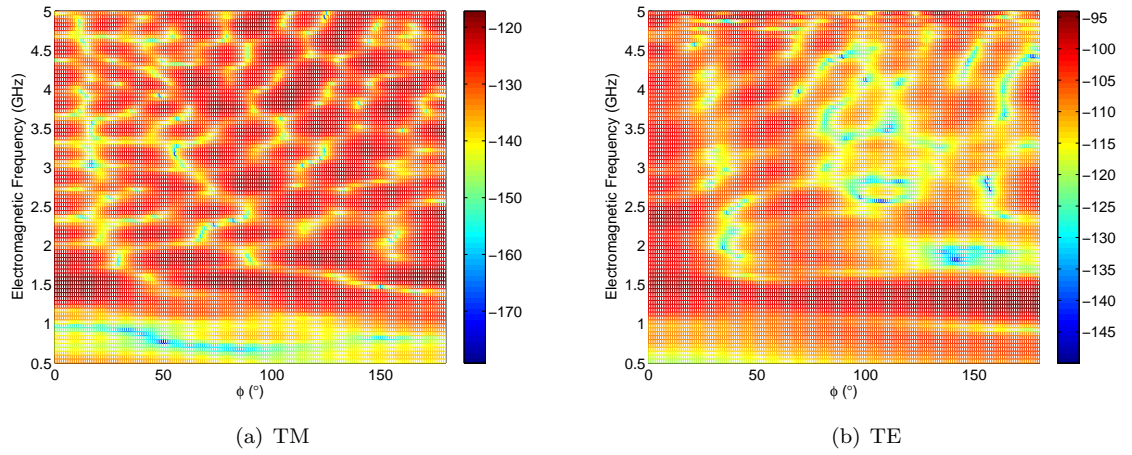


Figure 7.25: The Doppler component for the $(0,3)$ mode of the uncracked layered cylinder for TM and TE polarizations. The Doppler component is normalized to the unshifted RCS at $\phi = 0^\circ$.

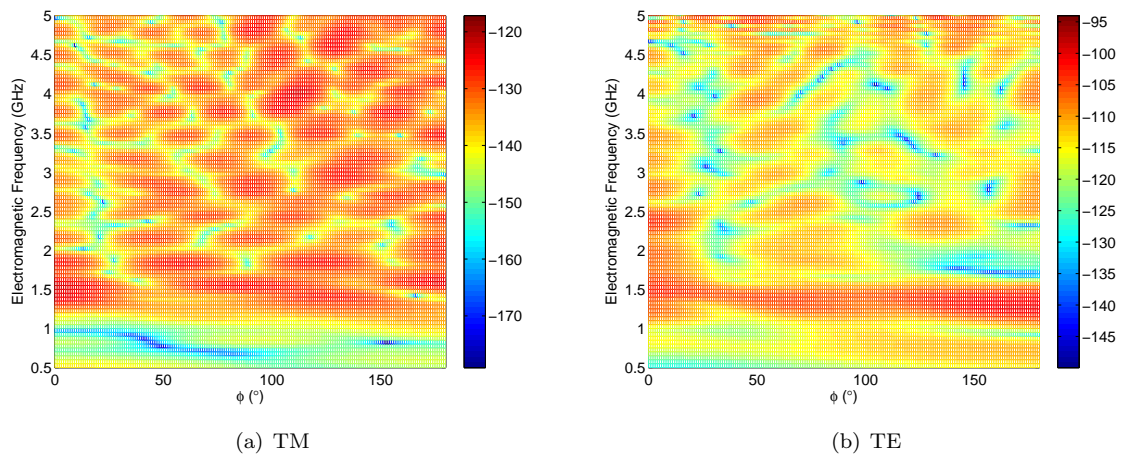


Figure 7.26: The Doppler component for the $(0,3)$ mode of the cracked layered cylinder for TM and TE polarizations. The Doppler component is normalized to the unshifted RCS at $\phi = 0^\circ$.

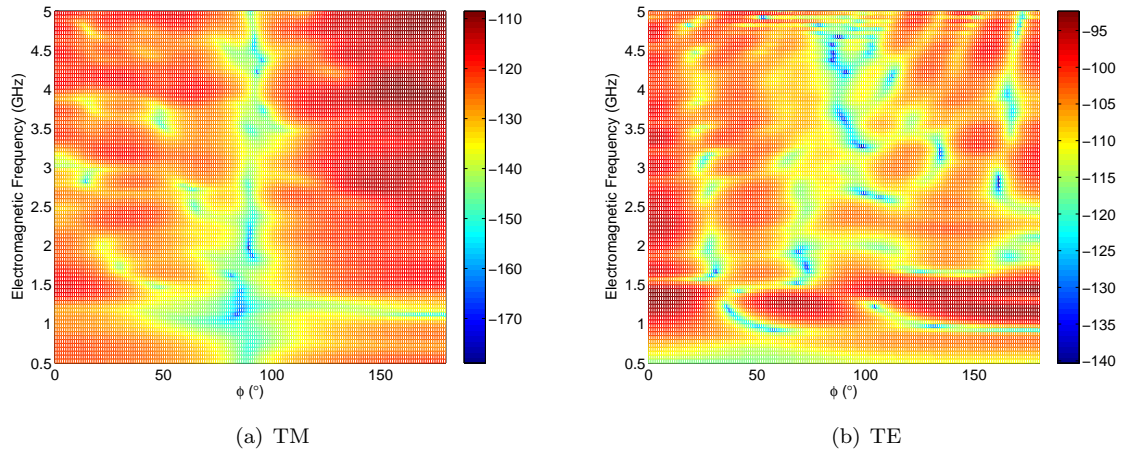


Figure 7.27: The Doppler component for the $(2, 7)$ mode of the uncracked layered cylinder for TM and TE polarizations. The Doppler component is normalized to the unshifted RCS at $\phi = 0^\circ$.

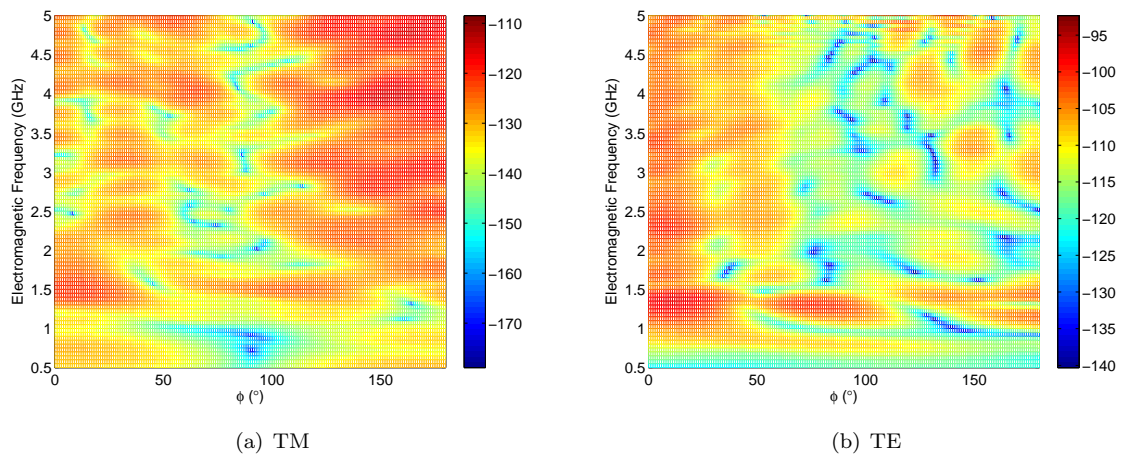


Figure 7.28: The Doppler component for the $(2, 7)$ mode of the cracked layered cylinder for TM and TE polarizations. The Doppler component is normalized to the unshifted RCS at $\phi = 0^\circ$.

resonance.

The relative sensitivity is the change in Doppler component RCS in dB for particular bistatic angles and a particular electromagnetic frequency compared to the change in unshifted field RCS, also on a dB scale, at the same angles and frequency. For example, the unshifted field RCS, shown in Figure 7.9 at an electromagnetic frequency of 5 GHz, is taken at various bistatic angles for a particular crack case. The change in the unshifted field RCS compared to the uncracked case then becomes the abscissa, or x coordinate, of the point locations; there is one point for each sampled bistatic angle. The change in the Doppler component RCS for the same crack case, relative to the uncracked Doppler component RCS, for the same bistatic angles and electromagnetic frequency as the unshifted field RCS, becomes the ordinate, or y coordinate of the point locations. Stated quantitatively, the x coordinate of the point becomes $\Delta \text{RCS}_o(\phi_i, f_{EM}) = \text{RCS}_o(\text{Crack}, \phi_i, f_{EM}) \text{ dB} - \text{RCS}_o(\text{No crack}, \phi_i, f_{EM}) \text{ dB}$, where ϕ_i are the sample bistatic angles and f_{EM} is the electromagnetic frequency of interest. The y coordinate of the point location becomes $\Delta \text{RCS}_d(\phi_i, f_{EM}) = \text{RCS}_d(\text{Crack}, \phi_i, f_{EM}) \text{ dB} - \text{RCS}_d(\text{No crack}, \phi_i, f_{EM}) \text{ dB}$. Values lying above the unit slope line indicate points where the Doppler component has greater sensitivity or exhibits a larger change in RCS value when the crack is present.

The (2, 1) mode of the homogeneous polyethylene for the three cracks considered previously in Section 7.2.1 is again considered. A fourth, larger crack, which is oriented along the x -direction and centered at the origin, is also considered; the crack dimensions are about $\Delta x \approx 5.4 \text{ cm}$ by $\Delta y \approx 6 \text{ mm}$, or roughly twice the size as crack #1. In this case, the (2, 1) mode resonance occurs at $f_a = 1621.5 \text{ Hz}$. The bistatic sample angles are taken at 1° increments between 0° - 180° . The result for the

relative sensitivity at an electromagnetic frequency of 3 GHz is shown in Figure 7.29. The unit slope line is also shown for reference; points lying above this line indicate angles at which the Doppler component has greater sensitivity to the crack than the unshifted field RCS. Values lying near the y axis demonstrate the highest, relative sensitivity. The same result is plotted at an electromagnetic frequency of 4 GHz in Figure 7.30.

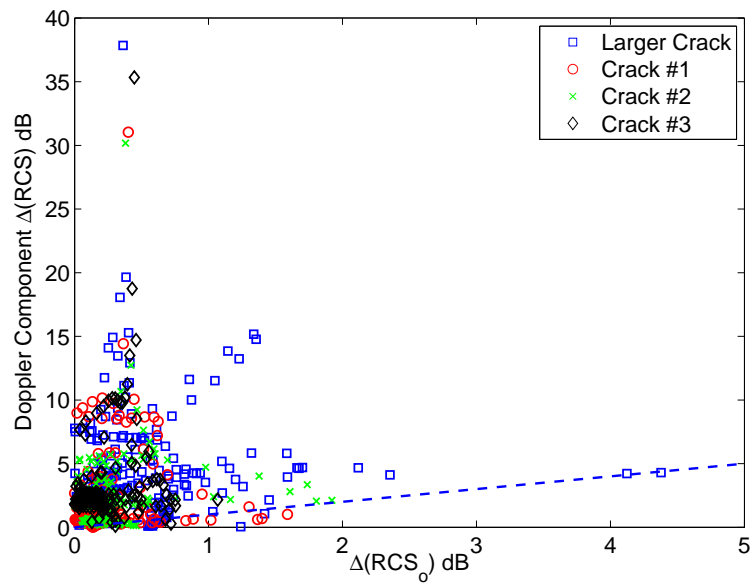


Figure 7.29: The relative sensitivity of the TM Doppler component for various bistatic angles at an electromagnetic frequency of 3 GHz. Four crack cases are shown.

Figures 7.29 and 7.30 allow comparison of the relative sensitivity for various crack locations, sizes, and at different electromagnetic frequencies. The plots indicate which crack location the Doppler component is most sensitive to as well as which cracks most greatly perturb the Doppler component and the unshifted field RCS. Two trends are noted. As the electromagnetic frequency increases, it is observed that the relative sensitivity of the Doppler component is reduced. This is expected because the size of the crack relative to the electromagnetic wavelength increases with

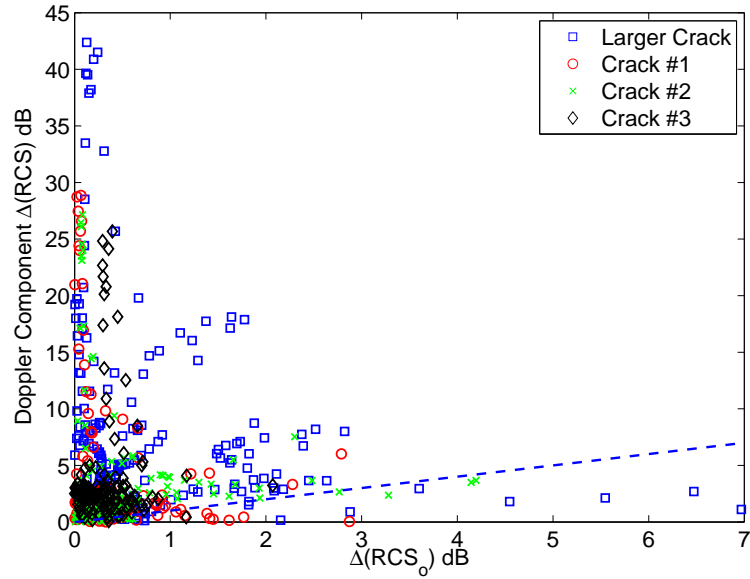


Figure 7.30: The relative sensitivity of the TM Doppler component for various bistatic angles at an electromagnetic frequency of 4 GHz. Four crack cases are shown.

increasing frequency. Also, as the crack grows the relative sensitivity of the Doppler component is expected to decrease because the unshifted field RCS is more easily able to detect it. Since the larger crack produces a larger change in the unshifted field RCS, the data points move out towards the unit slope line, showing the reduction in the relative sensitivity of the Doppler component.

7.2.6 Summary and Observations

In the preceding sections the Doppler component is shown versus bistatic scattering angle and electromagnetic frequency. The effect of a various small cracks internal to the target are investigated and it is observed that the bistatic Doppler component is sensitive to such flaws.

The detectability of the flaw in the homogeneous polyethylene cylinder using the Doppler component is then compared to the detectability using the unshifted fields scattered from the stationary cylinder. The different cracked cases of the

polyethylene cylinder are compared for the $(2, 1)$ mode of the cylinder. A parameter defined as the relative sensitivity of the Doppler component is described with the plots shown in Section 7.2.5; the plots monitor the change in RCS at various bistatic angles for a single electromagnetic frequency. These plots quantify the advantage of using the Doppler component to obtain increased sensitivity.

Despite showing high detectability for most bistatic angles, in some cases, the Doppler component only offers limited sensitivity. Generally, in order to easily observe the effect of the crack, it is necessary to have a dominant characteristic or feature in the pattern that can be perturbed by the crack. An example of such a feature is the deep null at $\phi = 90^\circ$ for the $n = 2$ mode. It is also observed that there is little variation from which to distinguish the crack location. In the next section, an alternative method of imaging scattering within the target for the Doppler component is investigated to obtain higher sensitivity and the location of flaws.

CHAPTER VIII

Time-Reversal Focusing for Applications in NDE

In the previous chapter the effect of a flaw on the bistatic scattered electromagnetic fields was considered. It was observed that measuring the bistatic RCS offers limited sensitivity to the presence of internal flaws. Only particular modes and polarizations exhibit sensitivity to the presence of small inhomogeneities, such as cracks. In some cases the internal perturbations to the strain and displacement due to the crack is overwhelmed by other contributions to the Doppler component, such as reflection from the boundary. In addition, the bistatic Doppler component provides little information regarding the location of the flaw. The location sometimes may be inferred if the mode shape and the extent of the effect of the flaw on the Doppler component are known; however, this approach is unable to conclusively locate flaws within the target.

In this chapter focusing is employed to improve sensitivity to flaws within the target and to provide information about the flaw location. Time-reversal focusing is used to focus the incident electromagnetic signal in the target interior. Sensitivity is improved because focusing internal to the target reduces the role the target exterior plays in determining the scattered electromagnetic fields. Information about the location of the flaw, as will be shown, is obtained by measuring the correlation

between the received fields and a reference signal corresponding to various source point locations within the target.

The chapter begins with a brief introduction to time-reversal focusing. A description of how the unshifted electromagnetic scattered fields are processed to obtain a map of the scattering intensity within the cylinder is then provided. Various examples are given to demonstrate the validity of this approach. Finally, a discussion on processing the Doppler component fields is given. The Doppler component results for the original, uncracked polyethylene cylinder and the cracked polyethylene cylinder are shown.

8.1 Source Focusing Using Time Reversal

Focusing using time reversal has been in use for some time. Initially, the technique was developed for ultrasound and biomedical applications [78]. The approach is robust and can provide source focusing in the presence of inhomogeneity. This type of focusing works because of reciprocity and invariance of the wave equation to changing the sign of the time variable. Technically, it is only valid in lossless media; if the medium is only weakly dispersive over the frequency range of interest, however, the approach still provides acceptable focusing.

The algorithm used to achieve focusing of the incident field within the target is briefly presented. Further information can be found in references [78] and [79]. The setup is shown in Figure 8.1. At the desired focal point, (x_i, y_i) , an incident signal, $u(t)$, is emitted. This signal propagates through the intervening, possibly complex media and arrives at the observation points, labeled (x_j, y_j) . The received signal is denoted by $F_{ij}(t)$, which is the convolution of the input signal, u , and the transfer function, $h_{ij}(t)$, between the source and receiver locations. The signals are recorded

at the observation points and reversed in time. The observation points then become new source points and send out the time reversed received fields, $F_{ij}(-t) = e_j(t)$. These signals propagate back and reconstruct a time reversed version of the original pulse, $u(-t)$, at the desired focal point, which was the initial source point. The quality of reconstruction depends on many factors, such as the wavelength and the number and separation of observation points.

8.2 Processing the Scattered Field

In the steps outlined above, source points send out the time-reversed received field, $e_j(t)$, resulting in focusing at the focal point. This signal interacts with and scatters off the target. The received signal at each source point, denoted by $r_j(t)$, is made up of incident signals from neighboring source points, $e(t) \sim \sum_j e_j(t)$, and scattered field, $s_j(t)$, contributions.

A source whose time dependence is the same as the original input signal, u , present at location i within the target will produce a signal at j , r_j , which is correlated with the reference function corresponding to a source at location i , $F_{ij}(t)$. However, in this application, there are two distinguishing points which should be made. First, if the scattered field is a result of an inhomogeneity present at location i within the target, then the reflected signal will have time dependence which is similar to the convolution of the transfer function, h_{ij} , and the time reversed input signal, $u(-t)$, since this is the signal which is reconstructed at the focal point. Also, here the signal of interest is the scattered field which arises due to volumetric scattering within the target. Considering the relationship between an equivalent volumetric source, J_v , and an incident field, E_i , given by

$$J_v = \epsilon_o(\epsilon_r - 1) \frac{\partial E_i}{\partial t}$$

the received signal, $r_j(t)$, and the input signal, $u(t)$, are seen to be related by a derivative with respect to time. The result of these two points is that the correlation between received fields, $r_j(t)$, and a reference signal given by

$$(8.1) \quad F_{ij}^d = \frac{\partial u(-t)}{\partial t} * h_{ij}(t)$$

is the quantity of interest. A scattering intensity coefficient is defined as follows:

$$(8.2) \quad d_i(t) = \frac{\sum_{j=1}^N \int_{-\infty}^{\infty} r_j(t) F_{ij}^d(t) dt}{\sum_{j=1}^N \int_{-\infty}^{\infty} (F_{ij}^d(t))^2 dt}$$

where N is the number of observation points where the r_j is recorded. The denominator is simply a normalization factor. Processing in this manner results in a value, $d_i(t)$, at each focal point within the target. This value indicates the correlation or similarity between return signal, r_j , and the signal received when a volumetric scattering point source is located at the focal point. If there is a scatterer at the focal point, the correlation will be high; the scatterer acts as a source, producing the same received signal at the observation points as the reference signal, F_{ij}^d .

A few points are made to clarify the details of this approach. First, any inhomogeneity, such as a crack or void, is assumed to be small enough to have little effect on the quality of focusing of the incident electromagnetic signal at the focal point. This implies that the time dependence of the focused incident wave is still the time-reversed version of the input signal, $u(-t)$. It also means that the scattered fields due to the abnormality are inherently neglected in processing the volumetric current; the time derivative relationship used in the correlation assumes that the dominant contribution to r_j is from volumetric scattering at the focal point. Second, if no scatterer is present the wave will continue to propagate, undisturbed through the target. In this case, equation (8.2) will produce some points where signals are more correlated than others but no dominant scattering locations. Comparing cases

without and with inhomogeneity shows that the correlation maxima with an inhomogeneity is many times larger than without. For example, if one cell of the FDTD mesh within the target is PEC, instead of the background permittivity, the maximum correlation is about two orders of magnitude larger than the homogeneous case. Finally, it is seen that two reference signals, F_{ij} and F_{ij}^d , are required to focus the incident electromagnetic field and to process the received fields, respectively. In review, F_{ij} , is the received signal at the observation points when the original input signal, u , is sent out from each focal point. F_{ij}^d is the received signal when the time derivative of the time-reversed input signal, $\partial u(-t)/\partial t$ is sent out from each focal point.

8.3 Results Using Focusing of the Unshifted Received Fields

The homogeneous cylinder from Section 6.1 is investigated. For the unperturbed fields in a cylinder with no crack there is no scatterer present; equation (8.2) produces no peaks that correspond to strong scattering. As will be seen, even when an abnormality is present, the unperturbed field scattering remains minimal because of the small size of the abnormality. In order to separate the effect of the inhomogeneity, the background received signal in the homogeneous case, $r_j^o(t)$, may be subtracted from the received signal in the case with the abnormality or crack, $r_j^a(t)$. This effectively isolates the scattered field due to the abnormality alone, $s_j^a = r_j^a - r_j^o$. Results with and without background subtraction for the scattering coefficient defined in equation (8.2) will be shown.

The cylinder radius is 10 cm or $1\lambda_o$ at the FDTD mesh frequency. The cylinder permittivity is $\epsilon_r = 2.25$, the cell size, Δ , is $\lambda_o/50 = 2$ mm, and the time step is, $\Delta t = 4.6$ ps, or 0.98 of the two-dimensional Courant limit. The UPML, which

terminates the FDTD mesh, is 10 cells thick. Since the incident field is not a plane wave and it is not necessary to calculate scattered far fields, the TF/SF formulation is not used. The total FDTD grid is 180 cells square and the simulation is run for 3000 time steps.

Figure 8.1 illustrates the problem geometry used in these results. Dimensions are indicated in terms of free space wavelength at the FDTD mesh frequency of 3 GHz. In this setup there are seven observation points. A differentiated Gaussian pulse is the initial incident signal at the focal points. The equation for the pulse is given by

$$(8.3) \quad s(t) = -\frac{(n - n_o)}{n_d^2} e^{-\frac{1}{2} \left(\frac{n - n_o}{n_d} \right)^2}$$

where n is the time step, n_o is the time delay to the start of the pulse, and n_d is related to the time duration of the pulse. This signal is an odd function of time, $u(-t) = -u(t)$, so $F_{ij}^d = -\partial u / \partial t * h_{ij}$. The time duration of the pulse is approximately 200 ps for $n_o = 1500$ and $n_d = 25$; the frequency content of the incident signal is limited to 0.5-5 GHz. The focal point is varied across a 15×15 grid of points within the cylinder, as shown in Figure 8.2. The focal point spacing is $0.08\lambda_o = 8$ mm.

The result of focusing the incident wave is shown in the series of images in Figure 8.3; the focal point in this case is chosen to be the origin. At approximately $n = 1820$ the input pulse is reconstructed at the focal point. Since there is no scatterer present at the focal point the signal continues to propagate through the focal point and off the FDTD grid.

The scattered field is then recorded at the observation points and post-processed as described in equation (8.2). Two examples of processing the unshifted fields are given.

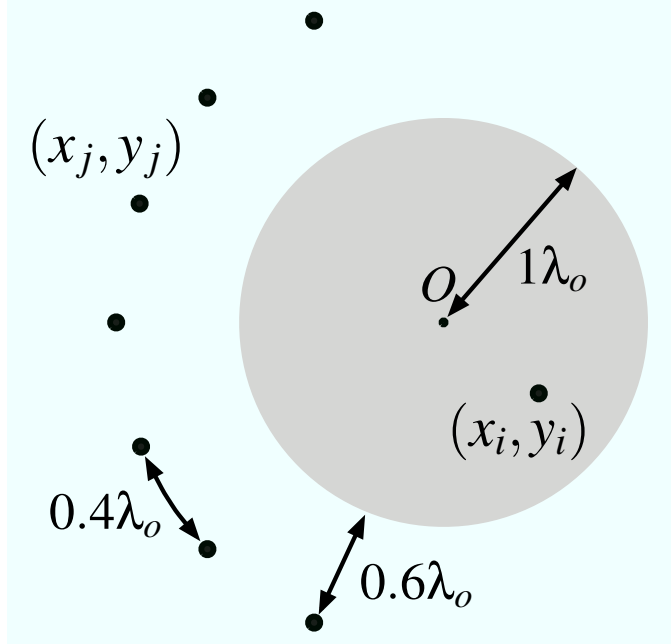


Figure 8.1: The source focusing problem geometry used in the FDTD simulation.

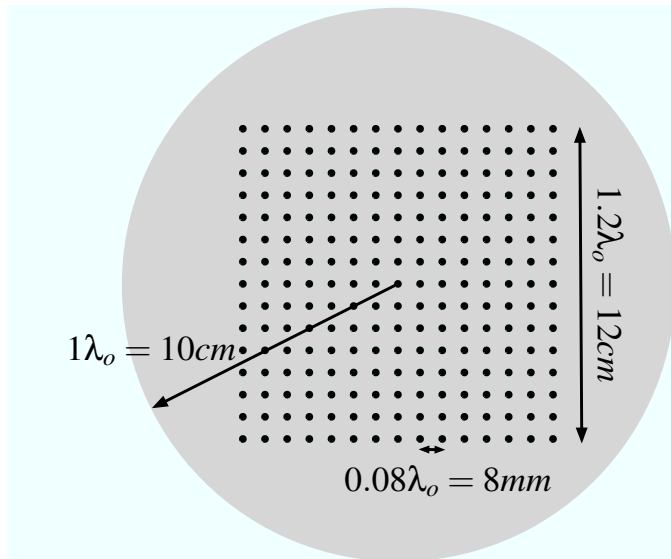


Figure 8.2: The 15×15 grid of focal points used in the FDTD simulation. Spacing between points is 8 mm, or $0.08\lambda_o$, at the FDTD mesh frequency of 3 GHz.

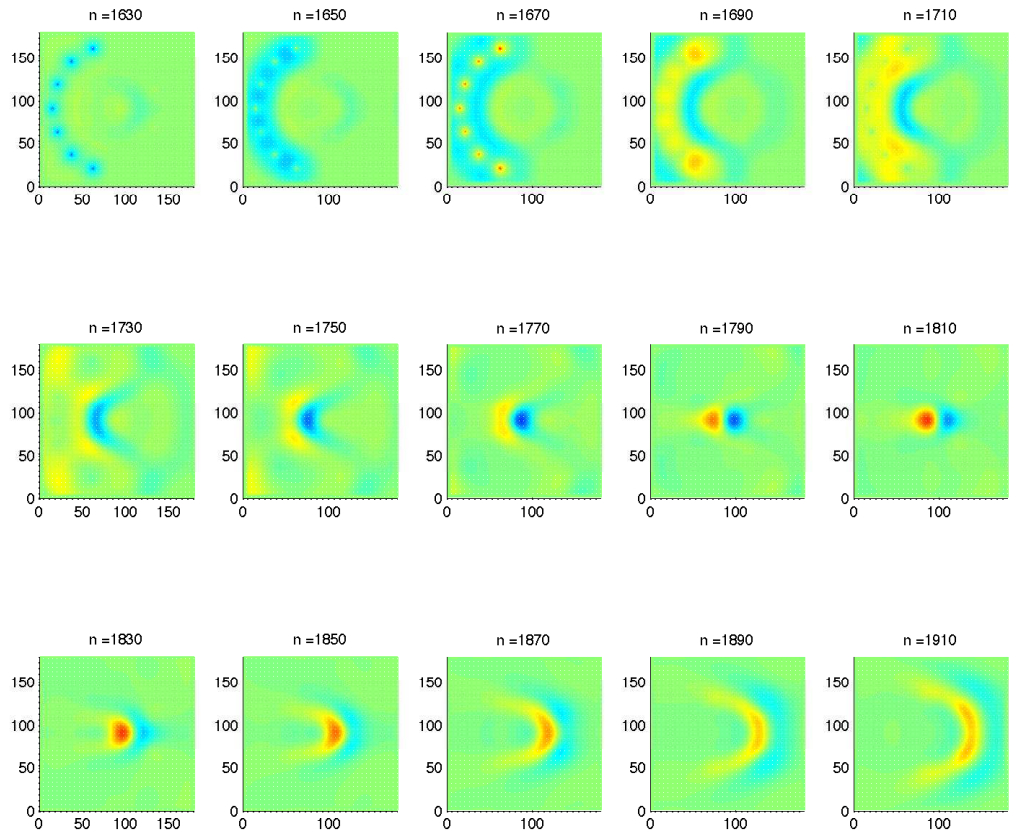


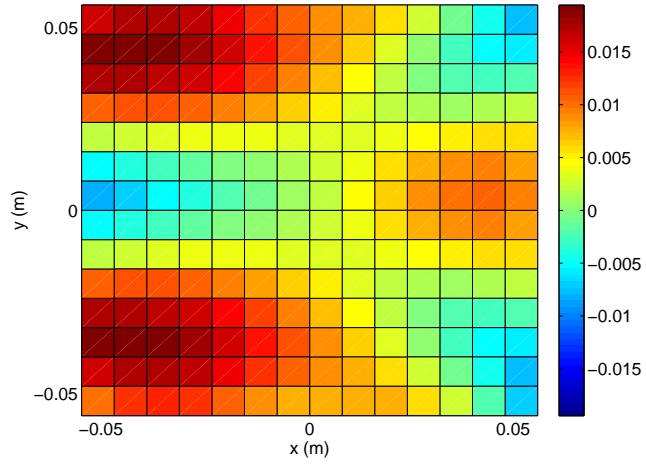
Figure 8.3: Sequence of snapshots of the electric field in the TM FDTD mesh as the incident wave propagates into the cylinder. The signal is reconstructed at time step $n = 1820$ at the desired focal point, which the origin in this case.

8.3.1 Small Dielectric Inclusion

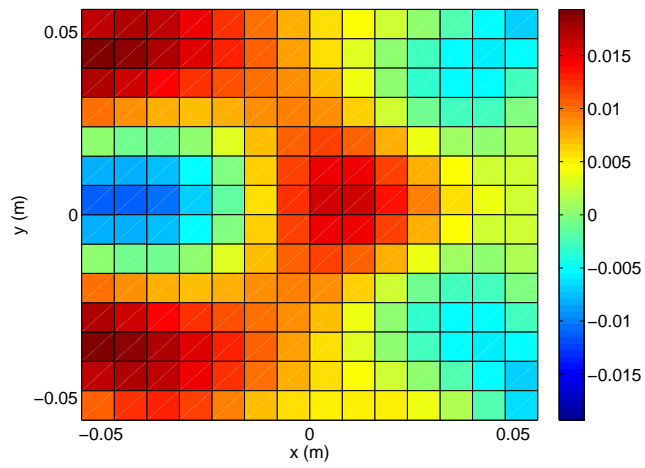
In the first example, the permittivity of a single FDTD cell within the cylinder is replaced with a higher value of $\epsilon_r = 15$, representing a small dielectric inclusion. The focal point is colocated with the inclusion. Processing the total received signal without (r_j^o) and with the inclusion (r_j^a) results in Figures 8.4(a) and 8.4(b), respectively, for TM polarization. For reference, Figure 8.5 illustrates the focal point and inclusion locations. It is seen that, even without subtracting the received signal in the homogeneous case, the presence of increased scattering at the location of the inclusion is evident. If the homogeneous received signal is subtracted off, however, and the scattered field due to the inclusion, s_j^a , is processed using equation (8.2) then the location of the flaw is plainly evident as a region of increased scattering; this may be seen in Figure 8.6.

8.3.2 Small Void

In the second example a single cell of the FDTD mesh within the cylinder is replaced with free space, representing a small void. The focal point coincides with the void location. The results for the scattering intensity coefficient without and with the void are shown in Figures 8.7(a) and 8.7(b), respectively, for TM polarization. Subtracting the homogeneous received fields and processing only the scattered field resulting from the void produces the result shown in Figure 8.8. As expected, at the location of the void there is less volumetric scattering than without the void. In this case, the contrast between the abnormality and the background permittivity is smaller than in the first case. The unperturbed fields cannot distinguish between both cases without subtraction of the homogeneous received signals.



(a) d_i Processing r_j^o Without Inclusion



(b) d_i Processing r_j^a With Inclusion

Figure 8.4: The scattering intensity coefficient within a homogeneous polyethylene cylinder and a polyethylene cylinder with one FDTD cell having $\epsilon_r = 15$.

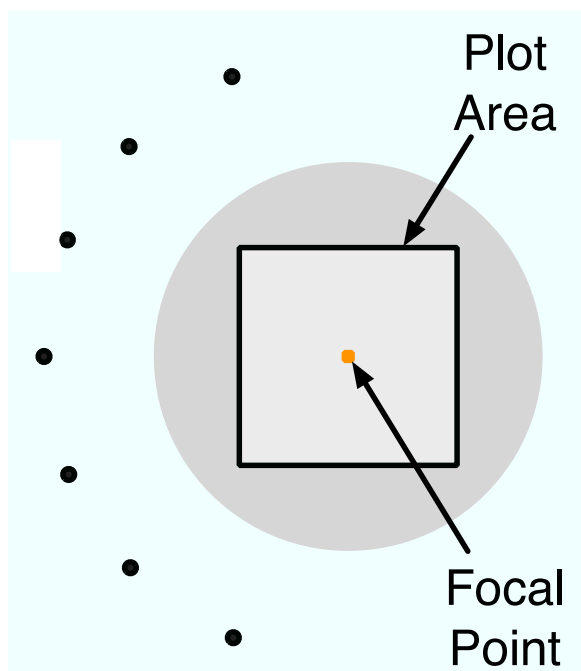


Figure 8.5: The focal point and inclusion locations within the cylinder. The plot area in Figures 8.4(a) and 8.4(b).

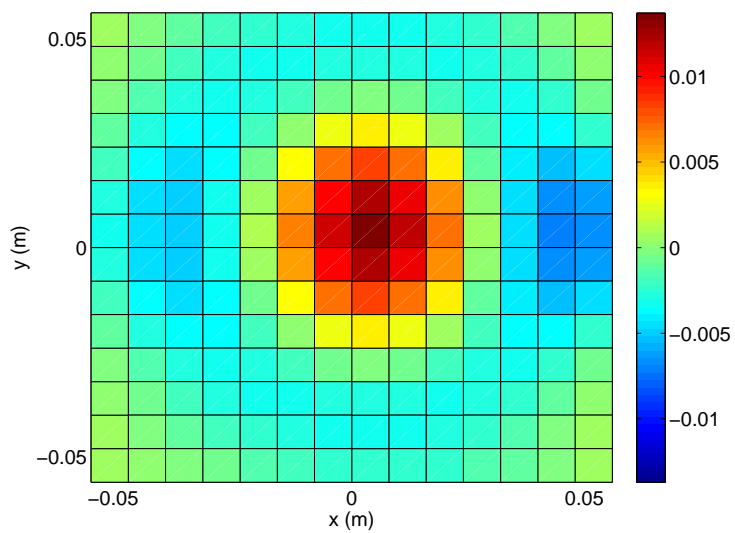
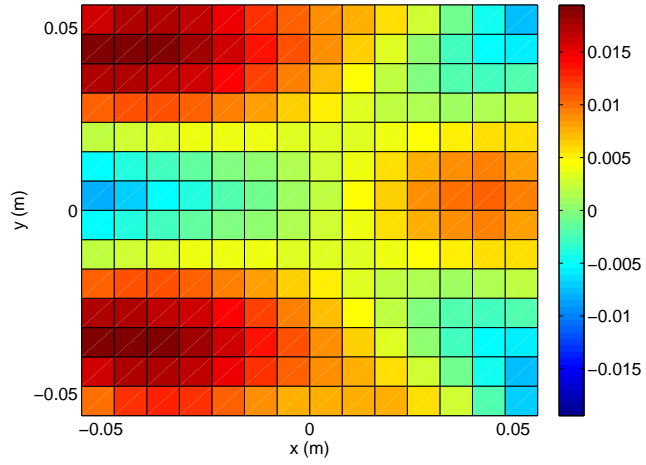
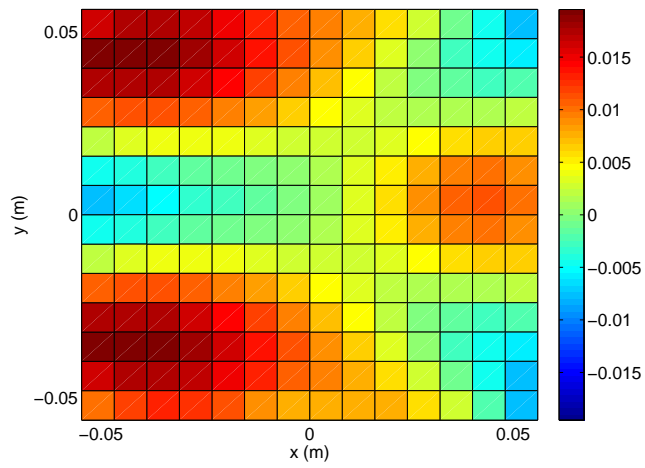


Figure 8.6: The scattering intensity coefficient, d_i , of equation (8.2) processing only scattered field contributions, s_j^a , the difference between the received signals with and without the inclusion.



(a) d_i Processing r_j^o Without Void



(b) d_i Processing r_j^a With Void

Figure 8.7: The scattering intensity coefficient within a homogeneous polyethylene cylinder and a polyethylene cylinder with one FDTD cell having $\epsilon_r = 1$.

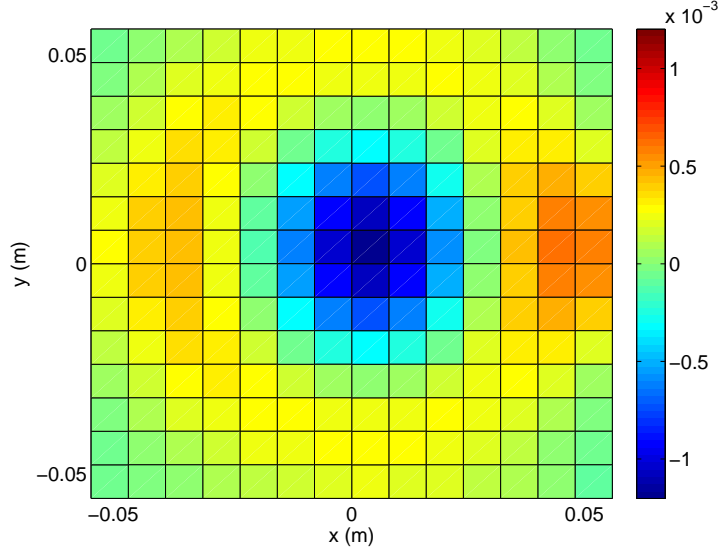


Figure 8.8: The scattering intensity coefficient, d_i , of equation (8.2) processing only scattered field contributions, s_j^g , the difference between the received signals with and without the void.

8.4 Processing the Doppler Component Scattered Field

In the examples above it is seen that the unshifted fields cannot distinguish low contrast abnormalities without subtraction of the homogeneous received fields. It is also observed that the received signal is a function of both the incident focused signal and whether or not a scatterer or abnormality is present. The Doppler component fields differ since they are also a function of the displacement and the divergence of the displacement within the target. Under acoustic excitation, there is increased displacement and strain surrounding an abnormality, meaning that the Doppler component should have more sensitivity to the presence of the abnormality.

The Doppler component received field is denoted by \tilde{r}_j . There is no incident field component in the received signal since it is a product of the Doppler component sources; therefore, the received field is entirely a result of scattered field contributions, i.e. $\tilde{r}_j = \tilde{s}_j$. As derived in Section 4.2.2, the volumetric current which produces the

Doppler component received fields, \tilde{r}_j , for TM polarization is given by

$$(8.4) \quad J_{z,\tilde{\epsilon}} = -(\epsilon_d - \epsilon_o)\nabla \cdot \mathbf{u} \frac{\partial E_o}{\partial t}$$

where E_o is the total unshifted field and the dependence on the displacement is evident. It is assumed that the volumetric scattered field, which itself is related to the total incident field with a time derivative, is not included in the total unshifted field, E_o . For TE polarization, as seen in equation (4.6), the relationship is similar except for an additional term that is proportional to the electric field. Using Maxwell's equations, the Doppler component field scattered as a result of this term is also related to the unshifted field with a time derivative operation. Therefore, processing the Doppler component for TE polarization is identical to TM.

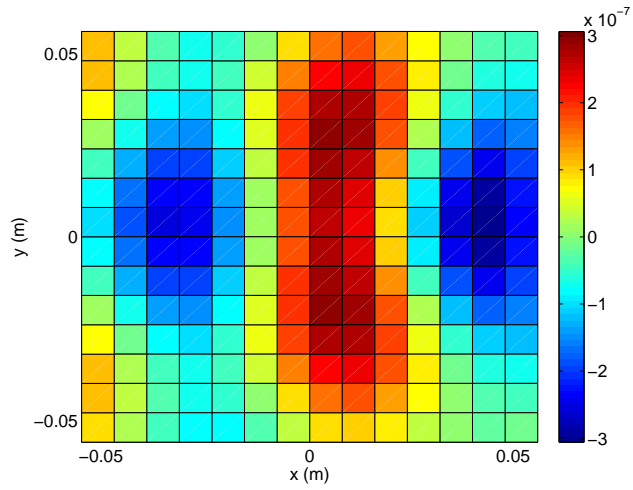
As in the case of the unshifted fields, a scatterer or abnormality at location i will produce received fields, \tilde{r}_j , which are correlated with the reference signal F_{ij}^d . The scattering intensity coefficient for the Doppler component fields is defined as

$$(8.5) \quad \tilde{d}_i = \frac{\sum_j \int_{-\infty}^{\infty} \tilde{r}_j(t) \times F_{i,j}^d dt}{\sum_j \int_{-\infty}^{\infty} (F_{i,j}^d)^2 dt}$$

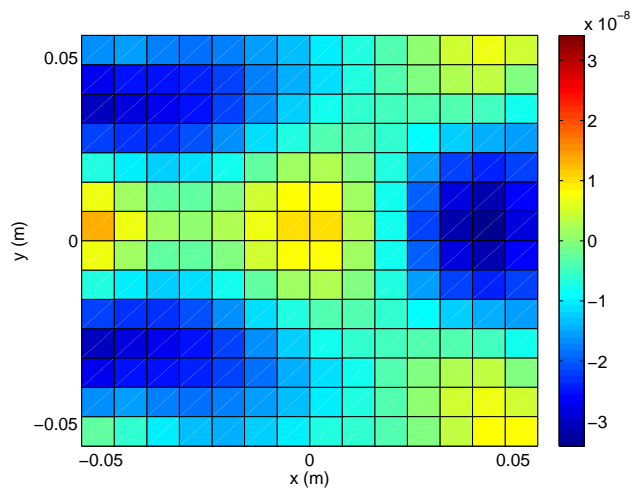
which is nearly identical to the unshifted field scattering coefficient.

Two modes of the homogeneous polyethylene cylinder are considered to show the effect of mode shape on the Doppler scattering coefficient. In both cases, the result for TM polarization with the focal point located at the origin is shown. The first mode, shown in Figure 8.9(a), is the (2, 1) mode at $f_a = 1.84$ kHz; the second mode, shown in Figure 8.9(b), is the (0, 1) mode at $f_a = 4.82$ kHz.

The TM polarized Doppler component scattering coefficient of three cases for the (2, 1) mode of resonance are shown in Figure 8.10. In Figure 8.10(a), the case without any crack, is shown again for ease of comparison with the other cases. In Figure 8.10(b) the focal point coincides with the location of the crack. Increased



(a) TM \tilde{d}_i for (2,1) Mode



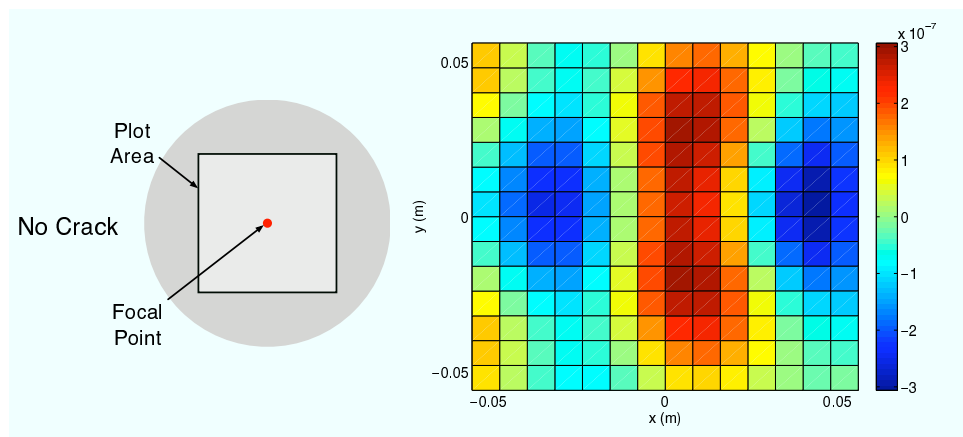
(b) TM \tilde{d}_i for (0,1) Mode

Figure 8.9: The Doppler component scattering intensity coefficient within a homogeneous polyethylene cylinder for two modes. The focal point is located at the origin, or center of the cylinder.

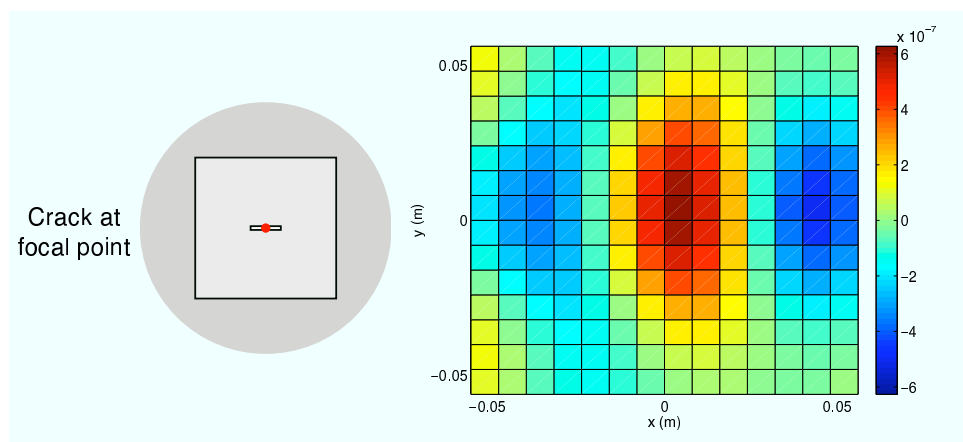
scattering, which dominates the scattering coefficient over the plot area, is observed from the crack location. In Figure 8.10(c) the focal point is offset from the location of the crack; the shape of the scattering coefficient is not greatly perturbed from the case without the crack shown in Figure 8.10(a).

In Figure 8.11 the focal point is moved from the origin to (-4 cm, 0 cm). The same three cases as above are considered for the TM polarized Doppler component. The case without any crack is shown in Figure 8.11(a). Crack #1, which is now offset from the focal point, is shown in Figure 8.11(b); the scattering coefficient is nearly the same as in the case without a crack. Figure 8.11(c), where the crack and focal point are colocated, shows the increased scattering that is a result of the large displacements surrounding the crack location.

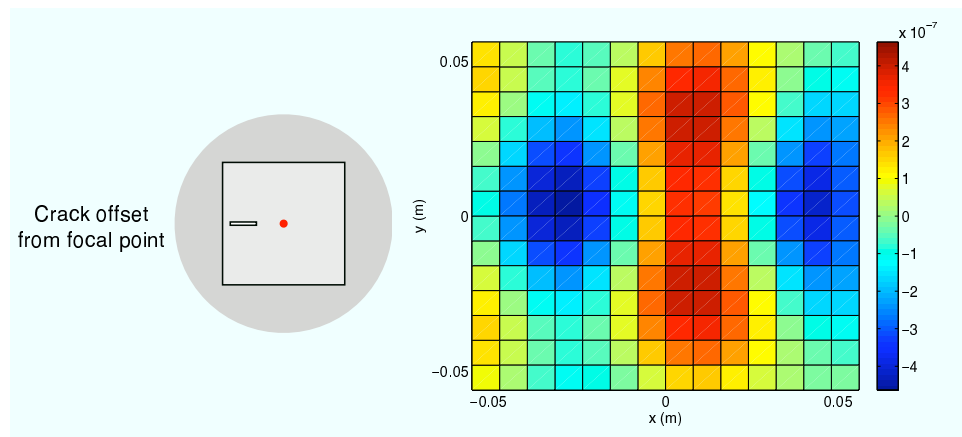
In this chapter, focusing is used to improve sensitivity to interior flaws and to provide information about the location of the flaw. The sensitivity of the Doppler component to the presence of flaws as well as its ability to locate regions of large strain or displacement are demonstrated. It is unnecessary to subtract the received Doppler component fields in the homogeneous case in order to distinguish the crack; this is in contrast to the unshifted field which is unable to detect the presence of low contrast abnormalities without subtracting the homogeneous received fields. This is an advantage in practical systems where the homogeneous received fields are generally unavailable. Suggestions for future work to improve the approach are discussed in Chapter XI.



(a) (2, 1) No Crack

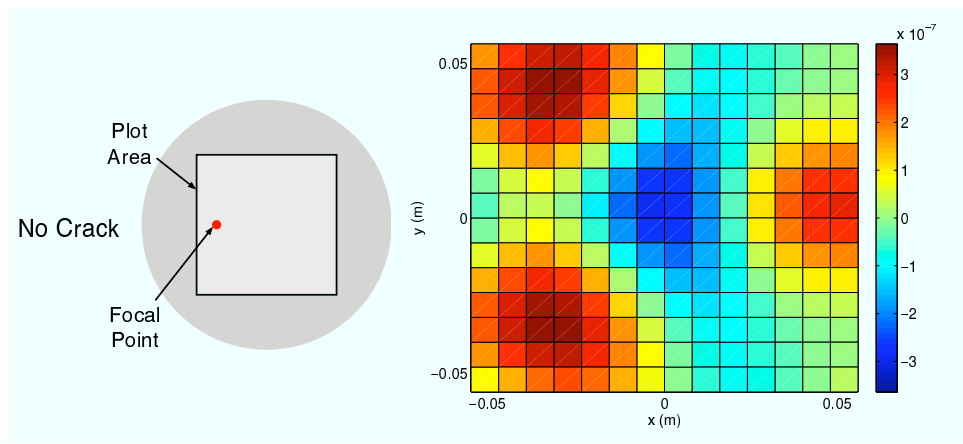


(b) (2, 1) Crack #1

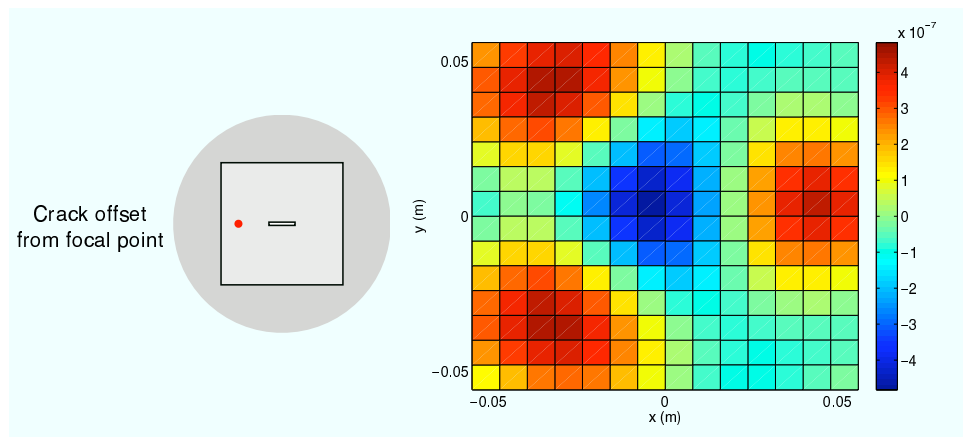


(c) (2, 1) Crack #3

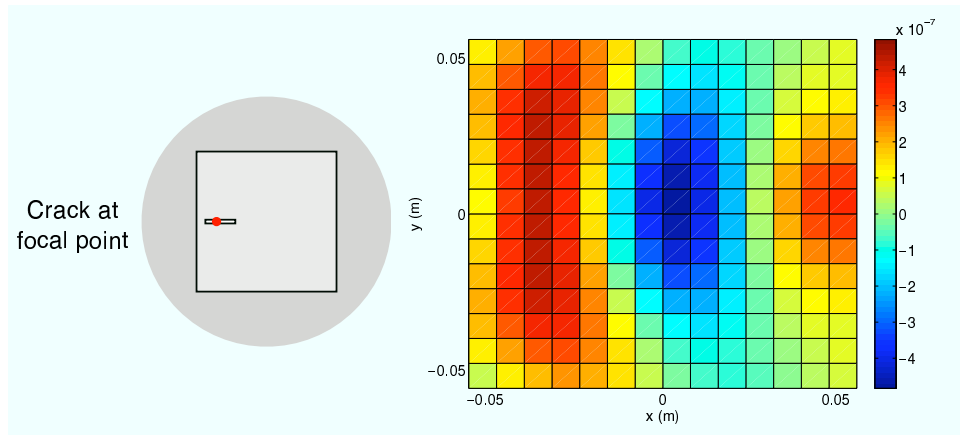
Figure 8.10: Doppler fields scattered from the cylinder in the (2, 1) resonant mode without the crack, with crack #1, and with crack #3. The focal point is chosen to be at (0 cm, 0 cm).



(a) (2, 1) No Crack



(b) (2, 1) Crack #1



(c) (2, 1) Crack #3

Figure 8.11: Doppler fields scattered from the cylinder in the (2, 1) resonant mode without the crack, with crack #1, and with crack #3. The focal point is chosen to be at (-4.0 cm, 0 cm).

CHAPTER IX

Systems for Detection

The purpose of this section is to provide an overview of acousto-EM systems for Doppler component detection. Various parameters and their effect on system performance are qualitatively discussed. The system must be specially designed to successfully recover the extremely small Doppler component from the return signal, extracting it from surrounding clutter and the relatively large, unshifted scattered electromagnetic field. There are numerous system architectures which could be used for acousto-EM detection. For example, pulsed acoustic signals could be used to excite multiple resonant modes simultaneously. This is equivalent to hitting the target with a delta forcing function and monitoring the impulse response. This type of acoustic excitation would produce multiple Doppler shifts on the electromagnetic signal, corresponding to the mode frequencies. In another approach, an electromagnetic pulse could be used to obtain scattering results over a range of electromagnetic frequencies. Extracting the Doppler component in these configurations, however, would require more complex processing than it does in the system described below.

9.1 System Overview

A basic configuration for the acousto-EM system is outlined herein. In this system, a narrow band acoustic source is used to excite a single acoustic resonant mode of the

target; a continuous wave (CW) electromagnetic signal then scatters off of the target and is received. The Doppler shifted component embedded in this signal is extracted using a detector. By sweeping the acoustic frequency of excitation, various resonant modes of the object can be excited. This architecture builds on a previous FM-CW radar design used to recover the Doppler signal scattered from resonant tuning forks [80]. The system shown in Figure 9.1 can be broken into three main blocks: the acoustic source and transducer, the electromagnetic transmitter and receiver front end, and the Doppler component detector.

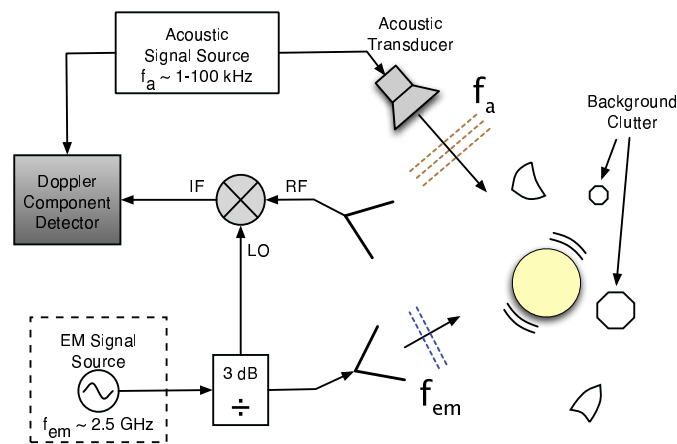


Figure 9.1: A block diagram of the acoustic and electromagnetic system.

9.1.1 Acoustic Source Parameters

The acoustic source power is the most critical system parameter, in terms of producing a measurable Doppler component, since both the boundary displacement and strain within the target are proportional to it. It is noted from the results in Chapter VI that the Doppler component is quite small. In all of the Ansys simulations, excluding those employing line source contact excitation, the incident acoustic pressure wave amplitude is 1 Pa. Pressure amplitudes can easily exceed this value, however, producing a correspondingly larger Doppler component. Increasing the pressure amplitude by a factor of 10 results in a 20 dB increase in the first

Doppler component of the bistatic RCS.

Most data sheets for acoustic sources quote a figure known as *sound pressure level*, or SPL. This figure, which specifies the deviation in pressure caused by an acoustic disturbance from an ambient value, is calculated as follows:

$$(9.1) \quad \begin{aligned} SPL(dB) &= 10 \log_{10} \left(\frac{p}{p_o} \right)^2 \\ &= 20 \log_{10} \left(\frac{p}{p_o} \right). \end{aligned}$$

where p is the pressure wave amplitude and p_o is the designated reference pressure. In air, p_o is generally chosen to be $20\mu\text{Pa}$, which is the threshold for human hearing. For example, the SPL of a jet engine is approximately 130 dB which corresponds to $p = 200 \text{ Pa}$ and the SPL of normal conversation is about 60 dB [81].

The second acoustic source parameter is the frequency of operation, which corresponds to the frequency of the desired modes. The frequency range of interest is target and application specific since these factors primarily determine the resonance frequencies. There is some level of choice in the system, however, and choosing an appropriate range can ease some system requirements. As an example, using higher order modes rather than the lowest order modes is one way to adjust the frequency range. The acoustic source also should exhibit fine tunability over the desired frequency range since the resonances are usually quite narrowband.

The available acoustic power also depends on the desired frequency of operation of the acousto-EM system. Two factors contribute to the difficulty in generating high amplitude air-coupled ultrasonic pressure waves at an appreciable distance from the source. The first is the large acoustic impedance mismatch between the transducer material and the surrounding air. This greatly reduces the transfer efficiency, or the efficiency of converting input electrical energy into mechanical energy, of the

transducer. The second factor is attenuation. At higher, ultrasound frequencies it becomes more difficult to create large amplitude pressure waves because of significantly higher attenuation in air with increasing frequency [82]. Between 10 kHz-100 kHz the attenuation is approximately 10-100 dB/m [83]. On the other hand, at lower acoustic frequencies, the phase noise in the electromagnetic radar system, which will be discussed shortly, becomes an issue as well. In addition, using large acoustic power at audible frequencies is potentially hazardous if the maximum pressure is not localized and controlled. A further disadvantage of low acoustic frequency operation is ambient noise, most of which occurs below 40 kHz [82]. For these reasons, in most applications it is advisable to operate between 50-500 kHz, if possible.

It is noted that the poor resolution at these relatively low ultrasound frequencies is not an issue in this application. Unlike in an all-acoustic system, the acoustic source is not being used for imaging the target; it only serves to provide acoustic excitation for the target resonant modes. In addition, it is generally desirable to have wide transducer bandwidth in ultrasound applications to improve range resolution in pulse-echo measurements and to reduce the pulse time duration which decreases the minimum distance of operation. There is a tradeoff between acoustic power and bandwidth, however; as bandwidth increases, the radiated sound pressure amplitude at a given distance goes down [82]. In this application, wide bandwidth is not required as the source is only required to provide excitation for the resonant mode. A few percent bandwidth that includes target resonances would be acceptable.

There are many types of ultrasound transducers which have different principles of operation. In this application, it is desired to generate high amplitude pressure waves in air at relatively low ultrasound frequencies, which suggests using electrostatic or piezoelectric type transducers. These types of transducers have previously been

investigated for non-contact air-coupled ultrasound applications [82, 83].

Possible candidates for use as acoustic sources in an acousto-EM system are given. The first source to be described is a piezoelectric ceramic speaker that operates between 15 kHz and 100 kHz [84]. This speaker is capable of producing an SPL of 90 dB/W/m. At the maximum rated power of 20 W, 1 m away from the speaker, the sound wave amplitude is $p \approx 13$ Pa. Recent advances in air-coupled ultrasonic transducers have led to the development of high-power units which could also prove effective for this application. For example, a 25 V input voltage signal to a transducer described in [85] that operates at 100 kHz is capable of producing approximately 131 dB SPL 1 m away from the transducer. This is equivalent to a pressure wave amplitude of 68 Pa. The same transducer at 27 cm can produce 142 dB SPL. Pressure wave amplitudes in this range can increase the Doppler component RCS by nearly 30 dB.

Another option to increase the available acoustic power is to array multiple transducers and focus the radiated pressure. In [86], an array of electrostatic transducers is designed for NDE applications at an operational frequency of 80 kHz. The array consists of 20 transducers arranged in a two-dimensional fashion and curved in the horizontal plane to focus the radiated pressure waves. At the desired focal point 20 cm from the array the measured SPL is 143 dB, corresponding to a pressure wave amplitude of about 200 Pa.

In some NDE applications it may be possible to place a transducer directly on the surface of the target to reduce the acoustic power requirement. This means of acoustic excitation is simulated in Section 6.2. It is noted that this approach somewhat detracts from an initial advantage of using the acousto-EM approach, which is remote, noncontact detection and identification.

9.1.2 Electromagnetic System Parameters

The electromagnetic components of the acousto-EM system in Figure 9.1 are responsible for generating and transmitting the electromagnetic signal, receiving the scattered fields, and extracting the Doppler component from this return signal. This portion of the system can further be broken down into the antenna, the receiver front end, and the Doppler component detector. Discussion of the desired antenna characteristics is reserved until the next chapter.

The electromagnetic transmitter is made up of a local oscillator (LO) and 3 dB power splitter. The LO frequency is largely determined by the application; $f_{LO} = 2.5$ GHz and $f_{LO} = 3.0$ GHz are used in Chapter VI. The LO also must have extremely low phase noise since this noise will eventually be mixed down along with the Doppler component. As the Doppler shift, or acoustic frequency of interest, increases the LO phase noise is reduced and detection becomes easier. Therefore, the minimum acoustic frequency of interest determines the required LO phase noise performance. The data sheets for the HP ESG 4000A signal generator specify the SSB phase noise to be -110 dBc/Hz at 20 kHz offset from $f_{LO} = 2$ GHz [87]. Higher performance signal generators are capable of producing as little as -124 dBc/Hz of phase noise at 10 kHz from a 2 GHz carrier [88].

It is noted that, if the target resonances are going to be on the order of 100 kHz, as suggested above, the target size, depending on the material, will generally be smaller unless relatively high order modes are used. The electromagnetic frequency, in this case, would have to be increase so that the electromagnetic wave can have appreciable interaction with the target. This would need to be considered in light of the application; for example, in a GPR or NDE configuration the frequency cannot be too high or loss in the soil or moist concrete becomes a problem. With some signal

generators, it also becomes more difficult to maintain low phase noise if the carrier frequency increases; for the generator in reference [88], if the carrier frequency is in the range 3-9 GHz, the SSB phase noise degrades to -110 dBc/Hz at 10 kHz offset.

The received electromagnetic signal is amplified and mixed down to baseband before being sent to the Doppler component detector. The signal levels obtained in Chapters VI and VII imply that an extremely sensitive detector must be used to extract the Doppler component. Since the Doppler shift is known a dual-phase lock-in amplifier may be used as the detector. This type of amplifier is also chosen for its ability to recognize signals of a particular frequency despite high noise levels. A block diagram of a basic single-phase lock-in amplifier is shown in Figure 9.2. The input signal is filtered to remove out of band noise and then mixed with a reference signal at the desired frequency. In this case, the reference signal is that which drives the acoustic transducer. The reference is phase shifted and then mixed with the filtered input. The mixer acts as a phase sensitive detector, producing an output whose average value is a function of the two input amplitudes and their relative phase. The output is low-pass filtered to recover the desired signal at DC. In a dual-phase system the input is also mixed with a reference signal that is shifted by 90° . By adding the magnitude of both signals, the dependence on phasing between the input and reference signals is removed.

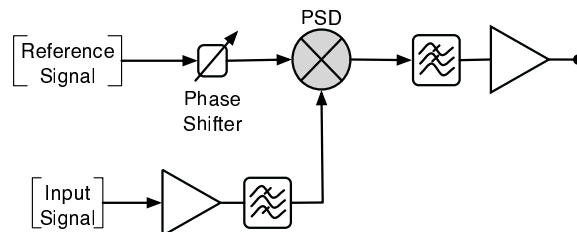


Figure 9.2: Block diagram of a basic lock-in amplifier.

A commercially available digital lock-in amplifier (SRS SR-850) operates from

0.001 Hz to 100 kHz, covering a portion of the acoustic frequency range of interest in this application [89]. This amplifier has 100 dB of dynamic reserve, meaning that it is capable of handling noise up to 100 dB higher than the desired signal before saturation occurs.

This chapter reviews basic requirements for an acousto-EM system. Further details depend on the application. Once a desired application is chosen, this information can be used as a guide in system development.

CHAPTER X

Antennas for Detection

This chapter focuses on antennas for electromagnetic detection in an acousto-EM system. Desirable features for the receiver include wide bandwidth, small size, and high efficiency. In an effort to maximize bandwidth volumetric sources, specifically dielectric resonator antennas (DRA), are used [90]. Three designs are have been completed. Two of the three will be covered in detail in this chapter. Details regarding the third design may be found in the Appendix.

The antenna designs presented in this chapter were initially intended for other applications instead of as part of an acousto-EM system. As a result, the designs may not be directly applicable to such systems. However, the basic principles used in their design can be applied to antennas designed for use in an acousto-EM system. For example, the design could be scaled to yield an antenna which operates at a frequency appropriate to a specific application. Or, the concepts used to increase the antenna bandwidth of these designs could be adapted to other types of antennas more suited to the desired acousto-EM application.

The first design achieves wider bandwidth by merging two resonant structures. The second design builds on this approach, adding addition resonances from parasitic elements, and it incorporates the bandwidth enhancing capabilities of magneto-

dielectric materials. The third design is an array of DRA's, which is especially relevant to the electromagnetic focusing described in Chapter VII.

10.1 Double-resonant DRA design

Antenna miniaturization is becoming increasingly important especially in wireless and low frequency applications. The demand for wireless technology has increased dramatically in the past decade. Antennas which are small, efficient, and integrable into mobile devices must be developed. Alternatively, as the frequency of operation is lowered, miniaturization techniques must be employed to keep antenna size practical. There are two primary techniques to achieve antenna miniaturization. The first is using novel topology to reduce the overall area consumed by the radiating structure. The second is using materials with permittivity, permeability, or both, greater than one; since wavelengths inside such materials are reduced, the characteristic size of the antenna decreases. This study uses the latter technique to achieve antenna miniaturization by employing a dielectric resonator as a superstrate for the slot antenna as shown in Figure 10.1. This increases the effective permittivity seen by the slot and lowers its resonant frequency. Truncating the dielectric superstrate yields a resonant structure called a dielectric resonator antenna. Dielectric resonator antennas are experiencing increased use in antenna applications due to favorable properties including low cost, inherently wide bandwidth, small size, and high efficiency due to the absence of conductors and surface wave losses. They are simple to integrate into existing fabrication technology and have a flexible design process with numerous design parameters, such as shape, size, aspect ratios, and permittivity. The current technique improves the bandwidth of these antennas without compromising their efficiency and other positive characteristics.

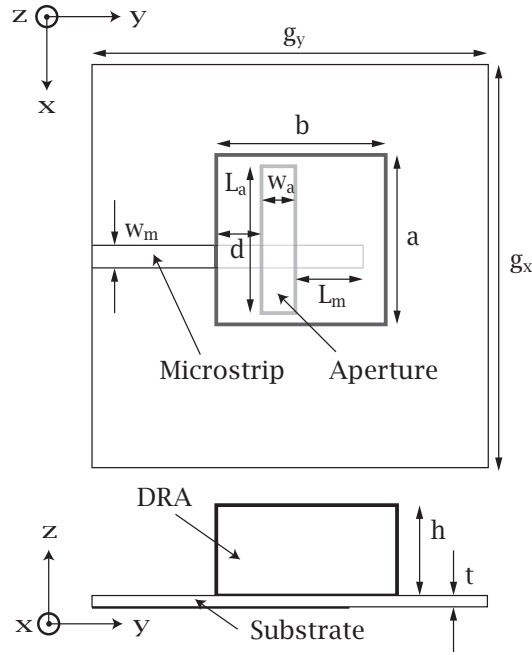


Figure 10.1: Diagram of antenna design. The dielectric resonator is coupled to a microstrip-fed slot in the ground plane.

It is known that miniaturization directly affects an antenna's ability to radiate. In [90] Wheeler constructs the radiation power factor (RPF) to quantify the radiation properties of electrically small antennas. The value, which is inversely related to Q , indicates the amount of real power radiated away from the antenna relative to the amount of reactive power which is stored in the antenna's near field. Wheeler derives a formulation of the RPF in terms of the volume of the antenna:

$$(10.1) \quad PF \propto \frac{V_a}{V_s}$$

where V_a represents the effective antenna volume, which is related to its physical volume, and V_s the volume of the radian sphere in terms of the free-space operational wavelength, $V_s = \frac{4\pi}{3}(\lambda/2\pi)^3$. Often miniaturized antennas, especially linear or surface radiators, which have small effective volumes exhibit poor radiation capability and tend to store energy in the near field surrounding them. For a volumetric source,

such as the dielectric resonator, the RPF is improved because V_a is much larger. The dielectric resonator can be modeled by an equivalent volumetric current source of the form

$$(10.2) \quad \mathbf{J}_v = j\omega\epsilon_o(\epsilon_r - 1)\mathbf{E}$$

where ϵ_r is the relative permittivity of the resonator and \mathbf{E} is the electric field inside the resonator. The DRA is a good radiator because it fills the radian sphere surrounding it, making $V_a \approx V_s$ depending on frequency. In the same way, the DRA improves the radiation power factor of the underlying slot antenna at its radiation frequency by more effectively filling its radian sphere, i.e. it fills the near field of the slot antenna, increasing its effective volume and the amount of real power radiated away from the antenna into the far field.

As the primary goal of this study is to improve bandwidth while maintaining small size, the relationship between the maximum possible bandwidth of an antenna relative to its size must be investigated. In 1948 Chu derived fundamental limitations on achievable bandwidth for a small antenna, or one which fits inside the radian sphere. His results show that as size is reduced, the maximum possible bandwidth decreases. If a multi-resonant structure is used these limitations, while qualitatively relevant, do not directly apply. This is justifiable by noting that in filter design many high-Q resonators can be used to achieve the desired wide bandwidth of operation. By applying this technique of merging the slot and DRA resonances bandwidths approaching and surpassing Chu's limit may be obtained. It is noted that the DRAs used in this study have moderate permittivity ($\epsilon_r = 12$) and do not adhere to the strict definition of a small antenna over the entire bandwidth. Using a higher permittivity DRA, however, in similar designs would allow the bandwidth to approach Chu's limit.

A miniaturized antenna figure of merit (MAFM) is defined to facilitate comparison between miniaturized antennas' performance. Comparison between antennas becomes difficult when size is reduced and other characteristics must be considered. This is especially true when multiple resonances are used to enhance bandwidth because Q becomes less well-defined. The MAFM is defined as follows:

$$(10.3) \quad MAFM_{dB} = 10 \log_{10} \left(\eta \cdot \frac{\Delta f}{f_c} \cdot \frac{\lambda}{D} \right) = \eta_{dB} + \left(\frac{\Delta f}{f_c} \right)_{dB} + \left(\frac{\lambda}{D} \right)_{dB}$$

where η is the antenna efficiency relating its gain and directivity at the operational frequency, Δf is the -10 dB bandwidth, f_c is the center frequency, D is the largest linear dimension of the antenna, and λ is the freespace wavelength. By simultaneously accounting for the efficiency, bandwidth, and miniaturization, the MAFM is a more comprehensive means of comparison between antennas. A metallic $\lambda/2$ dipole with 5% bandwidth and 99% efficiency, for example, has a MAFM of -0.04 dB - 13 dB + 3 dB = -10.04 dB. A 10 GHz patch antenna fabricated on duroid ($\epsilon_r = 2.2$) with 1% bandwidth and 86% efficiency has a MAFM of -15.9 dB. In Section 10.1.3, the MAFM for the proposed antennas is computed from measured results and is found to be near 0 dB.

Numerous studies on dielectric resonator antennas have been carried out. It is interesting to note that previous studies on DRA's neglect constructive use of the feed resonance which is inherently present in the system. McAllister, et al., mention the presence of the probe resonance in [91] but do not address its usefulness in achieving wide bandwidths. Designing the probe feed to optimize the bandwidth of the DRA resonance has been noted in [92, 93]; however, the probe's own resonance is not used. In this study, a probe feed was initially used to feed the DRA. However, the probe length was limited by the dielectric size and matching was sometimes difficult to achieve. In addition, the probe possesses large self-reactance at high

frequencies and is a source of ohmic loss [94]. A slot feed was adopted to simplify fabrication and improve matching to a 50Ω microstrip line. Low cross-polarization levels are also maintained by using a slot feed because both the slot and the DRA radiate as horizontal magnetic dipoles. Many other studies use a non-resonant slot to feed the dielectric resonator [95, 96, 97, 98]. As discussed, since multiple resonance systems are not subject to typical bandwidth limitations that afflict electrically small antennas, Chu's lower bound on Q is not a limiting factor on the bandwidth of the proposed structures.

The technique of merging the resonance of the feed mechanism with that of the radiating structure has been employed with other types of antennas, specifically aperture-fed microstrip patch antennas [99]. The benefits of DRA's over existing microstrip antennas which include wider bandwidth, higher efficiency, and more feeding options, encourage the extension of this principle to DRA's. Wideband DRA's have also been under development for some time; a review of many current designs may be found in [100]. Often resonator geometry is altered to maximize bandwidth. For example, [96, 93, 101, 92] study the impedance and radiation characteristics of triangular, conical, tetrahedral, and split cylindrical resonator geometries; 50% impedance-bandwidth using split cylindrical resonators has been reported. Notched rectangular DR structures have also been used to obtain impedance-bandwidths up to 28% [102] and multi-segment DRAs (MSDRA), in which layers of high permittivity dielectric are placed beneath the DRA to improve matching to the microstrip feed, offer bandwidths up to 20% [103]. These are more complex designs, however, and are more difficult to fabricate than the current method. It is noted that the proposed technique also has non-negligible back radiation making these designs more appropriate in applications which require a high front-to-back ratio.

Refinements in the design are carried out using the finite-difference time-domain method (FDTD). The effects of varying design parameters are investigated in a parametric study, the results of which are given in Section 10.1.2. Knowledge from this analysis is used to merge the two resonances in further design simulations. Two designs with bandwidths exceeding 25% are built; previous designs based on a single resonance and of comparable structural complexity exhibit much smaller bandwidths.

In Section 10.1.1 the antenna configuration is presented and the design variables are reviewed. In Section 10.1.2 a detailed parametric study is summarized and observed trends are given to aid in the design procedure. Finally, in Section 10.1.3 measurements of fabricated designs are given and compared with simulation results.

10.1.1 Concept and Design

The DRA and slot are both resonant structures. Together they yield a double resonant structure with low cross-polarization levels and identical radiation patterns. With proper design, the two resonances can be merged to achieve wide bandwidth. The design process is initiated with a choice of the desired frequency of operation. The corresponding size of resonator can be approximated using various methods some of which are evaluated in [104, 105]. In this study the conventional dielectric waveguide model (CDWM) is used. The resonant frequency of the slot can be approximated using the length of the slot and the permittivity of the dielectric resonator. In general, the relative frequencies of the resonances are particular to the design. In this study the lower resonance is associated with the feed mechanism while the upper resonance results from the resonator itself.

The DR is coupled to a microstrip-fed slot in the ground plane, as shown in Figure 10.1. To a first order approximation the DRA and slot resonance may be designed independently of each other. However, in reality the resonances are coupled and even

minor parameter variations affect loading and matching at both resonances. There are many parameters which can be varied to achieve matching and wide bandwidth; these include, among others, slot dimension, relative position of the slot and the DRA, and microstrip parameters. In this section, the design variations employed in the study are evaluated from a theoretical point of view. The effect of slot position and size on resonance location and matching will first be discussed; then the DRA parameters will be evaluated. A more detailed review of the observed effects of varying single parameters in simulation is given in the next section.

The size and position of the slot are varied in order to improve matching and control resonance frequency. The slot resonance occurs at approximately $\lambda_g/2$, where $\lambda_g = \lambda_o/\sqrt{\mu_{eff}\epsilon_{eff}}$ is the wavelength inside the dielectric material. The slot sees an effective permittivity

$$(10.4) \quad \epsilon_{eff} = \frac{H_{total}}{h/\epsilon_{dra} + t/\epsilon_{ss}}$$

[103], where H_{total} is the total height of the antenna structure, h is the height of the DRA with permittivity ϵ_{dra} , and t is the thickness of the substrate of permittivity ϵ_{ss} . Other design parameters affect the slot resonance frequency as well but to a lesser degree. The width of the slot is kept small relative to the wavelengths of operation; therefore, the electric field is primarily in the \hat{y} direction. The slot can be modeled by a magnetic current source, $\mathbf{M} = -\hat{z} \times E_a \hat{y}$, where $E_a \hat{y}$ is the electric field in the slot induced by currents on the ground plane. In this case a magnetic current source lies along the \hat{x} direction along the bottom of the DRA.

It has been shown that the slot and antenna appear as a series load along a transmission line which is terminated in an open circuit at the end of the microstrip [58]. Matching is achieved when the input reactance is completely compensated for and the input impedance has only a resistive component. The reactive portion of the

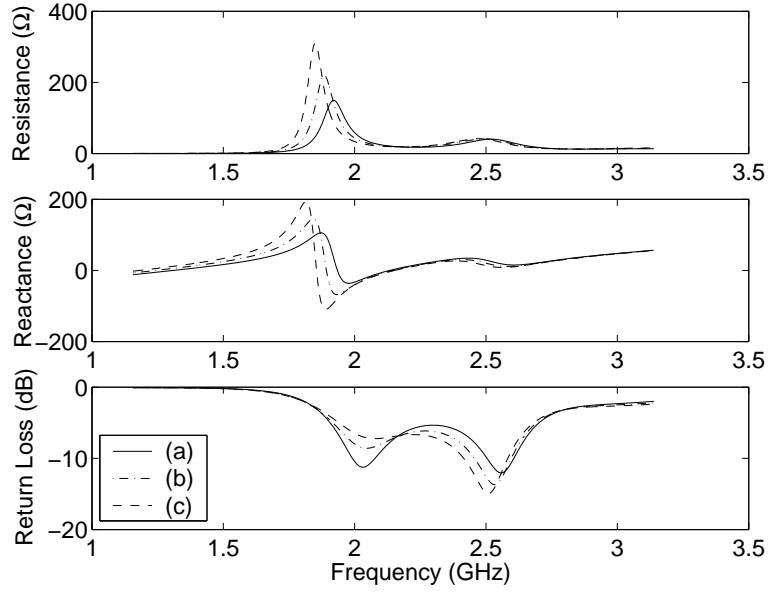


Figure 10.2: The length of the microstrip is varied. $L_s = 2.33$ cm, $w_s = 0.5$ cm, and $d = 0.33$ cm
(a) $L_m = 0.67$ cm (b) $L_m = 0.83$ cm (c) $L_m = 1$ cm

input impedance can be compensated for using the appropriate length of microstrip line which acts as an open stub tuner. It is observed in Figure 10.2 the microstrip length plays a minor role in resonance location as well. However, as microstrip length affects matching this is a difficult parameter with which to control resonances beyond minor adjustments. Moving the slot in the \hat{y} direction, which in effect changes the length of the microstrip but also affects coupling to the DRA, is observed to move the resonances more effectively as seen in Figure 10.5.

The real part of the input impedance is affected by moving the slot in the \hat{x} direction, perpendicular to the microstrip. The electric field in the slot, $E_a\hat{y}$, and the resulting equivalent magnetic current source, must go to zero at the ends of the slot due to the boundary condition on tangential components of the electric field. The current, \mathbf{J} , on the ground plane does the reverse, reaching its maximum around the edges of the slot and going to zero in the middle. The resistance varies as the ratio of the magnetic current to the physical electric current over the length of the slot;

therefore, by placing the slot at the correct \hat{x} location matching to any resistance can theoretically be realized. Movement along the \hat{x} direction is not observed to affect resonance location. In this study the DRA is moved with the slot, and remains covering the slot where possible.

The approximate expressions for each field component inside the resonator may be obtained from the electric vector potential and the boundary conditions for the CDWM. The formulas are here reviewed in brief; additional information may be found in [95]. With reference to Figure 10.1, and taking the origin at the center of the DRA, perfect magnetic walls are assumed to lie in the x - z plane at $y = -b/2$ and at $y = b/2$, and in the y - z plane at $x = -a/2$ and $x = a/2$. Continuity of the tangential fields is enforced at $z = h$ and, by image theory, at $z = -h$. The electric vector potential, \mathbf{F} , for the TE_{111}^z mode is then given by

$$(10.5) \quad i\mathbf{F} = F_z \hat{z} = A \cos(k_x x) \cos(k_y y) \sin(k_z z)$$

where A is a constant and the wavenumbers are as follows [106]:

$$(10.6) \quad k_x = \frac{n\pi}{a} \quad k_y = \frac{m\pi}{b} \quad k_z \tan(k_z h) = \frac{\mu_{dra}}{\mu_o} \sqrt{k_x^2 + k_y^2 - k_o^2}$$

where k_o is the free space wavenumber, μ_{dra} is the permeability of the DRA, and k_x , k_y , k_z are the wavenumbers in the x , y , and z directions, respectively. By replacing μ with ϵ in these equations, analogous expressions for TM modes may be found. The wavenumbers satisfy the following characteristic equation:

$$(10.7) \quad k_x^2 + k_y^2 + k_z^2 = \mu_{r,dra} \epsilon_{r,dra} k_o^2$$

where $\mu_{r,dra}$ and $\epsilon_{r,dra}$ are the relative permeability and permittivity of the medium and the remaining variables are the same as above. These equations may be used to relate size with operational frequency. For example, the fabricated DRA discussed

in Section 10.1.3 has dimensions $a = b = 2.67$ cm and $h = 1.67$ cm resulting in a resonant frequency of 2.49 GHz, which is within 5% of the measured value.

Assuming matching to the resonator is adequate the resulting magnetic dipole current source lies along the \hat{x} direction and excites the TE_{111}^x mode of the DRA. In reality, this is a hybrid mode so E_x is small but non-zero.

Consideration should be given to the choice of material permittivity to use in the DRA; along with operational frequency this parameter determines the antenna size. High permittivity materials, while allowing smaller antenna size, make it more difficult to merge resonances as they result in narrower bandwidths. As shown in [95], the quality factor, $Q \propto \epsilon_r^{3/2}$, where ϵ_r is the relative permittivity of the resonator; therefore, bandwidth which is inversely related to Q decreases as permittivity increases. The DRA permittivity also determines the effective permittivity seen by the slot, effecting its resonant frequency and the input impedance as well [98].

As expected, ground plane size significantly affects the results. In Section 10.1.3, for example, the second fabricated antenna on the 8 cm ground plane was adopted from the first design on a smaller ground plane. The design parameters of the second design had to be changed significantly in order to achieve matching and merge the resonances.

10.1.2 Parametric Study

This section gives the observed simulation results when the parameters discussed in Section 10.1.1 are systematically varied. Simulations are carried out using the finite-difference time-domain approach [107]. In reference to Figure 10.1, a and b are the x and y dimensions of the dielectric resonator, respectively, and g_x and g_y are those of the ground plane. The height of the DRA is denoted by h and the thickness of the substrate by t . The microstrip line has width w_m ; L_m is the microstrip length

beyond the slot. L_s is the slot length and w_s is the width. The distance from the edge of the DRA to the edge of the slot on the feed side is d . Throughout this analysis the DRA is centered over the slot along the x direction.

All of the simulated designs in this section, except where otherwise stated, have dielectric resonators that are 2.67 cm square in the x - y plane and 1.67 cm tall; a permittivity of 12 is used with a loss tangent of 5.6×10^{-4} . The ground plane is 5.66 cm square with a substrate thickness of 0.167 cm, $\epsilon_r = 2.2$, and $\tan \delta_e = 5.6 \times 10^{-4}$. The microstrip feeding the slot is 0.5 cm wide; its length varies with the design.

Slot Dimensions

In Figure 10.3, the variation of return loss is shown as the slot length, L_s (see Figure 10.1), is varied from 3.33 cm to 2 cm while the width, w_s , is maintained at 0.5 cm. All other parameters such as resonator size and position are kept constant. In the first case the slot extends beyond the dielectric for 0.33 cm on each end; in the last three designs it remains covered by the DRA. The upper resonance mainly stays fixed at the same frequency while the lower resonance shifts up with decreasing slot length. Similar results are obtained when the slot width, w_s , is varied from 0.33 cm to 0.67 cm while the length is maintained at 2.33 cm. In agreement with [108], slot width has a smaller effect on matching than slot length; however, it too affects the lower resonance. These results provide evidence that the lower frequency resonance is due to radiation from the coupling slot.

Resonator Dimensions

In Figure 10.4, the dimensions of the DRA are varied; all designs have a 6 cm square ground plane, dielectric resonator height 1.67 cm, and slot dimensions 2 cm

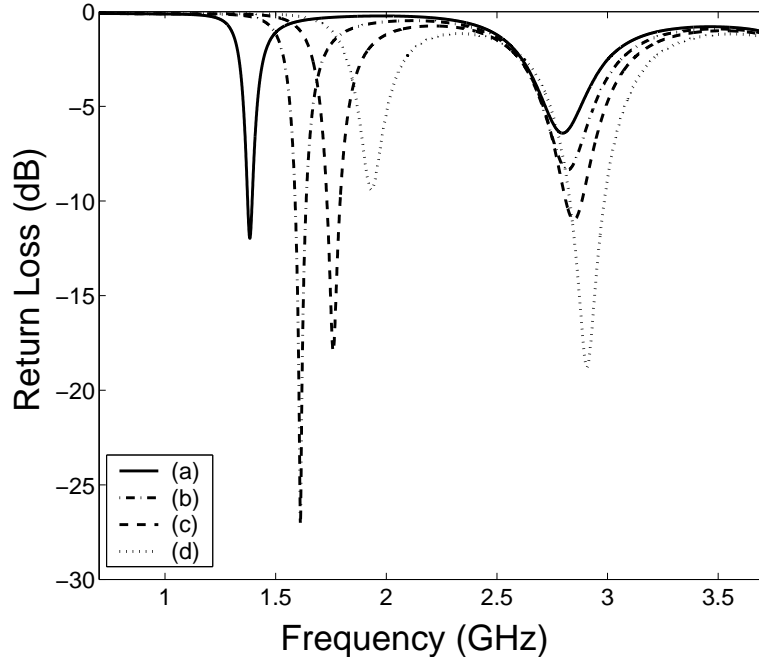


Figure 10.3: The length of the slot is varied. $w_s = 0.5$ cm, $d = 1$ cm, $L_m = 0.167$ cm (a) $L_s = 3.33$ cm, 0.33 cm longer on both ends of the DRA (b) $L_s = 2.67$ cm, the same size as the DRA (c) $L_s = 2.33$ cm, 0.167 cm shorter than the DRA at both ends (d) $L_s = 2$ cm, 0.33 cm shorter than the DRA at both ends.

by 0.5 cm. The result from a 2.67 cm square DRA is shown in (a). In the structure in curve (b), $a = 3.34$ cm and b remains 2.67 cm in y . In that of curve (c), $b = 3.34$ cm and $a = 2.67$ cm. Finally, (d) corresponds to a 3.34 cm square resonator. Figure 10.4 also demonstrates that the TE_{111}^x mode is excited by the slot which is expected given the orientation of the slot in the ground plane. Similar results are obtained when the DRA height, h , is varied while a and b remain 2.67 cm each. From this evidence it is concluded that the upper resonance is predominantly effected by the dielectric resonator dimensions.

Microstrip Length

In addition to affecting the reactive portion of the input impedance the length of the microstrip also influences the relative position of the resonances. Increasing its length is observed to merge the two resonances while decreasing it tends to sepa-

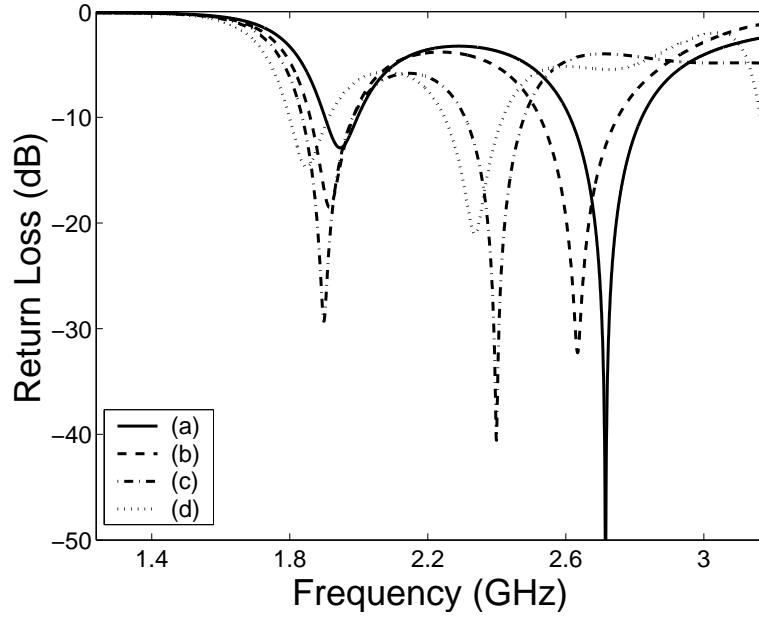


Figure 10.4: The x and y dimensions of the DRA are varied. The height, h , remains at 1.67 cm, $L_s = 2$ cm, and $w_s = 0.5$ cm. (a) $a = b = 2.67$ cm (b) $a = 3.34$ cm, $b = 2.67$ cm (c) $a = 2.67$ cm, $b = 3.34$ cm (d) $a = b = 3.34$ cm. The ground plane is 6 cm square.

rate them. Figure 10.2 illustrates the effect of microstrip length on input impedance and resonance location. As the microstrip length is increased both the input resistance and reactance associated with the first resonance increase resulting in poorer impedance matching.

Figure 10.5 shows the result if the position of the slot is moved back along the microstrip, corresponding to changing d in Figure 10.1; this is similar to increasing the length of the microstrip however the interaction between the DRA and the slot is affected as well. In simulation moving the slot back along the microstrip effected the relative resonance positions more than altering the length of the microstrip alone. In all cases shown the slot remains under the DRA, which is left in its original position. Note that the resonances could be over-merged, as in the last case in Figure 10.5, however, separating them leads to larger bandwidths.

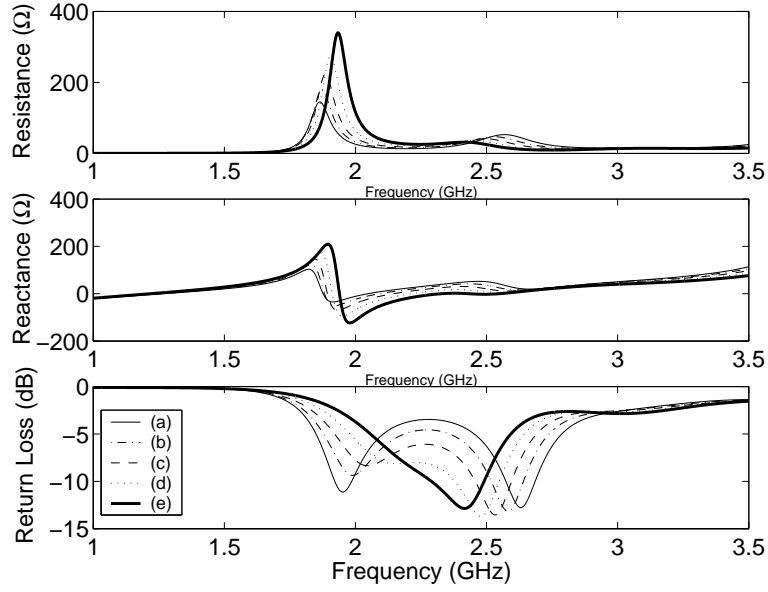


Figure 10.5: The slot, $L_s = 2$ cm, $w_s = 0.5$ cm, is moved back along the microstrip in the $-y$ direction. (a) $d = 0.5$ cm, $L_m = 0.67$ cm (b) $d = 0.42$ cm, $L_m = 0.75$ cm (c) $d = 0.33$ cm, $L_m = 0.83$ cm (d) $d = 0.25$ cm, $L_m = 0.92$ cm (e) $d = 0.167$ cm, $L_m = 1$ cm

10.1.3 Measured Results

Two antennas similar to those simulated above are fabricated and measured. In both cases, the DRA, made from TransTech's SMAT12, is 2.67 cm square by 1.67 cm tall and have $\epsilon_r = 12$ with $\tan \delta_e < 1.5 \times 10^{-4}$. The substrate is 1.575 mm thick Rogers RT5880 ($\epsilon_r = 2.2$, $\tan \delta_e = 4-9 \times 10^{-4}$). The DRA and slot are offset in the $-x$ direction perpendicular to the microstrip; the slot remains centered in x under the DRA. The first antenna is on a 5.5 cm square ground plane while the second is on an 8 cm square. The larger ground plane design was made to improve the radiation patterns and the front-to-back ratio.

For the antenna with the 5.5 cm square ground plane, the microstrip is 0.5 cm wide, $L_m = 0.33$ cm, and $d = 0.25$ cm. The slot is 2 cm long by 0.5 cm wide. The simulated and measured return losses are shown in Figure 10.6. The measured 10 dB bandwidth is 24.7%. The lack of agreement between the return losses of the

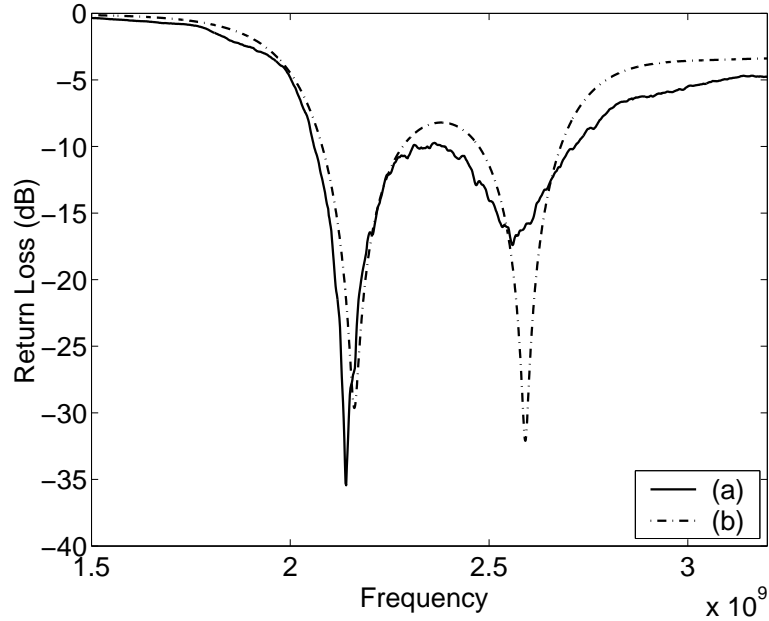


Figure 10.6: Return loss for the 5.5 cm ground plane design (a) measured (b) simulated

simulated and measured designs may be due to an air gap between the ground plane and the resonator which is absent in simulations. The effect of such an air gap is studied extensively in [109, 110, 111]. Also, the simulation parameters and lengths are limited by the resolution of the FDTD grid. Therefore, they are not always equal to the physical antenna dimensions.

The radiation patterns in the E and H planes at the DRA resonance are shown in Figure 10.7. The simulated patterns are shown as well; the bold lines correspond to the measurements. Since both the slot and the lowest order modes of the DRA radiate as horizontal magnetic dipoles, low cross-pol levels are maintained. Lower cross-pol levels are possible using a slot which is centered under the DRA in the \hat{y} direction; this would mitigate the excitation of other resonator modes which contribute to cross-pol levels. The E-plane asymmetry is primarily an effect of the presence of the coaxial feed on the side of the ground plane. The poor H-plane pattern symmetry and large back radiation are mostly a result of the small size of the ground plane. The larger,

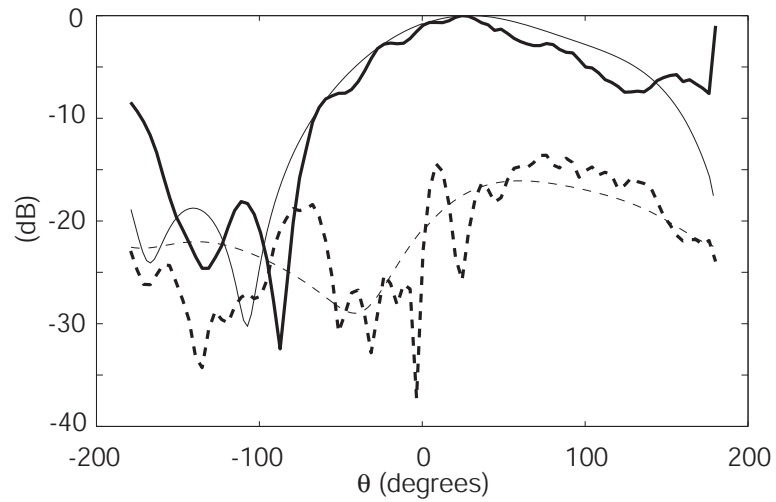
8 cm design patterns are much improved. In addition, the possible presence of other resonator modes due to the offset slot contributes to pattern asymmetries which are still present in the 8 cm case.

The gain at the lower and upper resonance frequencies is approximately 4.6 dBi and 2.8 dBi, respectively. Using $D = 2.7$ cm, the resonator size, the MAFM becomes 1.05 dB at the lower resonance and -0.19 dB at the upper resonance. These values demonstrate that the design maintains reasonable efficiency while simultaneously providing enhanced bandwidth and miniaturization.

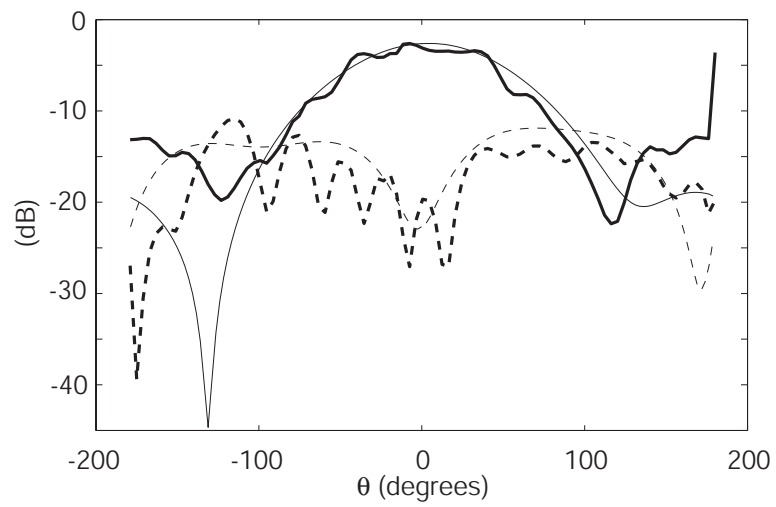
For the antenna with the 8 cm square ground plane, the microstrip is 0.5 cm wide, $L_m = 0.58$ cm, and $d = 1.2$ mm. The slot dimensions are 2.1 cm by 0.6 cm. The simulated and measured return losses are shown in Figure 10.8. The measured 10 dB bandwidth is 29%; the simulated 10 dB bandwidth does not correspond to the merged resonance bandwidth. Disagreement between simulated and measured return loss is due to the reasons discussed in the 5.5 cm design. However, in this case, the problem of the air gap between the ground plane and the resonator is exacerbated due to the larger size of the flexible ground plane.

Measured antenna patterns for the 8 cm design at both resonance frequencies in the E-plane are shown in Figure 10.9; those of the H-plane are shown in Figure 10.10. Again, the E-plane pattern asymmetry is, in part, due to the presence of the coaxial feed to the microstrip. Note the low cross-pol levels. As discussed in [95] and [108], the backlobe radiation usually present with a slot antenna is reduced by the DRA which radiates more effectively above the ground plane. This can be seen in the slot resonance frequency measurements which show less back radiation than would a regular slot antenna without the DRA.

The gain at the lower and upper resonant frequencies is approximately 4.6 dBi



(a) E-plane



(b) H-plane

Figure 10.7: E-plane and H-plane antenna patterns for the 5.5 cm ground plane design at the DRA resonance of $f = 2.5$ GHz. Measurements are shown in bold and simulations in regular line weight.

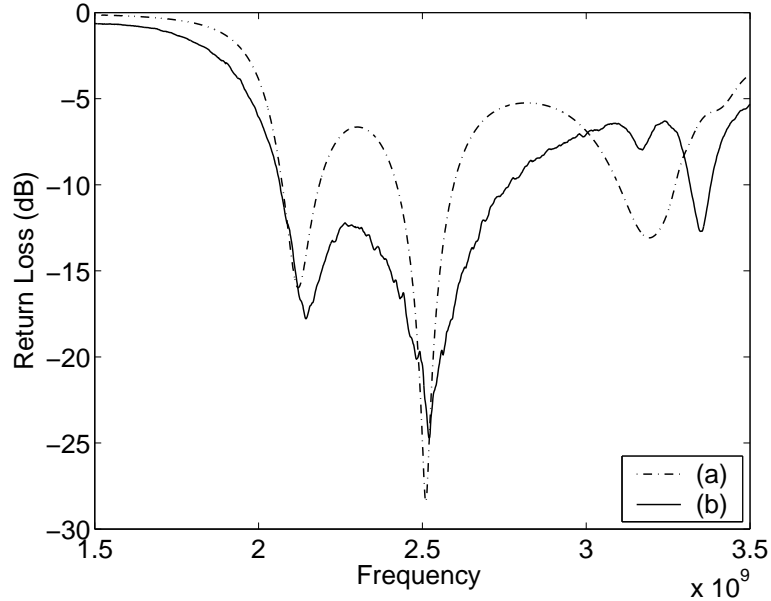
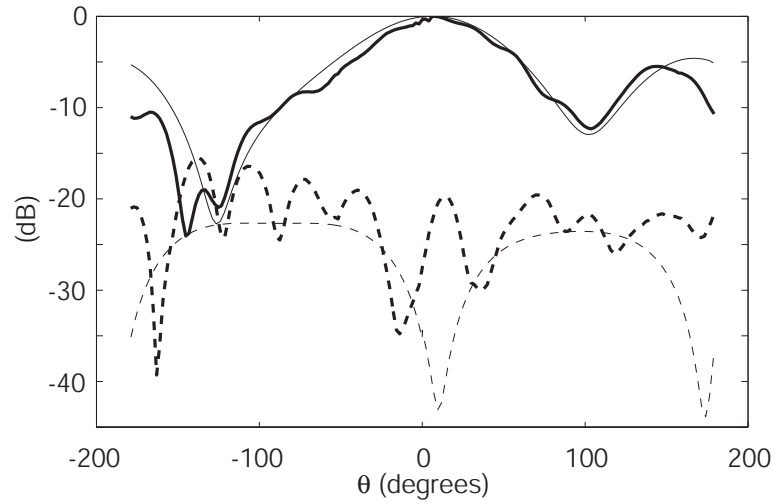


Figure 10.8: Return loss for the 8 cm ground plane design (a) simulated (b) measured and 4 dBi, respectively. Again using $D = 2.7$ cm, the MAFM values are 0.41 dB and -0.44 dB at the lower and upper resonance frequencies, respectively.

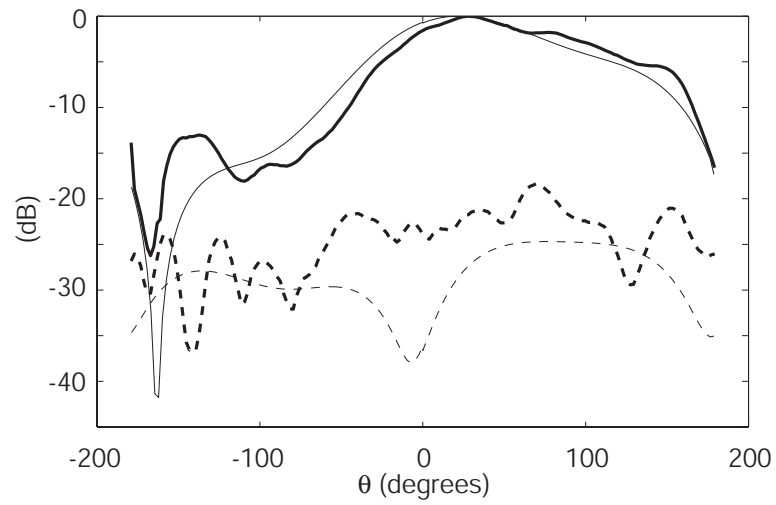
10.1.4 Summary

In this design, it is shown that two resonances inherent to all DRA designs with resonant feed structures can be controlled for bandwidth optimization. A new, comprehensive figure of merit, or MAFM, is defined to allow comparison between various miniaturized antennas. Values obtained for the present antennas demonstrate that they provide enhanced bandwidth and miniaturization without degradation in gain. In addition, the similarity of the slot and DRA radiation characteristics allows preservation of the radiation patterns and polarization over the entire bandwidth. The design process is reviewed and the effects of varying design parameters are summarized. Two antennas exhibiting over 25% bandwidth and gain exceeding 4 dBi are built and characterized.

Further increases in bandwidth may be obtained by incorporating the MSDRA

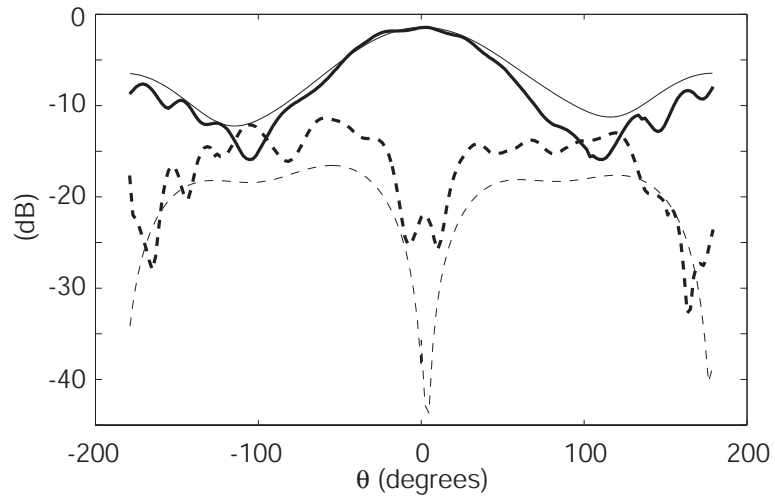


(a) Slot Resonance $f = 2.17$ GHz

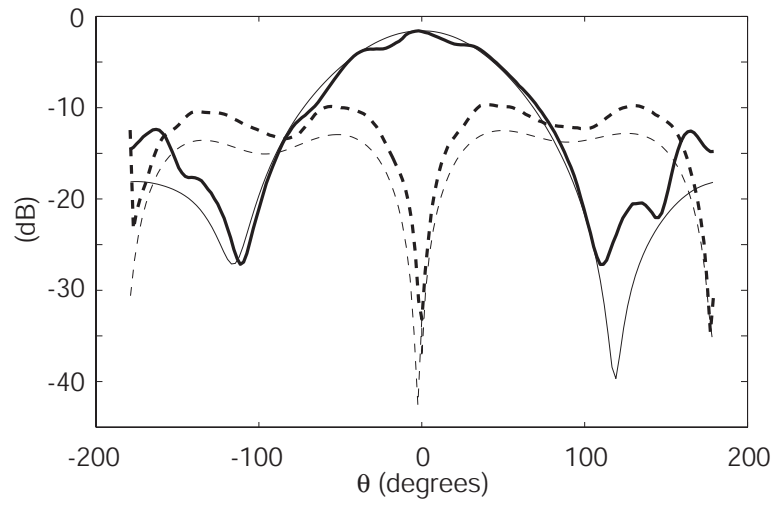


(b) DRA Resonance $f = 2.57$ GHz

Figure 10.9: E-plane antenna patterns for the 8 cm ground plane design (a) $f = 2.17$ GHz (b) $f = 2.57$ GHz. Measurements are shown in bold and simulations are shown in regular line weight.



(a) Slot Resonance $f = 2.17$ GHz



(b) DRA Resonance $f = 2.57$ GHz

Figure 10.10: H-plane antenna patterns for the 8 cm ground plane design (a) $f = 2.17$ GHz (b) $f = 2.57$ GHz. Measurements are shown in bold.

technique referenced earlier and using a layer of higher permittivity dielectric on the bottom on the DRA, shifting the lower, slot resonance further down in frequency. The next antenna design also uses the bandwidth enhancing properties of magneto-dielectric metamaterials with this technique to yield extremely wide bandwidths [112, 107].

10.2 Magneto-dielectric resonator antenna design

This UHF antenna is designed to meet the stringent requirements for satellite communications of simultaneous compact size, high bandwidth, high to moderate efficiency, and circular polarization operation. Percentage bandwidth values in excess of 50% for an antenna with a maximum dimension of 0.15λ are obtained. The radiating structure is made up of layered magneto-dielectric material with proper design of permittivity and permeability values forming a magneto-dielectric resonator antenna (MDRA). Noting that miniaturization and wave impedance in the MDRA are, respectively, proportional to the square-root of the product and ratio of the permeability and permittivity, moderate values of permittivity and permeability are used to enhance the bandwidth while achieving considerable miniaturization. The previous approach used to increase the bandwidth of a DRA is extended in this design, where a resonant feed and many parasitic elements are integrated into the MDRA structure. Square symmetry of the MDRA is used to obtain circular polarization operation. A prototype small UHF antenna operating over 240MHz-420MHz with a linear dimension smaller than 0.15λ at the lowest frequency is fabricated and tested. This design is described in detail in the Appendix.

10.3 DRA Array Design

10.3.1 Design Background and Motivation

The primary purpose of this research is to demonstrate the application of ceramic stereolithographic (CSLA) processing to the fabrication of dielectric antenna arrays. Recent research efforts have developed stereolithographic prototyping methods that achieve a dense, entirely ceramic end product. CSLA is a fully 3D additive layer-by-layer fabrication process that constructs parts from a photoreactive ceramic/monomer suspension. Since many ceramics exhibit low loss characteristics through millimeter-wave (MMW) frequencies and above, CSLA has enabled a range of solutions for MMW applications. It is an ideal process for monolithic construction of MMW subsystems composed of all-dielectric resonators, filters, waveguides, and antennas. Recently CSLA has successfully been employed to fabricate the first ceramic Luneberg lens [113]. The variable dielectric profile of the Luneberg lens is realized by controlling the ceramic volume fraction through minor alterations to an isotropic periodic lattice. The initial design, as presented in the following, is not immediately useful in the focusing approach outlined previously at the end of Chapter VII. However, this design demonstrates how CSLA could be used to fabricate an array specifically designed for that application.

Antenna arrays are good candidates for stereolithographic fabrication because of the increase in both difficulty and cost of individual element placement and bonding with increasing frequency. For example, automotive radar systems operating around 75 GHz are often implemented using printed circuit technology with patch antennas as radiating elements. Although patch arrays are both low-cost and low profile, they are undesirable at high frequencies due to their low radiation efficiency. The present approach combines the advantages of the monolithic structure resulting from

stereolithographic processing and the high radiation efficiency of ceramic DRAs. Such arrays can be fed by an elaborate dielectric waveguide corporate feed or by a traditional microstrip feed network.

The array elements shown in this work are rectangular dielectric resonator antennas (RDRA). The basic array is a four-by-four element configuration. A larger, eight-by-eight design is made using the four-by-four arrays as building blocks. For the sake of simplicity, a microstrip corporate feed network is used to uniformly excite the array. In the following, a review of the design process for the antenna elements and the feed network is provided. Return loss and pattern measurement results are also given.

10.3.2 Ceramic Stereolithography

In CSLA processing a photoreactive ceramic suspension in monomer is cured using a UV laser over a prescribed area. This step is repeated layer-by-layer while the part is gradually submerged, creating a three-dimensional “green” part, which has a high volume fraction of ceramic. The remaining polymer is then removed through a binder-burnout at 350°-450° C and sintering at 1600° C [114]. The result is a pure ceramic structure.

The ceramic material used in the fabrication process for the array is 99.8% alumina (Al_2O_3). Alumina has a loss tangent on the order of 10^{-4} and a permittivity of 9.7 through Ka-band. While the effective dielectric constant of the resonators may be altered by latent porosity or delamination errors, the biggest constraint on the DRAs is the warpage introduced by the binder-burnout process.

10.3.3 DRA Array Elements

DRAs' high efficiency and low profile make them attractive candidates for applications at microwave and millimeter-wave frequencies. In this case, RDRA's are also chosen as the antenna elements because they are able to provide fractional bandwidths on the order of 10% for materials with moderate relative permittivity values ($\epsilon_r \sim 10$ or lower) [115]. This allows greater design flexibility and improved operational bandwidth for the array. Using the dielectric waveguide model [116] and the ceramic permittivity, the elements' resonant frequency is predicted to be between 19 and 20 GHz for resonators that are 3.6 mm square by 1.8 mm tall.

The element spacing is 0.8λ at an operating frequency of 20 GHz. A monolithic four by four array structure is obtained by using thin ceramic support beams between adjacent RDRA elements. Two support beams with cross-sectional dimensions of 0.7 mm square are located on each side of the RDRA, connecting it to its nearest neighbors. It is assumed that the supports have minimal effect on the radiation pattern and input impedance of the elements; simulation results confirm this assumption. Figure 10.11 is a photograph of the CSLA fabricated four-by-four array; one cell is also shown in detail with the dimensions of the RDRA, coupling aperture, and supports.

10.3.4 Microstrip Corporate Feed Network

Uniform element excitation is achieved using a corporate feed network and aperture coupling between the printed circuit and ceramic dielectric structure. Although the corporate feed suffers from low efficiency caused by long path lengths and reflections at the T-junctions, it is chosen in this study for its simplicity.

One quarter of the eight-by-eight feed network is shown in Figure 10.12; the design

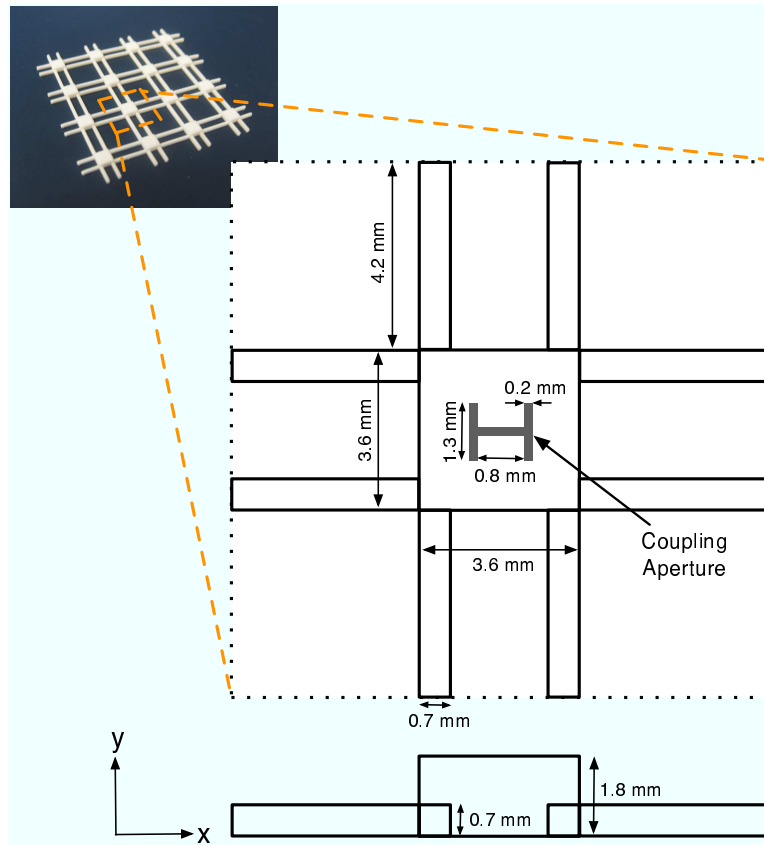


Figure 10.11: Monolithic four-by-four array of RDRA's fabricated using CSLA. One cell of the array is shown in detail with the dimensions of the RDRA, supports, and coupling aperture.

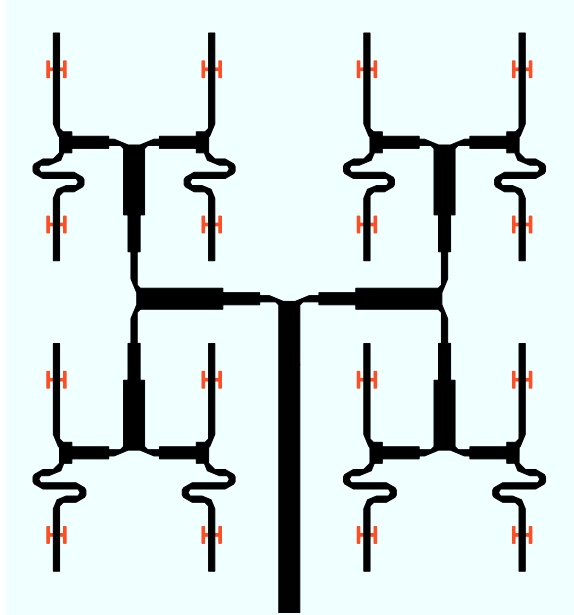


Figure 10.12: Four-by-four microstrip feed network with dogbone-shaped coupling apertures. The design is replicated to feed the eight-by-eight array.

is replicated to feed the sixty-four RDRA elements. A 50Ω line is used at the input while 100Ω line feeds each element. To achieve uniform phase distribution, the lower element of each pair of RDRA's is fed using an extra microstrip line length of 180° . The microstrip design is fabricated on $20mil$ Roger's RT5880/Duroid ($\epsilon_r = 2.2$, $\tan \delta_e = 0.0009$).

The coupling apertures, which are dogbone-shaped, are centered under the RDRA's. As reported in [117] the dogbone shape increases coupling by allowing a more uniform field distribution than a rectangular aperture. In addition, this geometry reduces back-radiation. The dimensions of the coupling apertures are shown in Figure 10.11.

10.3.5 Simulation Notes

The four-by-four microstrip feed network is simulated using Agilent Advanced Design System (ADS). The simulation provides a means of checking uniformity in feeding amplitude and phase across the array. A single antenna element with a microstrip feed and ground plane is then modeled in Ansoft High Frequency Structure

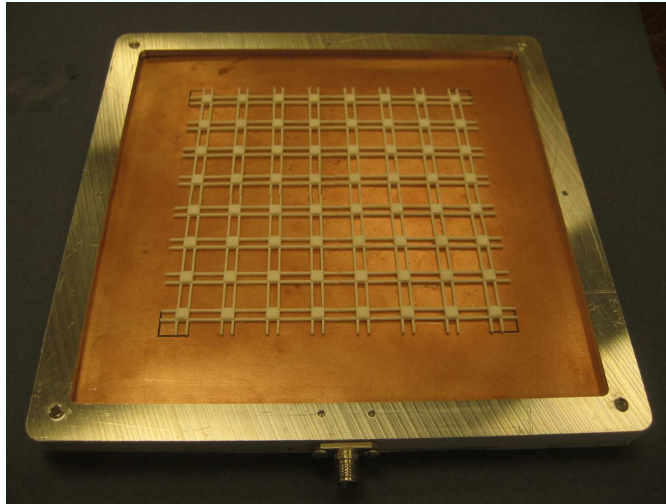


Figure 10.13: The eight by eight array in the measurement fixture. Copper tape (not shown) is used around the border of the frame to ensure electrical contact with the ground plane.

Simulator (HFSS). The aperture geometry and open-circuit microstrip stub length necessary to obtain a sufficient input match are determined. The four by four array is then simulated in HFSS by importing the feed network from ADS and including the remaining antenna components. The entire eight-by-eight configuration is not simulated because of the required computational effort.

10.3.6 Assembly

An aluminum fixture has been built in order to facilitate pattern measurement, keep the substrate flat, and simplify the coaxial to microstrip transition at the input. The arrays are attached by the supports to the ground plane of the substrate. The substrate is held in the measurement fixture with screws. Silver epoxy is also used around the frame to ensure electrical contact with the ground plane. Simulation and measurements indicate that the frame has a tendency to increase the sidelobe level. Figure 10.13 is a photograph of the eight by eight array in the measurement fixture.

A small air gap between the ceramic array and the ground plane is a potential problem that is not included in simulation. The gap is caused by the combination of

substrate warping and lack of flatness on the bottom of the arrays. During assembly, pressure is applied to establish contact at each element and minimize the air gap, effectively molding the flexible substrate material to whatever curvature exists on the bottom of the array. The air gap is estimated to be smaller than $25\mu\text{m}$.

To protect the feed and eliminate the possibility of any back-radiation, an aluminum plate is screwed onto the back of the aluminum fixture. The plate is approximately 3 mm away from the microstrip. The return loss does not significantly change when the plate is in place, indicating that the currents on the microstrip are not significantly altered by its presence.

10.3.7 Measurement Results

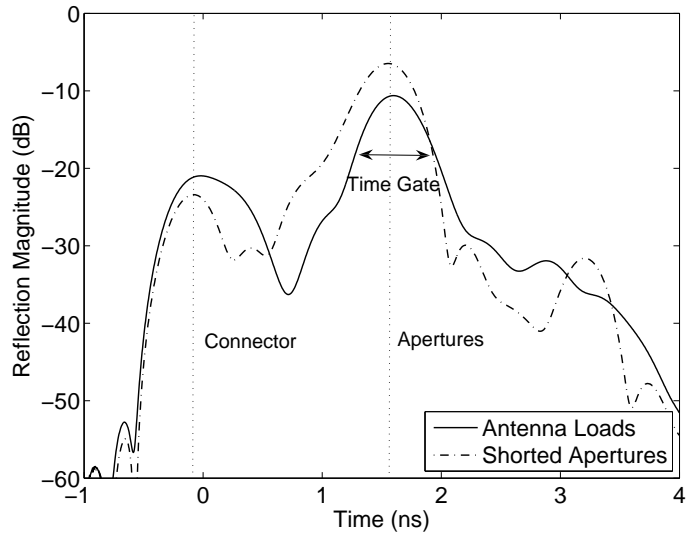
The array return loss was measured using an Agilent 8722ES vector network analyzer. The loss in the feed network is estimated using time domain measurements. A return loss measurement is done with the coupling apertures short-circuited, before the RDRA arrays are glued in place. The results are shown as the dashed curve in Figure 10.14(a); the corresponding frequency range is 17.5-21 GHz. Using the magnitude of the reflection from the shorted apertures, along with the magnitude of the reflection at the input connector, the loss in the feed network is estimated to be 3.2 dB.

The measured return loss with and without time gating for the array is shown in Figure 10.14(b). In the first curve, corresponding to no time gating, achieving a wideband match that is better than 10 dB is difficult because of reflections within the feed network. The nulls occur approximately every 600 MHz, corresponding to a microstrip length of about 20 cm, or about the total distance between the coaxial connector and the RDRA's aperture. The second, bold curve in Figure 10.14(b) is the return loss after time gating the reflected signal. As indicated by the time domain

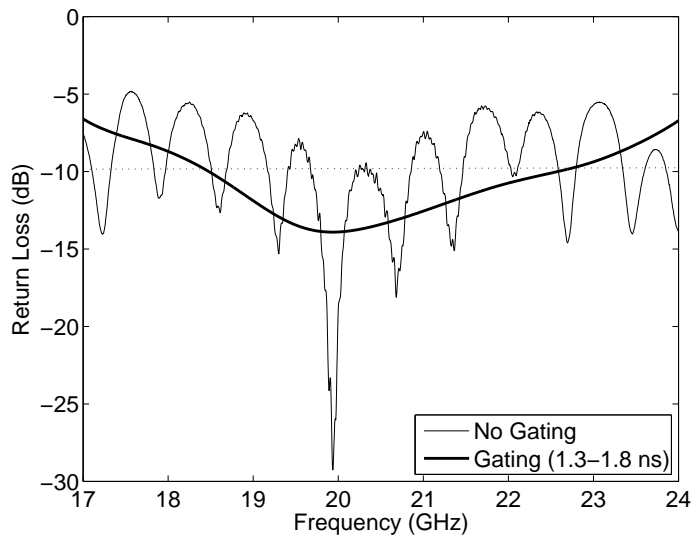
measurement with the antenna loads in place (the solid curve in Figure 10.14(a)), the time gate surrounds the peak corresponding to reflections from the RDRA's (1.3-1.8 ns). The match to the RDRA elements is found to be approximately 8 dB after measuring 6.4 dB of total loss in the round trip from the coaxial connector to the RDRA feed points. As mentioned, the lack of a perfect match can be attributed to the existence of very small air gaps, which seem nearly unavoidable over such a large area.

The radiation patterns of the array in the principal planes are measured in the anechoic chamber at the University of Michigan. The measured E (y - z) and H (x - y) plane patterns at 20 GHz are shown in Figure 10.15. The beamwidth is approximately 9° . The sidelobe level is -12 dB in the E plane and -10 dB in the H plane. A cause of higher than expected sidelobes can be attributed to the metallic frame and residual phase and amplitude errors introduced by the airgaps. It was verified that once the frame was covered by absorbers the side-lobe levels could be reduced slightly (1-2 dB).

The observed pattern asymmetry is also a result of the residual errors in feeding phase and amplitude. The measured gain is 21.3 dBi. For reference, an aperture antenna of the same size and an aperture efficiency of 81% would have about 26 dB of gain [106]. The 4.7 dB difference is due to losses in the feed network (3.2 dB) and inadequate matching at the antenna elements caused by array misalignment and the air gap. The ceramic RDRA elements contribute negligible loss. To make the array less susceptible to residual feeding errors and to the effects of air gaps, smaller element spacing is recommended.



(a) Time domain reflections of feed network with shorted coupling apertures and with antenna loads.



(b) Return loss of the eight-by-eight array in the measurement fixture with the back plate.

Figure 10.14: Measurement results for the RDRA array.

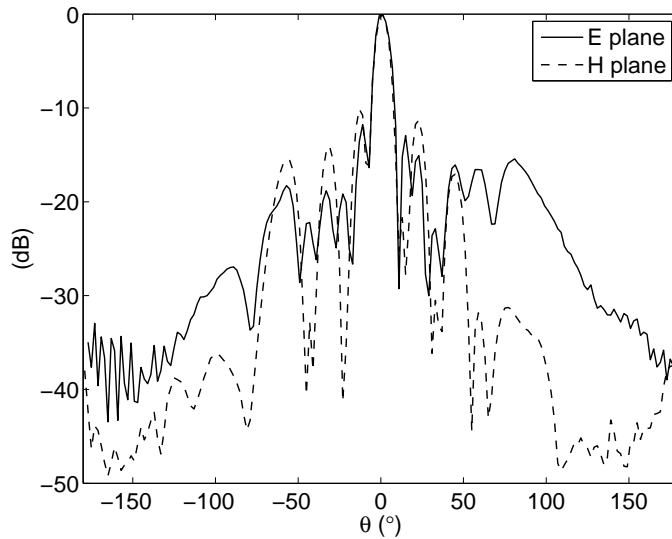


Figure 10.15: E- and H-plane radiation patterns at 20 GHz for the eight-by-eight array in the measurement fixture. Absorber is placed around the frame periphery in reduce its effects on the pattern.

10.3.8 Design Summary and Future Efforts

The advantage of the monolithic array structure is evident in the straightforward extension of a four-by-four configuration into an eight-by-eight array. The measured results indicate the array behaves in essentially the same way as an array with individual elements.

There are simple improvements that could be made to obtain superior performance. An inflexible substrate material, such as Rogers TMM3, could be used instead of Duroid. Initially, achieving adequate flatness on the bottom of the array was a potential difficulty in fabrication; the flexible Duroid substrate was chosen to make up for any lack of flatness. However, the fabricated ceramic arrays are sufficiently flat for the frequency of operation. An inflexible substrate would reduce the need for a measurement fixture and simplify analysis of the radiation patterns. The array performance could also be improved by using smaller element spacing and an alternative feed network topology.

The design is a first step in using CSLA in antenna array applications. Future work will include developing a ceramic feed network to achieve much higher efficiency and eliminating the air gap problem.

CHAPTER XI

Conclusions

A unique formulation of the acousto-EM problem is implemented in the finite-difference time-domain method. The result is a tool which is capable of predicting the Doppler component scattered from general two-dimensional objects. This more general model provides information on system feasibility and is a major step towards implementing the acousto-electromagnetic method in real-world systems.

A two-step model to simulate acousto-EM scattering from arbitrary two-dimensional targets has been presented; the model builds on previously developed analytical solutions for acousto-EM scattering from infinite circular cylinders [1, 69]. The total Doppler component is separated into contributions from the boundary perturbation and density modulation. The first step of the model is to detect resonant modes and simulate acoustic scattering from the target at resonance. The resulting target displacements are used in the FDTD implementation of the acousto-EM model. In this implementation, which is described in Chapter IV, the standard two-dimensional FDTD method is modified to include boundary and volumetric currents that produce the boundary perturbation and density modulation Doppler components, respectively. Unique Doppler signatures obtained for various modes of homogeneous and layered cylinders are presented in Chapter VI. The bistatic Doppler compo-

ment is also presented over a range of electromagnetic frequencies in Chapter VII. Various applications of the acousto-EM approach have been described in Chapter II. Chapters VII and VIII investigate applications in non-destructive evaluation; in particular, the ability of the Doppler component to detect the presence of small flaws in the target interior is demonstrated. A relative sensitivity parameter is introduced to quantify the improvement in sensitivity using the Doppler component relative to the unshifted fields. Parameter values routinely indicate factors of ten improvement at certain bistatic angles, depending on the crack orientation. In Chapter VIII, time-reversal focusing is used to improve sensitivity and locate flaws. Chapter IX describes systems for detection of the Doppler component. Various practical issues are described from a system-level design perspective. Finally, Chapter X presents multiple antenna designs for detection systems. The designs were not originally intended for use in an acousto-EM system; however, various techniques used in their development would be useful for an antenna designed specifically for use in an acousto-EM system.

11.1 Future Work

Experimental verification of the predicted bistatic Doppler component is necessary. A simple system measuring the bistatic Doppler component scattered from circular cylinders at various modes of resonance would confirm the accuracy of the model presented in reference [1] and reviewed in Chapter III.

In order to use the acousto-EM approach in practical applications, such as those outlined in Chapter II, it is also necessary to estimate the minimum detectable Doppler signal. This is application dependent and requires estimating the amount of loss in both the acoustic and electromagnetic propagation problems. In landmine

detection, for example, the amount of acoustic and electromagnetic energy that is able to propagate to the target is dependent on many factors and will ultimately determine the detectability of the Doppler component. In addition to propagation loss, there are various practical issues inherent to the acousto-EM approach because of its dependence upon acoustic resonances. First, targets which are surrounded with materials other than air exhibit much lower Q resonances. This implies the Doppler component scattered from such targets will be smaller. The extent of signal degradation depends on the application and the surrounding material but some loss due to this effect is expected in a practical system. Also, nearby objects, which are also acoustically excited, would produce cluttering signals in the Doppler component. However, as long as the desired target does not share resonant mode frequencies with nearby objects, this effect should not be pronounced.

There are also various practical issues and improvements related to focusing, as presented in Chapter VIII. Two reference signals were required to focus the incident signal and then to measure correlation, or scattering intensity throughout the target. In practice, neither signal is readily available and some means of acquiring or estimating them is necessary. This raises an important question of the sensitivity of focusing and correlation to errors in the reference signals. For example, if the permittivity of the target is estimated with a certain amount of error, what is the error that can be expected in focusing and in mapping the scattering intensity? Sensitivity to incorrectly estimating the target geometry would also be useful in determining accuracy of the calculated results.

Developing a three-dimensional model is also a logical next step. Three-dimensional sheet boundary conditions need developed for the boundary perturbation Doppler component. A similar approach as that used in the two-dimensional derivation in

reference [21] could be used. The density modulation contribution would be identical to that used in the two-dimensional model.

APPENDICES

APPENDIX A

Magneto-Dielectric Resonator Antenna

This appendix provides a detailed description of the layered magneto-dielectric resonator antenna briefly discussed in Section 10.2.

A.1 Introduction

Satellite communications is the most reliable and secure means of communication for civilian and military mobile platforms which provide global coverage. Operational satellite systems often require wide bandwidth or dual band operation. Circular polarization is also often required to remove the effects of polarization rotation due to propagation through the ionosphere. GPS systems, for example, which have low bandwidth requirements use microstrip patch antennas and, in some cases, quadrifilar helix antennas [118], [119]. In contrast, the civilian satellite system Globalstar is dual band, using 1.610-1.625 GHz for uplink and 2.4835-2.5 GHz for downlink [120]. Quadrifilar helix antennas are also used in this system [121]. Helical and spiral antennas inherently are able to produce circular polarization over a wide bandwidth [106]. However, such traveling wave type antennas must be large in dimension or comparable to the wavelength at the lowest frequency for proper operation. For mobile platforms, and specifically for airplanes and UAV's, this may pose a limitation. This problem is exacerbated when operating at low UHF band where the wavelength

is of the order of a meter. The challenges posed by a high bandwidth requirement in addition to possessing simultaneously compact size, high to moderate efficiency, and circular polarization have been met with a unique antenna design employing layered magneto-dielectric materials.

The design begins with a dielectric resonator antenna (DRA) which, being a volumetric source, has inherently wider bandwidth than a linear or surface radiator [90]. In an effort to reduce the size, the DRA is composed of layers of magneto-dielectric and dielectric materials, forming the MDRA. Finally, a previously developed method to improve the bandwidth of a DRA using a double resonant structure is used [122]. Extending this approach, parasitic elements are also included yielding a multi-resonant design.

The design attributes are reviewed in Section A.2. The resonance frequency of the layered MDRA is approximated in Section A.3, the simulation setup is described in Section A.4, and the fabrication details are given in Section A.5. Finally, measurement results are given in Section A.6.

A.2 Design Development

A.2.1 Volumetric Radiator

As discussed in Section 10.1, the radiation power factor (RPF), developed by Wheeler, quantifies the ability of electrically small antennas to radiate [90]. The factor, which is inversely related to antenna Q , indicates the amount of real power radiated away from the antenna compared to the amount of reactive power stored in the antenna's near field. It is proportional to the ratio of effective antenna volume, which is related to its physical volume, to the volume of the radian sphere ($\frac{4\pi}{3}(\lambda/2\pi)^3$). Volumetric sources, such as the MDRA, which more effectively fill the radian sphere have higher RPF and exhibit improved radiation capability and

bandwidth. This is in contrast to linear and surface radiators which demonstrate considerably lower radiation bandwidth.

A.2.2 Magneto-dielectric Materials

New materials are sought for enhanced miniaturization and simultaneously increased bandwidth. Here we present the application of a recently developed magneto-dielectric in the design of a MDRA. Antenna size is generally determined by the wavelength in the antenna material:

$$(A.1) \quad \lambda_d = \frac{\lambda_o}{\sqrt{\mu_r \epsilon_r}}$$

where λ_o is the freespace wavelength and ϵ_r and μ_r are the relative permittivity and permeability, respectively. In the past, only high permittivity materials were available to decrease antenna size; however, the use of such materials leads to increased energy storage in the antenna near field which in turn reduces the antenna bandwidth. Incorporating artificial materials with both μ_r and ϵ_r greater than unity can result in the same size antenna without the adverse effects of using high permittivity materials [112]. The lower contrast in wave impedance inside and outside the structure results in reduced entrapment of electromagnetic waves. Since energy storage is reduced, the ability of the structure to radiate power over a wider bandwidth is improved.

A study is carried out in simulation using the finite-difference time-domain (FDTD) method in order to investigate the effect of μ and ϵ on bandwidth [107]. Optimal values which maximize bandwidth for a particular slot-fed MDRA design are found. The results are given to provide qualitative evidence of the bandwidth improvement when both μ and ϵ are used. In each case, the intrinsic impedance ($\sqrt{\mu/\epsilon}$) is varied while the product of μ_r and ϵ_r is kept at 25, and the MDRA dimensions,

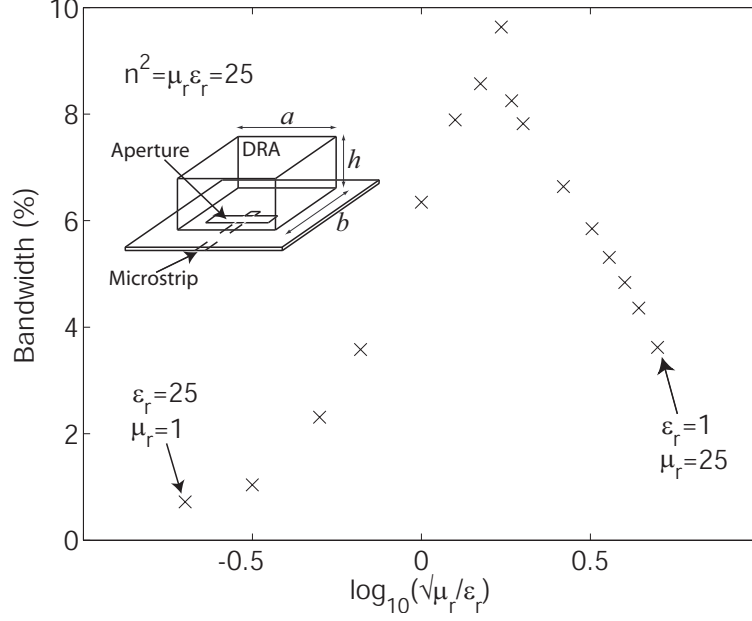


Figure A.1: Percent bandwidth versus the log of the MDRA intrinsic impedance. The slot-fed MDRA of dimensions $a \times b \times h$ is also shown.

$a = 0.2\lambda \times b = 0.2\lambda \times h = 0.13\lambda$, are held constant (see Figure A.1). The degree of matching varied as the permittivity and permeability were adjusted; modifications such as changing the slot length and position of the MDRA over the slot were made in order to achieve a -10 dB match. The fractional bandwidth of the MDRA resonance is plotted versus the log of the intrinsic impedance of the material ($\log_{10} \sqrt{\mu_r/\epsilon_r}$) in Figure A.1. It is observed that optimal bandwidth for this MDRA configuration is achieved when $\sqrt{\mu_r/\epsilon_r} = 1.74$, corresponding to $\mu_r = 8.62$ and $\epsilon_r = 2.9$. It is clearly demonstrated that, in general, by using a combination of both μ_r and ϵ_r the bandwidth can significantly be improved. In this case, a factor of improvement as large as 13 is observed. It is important to note that a high ratio of μ to ϵ may not be achievable even with a layered structure. In the fabricated design, as will be shown, $\sqrt{\mu_r/\epsilon_r} \approx 0.8$. If a similar design were attempted with dielectric materials, for the same resonant frequency and size, a higher permittivity material would be necessary. Using high permittivity materials alone makes the task of impedance matching and

the use of multi-resonant structures more complicated and sometimes impossible. Simulation results confirm narrower resonances and indicate poor coupling to the parasitic elements.

It is important to note that obtaining arbitrary ϵ and μ may not be possible physically. Until recently, low loss, high permeability, ferrite materials that operate over VHF-UFH bands were not available. Through a collaborative effort, supported by the DARPA metamaterials program, Trans-Tech, Inc. and the University of Michigan have developed a new class of these materials. In this design the magneto-dielectric is an aligned Z-type hexaferrite ceramic. It is composed of barium hexaferrite blended with cobalt oxide and barium carbonate. The material's magnetic Q and the real part of the relative permeability are shown versus frequency in Figure A.2. Over the frequency range of interest, the magnetic loss tangent ($\tan \delta_m$) is approximately 0.04 but increases at higher frequencies; $\tan \delta_e$ is estimated to be five to ten times smaller than $\tan \delta_m$. The relative permittivity and permeability are approximately 16 and 8.5, respectively. Currently, the manufacturing process limits the hexaferrite layer thickness. Also, according to results in Figure A.1 a higher ratio of μ_r to ϵ_r than may be achieved with this material alone is desirable. As will be shown, an increased ratio can be achieved with a layered design of alternating hexaferrite and regular dielectric layers. Arranging the materials this way also improves the effective loss tangents.

A.2.3 Multi-resonant Design for Increased Bandwidth

The technique used in [122] is shown to increase the impedance bandwidth of an antenna by using multiple resonant structures in the design. In particular, it combines a slot antenna and a DRA to effectively double the available bandwidth. With proper design it is observed that the resonance of the slot and that of the

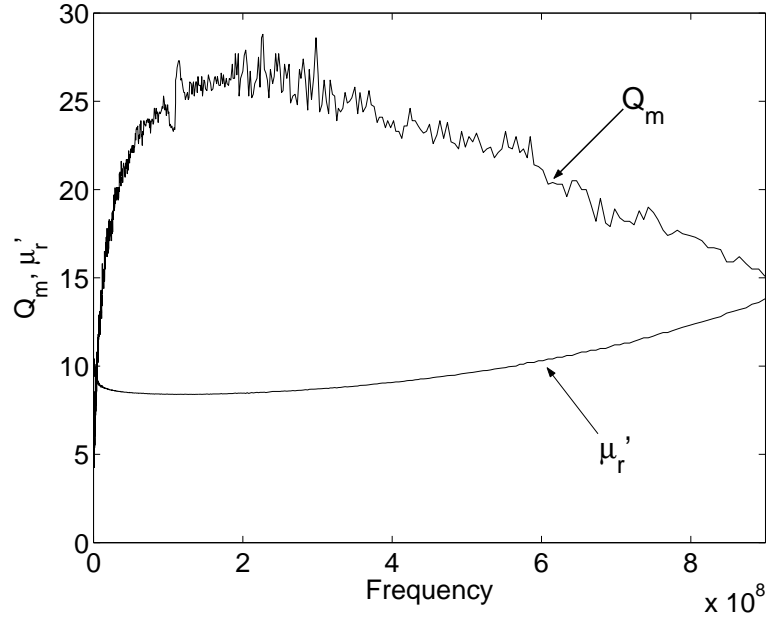


Figure A.2: Magnetic Q_m and relative permeability, μ_r' , of the hexaferrite magneto-dielectric versus frequency.

dielectric structure itself may be merged to achieve 100% bandwidth improvement over which the antenna polarization and radiation pattern are preserved. Using only dielectric materials fractional bandwidths on the order of 25% were demonstrated with moderate miniaturization.

One drawback of using a slot to feed the MDRA is back radiation; the slot dimensions necessary to merge the resonances may be large enough to allow non-negligible radiation below the ground plane. In cases where isolation from the lower half-space is needed, a probe feed can be used. The probe feed approach also allows for easier implementation of a CP design. A minor drawback of using the probe feed is higher cross-pol levels in the H-plane of the MDRA (the $x - z$ plane in Fig. A.3). Loop feeds could instead be used to mitigate cross-pol radiation and allow for improved axial ratios; however, loop feeds are more difficult to fabricate than straight probes.

The concept of merging resonances to augment bandwidth can also be extended to include additional resonances from parasitic elements. If properly designed the

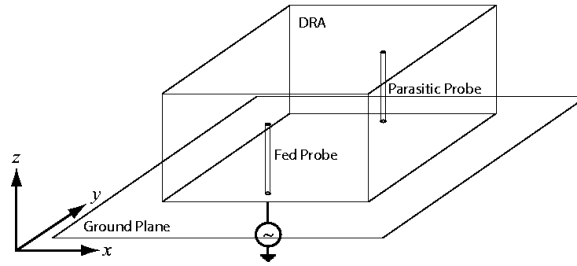


Figure A.3: Probe fed DRA with parasitic probe.

parasitic element yields a third resonance at the proper frequency. For example, in the original design, an additional aperture was added next to the fed aperture. The two apertures are coupled through the electric field in the MDRA, each producing a distinct resonance; all three resonances would share the same linear polarization. The presence of the second aperture, however, exacerbates the problem of back radiation. Alternatively, a parasitic probe can be added on the other side of the MDRA, as shown in Figure A.3. In this design a parasitic probe is short circuited to the ground plane opposite from the fed probe. Additional parasitic probes can be added to achieve more resonances that would lead to increased bandwidth.

This multi-resonance approach is used to design a circularly polarized antenna. A square MDRA is ideal for CP implementation because two orthogonal modes can be excited using two probes along adjacent walls, as shown in Figure A.4. At the MDRA resonance E_z has a null at the midpoint of the MDRA length in the y direction so the presence of the second probe should not affect the return loss at this frequency. At the probe resonance the effect of the second probe may be non-negligible. However, based on the return loss simulated with and without the second CP probe the effect is not substantial.

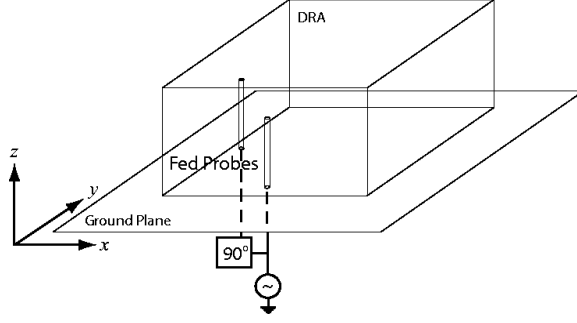


Figure A.4: Circularly polarized probe fed DRA.

A.3 First-order MDRA Design

A simple procedure is outlined in order to provide a starting point for design. Effective medium theory is invoked to approximate the resonant frequency of the MDRA and probe. Since the layer thickness is small compared to the wavelength inside the MDRA an effective permittivity and permeability may be used to estimate the resonance frequency. Effective parameters are obtained by modeling the MDRA layers as series capacitors and inductors with values corresponding to their respective permittivity and permeability. These expressions should only apply to the z component of the parameters (ϵ_z, μ_z) as the transverse components ($\epsilon_{x,y}, \mu_{x,y}$) are not affected by the layered design. However, the resulting anisotropy is neglected in this approximation. This is acceptable for the dominant mode because the electric field is primarily in the \hat{z} direction, perpendicular to the layers. In the case of equal thickness, alternating hexaferrite and dielectric layers:

$$(A.2) \quad \mu_{r,eff} \approx \frac{\mu_{r1} + \mu_{r2}}{2} \approx 4.75 \quad \epsilon_{r,eff} \approx 2 \left(\frac{1}{\epsilon_{r1}} + \frac{1}{\epsilon_{r2}} \right)^{-1} \approx 7$$

where subscripts 1 and 2 refer, respectively, to the hexaferrite ($\epsilon_{r1} = 16, \mu_{r1} = 8.5$) and the dielectric ($\epsilon_{r2} = 4.5, \mu_{r2} = 1$) materials. Using these approximate values an effective index of refraction $n_{eff} = \sqrt{\mu_{r,eff}\epsilon_{r,eff}} \approx 5.8$ is achieved. The resonant frequency may be found using the familiar expressions given in [122] using

the effective parameters derived above. The fundamental resonant frequency for the MDRA is chosen to be 264 MHz, slightly above the lower edge of the desired frequency band of 245 MHz. Solving the equations in [122] yields dimensions of 17.2 cm \times 17.2 cm \times 7.5 cm.

The first resonance of the feed and parasitic probes occurs at $\lambda_d/4$, where λ_d is the wavelength inside the MDRA. A length is selected such that the resonance occurs at a frequency adjacent to that of the MDRA.

A.4 Simulation Results

The design is simulated using the FDTD method. In order to simplify the simulation model for the CP designs, the first probe is fed while the other fed probe is matched with a 50 Ω termination as it would be with the coupler. Therefore, the return loss reference plane is at the base of the fed probe rather than at the input to the coupler. Since the design is symmetric an identical result is obtained when the other input probe is fed. Isolation between the two antenna feeds is not investigated with FDTD simulation.

The return loss for the double resonant CP design, shown in Figure A.4, is given in Figure A.5. The MDRA resonance is around 265 MHz and the probe resonance is at 315.4 MHz. The size of the MDRA in this design is that obtained above, 17.2 cm \times 17.2 cm \times 7.5 cm, and the probe length is 4.3 cm.

The simulations were initiated with wire probes, as shown in Figures A.3 and A.4. During initial measurements, it was observed that wider probes placed on the MDRA surface rather than wire probes inside result in better coupling to the MDRA. This type of probe also allows for easier setup and tuning. The simulated configuration was then updated to reflect the external probes.

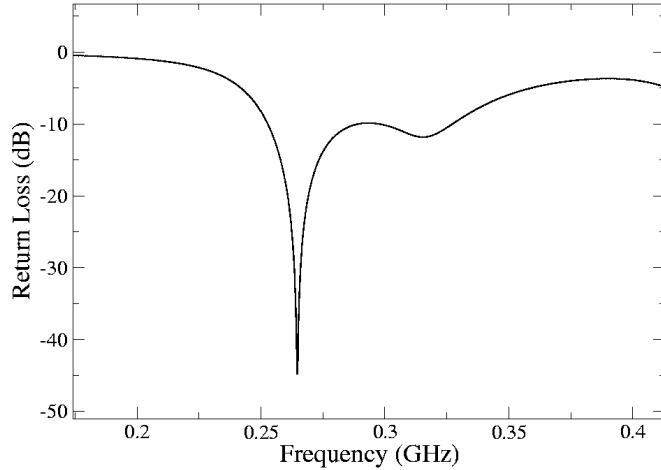


Figure A.5: The simulated return loss for the design shown in Figure A.4. Two fed, wire probes are used in this simulation; no parasitic probes are present.

Figure A.6 shows the simulation results for the return loss of the CP design shown in Figure A.7, which yields the measured results in Section A.6. The resonance near 265 MHz is from the MDRA; additional resonances are from the fed and parasitic probes. The primary cause for disagreement between simulations and measurements is uncertainty in the isotropy and homogeneity of the hexaferrite antenna material. Since these properties have not yet been characterized they cannot be accounted for in simulation. The variation in the permeability within each hexaferrite tile is as large as $\mu_r = 8.5 \pm 0.5$; in addition, as seen in Figure A.2, both real and imaginary parts of μ vary over the band of interest. We use the FDTD method as a first order design tool. Primarily, it is used to obtain the size of the antenna necessary to operate at the desired band of frequencies (245 MHz - 310 MHz). Following fabrication, further tuning was carried out in the lab.

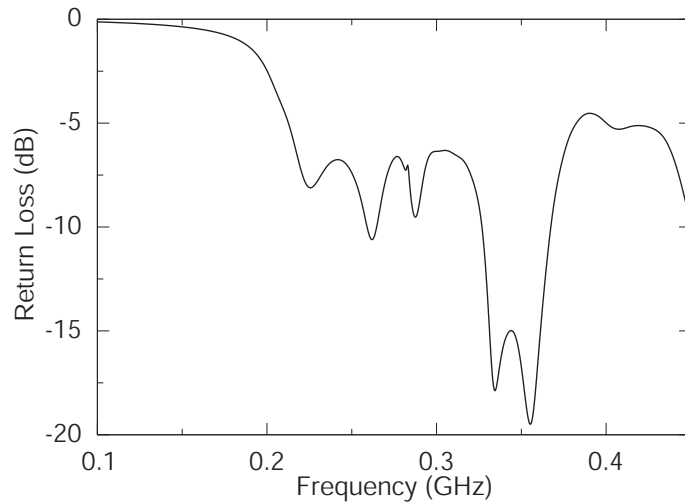


Figure A.6: The return loss simulated for the final design. Wider probes are used as in the antenna in the measurement section.

A.5 Fabrication Details

As mentioned, the current fabrication procedure limits the hexaferrite thickness to roughly 0.5 cm. For this reason and also to improve the effective permeability to permittivity ratio of the MDRA, a layered design using regular dielectric layers alternated with hexaferrite layers is used. The dielectric layers used in the fabricated design are Roger's TMM4 and have relative permittivity of 4.5 with $\tan \delta_e < 0.002$.

¹ The antenna is made of fourteen layers, each of which is 0.54 cm thick and 17.2 cm square. The hexaferrite layers are made up of smaller, 5 cm \times 5 cm tiles that are glued together and machined to yield a smooth surfaced layer of uniform thickness. The total antenna height is about 7 cm. The fabricated antenna with feed and parasitic elements is shown in Figure A.7.

Two configurations using the same MDRA are built: a dual linearly polarized design and a CP design. The dual linearly polarized design consists of the two feed

¹Rogers Corporation, Rogers, CT. <http://www.rogers-corp.com>

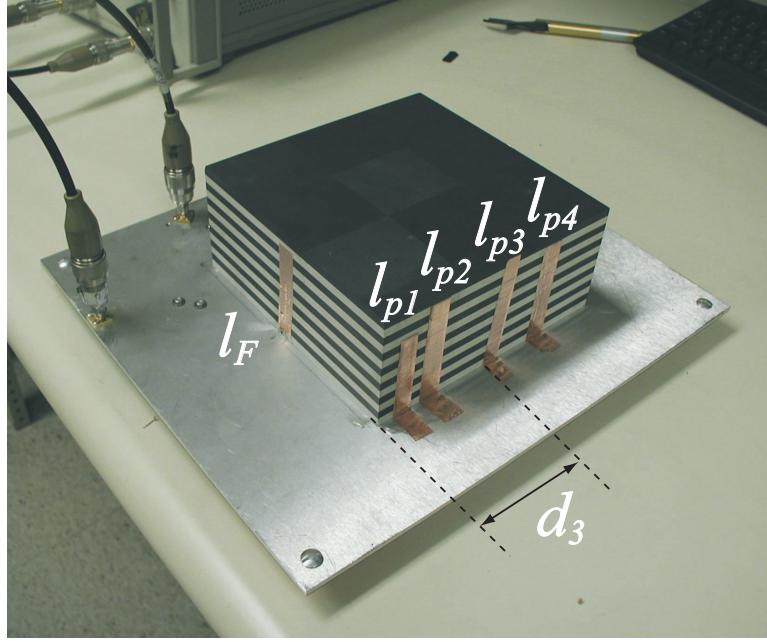


Figure A.7: Fabricated antenna in measurement setup with feed and parasitic elements.

probes, eight parasitic elements (four for each fed probe), and the MDRA on a 30 cm square ground plane. This design is the same as that in the FDTD simulations. The CP design uses a 90° hybrid coupler to divide the input power to feed the two probes via microstrip as shown in Figure A.8. Coaxial feeds could also be used rather than microstrip. In this design the ground plane is approximately 30 cm by 34 cm. The probe dimensions and locations used in both designs are given in Table A.1; the probe designations correspond to those in Figure A.7. The location of the probe refers to the distance between the left edge of the MDRA and the left edge of the probe; for example, in Figure A.7 the location of probe l_{p3} is indicated as d_3 .

Probe	Width (cm)	Height (cm)	Location (cm)
l_F	1.2	6.9	8
l_{p1}	1.2	5.6	1.1
l_{p2}	1.4	7	3
l_{p3}	1.2	7.2	8
l_{p4}	1.4	7	11.5

Table A.1: Probe dimensions and locations for the dual linearly polarized and CP designs.

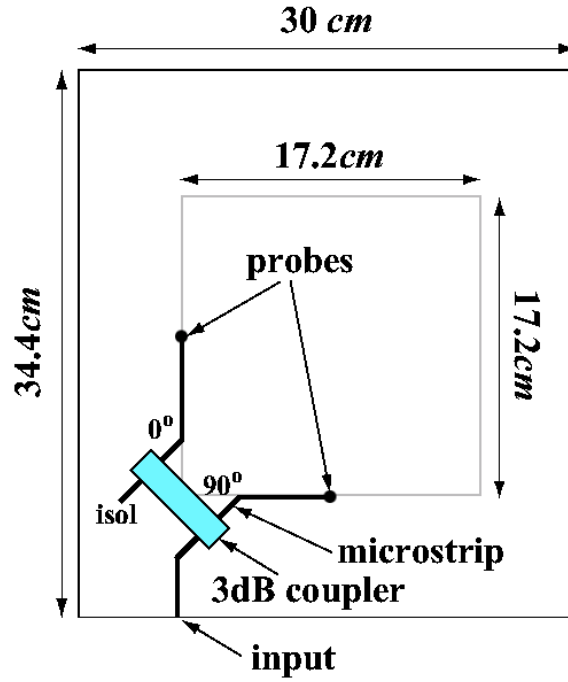


Figure A.8: Diagram of feed network using microstrip and a hybrid coupler.

A.6 Measurements

A.6.1 Return Loss and Isolation

The RF characteristics (return loss and port isolation) of the MDRA design shown in Figure A.7 are measured and reported in this section. The first set of measurements are carried out on the dual linearly polarized design; one port of the antenna is fed while the other is terminated with a matched load.

The return loss measured from each port is shown in Figure A.9. The measured impedance bandwidth covers a very wide bandwidth from 240-425 MHz. In order to ensure the input power is not absorbed in the matched load at the other port the isolation is measured as well. The result is also shown in Figure A.9. The isolation has a minimum of about -8 dB around 245 MHz, at the lower end of the operational bandwidth. This indicates that approximately 15% of the input power is lost in the matched termination. These results could be improved through further tuning, by

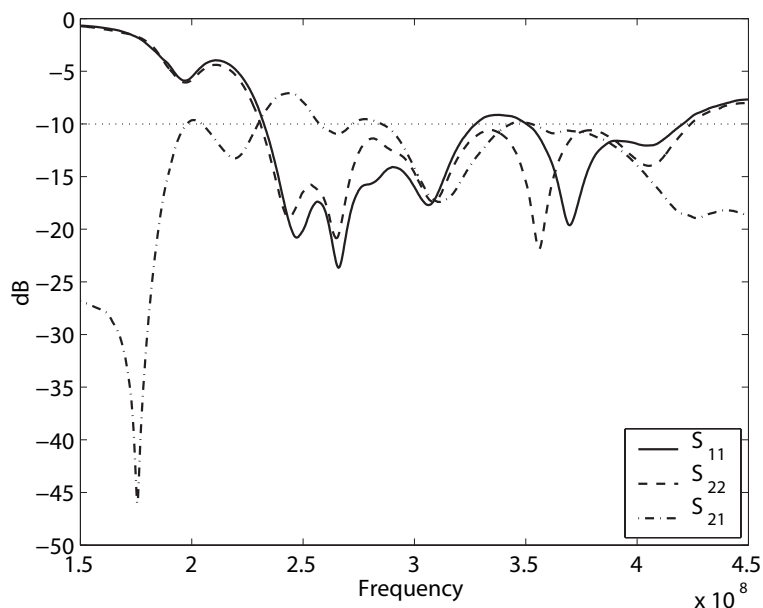


Figure A.9: The return loss and isolation of the dual linearly polarized design.

compromising bandwidth for higher isolation.

The return loss is also measured with the CP feed network shown in A.8. The second port of the network analyzer is connected to the isolated port of the coupler and is used to monitor the power reflected from the antenna ports. The result is shown in Figure A.10. The return loss is about -10 dB over the entire band; a minimum of -7.6 dB occurs at 248 MHz. The wideband matching is expected because power reflected from the antenna feeds goes to the isolated port of the coupler and shows up in S_{21} . The antenna operates when both S_{11} and S_{21} are below -10 dB; as in the previous measurement, this is above roughly 240 MHz.

A.6.2 Pattern and Gain Measurements

The patterns of the dual linearly polarized design are measured; the CP feed network is not used in pattern measurements. The E and H plane designations correspond to the MDRA planes. The E_1 and H_2 planes coincide as do the E_2 and H_1 planes. The cross-pol level in the E plane may be effected by the presence of the

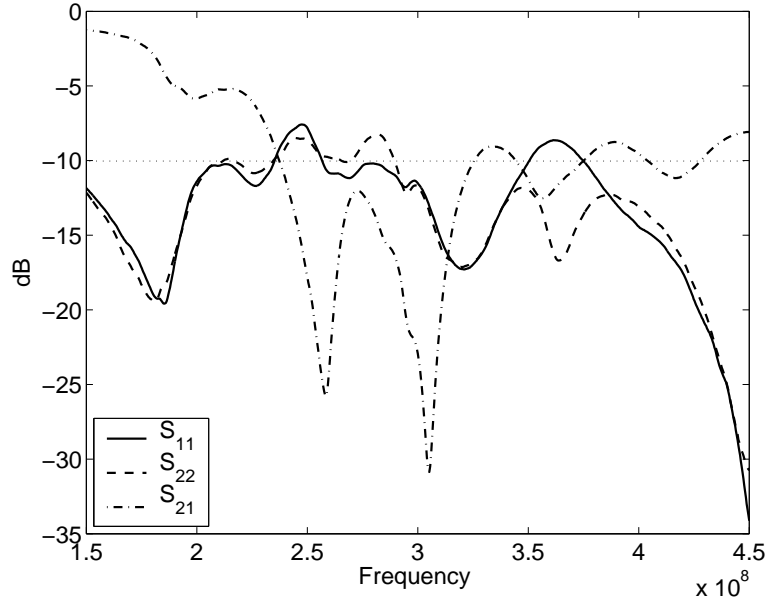
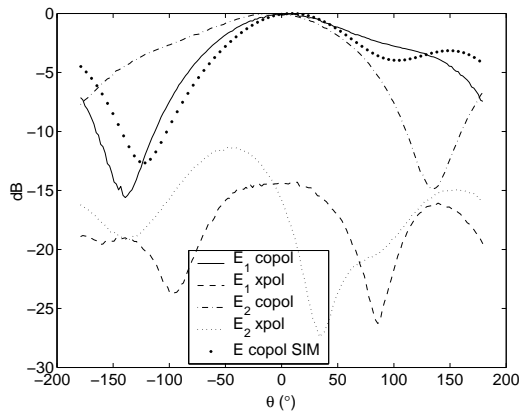


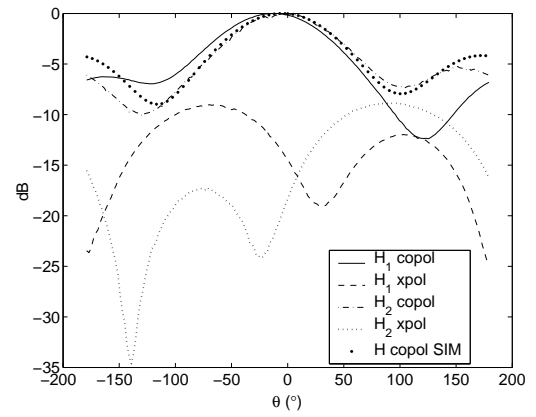
Figure A.10: Return loss and isolation measured with the CP feed network.

cable during measurement. It is also noted that the anechoic chamber is designed for frequencies above 400 MHz. Therefore, these results may change with further measurement in an improved environment. The patterns measured at 246 MHz, 265 MHz, 285 MHz, and 310 MHz. Those at 265 and 285 MHz are shown in Figures A.11 and A.12 with the simulated copol patterns. Patterns at the remaining frequencies are not shown because of space limitations. The symmetry in the design is evident in the patterns. The offset of the main beam is likely due to the presence of the parasitic probes.

The gain of the dual linearly polarized design is also measured. The results are shown in Table A.2. The size of the ground plane, in this case, is 50 cm square. The gain at higher frequencies is limited by the magnetic loss of the hexaferrite material which, as shown in Figure A.2, increases with increasing frequency. Considering the return loss and isolation between the two ports the expected antenna gain in the absence of dielectric and magnetic losses is about +2 dBi. This is about 3 – 4 dB

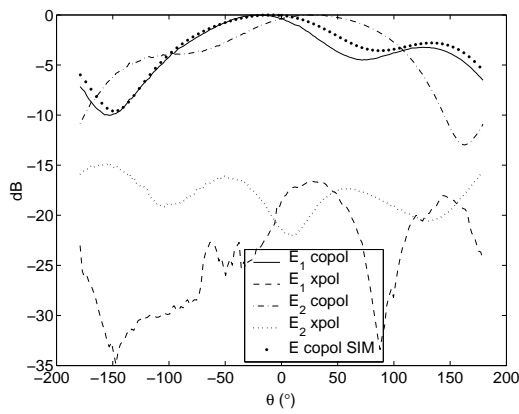


(a) E plane pattern at $f = 265$ MHz.

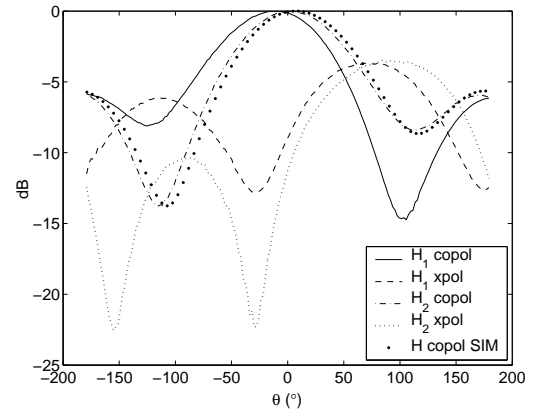


(b) H plane pattern at $f = 265$ MHz.

Figure A.11: E and H plane patterns at $f = 265$ MHz.



(a) E plane pattern at $f = 285$ MHz.



(b) H plane pattern at $f = 285$ MHz.

Figure A.12: E and H plane patterns at $f = 285$ MHz.

higher than the measured gain values. Improving the magnetic loss can improve the antenna gain and current efforts are underway to reduce the magnetic loss tangent to values better than 10^{-2} .

A.7 Conclusions

This design combines three techniques to achieve percentage bandwidth values in excess of 50% for an antenna with a maximum dimension of 0.15λ . A volumetric MDRA structure, as opposed to printed planar or wire, is used. The MDRA is made up of layered magneto-dielectric material with properly designed permittivity and permeability values. A resonant feed and parasitic elements are integrated into the MDRA design for enhanced bandwidth. Finally, the square symmetry of the MDRA is used in a CP design. Measurement results show the impedance percentage bandwidth is on the order of 58%. The design's primary limitations are in the cross-pol caused by the probe feeds and its efficiency. As noted, loop feeds could be used in a similar design with reduced cross-pol. Development of a lower loss hexaferrite is currently under consideration to improve the gain.

f	G
250 MHz	-1 ± 1 dBi
259 MHz	-1.7 ± 1 dBi
280 MHz	-2 ± 1 dBi
310 MHz	-3 ± 1 dBi *

Table A.2: Gain measurement results for the dual linearly polarized design on 50 cm ground plane (* 30 cm sq).

BIBLIOGRAPHY

BIBLIOGRAPHY

- [1] Kamal Sarabandi and Daniel E. Lawrence. Acoustic and Electromagnetic Wave Interaction: Analytical Formulation for Acousto-Electromagnetic Scattering Behavior of a Dielectric Cylinder. *IEEE Trans. Antennas and Propagation*, 49(10):1382–1392, 2001.
- [2] Adrian Korpel. *Acousto-Optics*. Marcel Dekker, Inc., 1997.
- [3] L. Brillouin. Diffusion de la lumiere et des rayons x par un corps transparent homogène. *Annals of Physics (Paris)*, 17:88–122, 1922.
- [4] P. Debye and F. W. Sears. On the scattering of light by supersonic waves. *Proceedings of the National Academy of Sciences*, 18(6):409–414, 1932.
- [5] G. Benedek and T. Greytak. Brillouin scattering in liquids. *Proceedings of the IEEE*, 53(10):1623–1629, 1965.
- [6] E. Max North, Allen M. Peterson, and H. Dean Perry. RASS, a remote sensing system for measuring low-level temperature profiles. *Bulletin of the American Meteorological Society*, 54(9):912–919, 1973.
- [7] Gerhard Peters. History of RASS and its Use for Turbulence Measurements. 3:1183–1185, 2000.
- [8] Steven F. Clifford, J. Chandran Kaimal, Richard J. Latatits, and Richard G. Strauch. Ground-Based Remote Profiling in Atmospheric Studies: An Overview. *Proceedings of the IEEE*, 82(3):313–355, 1994.
- [9] Wayne M. Angevine. Radio Acoustic Sounding System (RASS) Applications and Limitations. 3:1180–1182, 2000.
- [10] Peter T. May, Kenneth P. Moran, and Richard G. Strauch. The Accuracy of RASS Temperature Measurements. *Journal of Applied Meteorology*, 28:1329–1334, 1989.
- [11] Michael S. Frankel, Norman J. F. Chang, and Melvin J. Sanders. A High-Frequency Radio Acoustic Sounder for Remote Measurement of Atmospheric Winds and Temperature. *Bulletin of the American Meteorological Society*, 58(9):928–934, 1977.
- [12] R. A. Albanese, H. T. Banks, and J. K. Raye. Nondestructive evaluation of materials using pulsed microwave interrogating signals and acoustic wave induced reflections. *Inverse Problems*, 18:1935–1958, 2002.
- [13] H. T. Banks and V. A. Bokil. A computational statistical framework for multidimensional domain acoustooptic material interrogation. Technical report, Center for Research in Scientific Computation, January 2005.
- [14] G. M. Kepler, R. A. Albanese, H. T. Banks, and V. A. Bokil. Reflection of microwave pulses from acoustic waves: Summary of experimental and computational studies. Technical report, Center for Research in Scientific Computation, May 2005.

- [15] C. Stewart. Summary of Mine Detection Research. Technical Report 1636-TR., May 1960.
- [16] G. S. Smith. Summary Report: Workshop on New Directions for Electromagnetic Detection of Non-Metallic Mines. Technical report, June 1992.
- [17] W. R. Scott, C. Schroeder, and J.S. Martin. A Hybrid Acoustic/Electromagnetic Technique for Locating Land Mines. *Proceedings of the International Geoscience and Remote Sensing Symposium*, pages 216–218, 1998.
- [18] W. R. Scott, C. Schroeder, and J.S. Martin. An acousto-electromagnetic sensor for locating land mines. *Proceedings SPIE*, pages 176–186, 1999.
- [19] C. T. Schroeder, W. R. Scott, and G. D. Larson. Elastic Waves Interacting With Buried Land Mines: A Study Using the FDTD Method. *IEEE Transactions on Geoscience and Remote Sensing*, 40(6):1405–1415, 2002.
- [20] C. T. Schroeder and W. R. Scott. A Finite-Difference Model to Study the Elastic-Wave Interactions with Buried Land Mines. *IEEE Transactions on Geoscience and Remote Sensing*, 38(4):1505–1512, 2000.
- [21] Daniel E. Lawrence and Kamal Sarabandi. Electromagnetic Scattering from Vibrating Penetrable Objects Using a General Class of Time-Varying Sheet Boundary Conditions. *IEEE Trans. Antennas and Propagation*, 54(7):2054–2061, 2006.
- [22] J. MacDonald, J. R. Lockwood, J. McFee, T. Altshuler, T. Broach, L. Carin, C. Rappaport, W. R. Scott, and R. Weaver. Alternatives for Landmine Detection. Technical Report MR-1608-OSTP, 2003.
- [23] Y. Das, J. E. McFee, J. Toew, and G.C. Stuart. Analysis of an Electromagnetic Induction Detector For Real-Time Location of Buried Objects. *IEEE Transactions on Geoscience and Remote Sensing*, 28(3):278–288, 1990.
- [24] K. D. Sherbondy and D. A. Lang. Developmental GPR mine detection technology known as the balanced bridge. *Proceedings SPIE*, 2496:31–41, 1995.
- [25] A. Andrews, J. Ralston, and M. Tuley. Research on Ground-Penetrating Radar for Detection of Mines and Unexploded Ordnance: Current Status and Research Strategy. Technical report, 1999.
- [26] T. R. Witten, K. Sherbondy, and J. Habersat. Acoustic Technology for Land Mine Detection - Past Tests, Present Requirements, and Future Concepts. *Proceedings SPIE*, 4038:781–789, 2000.
- [27] T. Hanshaw. Multi-sensor fusion for the detection of mines and “mine like” targets. *Proceedings SPIE*, 2496:152–158, 1995.
- [28] <http://www.globalsecurity.org/military/systems/ground/hstamids.htm>.
- [29] B. A. Baertlein and A. Gunatilaka. Improving detection of buried land mines through sensor fusion. *Proceedings SPIE*, 3392:1122–1133, 1998.
- [30] T. Witten, P. Lacko, and J.M. Sabatier. Fusion of ground penetrating radar and acoustics data. *Proceedings SPIE*, 4742:903–910, 2002.
- [31] Kamal Sarabandi and Daniel E. Lawrence. Acoustic and Electromagnetic Wave Interaction: Estimation of Doppler Spectrum From an Acoustically Vibrated Metallic Circular Cylinder. *IEEE Trans. Antennas and Propagation*, 51(7):1499–1507, 2003.
- [32] X. Li, E. J. Bond, B. D. Van Veen, and S. C. Hagness. An Overview of Ultra-Wideband Microwave Imaging via Space-Time Beamforming for Early-Stage Breast Cancer Detection. *IEEE Antennas and Propagation Magazine*, 47(1):19–34, 2005.

- [33] E. J. Bond, X. Li, S. C. Hagness, and B. D. Van Veen. Microwave Imaging via Space-Time Beamforming for Early Detection of Breast Cancer. *IEEE Transactions on Antennas and Propagation*, 51(8):1690–1705, 2003.
- [34] X. Li, S. K. Davis, S. C. Hagness, D. W. van dar Weide, and B. D. Van Veen. Microwave Imaging via Space-Time Beamforming: Experimental Investigation of Tumor Detection in Multilayer Breast Phantoms. *IEEE Transactions on Microwave Theory and Techniques*, 52(8):1856–1865, 2004.
- [35] W. T. Joines, Y. Zhang, C. Li, and R. L. Jirtle. The measured electrical properties of normal and malignant human tissue from 50 to 900 MHz. *Medicine in Physics*, 21:547–550, 1994.
- [36] J. F. Greenleaf, M. Fatemi, and M. Insana. Selected Methods for Imaging Elastic Properties of Biological Tissues. *Annual Review of Biomedical Engineering*, 5:57–78, 2003.
- [37] K. J. Parker, L. Gao, R. M. Lerner, and S. F. Levinson. Techniques for Elastic Imaging: A Review. *IEEE Engineering in Medicine and Biology*, 15(6):52–59, 1996.
- [38] A. P. Sarvazyan, O.V. Rudenko, S. D. Swanson, J. B. Fowlkes, and S. Y. Emelianov. Shear Wave Elasticity Imaging: A New Ultrasonic Technology of Medical Diagnostics. *Ultrasound in Medicine and Biology*, 24(9):1419–1435, 1998.
- [39] J. Ophir, B. Garra, F. Kallel, E. Konofagou, T. Krouskop, R. Righetti, and T. Varghese. Elastographic Imaging. *Ultrasound in Medicine and Biology*, 26:S23–S29, 2000.
- [40] K. J. Parker, S. R. Huang, R. A. Musulin, and R. M. Lerner. Tissue Response to Mechanical Vibrations for Sonoelasticity Imaging. *Ultrasound in Medicine and Biology*, 16(3):241–246, 1990.
- [41] J. Ophir, S. K. Alam, B. Garra, F. Kallel, E. Konofagou, T. Krouskop, and T. Varghese. Elastography: ultrasonic estimation and imaging of the elastic properties of tissues. *Proceedings Institute Mechanical Engineers, Part H*, 213:203–233, 1999.
- [42] M. Fatemi and J. F. Greenleaf. Probing the dynamics of tissue at low frequencies with the radiation force of ultrasound. *Physics in Medicine and Biology*, 45:1449–1464, 2000.
- [43] M. Fatemi, L. E. Wold, A. Alizad, and J. F. Greenleaf. Vibro-Acoustic Tissue Mammography. *IEEE Transactions on Medical Imaging*, 21(1):1–8, 2002.
- [44] M. Fatemi and J. F. Greenleaf. Vibro-acoustography: An imaging modality based on ultrasound-stimulated acoustic emission. *Proceedings of the National Academy of Science*, 96:6603–6608, 1999.
- [45] P. Trompette F. G. Mitri and J. Chapelon. Improving the Use of Vibro-Acoustography for Brachytherapy Metal Seed Imaging: A Feasibility Study. *IEEE Transactions on Medical Imaging*, 23(1):1–6, 2004.
- [46] Genevieve F. Pla-Rucki and Marc O. Eberhard. Imaging of Reinforced Concrete: State-of-the-Art Review. *Journal of Infrastructure Systems*, (June):134–141, 1995.
- [47] M.R. Clark, D.M. McCann, and M.C. Forde. Application of infrared thermography to the non-destructive testing of concrete and masonry bridges. *NDT & E International*, 36:265–275, 2003.
- [48] M. Fatemi, A. Manduca, and J. F. Greenleaf. Imaging Elastic Properties of Biological Tissues by Low-Frequency Harmonic Vibration. *Proceedings of the IEEE*, 91(10):1503–1519, 2003.
- [49] Jeffery Cooper. Scattering of Electromagnetic Fields by a Moving Boundary: The One-Dimensional Case. *IEEE Trans. Antennas and Propagation*, 28(6):791–795, November 1980.

- [50] Jean Van Bladel and Daniel De Zutter. Reflections from Linearly Vibrating Objects: Plane Mirror at Normal Incidence. *IEEE Trans. Antennas and Propagation*, 29(4):629–637, July 1981.
- [51] Fady Harfoush, Allen Taflove, and Gregory A. Kriegsmann. A Numerical Technique for Analyzing Electromagnetic Wave Scattering from Moving Surfaces in One and Two Dimensions. *IEEE Trans. on Antennas and Propagation*, 37(1):55–63, January 1989.
- [52] Regis Wunenburger, Nicolas Mujica, and Stephan Fauve. Experimental study of the Doppler shift generated by a vibrating scatterer. *Journal of the Acoustical Society of America*, 115(2):507–514, February 2004.
- [53] V.C.Chen, F. Li, S.S.Ho, and H. Wechsler. Analysis of micro-Doppler signatures. *IEEE Proc. Radar and Sonar Navigation*, 150(4):271–276, August 2003.
- [54] Daniel E. Lawrence and Kamal Sarabandi. Electromagnetic Scattering from Vibrating Metallic Objects Using Time-Varying Generalized Impedance Boundary Conditions. *Antennas and Propagation Society International Symposium*, 2:782–785, June 2002.
- [55] Kane S. Yee. Numerical Solution of Initial Boundary Value Problems Involving Maxwell’s Equations in Isotropic Media. *IEEE Transactions on Antennas and Propagation*, 14(3):302–307, 1966.
- [56] Allen Taflove and Morris E. Brodwin. Numerical Solution of Steady-State Electromagnetic Scattering Problems Using the Time-Dependent Maxwell’s Equations. *IEEE Transactions on Microwave Theory and Techniques*, 23(8):623–630, 1975.
- [57] Allen Taflove, editor. *Advances in Computational Electrodynamics: The Finite-Difference Time-Domain Method*. Artech House, 1998.
- [58] P. L. Sullivan and D. H. Schaubert. Analysis of an Aperture Coupled Microstrip Antenna. *IEEE Transactions on Antennas and Propagation*, 34(8):977–984, 1986.
- [59] Jean-Pierre Berenger. A Perfectly Matched Layer for the Absorption of Electromagnetic Waves. *Journal of Computational Physics*, 114:185–200, 1994.
- [60] Jean-Pierre Berenger. Perfectly Matched Layer for the FDTD Solution of Wave-Structure Interaction Problems. *IEEE Transactions on Antennas and Propagation*, 44(1):110–117, 1996.
- [61] Stephen D. Gedney. An Anisotropic Perfectly Matched Layer-Absorbing Medium for the Truncation of FDTD Lattices. *IEEE Transactions on Antennas and Propagation*, 44(12):1630–1639, 1996.
- [62] Rose M. Joseph, Susan C. Hagness, and Allen Taflove. Direct time integration of Maxwell’s equation in linear dispersive media with absorption for scattering and propagation of femtosecond electromagnetic pulses. *Optics Letters*, 16(18):1412–1414, 1991.
- [63] Korada Umashankar and Allen Taflove. A Novel Method to Analyze Electromagnetic Scattering of Complex Object. *IEEE Transactions on Electromagnetic Compatibility*, 24(4):397–405, 1982.
- [64] Allen Taflove and Korada Umashankar. Radar Cross Section of General Three-Dimensional Scatterers. *IEEE Transactions on Electromagnetic Compatibility*, 25(4):433–440, 1983.
- [65] Raymond J. Luebbers, Karl S. Kunz, Michael Schneider, and Forrest Hunsberger. A Finite-Difference Time-Domain Near Zone to Far Zone Transformation. *IEEE Transactions on Antennas and Propagation*, 39(4):429–433, 1991.

- [66] Raymond J. Luebbers, Deirdre Ryan, and John Beggs. A Two-Dimensional Time-Domain Near-Zone to Far-Zone Transformation. *IEEE Transactions on Antennas and Propagation*, 40(7):848–851, 1992.
- [67] Torleif Martin. An Improved Near- to Far-Zone Transformation for the Finite-Difference Time-Domain Method. *IEEE Transactions on Antennas and Propagation*, 46(9):1263–1271, 1998.
- [68] J. G. Maloney and G. S. Smith. The Use of Surface Impedance Concepts in the Finite-Difference Time-Domain Method. *IEEE Trans. Antennas and Propagation*, 40(1):38–48, January 1992.
- [69] Kamal Sarabandi and Daniel E. Lawrence. Acoustic and Electromagnetic Wave Interaction: Estimation of Doppler Spectrum From an Acoustically Vibrated Metallic Circular Cylinder. *IEEE Trans. Antennas and Propagation*, 51(7):1499–1507, 2003.
- [70] R. Davies-Jones. Useful Formulas for Computing Divergence, Vorticity, and Their Errors from Three or More Stations. *Monthly Weather Review*, 121:713–725, 1993.
- [71] James J. Faran. Sound Scattering by Solid Cylinders and Spheres. *Journal of the Acoustical Society of America*, 23(4):405–418, July 1951.
- [72] R. D. Doolittle and H. Uberall. Sound Scattering by Elastic Cylindrical Shells. *Journal of the Acoustical Society of America*, 39(2):272–275, 1966.
- [73] H. Uberall, L. R. Dragonette, and L. Flax. Relation between creeping waves and normal modes of vibration of a curved body. *Journal of the Acoustical Society of America*, 61(3):711–715, March 1977.
- [74] J.J. Faran. Sound scattering by solid cylinders and sphere. *Journal Acoustical Society of America*, 23(4):405–418, 1951.
- [75] T. J. Cavicchi and W. D. O’Brien. Acoustic Scattering of an Incident Cylindrical Wave by an Infinite Circular Cylinder. *IEEE Transactions on Ultrasonics, Ferroelectrics, and Frequency Control*, 35(1):78–80, January 1988.
- [76] W. Huang, S. Brisuda, and S. I. Rokhlin. Ultrasonic wave scattering from fiber-matrix interphases. *Journal of the Acoustical Society of America*, 97(2):807–815, February 1995.
- [77] D. Firth. Acoustic Vibration of Structures in Liquids. *The Shock and Vibration Digest*, 9(9):3–7, 1977.
- [78] Mathias Fink. Time Reversal of Ultrasonic Fields - Part I: Basic Principles. *IEEE Transactions on Ultrasonics, Ferroelectrics, and Frequency Control*, 39(5):555–566, 1992.
- [79] Darrell R. Jackson and David R. Dowling. Phase conjugation in underwater acoustics. *Journal of the Acoustical Society of America*, 89(1):171–181, January 1991.
- [80] J. P. Stockmann and K. Sarabandi. Doppler Radar Detection of Mechanically Resonating Objects. volume 48, 2005.
- [81] John Pike. Underwater Acoustics. <http://www.fas.org/man/dod-101/sys/ship/acoustics.htm>, 1998.
- [82] W. Manthey, N. Kroemer, and V. Magori. Ultrasonic transducers and transducer arrays for applications in air. *Measurement Science and Technology*, 3:249–261, 1992.
- [83] W.A. Grandia and C.M. Fortunko. NDE Applications of Air-Coupled Ultrasonic Transducers. 1994.

- [84] Murata Manufacturing Co. Super Tweeter Driver Datasheet. <http://www.murata.com/catalog/p57e.pdf>, 2005.
- [85] Non-Contact Ultrasound (NCU) Catalog. <http://www.ultrangroup.com/Transducers/Catalogs/NCU.pdf>.
- [86] Frank Blum, Jacek Jarzynski, and Laurence J. Jacobs. A focused two-dimensional air-coupled ultrasonic array for non-contact generation. *NDT&E International*, 38:634–642, 2005.
- [87] HP E4431A Digital RF Signal Generator Data Sheet. http://www.home.agilent.com/upload/cmc_upload/A11/EP5G084587.pdf.
- [88] Agilent E8663B Analog Signal Generator Data Sheet. <http://cp.literature.agilent.com/litweb/pdf/5989-4866EN.pdf>.
- [89] Stanford Research Systems. SR850 100 kHz DSP Lock-in Amplifier Data Sheet. <http://www.thinksrs.com/products/SR850.htm>.
- [90] H. A. Wheeler. Fundamental Limits of Small Antennas. *Proc. IRE*, 1947.
- [91] M. W. McAllister, S. A. Long, and G. L. Conway. The Rectangular Dielectric Resonator. Antennas and Propagation Society International Symposium, 1983.
- [92] A. Kishk, A. Glisson, and G. Junker. Bandwidth Enhancement for Split Cylindrical Dielectric Resonator Antennas. *Progress in Electromagnetics Research, PIER 33*, pages 97–118, 2001.
- [93] A. Kishk, Y. Yin, and A. Glisson. Conical Dielectric Resonator Antennas for Wide-Band Applications. *IEEE Transactions on Antennas and Propagation*, 50(4):469–474, 2002.
- [94] K. W. Leung, K. Y. A. Lai, K. M. Luk, and D. Lin. Input impedance of aperture coupled hemispherical dielectric resonator antenna. *Electronics Letters*, 29(13):1165–1167, 1993.
- [95] R. K. Mongia and A. Ittipiboon. Theoretical and Experimental Investigations on Rectangular Dielectric Resonator Antennas. *IEEE Transactions on Antennas and Propagation*, 45(9):1348–1356, 1997.
- [96] A. Ittipiboon, R. Mongia, Y. Antar, P. Bhartia, and M. Cuhaci. Aperture fed rectangular and triangular dielectric resonators for use as magnetic dipole antennas. *Electronics Letters*, 29(23):2001–2002, 1993.
- [97] J. Shin, A. Kishk, and A. Glisson. Analysis of Rectangular Dielectric Resonator Antennas Excited Through a Slot Over a Finite Ground Plane. *Antennas and Propagation Society International Symposium*, 4:2076–2079, 2000.
- [98] G. Junker, A. Kishk, and A. Glisson. Input Impedance of Aperture-Coupled Dielectric Resonator Antennas. *IEEE Transactions on Antennas and Propagation*, 44(5):600–607, 1996.
- [99] F. Croq and A. Papiernik. Large bandwidth aperture coupled microstrip antenna. *Electronics Letters*, 26(16):1293–1294, 1990.
- [100] A. Petosa, A. Ittipiboon, Y. M. M. Antar, D. Roscoe, and M. Cuhaci. Recent Advances in Dielectric-Resonator Antenna Technology. *IEEE Antennas and Propagation Magazine*, 40:35–48, 1998.
- [101] A. Kishk. Wide-Band Truncated Tetrahedron Dielectric Resonator Antenna Excited by a Coaxial Probe. *IEEE Transactions on Antennas and Propagation*, 51(10):2913–2917, 2003.
- [102] A. Ittipiboon, A. Petosa, D. Roscoe, and M. Cuhaci. An Investigation of a Novel Broadband Dielectric Resonator Antenna. *Antennas and Propagation Society International Symposium*, 3:2038–2040, 1996.

- [103] A. Petosa, N. Simons, R. Siushansian, A. Ittipiboon, and M. Cuhaci. Design and Analysis of Multisegment Dielectric Resonator Antennas. *IEEE Transactions on Antennas and Propagation*, 48(5):738–742, 2000.
- [104] M. H. Neshati and Z. Wu. The determination of the resonance frequency of the TE_y^{111} mode in a rectangular dielectric resonator for antenna applications. 11th International Conference on Antennas and Propagation, 2001.
- [105] R. K. Mongia. Theoretical and experimental resonant frequencies of rectangular dielectric resonators. volume 139, pages 98–104. Proc. Inst. Elect. Eng., 1992.
- [106] Constantine Balanis. *Antenna Theory*. John Wiley & Sons, 1997.
- [107] H. Mosallaei. *Complex Layered Materials and Periodic Electromagnetic Band-Gap Structures: Concepts, Characterizations, and Applications*. PhD thesis, University of California, Los Angeles, 2001.
- [108] Y. M. Antar and Z. Fan. Theoretical investigation of aperture-coupled rectangular dielectric resonator antenna. *IEE Proceedings on Microwaves, Antennas and Propagation*, 1996.
- [109] G. Junker, A. Kishk, A. Glisson, and D. Kajfez. Effect of Fabrication Imperfections for Ground-Plane-Backed Dielectric-Resonator Antennas. *IEEE Antennas and Propagation Magazine*, 37(1):40–47, 1995.
- [110] G. Junker, A. Kishk, A. Glisson, and D. Kajfez. Effect of air gap on cylindrical dielectric resonator antenna operating in TM_{01} mode. *Electronics Letters*, 30(2):97–98, 1994.
- [111] G. Drosses, Z. Wu, and L. Davis. Aperture-Coupled Cylindrical Dielectric Resonator Antenna. *Microwave and Optical Technology Letters*, 20(6):407–414, 1999.
- [112] K. Sarabandi and H. Mosallaei. Novel artificial embedded circuit meta-material for design of tunable electro-ferromagnetic permeability medium. volume 3, pages 2061–2064. Microwave Symposium Digest, 2003 IEEE MTT-S International, 2003.
- [113] Karl Brakora and Kamal Sarabandi. Design of 3-D Monolithic MMW Antennas Using Ceramic Stereolithography. *IEEE Transactions on Antennas and Propagation*, 55(3):790–797, 2007.
- [114] P. F. Jacobs. *Stereolithography and Other RP&M Technologies*. ASME Press, 1996.
- [115] A. Petosa, A. Ittipiboon, Y. M. M. Antar, D. Roscoe, and M. Cuhaci. Recent Advances in Dielectric-Resonator Antenna Technology. *IEEE Antennas and Propagation Magazine*, 40:35–48, 1998.
- [116] R. K. Mongia and A. Ittipiboon. Theoretical and Experimental Investigations on Rectangular Dielectric Resonator Antennas. *IEEE Transactions on Antennas and Propagation*, 45(9):1348–1356, 1997.
- [117] D. M. Pozar and S. D. Targonski. Improved Coupling for Aperture Coupled Microstrip Antennas. *Electronics Letters*, 27:1129–1131, 1991.
- [118] R. Lelaratne and R. J. Langley. Performance of a scannable linear array of hi-lo stacked patches. *IEE Proc. on Microwaves, Antennas, and Propagation*, 150(1), 2003.
- [119] J. M. Tranquilla and S. R. Best. A Study of the Quadrifilar Helix Antenna for Global Positioning System (GPS) Applications. *IEEE Trans. on Antennas and Propagation*, 38(10), 1990.
- [120] Globalstar Retains Access to all of its Allocated U.S. Frequencies FCC Announcement Rules. Technical report, June 2004. www.globalstarusa.com.

- [121] D. F. Filipovic, M. A. Tassoudji, and E. Ozaki. A coupled-segment quadrifilar helical antenna. *Wireless Applications Digest, IEEE MTT-S Symposium on Technologies*, 1997.
- [122] A. Buerkle, K. Sarabandi, and H. Mosallaei. Compact Slot and Dielectric Resonator Antenna with Dual-resonance, Broadband Characteristics. *IEEE Trans. on Antennas and Propagation*, 53(3):1020–1027, 2005.

ABSTRACT

Modeling and Applications of Acoustic and Electromagnetic Wave Interaction

by

Amelia Marie Buerkle

Chair: Kamal Sarabandi

Acousto-electromagnetic wave interaction occurs when an electromagnetic wave scatters from an object under seismic or acoustic illumination. The vibration of the object under acoustic excitation gives rise to a frequency modulated scattered field which depends on the object and both the electromagnetic and acoustic source parameters. Previous work in this area has been limited to analytical solutions for homogeneous, circular cylinders and limited experimental work for specific applications. The objective of this research is to accurately predict the first Doppler component of the frequency modulated scattered field for arbitrary two-dimensional objects.

A unique formulation of the problem, which is built on the analytical solution, is implemented in the finite-difference time-domain method. The result is a tool which is capable of predicting the Doppler component scattered from general two-dimensional objects. This more general model provides information on system feasibility and is a major step towards implementing the acousto-electromagnetic method

in real-world systems.

Using the generalized model, the acousto-EM approach is also investigated for non-destructive evaluation applications. The Doppler component is inherently affected by the presence of interior flaws, which perturb the acoustic mode frequency and shape. Unique bistatic signatures for the Doppler component, which exhibit sensitivity to interior abnormalities, are presented. Depending on the flaw orientation, the target, and the mode of interest, the Doppler component can be orders of magnitude more sensitive than the unshifted electromagnetic fields scattered from the stationary target. A relative sensitivity parameter is introduced to quantify the improved sensitivity of the Doppler component relative to the unshifted fields; parameter values routinely indicate factors of ten improvement in sensitivity at certain bistatic angles. In addition, time-reversal focusing is used to locate regions of enhanced scattering, such as those surrounding a flaw, within the target. The results demonstrate that the Doppler component would be useful for detecting the presence of such abnormalities in a non-destructive evaluation system.